

# ION-BEAM INDUCED NANOSTRUCTURING OF SILICON AND ITS APPLICATIONS

*By*

**TANMOY BASU**

**PHYS07200804006**

**INSTITUTE OF PHYSICS, BHUBANESWAR**



*A thesis submitted to the*

*Board of studies in physical sciences*

*In partial fulfilment of requirements*

*For the degree of*

**DOCTOR OF PHILOSOPHY**

*of*

**HOMI BHABHA NATIONAL INSTITUTE**



**March, 2015**

# HOMI BHABHA NATIONAL INSTITUTE

## Recommendations of the Viva Voce Board

As members of the Viva Voce Board, we certify that we have read the dissertation prepared by Tanmoy Basu entitled “Ion-beam induced nanostructuring of silicon and its applications” and recommend that it may be accepted as fulfilling the dissertation requirement for the Degree of Doctor of Philosophy.

\_\_\_\_\_ **Date:**

**Chairman-**

\_\_\_\_\_ **Date:**

**Convener-**

\_\_\_\_\_ **Date:**

**Mamber1-**

\_\_\_\_\_ **Date:**

**Mamber2-**

\_\_\_\_\_ **Date:**

**Mamber3-**

Final approval and acceptance of this dissertation is contingent upon the candidate's submission of the final copies of the dissertation to HBNI.

I hereby certify that I have read this dissertation prepared under my direction and recommend that it may be accepted as fulfilling the dissertation requirement.

**Date:**

**Place:**

## **STATEMENT BY AUTHOR**

This dissertation has been submitted in partial fulfilment of requirements for an advanced degree at Homi Bhaba National Institute (HBNI) and is deposited in the Library to be made available to borrowers under rules of the HBNI.

Brief quotation from this dissertation are allowable without special permission, provided that accurate acknowledgement of source is made. Requests for permission for extended quotation from or reproduction of this manuscript in whole or in part may be granted by the Competent Authority of HBNI when in his or her judgement the proposed use of the material is in the interests of scholarship. In all other instances, however, permission must be obtained from the author.

**TANMOY BASU**

## **DECLARATION**

I, hereby declare that the investigation presented in the thesis has been carried out by me. The work is original and has not been submitted earlier as a whole or in part for a degree / diploma at this or any other Institution / University.

**Tanmoy Basu**

*To my parents*

## Acknowledgments

The exciting and challenging journey of Ph. D. life and all the accomplishments that I have achieved during my stay at Institute of Physics, Bhubaneswar won't be possible without the support, help, and guidance of my advisor, Prof. T. Som. I take this opportunity to express my sincere gratitude to him, for his constant encouragement and enormous energy towards my cause. His innovative way of looking into the problem with an admixture of professionalism and perfectionism will remain as assets for the rest of my life. I sincerely thank him and his family for their care and hospitality which never let me feel away from home during my stay in abroad and in IOP. It has been truly a life time achievement for me to work under his guidance.

I am thankful to Dr. A. Kanjilal, SNU, Noida, and Prof. R. M. Bradley, Colorado University, USA, for allowing me to work with them. I must thank Dr. Stefan Facsko, HZDR, Germany, for his hospitality during my stay in Germany. I would like to express my high regards for Dr. D. Kanjilal, IUAC, New Delhi who always helped me to solve various ion-source related problems.

I would like to thank Prof. P. Ayub, TIFR, Mumbai, Dr. B. Satpati, SINP, Kolkata, Dr. J. Ghatak, JNCASR, Bengaluru, Dr. S. Chatterjee, IMMT, Bhubaneswar, Dr. J.K. Tripathi, and Dr. P.K. Sahoo, NISER, Bhubaneswar for extending their lab facilities and precious time towards characterization of my research samples and relevant discussion.

I would also like to acknowledge my senior group members Dr. V. Venugopal, SIT, Tumkur, Dr. O.P Sinha, Amity University, Noida, and Dr. D.P. Datta for our valuable discussion and providing me a chance to work with them. My special thanks to Dr. D.P. Datta for spending his valuable time in finalizing the thesis. My special thanks go to Dr. S. Chnadramoham, Dr. S. Nandy, Dr. S. Hazra, Dr. A.K. Mahapatra, and Dr. S.P. Patel for their helps during various stages of my research life.

I would like to thank my lab mates, viz. Mr. Sandeep Garg, Mr. Mohit Kumar, and Mr. Jyoti Ranjan Mohanty, Mr. Ranveer Singh, and Mr. Mahesh Saini for their constant helps in every aspects of my life. I must acknowledge Mr. Lingraj for his dedicated service, given to the SUNAG lab and keeping it always clean.

I thank all my teachers who taught me in pre-doctoral course and all the experimental condensed matter group faculties of IOP, Bhubaneswar for their generous support. I also thank to scientific staff of IOP, especially Mr. S.K. Choudhury and Dr. S.N. Sarangi for making themselves available wherever their expertise was required for the lab. In fact, I have learnt a lot about vacuum systems from Mr. S.K. Choudhury.

I am grateful to the former directors: Prof. Y.P. Viyogi, Prof. A. Khare, Prof. A.M. Jayannavar, Prof. A.M. Srivastava, and the present director, Prof. S. Panda, Dean HBNI at IOP, Prof. A.M. Srivastava, members of my Doctoral committee: Prof. S. Varma, Prof. S. K. Patra, and Prof. A.M. Jayannavar, and all the members (academic and non-academic) for their timely help, cooperation, and support whenever needed.

A special acknowledgment goes to my friends who have been invaluable to the success of my research and to my happiness during these Ph. D. days. In particular: my batch mates Raghu, Raj, and Pramita are among the best friends that I can ever have. I would also like to thank my friends Mr. Arup Das and Mr. Amit Das for their helps during very critical period of my life. Of course, I cannot forget the football team of IOP and thanks to all the members of the team for making me happy with all the victories we got. Thanks to all the seniors and junior scholars of IOP for their direct or indirect assistances in many cases during the stay.

Most importantly, I have always been fortunate in being able to count on continuous support from my parents, brother, relatives, and my wife, Ambika. They have always believed in me and their constancy has kept me going during all these years. In particular, I am indebted to my

parents for providing me with their love, education, and it is because of them that I was able to become the person I am today.

Date:

Place:

Tanmoy Basu

## List of Publications

### Published In Journal

1. \*Thickness-controlled photoresponsivity of ZnO:Al/Si heterostructures: Role of junction barrier height by **T. Basu**, M. Kumar, and T. Som: Materials Letters 135 (2014) 188
2. \*Tunable antireflection from conformal Al-doped ZnO films on nanofaceted Si templates by **T. Basu**, M. Kumar, P.K. Sahoo, A. Kanjilal, and T. Som: Nanoscale Research Letters 9 (2014) 192.
3. \*Temporal evolution of ripple pattern on silicon surface: An ion induced solid flow approach by **T. Basu**, and T. Som: Applied Surface Science 310 (2014) 142.
4. \*Transition from ripples to faceted structures under low-energy argon ion bombardment of silicon: Understanding the role of shadowing and sputtering by **T. Basu**, D.P. Datta, and T. Som: Nanoscale Research Letters 8 (2013) 289.
5. \*Unusual pattern formation on Si(100) due to low energy ion bombardment by **T. Basu**, J.R. Mohanty, and T. Som: Applied Surface Science 258 (2012) 9944.
6. Formation of self-organized nanostructures on semi-insulating InP by 100 keV Ar<sup>+</sup>-ion implantation by J.R. Mohanty, **T. Basu**, D. Kanjilal, and T. Som: Applied Surface Science 258 (2012) 4139.
7. Ion erosion induced nanostructured semiconductor surfaces by V. Venugopal, **T. Basu**, S. Garg, J.K. Tripathi, S. Chandramohan, P. Das, T.K. Chini, S.R. Bhattacharyya, D. Kanjilal, and T. Som: International Journal of Nanotechnology 9 (2012) 1007.
8. Nanostructures on GaAs surfaces due to 60 keV Ar<sup>+</sup>-ion beam sputtering by V. Venugopal, S.K. Garg, **T. Basu**, O.P. Sinha, D. Kanjilal, S.R. Bhattacharyya, and T. Som: Applied Surface Science 258 (2012) 4144.
9. Evolution of ripple morphology on Si(100) by 60 keV argon ions by, S.k. Garg, V. Venugopal, **T. Basu**, O.P. Sinha, S. Rath, D. Kanjilal, and T. Som: Applied Surface Science 258 (2012) 4135.
10. Evolution of microstructure and surface topography of gold thin films under thermal annealing by P. Dash, H. Rath, B.N. Dash, P. Mallick, **T. Basu**, T. Som, U.P. Singh, and N.C. Mishra: AIP Conference Proceedings 1461 (2012) 214.

11. Evolution of surface topography on GaAs (100) and GaAs (111) at normal and oblique incidence of Ar<sup>+</sup>-ions by V. Venugopal, S.K. Garg, **T. Basu**, S. Majumder, S.N. Sarangi, T. Som, P. Das, S.R. Bhattacharyya, and T.K. Chini: AIP Conference Proceedings 1276 (2010) 50.

### **Communicated**

1. \*Substrate morphology driven shift in excitonic peak of Al doped ZnO nanobeads on rippled silicon surface by **T. Basu**, M. Kumar, S. Nandy, B. Satpati, and T. Som: Journal of Applied Physics.
2. Tailoring room temperature photoluminescence of antireflective silicon nanofacets by **T. Basu**, M. Kumar, A. Kanjilal, J. Ghatak, P.K. Sahoo, and T. Som: Journal of Applied Physics.

### **To be communicated**

1. \*Roughness engineering using continuous substrate rotation during sputtering of silicon by **T. Basu**, M. Kumar, R.M. Bradley, and T. Som
2. \*Field emission from Si nanofacets: Role of native oxide layer, **T. Basu**, M. Kumar, and T. Som

(\*) indicates papers on which this thesis is based.

# Synopsis

Nowadays, cutting edge research requires tailor-made properties of materials for advanced technological applications. In the context of synthesis and modification of physical (e.g. structural, optical, and magnetic) properties of materials in micro- and/or nano-scale, ion irradiation offers a precise control to achieve the same. Ion bombardment is a non-equilibrium processing route which offers deposition of energy in a target material, leading to radiation damage, introduction of foreign atoms into the target beyond equilibrium thermodynamics in the form of ion implantation, and also removal of surface atoms of the target known as sputtering. Recently, a lot of effort has been put to make use of ion-beam sputtering in creating self-organized patterns on materials surfaces.

Fabrication of semiconductor nanostructures in a controlled manner is one of the key requirements for developing optoelectronic devices. Although electron-beam lithography is able to fabricate nanoscale structures, the low throughput of serial lithographic methods and high production cost pose severe problems. Thus, a constant effort is being put to look for smart techniques to generate surface nanostructures. Ion beam sputtering is commonly employed in many industrial processes to modify the properties of solid surfaces. Under certain experimental conditions, the bombardment of solid surfaces by low and medium energy ions may induce a surface instability that results in the formation of periodic patterns with nanometer periodicity on irradiated surfaces [1]. Depending on the irradiation conditions, different nanoscale patterns can evolve in the form of periodic ripple patterns, hexagonally ordered dot arrays, and faceted structures [2], with periodicities ranging from few tens to several hundreds of nanometres. Over the years, sputter-induced ripple structures were observed in different materials like insulators, semiconductors, and metals [1].

For last two or three decades continuous effort is being made to explain evolution of solid surface topography during ion-beam irradiation. It started with the notion that pattern formation is usually governed by an interplay between the dynamics of surface roughening due to sputtering and smoothing due to material transport during surface diffusion. Models have shown that surface instabilities can arise from curvature-dependent sputter erosion or due to ion impact-induced mass redistribution. The first successful continuum theory to explain ripple formation was developed by Bradley and Harper (BH) on the basis of so called micro-roughening instabilities [3]. By using Sigmund's theory [4] of sputtering, they were able to show that the curvature-dependent sputtering yield induces an instability at the surface which leads to an amplification of initial modulation. Under the presence of smoothening process like surface self-diffusion, a wavelength selection is observed. BH theory is able to reproduce early stage of ripple evolution and ripple rotation albeit the presence of a stable surface up to a critical angle of incidence in case of monatomic materials (e.g. Si and Ge) remained unsolved. In another note, the smoothing at angles below the critical angle was addressed by Carter and Vishnyakov (CV) [5]. These two effects, viz. BH and CV have been combined into a single framework by Madi *et al.* where they have clearly enunciated that it was actually the prompt atomic redistribution (rephrased CV effect) as compared to sputter erosion which governs the pattern formation on Si under ion bombardment and explained the presence of a stable surface below the critical angle as well [6].

On the other hand, an alternative model known as hydrodynamic approach, also describes low energy ion induced pattern formation. It, basically, deals with the idea of amorphous solid flowing due to ion impact at a proper time scale. A small extension of this approach is the solid flow model [7] where ion-induced stress eventually drives the solid to flow with the pre-amorphized layer generated due to ion bombardment and as a result surface nanopattern develops. Solid flow model offers the advantage of time dependent (dynamic) evolution of

ripple patterns at a timescale where molecular dynamics (MD) based calculations cannot probe properly. In fact, this is the first theory to predict the timescale (intrinsic timescale) beyond which nonlinear effect starts appearing in the system. Although BH theory explains early stage of ripple evolution, the saturation of ripple amplitude at a longer timescale cannot be explained within the framework of a linear continuum model. In the nonlinear regime, surface roughness does not follow the exponential behaviour and ripple coarsening may take place [8]. Cuerno and Barabási developed a nonlinear continuum equation of Kuramoto-Shivashinsky (KS)-type [8]. It is to be noted that apart from nonlinear effects, the role of shadowing becomes crucial in pattern formation, particularly at higher oblique angles of incidence. According to Carter, due to shadowing of the incoming ion-beam, ripple structures can be transformed into triangular faceted structures [9]. However, this shadowing transition and the role of sputtering for the same are not well documented [especially in the low energy (few hundreds of eV) regime] till date. Thus, systematic experimental studies at higher oblique incidences are required to understand the underlying mechanisms, governing the pattern formation. These may be achieved by studying the temporal evolution of nanopatterns at grazing incidences where one can expect faceted/sawtooth morphology.

Apart from studying the fundamental aspects of pattern formation, nowadays, ion-induced nanopatterns become interesting for various technological applications. Experiments reveal the applicability of nanoripples in fabrication of optically active and electronic devices. Very recently, Martella *et al.* [10] reported on the broadband light trapping property of self-organized nanopatterned Si substrates which can be effectively used for photon harvesting in ultra-thin crystalline solar cells. In addition, rippled substrates are becoming potential templates for thin film deposition. For instance, Ranjan *et al.* [11] showed silver nanoparticles on Si ripples are capable of tuning the plasmon resonance while recently, tunability of magnetic anisotropy in Fe/Cr/Fe multilayer structures was demonstrated by Körner *et al.* [12] by using nanoscale

rippled Si templates for depositing. All the above-mentioned studies indicate the multifaceted applications of patterned substrates where they themselves or in the form of a template leads to modification of optical, photovoltaic, and magnetic properties of the materials.

For technological purpose, it is necessary to have a precise control over the patterns. This, in turn, requires detail knowledge of the pattern formation process and the underlying mechanisms. Different theories are emerging to explain the observed patterns which are accompanied by a large number of experimental data. However, the field is suffering from various issues like impurity induced pattern formation and the lack of lab-to-lab reproducibility. This indicates, up to now, the pattern formation mechanism is not fully understood. Thus, it is exigent to first optimize the pattern formation process and then explore the possible technological applications. In fact, systematic experimentation is needed to understand the role of sputtering, shadowing (at higher oblique incidences), and concurrent substrate rotation in pattern formation. The next step would be to use those patterns for some application purpose.

The second aspect is related to the application of the above-mentioned nanostructures where we have used rippled- and faceted-Si as templates for deposition of Al-doped zinc oxide (AZO) thin films which is known to be a transparent conducting oxide. The conformal growth of AZO overlayer was studied for both rippled- and faceted-Si. For rippled-Si substrates, a thickness-dependent shift in the excitonic peak of AZO was observed from the photoluminescence spectra which indicate the presence of quantum confinement effect. On the other hand, AZO on faceted-Si showed tunable antireflection property with varying AZO thickness. Moreover, AZO/faceted-Si heterojunction showed enhanced solar cell efficiency and spectral response.

Pulsed dc magnetron sputtering setup. To analyse the morphology, microstructure, composition, and crystallinity of the samples we used atomic force microscopy (AFM), scanning electron microscopy (SEM), cross-sectional transmission electron microscopy

(XTEM), energy dispersive X-ray spectrometry (EDS), X-ray photoelectron spectroscopy (XPS), and X-ray diffraction (XRD), respectively. In parallel, simulations of ion-solid interaction were performed using SRIM and TRIDYN codes. The optical properties of nanofaceted-Si and AZO grown on faceted-Si were investigated using UV-Vis spectroscopy and photoluminescence. Finally, the optoelectronic properties of AZO/Si heterojunctions thin films were studied by I-V, C-V, and photoresponsivity measurements.

The thesis is organized in seven chapters. The first chapter provides a brief introduction, the second chapter describes the experimental techniques used in this thesis, and the third chapter provides the theoretical background of ion-beam induced pattern formation. In chapter 4, the experimental results are presented where we describe pattern formation in the angular window of  $0^{\circ}$ - $85^{\circ}$ . The presence of stable surface up to  $50^{\circ}$  (explained by CV effect) is observed whereas ripple formation start taking place from  $51^{\circ}$ . The temporal evolution of ripple morphology in the angular window of  $51^{\circ}$ - $72.5^{\circ}$  and its explanation in light of solid flow model. With the help of this model, we could also identify the linear and nonlinear regimes of ripple evolution. In addition, for the same angular window and beyond (up to  $85^{\circ}$ ), we describe the pattern evolution in nonlinear regime. The present experiments show that beyond linear regime, with increasing ion incidence angle, coarsened ripple patterns (with wave vector oriented parallel to the direction of the ion-beam) are observed at  $67^{\circ}$ . Above this angle, a gamut of unusual patterns form (e.g. mounds, facets, and needle-like structures) before ripple rotation takes place (from parallel to perpendicular-mode) at  $80^{\circ}$ . It has been shown that the temporal evolution of morphology at higher oblique incidences ( $70^{\circ}$ - $72.5^{\circ}$ ) originates from the shadowing effect of the ion-beam, leading the ripples to get transformed faceted structures. At even higher fluences, coarsening of these facets are seen which is explained on the model proposed by Hauffe [13]. On the other hand, ripple rotation is explained in light of BH theory. It may be mentioned that beyond ripple rotation, we observe flat surface which is mostly attributed to low sputtering

yield and high degree of reflection of incident ions at grazing incidence angles. We have also shown the effect of concurrent substrate rotation on pattern formation in Si. It is observed that the stable surface remains stable while rippled and faceted surfaces get changed into mound-like structures. Corresponding temporal evolution study at a fixed angle of incidence ( $67^\circ$ ) revealed coarsening of mounds. In addition, for a fixed angle of incidence of ion-beam, rotation speed variation leads to saturation of surface roughness. All these observations has been explained by a nonlinear theory proposed by Bradley [14].

In chapter 5, we show that faceted structures are capable of showing tunable antireflection, photoluminescence, and field emission properties. Photoluminescence property is attributed to various defects and surface states present in facets whereas the improved antireflection property (in the range of 300-800 nm) is attributed to the graded refractive index effect. In fact, it is evident that higher antireflection leads to an enhancement of photoluminescence intensity up to two orders of magnitude.

Such nanofacets could be potentially useful as electron emitters where the field lines should concentrate at the apexes reducing the barrier for electron emission. It may be mentioned that although Si nanowires/nanocones are likely candidates for potentially good field emitters the limitation comes due to surface oxidation of Si nanostructures. In this thesis, we have undertaken the case study of field emission from such self-organized faceted nanostructures. In doing so, we have used both bulk and local probe techniques. Bulk measurements indicate a turn-on potential of  $4.7 \text{ Volt } \mu\text{m}^{-1}$  having a stability up to 1 h. However, bulk measurements cannot specifically identify the regions of faceted structures which give rise to field emission. To overcome this problem, we employed atomic force microscope-based local probe technique, namely tunnelling atomic force microscopy (TUNA) [15]. TUNA measurements clearly show that the sidewalls of Si faceted nanostructures actually contribute to the field emission process instead of the apexes. This observation can be explained in light of native oxide formation at

the apexes of the facets which corroborates well with transmission electron microscopy and scanning Kelvin probe microscopy based studies.

In chapter 6, we make use of nanostructured Si as templates for growth of ZnO:Al (AZO) thin films. At first, we show the conformal growth of AZO overlayer on rippled-Si and modification and tuning its optical property as a function of fluence. The role of quantum confinement has been highlighted to explain the observed blue shift in the near band excitonic peak. Next, we show the efficacy of AZO overlayers (30-90 nm) grown on ion-beam synthesized nanofaceted-Si for further suppressing the reflection down to very low values. In particular, we observe tunable antireflection property from conformally grown AZO layers, followed by a systematic shift in the reflection minima from ultraviolet to visible to near-infrared regions with increasing thickness. Tunable antireflection property is understood in light of depth-dependent refractive index of nanofaceted-Si and the AZO overlayers. The antireflection property helps increasing the fill factor of such textured AZO/Si heterostructure, which reaches its maximum for 60 nm AZO compared to the ones based on planar-Si. This thickness matches with the one that shows the maximum reduction in surface reflectance. In order to understand the decrease in the fill factor at higher AZO thicknesses (>60 nm), current-voltage (I-V) and capacitance-voltage (C-V) measurements were carried out. I-V measurements reveals increase in the leakage current beyond 60 nm thick AZO which in turn reduces the fill factor. However, thickness-dependent enhancement in the photoresponsivity is attributed to the reduced potential barrier across the *n*-AZO/*p*-Si junction due to the use of nanofaceted-Si templates as corroborated from the capacitance-voltage measurements.

In chapter 7, we provide a summary of this work which deals with low energy ion-beam induced self-organized nanopatterning of *p*-Si(100) surfaces. In order to do so, a large angular window (0°-85°) and energy in the range of 500-1750 eV were chosen. The experimental studies show the presence of stable surfaces up to 50° whereas surfaces become unstable in the angular

window of  $51^{\circ}$ - $80^{\circ}$ . In the linear regime, ripple evolution is explained by solid flow model, whereas ripples get coarsened in the nonlinear regime. In addition, at higher oblique incidences ( $70^{\circ}$ - $72.5^{\circ}$ ), ripple-to-facet transition has been demonstrated due to shadowing effect. The coarsening behaviour of the observed facets as a function of time at higher oblique incidences is attributed to the reflection of primary ions from the neighbouring facets. These ion-beam fabricated faceted nanostructures are seen to be capable of showing tunable antireflection, photoluminescence, and field emission. From the application point of view, the ion-beam fabricated rippled-Si substrates are demonstrated to be useful in modifying photoluminescence of AZO overlayer. On the other hand, upon using nanofaceted-Si as templates, for conformal growth of AZO, we show tunable antireflection and photovoltaic properties. The tunable antireflection due to the underlying nanofaceted-Si substrates leads to an enhancement in the fill factor (maximum for 60 nm thick AZO overlayer) of AZO/faceted-Si heterojunction solar cell by a factor of 2.5. In addition, concurrent substrate rotation during ion bombardment yields formation of mounds at those incidence angles where we observe ripples and facets in the static case. In this chapter, we also provide a scope of future work in this direction.

## **Bibliography**

1. T. Som, D. Kanjilal, Nanofabrication by ion-beam sputtering: Fundamentals and Applications. 2012: Pan Stanford, Singapore.
2. S. Facsko, T. Dekorsy, C. Koerdt, C. Trappe, H. Kurz, A. Vogt, and H. Hartnagel, Science 285 (1999) 1551.
3. R.M. Bradley, and J.M.E. Harper, J. Vac. Sci. Technol. A 6 (1988) 2390.
4. P. Sigmund, J. Mater. Sci. 8 (1973) 1545.
5. G. Carter and V. Vishnyakov, Phys. Rev. B 54 (1996) 17647.
6. C.S. Madi, E. Anzenberg, K.F. Ludwig Jr., and M.J. Aziz, Phys. Rev. Lett. 106 (2011) 066101.

7. M. Castro, R. Gago, L. Vázquez, J. Muñoz-García, R. Cuerno, *Phys. Rev. B* 86 (2012) 214107.
8. M.A. Makeev, R. Cuerno, and A.L. Barabási, *Nucl. Instrum. Meth. B* 197 (2002) 185.
9. G. Carter, *J. Appl. Phys.* 85 (1999) 455.
10. C. Martella, D. Chiappe, C. Mennucci, and F. Buatier de Mongeot, *J. Appl. Phys.* 115 (2014) 194308.
11. M. Ranjan, S. Facsko, M. Fritzsche, S. Mukherjee, *Microelectron. Eng.* 102 (2013) 44.
12. M. Körner, K. Lenz, M. O. Liedke, T. Strache, A. Mücklich, A. Keller, S. Facsko, and J. Fassbender, *Phys. Rev. B* 80 (2009) 214401.
13. W. Hauffe, *Phys. Stat. Sol. (a)* 35 (1976) K93.
14. R.M. Bradley, *Phys. Rev. E* 54 (1996) 6149.
15. V. Chatterjee, R. Harniman, P.W. May, and P.K. Barhai, *Appl. Phys. Lett.* 104 (2014) 171907

## Table of contents

Synopsis .....	xi
List of figures.....	xxiii
<b>1. Introduction .....</b>	<b>1</b>
1.1 Preamble .....	1
1.2 Self-organized nanopatterning by ion irradiation .....	2
1.3 Motivation.....	5
1.4 Outline of the thesis .....	10
<b>2. Experimental techniques and analysis methods .....</b>	<b>17</b>
2.1 Ion-beam induced surface nanostructuring setup (IBSN).....	17
2.2 DC Magnetron sputtering.....	23
2.3 Stylus profilometry .....	26
2.4 Atomic force microscopy (AFM) .....	28
2.5 Scanning electron microscopy (SEM) .....	36
2.6 Transmission electron microscopy (HRTEM).....	37
2.7 X-ray diffraction (XRD) .....	40
2.8 Compositional analysis .....	42
2.8.1 Energy dispersive x-ray spectrometry (EDS) .....	43
2.8.2 X-ray photoelectron spectroscopy (XPS).....	44
2.9 Optical studies.....	46
2.9.1 Reflectance.....	46
2.9.2 Photoluminescence.....	47
2.10 Electrical measurements .....	48
2.10.1 Resistivity .....	48
2.10.2 <i>I-V</i> characteristics.....	49
2.10.3 <i>C-V</i> characteristics .....	49
2.10.4 Photoresponsivity studies.....	50
2.10.5 Field emission studies .....	54
<b>3. Theoretical Background.....</b>	<b>59</b>
3.1 Statistical characterization of surfaces .....	59
3.2 Ion-Solid interaction .....	61
3.2.1 Stopping of ions in matter .....	63
3.2.2 Ion range and straggling.....	67
3.2.3 Basics of sputtering.....	69

3.2.4 Numerical simulation of ion-solid interaction .....	70
3.3 Continuum theories of ion-irradiated surface evolution .....	72
3.3.1 Bradley-Harper (BH) theory .....	75
3.3.2 Carter-Vishniyakov Theory .....	77
3.3.3 Relaxation mechanisms.....	80
3.3.4 Solid flow model.....	82
3.3.5 Effect of concurrent substrate rotation.....	85
3.4 Shadowing effect .....	88
<b>4. Evolution of morphology on Si surface under low energy Ar<sup>+</sup>-ion irradiation.....</b>	<b>94</b>
4.1 Introduction.....	94
4.2 Experimental .....	100
4.3 Results and discussion .....	102
4.3.1 Temporal evolution of ripple patterns.....	102
4.3.2 Role of ion incidence angle on pattern formation.....	108
4.3.3 Role of shadowing: Ripple to facet transition.....	112
4.3.4 Evolution of morphology under substrate rotation .....	120
4.4 Conclusions.....	129
<b>5. Tunable optoelectronic properties of nano- patterned-Si surfaces.....</b>	<b>134</b>
5.1 Tailoring room temperature photoluminescence of antireflective Si nanofacets.....	134
5.1.1 Introduction.....	134
5.1.2 Experimental .....	136
5.1.3 Results and discussion .....	137
5.1.4 Conclusions.....	148
5.2 Field emission from nanofaceted-Si: Role of native oxide.....	149
5.2.1 Introduction.....	149
5.2.2 Experimental .....	151
5.2.3 Results and discussion .....	152
5.2.4 Conclusions.....	157
<b>6. Nanopatterned-Si surfaces: Templates for growth of Al-doped ZnO (AZO).....</b>	<b>163</b>
6.1 Growth of AZO on rippled-Si.....	163
6.1.1 Introduction.....	163
6.1.2 Experimental .....	165
6.1.3 Results and discussion .....	167
6.1.4 Conclusions.....	177

6.2 Growth of AZO on nanofaceted Si .....	178
6.2.1 Tunable antireflection from conformal Al-doped ZnO films on nanofaceted Si templates .....	178
6.2.1.1 Introduction.....	178
6.2.1.2 Experimental .....	179
6.2.1.3 Results and discussion .....	181
6.2.1.4 Conclusions.....	189
6.2.2 Thickness-controlled photoresponsivity of ZnO:Al/Si heterostructures : Role of junction barrier height.....	190
6.2.2.1 Introduction.....	190
6.2.2.2 Experimental .....	191
6.2.2.3 Results and discussion .....	192
6.2.2.4 Conclusions.....	196
<b>7. Summary and future scope.....</b>	<b>201</b>

# List of figures

Figure 2.1: Ion-beam induced surface nanostructuring (IBSN) setup.....	18
Figure 2.2: Cross sectional view of the low energy ion source in IBSN.....	20
Figure 2.3: The outside view of the ion Tectra-make Gen II ECR-based source.....	21
Figure 2.4: Schematic of the high vacuum pulsed dc magnetron sputtering setup.....	24
Figure 2.5: Pulsed dc sputtering set up at SUNAG laboratory.....	25
Figure 2.6: Stylus surface profilometer.....	27
Figure 2.7: Schematic of AFM setup.....	29
Figure 2.8: Van der Waal's force as a function of tip to surface distance.....	30
Figure 2.9: MFPD AFM setup.....	32
Figure 2.10: Schematic representation of DPTCM using MFP-3D AFM setup.....	35
Figure 2.11: Schematic diagram of TEM parts, image formation and diffraction pattern formation process.....	39
Figure 2.12: Schematic diagram of Bragg's reflection.....	40
Figure 2.13: XRD setup.....	42
Figure 2.14: Schematic diagram of the XPS setup displaying different components.....	46
Figure 2.15: UV-Vis spectrophotometer.....	47
Figure 2.16: Schematic diagram of the Photoresponsivity measurement setup.....	53
Figure 3.1: Interaction of energetic ions with solid target.....	62
Figure 3.2: Rate of energy deposition, $dE/dx$ , for $Ar^+$ -ions in Si. Nuclear, electronic and total energy losses are plotted as a function of incident ion energy ( $E$ ). The energy losses are calculated using SRIM 2012 Monte Carlo simulation code.....	66
Figure 3.3: Schematic diagram for definition of penetration depth, spread, radial range, and projected range.....	68
Figure 3.4: Schematic demonstration of Gaussian energy deposition of an incoming ion inside a target. $\theta$ : global angle of incidence; $\gamma$ : local angle of incidence.....	74

Figure 3.5: Schematic illustration of the origin of the surface instability induced by ion beam erosion of non-planar surfaces. $\theta$ : global angle of incidence; $\gamma$ : local angle of incidence.....	76
Figure 3.6: Schematic illustration of the parallel-mode ripples.....	77
Figure 3.7: Schematic diagram of the laboratory coordinate frame ( $x, z$ ) along with the local coordinate frame ( $x', z'$ ) to represent the CV mechanism. The local normal to the surface is represented by the unit vector $z'$ which also the one axis of local coordinate frame.....	78
Figure 3.8: Illustration of geometry of ion bombardment on a sinusoidal profile.....	89
Figure 4.1: Cross-sectional TEM image corresponding to ion incidence angle of $60^\circ$ where the amorphous layer is marked by the red line. The inset shows slightly zoomed out version of the same sample.....	103
Figure 4.2: Roughness evolution plot corresponding to incidence angle of $60^\circ$ . The inset shows the AFM topographic images corresponding to exposure times of 1, 5.5, and 11 min, respectively.....	103
Figure 4.3: AFM micrographs of $p$ -Si(100): Exposed at an incidence angle of $51^\circ$ for different times starting from 5 to 66 min. The arrow indicates the direction of the incoming ion beam.....	104
Figure 4.4: Variation in roughness with exposure time for the incidence angle of $51^\circ$ where the exponential fit is well realized. The inset shows the plot for wavelength versus exposure time at $51^\circ$ .....	104
Figure 4.5: Temporal evolution of surface roughness at $\theta=65^\circ$ . Images corresponding to 2.2, 3.3, and 4.4 min of exposure times are shown as insets for a realization of the corresponding surface morphology.....	106
Figure 4.6: Complete temporal evolution of surface roughness at all incidence angles. The dashed lines indicate the time beyond which the nonlinear effects start under the solid flow model where the exponential growth of roughness does not occur anymore.....	108
Figure 4.7: AFM images of Si(100): (a) Pristine and exposed to 500 eV $\text{Ar}^+$ -ions to the fluence of $5 \times 10^{17}$ ions $\text{cm}^{-2}$ at incident angles of (b) $65^\circ$ , (c) $67^\circ$ , (d) $70^\circ$ , (e) $72.5^\circ$ , (f) $77.5^\circ$ , (g) $80^\circ$ , and (h) $82.5^\circ$ . Corresponding height scales in (a)-(h) are 1 nm, 15 nm, 23 nm, 37 nm, 51 nm, 19 nm, 3 nm, and 2 nm, respectively. Arrows indicate projection of the ion beam on the surface. Insets show the 2D FFT obtained from the corresponding images.....	109
Figure 4.8: AFM images of Si(100) exposed to 500 eV $\text{Ar}^+$ -ions to the fluence of $5 \times 10^{17}$ ions $\text{cm}^{-2}$ at incident angles of (a) $0^\circ$ , (b) $10^\circ$ , (c) $25^\circ$ , (d) $45^\circ$ , (e) $50^\circ$ , and (f) $51^\circ$ . Corresponding height scales in (a)-(f) are 1 nm, 1 nm, 1 nm, 1 nm, 1 nm, and 2 nm, respectively.....	111
Figure 4.9: (a) Evolution of rms surface roughness corresponding to different angle of incidence. (b) Plot of sputtering yield versus angle of incidence obtained from TRIDYN simulation performed for 500 eV $\text{Ar}^+$ -ions to the fluence of $5 \times 10^{17}$ ions $\text{cm}^{-2}$ .....	112

Figure 4.10: AFM images of (a) pristine-Si and those exposed to 500 eV Ar<sup>+</sup>-ions at an incidence angle of 70° to various fluences: (b) 1×10<sup>17</sup> ions cm<sup>-2</sup>, (c) 2×10<sup>17</sup> ions cm<sup>-2</sup>, (d) 5×10<sup>17</sup> ions cm<sup>-2</sup>, (e) 10×10<sup>17</sup> ions cm<sup>-2</sup>, (f) 15×10<sup>17</sup> ions cm<sup>-2</sup>, and (g) 20×10<sup>17</sup> ions cm<sup>-2</sup>, respectively. The corresponding height scales for (a)-(g) are: 1 nm, 4.3 nm, 9.9 nm, 39.5nm, 60.9 nm, 85.7 nm, and 182.2 nm. For better clarity (a)-(c) represent images acquired over a scan area of 1μm×1μm whereas (d)-(g) are of scan area 2μm×2μm. Insets show the 2D autocorrelation functions for corresponding images.....113

Figure 4.11: AFM images of silicon exposed to 500 eV Ar<sup>+</sup>-ions at 72.5° incidence angle at fluences of (a) 1×10<sup>17</sup> ions cm<sup>-2</sup>, (b) 2×10<sup>17</sup> ions cm<sup>-2</sup>, (c) 5×10<sup>17</sup> ions cm<sup>-2</sup>, (d) 1×10<sup>18</sup> ions cm<sup>-2</sup>, (e) 1.5×10<sup>18</sup> ions cm<sup>-2</sup>, and (f) 2×10<sup>18</sup> ions cm<sup>-2</sup>, respectively. The corresponding height scales for (a)-(f) are: 4 nm, 4 nm, 74 nm, 86 nm, 154nm, and 165 nm. For better clarity (a) & (b) have scan size of 1μm×1μm whereas (c)-(f) have scan size of 2μm×2μm. Insets show the 2D autocorrelation functions for corresponding images.....114

Figure 4.12: Line profiles extracted from the AFM images of ion exposed samples at 70° for various fluences: (a) 1×10<sup>17</sup>, (b) 2×10<sup>17</sup>, (c) 5×10<sup>17</sup>, (d) 10×10<sup>17</sup>, (e) 15×10<sup>17</sup>, and (f) 20×10<sup>17</sup> ions cm<sup>-2</sup>, respectively. Arrow indicates the direction of ion-beam onto the surface.....117

Figure 4.13: Line profiles extracted from the AFM images of ion exposed samples at 72.5° for different ion fluences: (a) 1×10<sup>17</sup>, (b) 2×10<sup>17</sup>, (c) 5×10<sup>17</sup>, (d) 10×10<sup>17</sup>, (e) 15×10<sup>17</sup>, and (f) 20×10<sup>17</sup> ions cm<sup>-2</sup>, respectively. Arrow indicates the direction of ion-beam onto the surface.....117

Figure 4.14: Schematic diagram depicting the mechanism responsible for coarsening of faceted structures at 72.5° (as a representative one). Arrows indicate the incident ion-beam.....118

Figure 4.15: Variation in rms surface roughness, ‘w’ with lateral feature dimension corresponding to both angles of incidence.....119

Figure 4.16: Variation in fractional change of the sputter erosion rate, ‘F’ with lateral feature dimension corresponding to both angles of incidence.....119

Figure 4.17: AFM images of (a) Pristine-Si and and exposed Si to 500 eV argon ions at a fluence of 5×10<sup>17</sup> ions cm<sup>-2</sup> at different angles under continuous substrate rotation in the angular range of 40°-85°. Corresponding height scales in (a-f) are 1 nm, 1 nm, 4 nm, 8 nm, 10 nm, and 2 nm, respectively. Insets shows 2D FFT obtained from the corresponding images. (g) Shows angular dependence of surface roughness for both static and rotating samples. The reduction in surface roughness is very clear in case of rotating samples.....120

Figure 4.18: Roughness evolution plot as a function of ion incidence angle (shown later). Solid lines are guide to the eyes.....121

Figure 4.19: Phase diagram for different patterns versus control parameters like ion incidence angle (θ) and ion-beam energy (E). Both phase diagram are in the linear regime corresponding to the respective angle of incidence.....122

Figure 4.20: Roughness evolution plot in linear regime as a function of ion incidence angle.....125

Figure 4.21: AFM images showing temporal evolution of mounds corresponding to different times (fluences) namely (a) 11 min, (b) 22 min, (c) 54 min, and (d) 108 min at an incidence angle of $67^\circ$ . Corresponding height scales in (a-d) are 6 nm, 8 nm, 8 nm, and 13 nm, respectively. Insets show 2D FFT obtained from the corresponding images.....	125
Figure 4.22: (a) Variation in the lateral dimension of mounds as a function of square root of the sputtering time. (b) rms roughness plot as a function of sputtering time at $67^\circ$ angle of incidence. Dashed lines are for guide to the eyes.....	126
Figure 4.23: (a) Variation of the lateral dimension of the mounds as a function of square root of the sputtering time. (b) rms roughness plot as a function of sputtering time at $60^\circ$ angle of incidence. Dashed lines are for guide to the eyes.....	127
Figure 4.24: AFM images showing the effect of rotational speed variation corresponding to different angular speeds, namely (a) 17.4, (b) 26.2, and (c) 43.6 $\text{rad s}^{-1}$ at an incidence angle $67^\circ$ . Corresponding height scale in (a-c) is 11 nm. Insets shows 2D FFT obtained from the corresponding images.....	128
Figure 4.25: (a) rms roughness versus rotational speed variation plot for $67^\circ$ and at a fixed fluence of $5 \times 10^{17}$ ions $\text{cm}^{-2}$ incidence angle. (b) and (c) show corresponding mound dimension and height versus rotational speed plots, respectively.....	128
Figure 5.1: Three-dimensional AFM micrographs corresponding to samples exposed to ion fluence of $2 \times 10^{18}$ $\text{cm}^{-2}$ at incidence angle of $70^\circ$ (a) and $72.5^\circ$ (b). Figure 1(c) depicts the evolution of average facet heights as a function of ion fluence at $\theta=70^\circ$ and $72.5^\circ$ .....	138
Figure 5.2: XTEM image showing silicon facets fabricated by using 500 eV Ar-ions to the fluence of $5 \times 10^{17}$ $\text{cm}^{-2}$ . The black circles depict the zones where <i>a</i> -Si and native oxides are present. Inset shows the FFT of the same image which reveals presence of different crystallographic planes.....	139
Figure 5.3: <i>2p</i> core level Si XPS spectra taken from (a) Pristine-Si and samples exposed to ion fluences of (b) $5 \times 10^{17}$ , (c) $2 \times 10^{18}$ $\text{cm}^{-2}$ , respectively.....	140
Figure 5.4:(a) Reflectance study corresponding to Pristine-Si and samples exposed to four different ion fluences, viz. $5 \times 10^{17}$ , $1 \times 10^{18}$ , $1.5 \times 10^{18}$ , and $2 \times 10^{18}$ $\text{cm}^{-2}$ for incidence angle of $72.5^\circ$ , (b) facet height versus percentage area covered by the faceted structures extracted by using SPIP software from the respective AFM images shown in Fig. 1, and (c) schematic of the refractive index profile from air to Si substrate due to the presence of a facet.....	142
Figure 5.5: PL spectra plotted against wavelength for ion incidence angle of $72.5^\circ$ and for fluences of (i) $5 \times 10^{17}$ , (ii) $1 \times 10^{18}$ , (iii) $1.5 \times 10^{18}$ , and (iv) $2 \times 10^{18}$ ions $\text{cm}^{-2}$ , respectively. Inset shows the PL spectrum corresponding to Pristine-Si: PL spectra plotted against wavelength for ion incidence angle of $72.5^\circ$ and for fluences of (i) $5 \times 10^{17}$ , (ii) $1 \times 10^{18}$ , (iii) $1.5 \times 10^{18}$ , and (iv) $2 \times 10^{18}$ ions $\text{cm}^{-2}$ , respectively. Inset shows the PL spectrum corresponding to Pristine-Si.....	144
Figure 5.6: (a) Field emission current density as a function of the applied electric field for the nanofaceted-Si (green) and pristine-Si nanotube (brown), (b) Fowler-Nordheim plot for the nanofacets. The straight line drawn is for guide to the eye.....	153

Figure 5.7: (a) Schematic of the DPTCM measurement using dual pass mode. (b) XTEM image showing silicon facets fabricated by using 500 eV Ar-ions to the fluence of  $5 \times 10^{17} \text{ cm}^{-2}$ . The yellow lines depict the zones where native oxides are present. (c) Topographical image of nanofaceted-Si surface in contact mode. Corresponding height scale is 0 to 414 nm. (d) Map of tunnelling current measurements showing clear contrast difference in the valley and apex. Corresponding height scale is 0 to 60 pA. Blue and green lines in (c) and (d) are for guide to eyes.....155

Figure 5.8: (a) topography image of a single nanofacet having a height scale of 101 nm. (b) SKPM image of nanofaceted-Si surface depicting variation of work function over the surface. Corresponding height scale is 70 to 120 mV. (i), (ii), (iii), and (iv) are the regions from where corresponding work functions are calculated.....157

Figure 6.1: Schematic of the ion-beam fabrication of rippled-Si and its further usage as a template for growth of AZO films. The projection of incoming flux during deposition was kept same as that of the ion-beam projection onto pristine-Si surface for fabrication of ripples.....166

Figure 6.2: AFM images: (a) rippled-Si, (b) R1, (c) R2, (d) R3, (e) pristine-Si, (f) P1, (g) P2, and (h) P3. Insets are 2D FFT of the respective images. The white arrow in (a) indicates the projection of argon ion-beam onto the pristine-Si substrate. The height scales in (a)-(h) are: 6 nm, 9 nm, 10 nm, 12 nm, 1 nm, 6 nm, 8 nm, and 9 nm, respectively.....168

Figure 6.3: XRD spectra corresponding to 30 nm-thick AZO overlayers: R3 and P3.....169

Figure 6.4: (a)-(c) present XTEM micrographs corresponding to R2: (a) Low-magnification image, showing a uniform and conformal growth of AZO on the native oxide covered rippled-Si substrate, (b) HRTEM image obtained from the marked region on (a), showing the interface regions of native oxide covered rippled-Si substrate and AZO overlayer, where columnar growth of AZO film is demonstrated by dashed yellow lines on the same. (c) HRTEM image taken from the marked region on (b), which shows lattice fringes.....170

Figure 6.5: Core-level  $\text{Zn}2p$  and  $\text{O}1s$  spectra of AZO films having thicknesses of 10 nm [(a)-(b)] and 15 nm [(c)-(d)] grown on rippled-Si templates.....172

Figure 6.6: PL spectra of AZO films recorded at room temperature: (a) 10 nm, (b) 15 nm, and (c) 30 nm-thick films on pristine- and rippled-Si substrates.....174

Figure 6.7: Variations in free excitonic shift and average grain size of R1, R2, and R3 as a function of thickness. The inset shows AFM phase contrast image of R1, where the presence of smaller grains are evident (marked by green closed loops). The range of the scale bar in this case is  $-3^\circ$  to  $+12^\circ$ . The solid lines are guide to the eyes.....176

Figure 6.8: Flow chart for ion-beam fabrication of nanofaceted Si followed by conformal growth of AZO films on the same.....180

Figure 6.9: Plan-view SEM images: (a) Faceted-Si nanostructures, (b) AFM topographic image where inset shows the 2D FFT, (c) and (d) after growing AZO films on nanofaceted Si having thicknesses of 30 and 75 nm, respectively. The black arrows indicate the direction of ion-beam bombardment whereas the yellow arrows represent the direction of AZO flux during sputter deposition.....182

Figure 6.10: (a) Representative EDS spectrum of 60 nm thick AZO overlayer grown on Si nanofacets, showing the presence of Si, Zn, and O; (b) plot of atomic concentration versus AZO overlayer thickness obtained from EDS analyses. The solid lines are guide to the eyes; (c) X-ray diffractograms of AZO films grown on nanofaceted silicon. The signal corresponding to the 30 nm thick AZO overlayer is not strong and therefore, the corresponding diffractogram is not shown here.....183

Figure 6.11: (a) Reflectance spectra corresponding to pristine-Si, nanofaceted-Si, and AZO overlayers grown on faceted Si having thicknesses of 30 nm, 60 nm, and 75 nm. (b) Reflectance spectra obtained from 30, 60, and 75 nm thick AZO films deposited on faceted Si where the dashed line corresponds to the domain of reflectance minima for different AZO layer thickness (all the reflectance spectra shown here do not contain any contribution from diffuse reflectance).....185

Figure 6.12: Photoresponsivity spectra of 30 nm thick AZO overlayer grown on planar and nanofaceted Si in the spectral range of 300-800 nm. The inset shows the optical reflectance spectra for these two samples mentioned above.....186

Figure 6.13: AFM images corresponding to (a) nanofaceted-Si template and (b) 75 nm AZO grown on nanofaceted-Si. Line profiles drawn on (a) and (b) are shown in (c) and (d) shows a high-resolution SEM image of (b).....192

Figure 6.14: (a) Thickness-dependent nonlinear  $I$ - $V$  characteristics where the inset shows a schematic view of an AZO/Si heterojunction diode. (b)  $1/C^2$ - $V$  characteristics for different AZO film thicknesses.....194

Figure 6.15: Thickness-dependent photoresponsivity spectra in the wavelength range of 300-800 nm. The inset shows variation in the barrier height and turn-on potential as a function of AZO thickness.....195

---

# CHAPTER 1

---

## **1. Introduction**

### **1.1 Preamble**

The famous quote by Richard F. Feynman, “There’s plenty of room at the bottom”, drew attention of numerous scientists to venture the journey in the world of nanoscale science and its capabilities. In the meeting of American Physics Society [1], his speech on the possibilities of the nano-objects unleashed new horizon in materials research. During last 50 years, the potential of manipulating materials on nanoscale are explored and currently, a multitude of devices in nanometre regimes are available in the market [2].

Among different techniques for fabricating nanostructures, e.g. chemical lithography [3] or electron-beam lithography [4], self-organized pattern formation are of special interest due to their cost-effectiveness and large area production. In this regard, ion bombardment is a versatile, efficient, and widely used technique for synthesis, modification, and characterization of materials. Because of a high control over energy and spatial distribution of the ion species, this technique has found important applications both in basic research as well as in technological applications. One of the ion-beam based techniques, i.e. ion-beam sputtering (IBS) (removal of material from the surface of solids through the impact of energetic particles) [5] results in various nanoscale periodic pattern formation on surfaces in a self-organized fashion.

In the context of ion-solid interaction, it is customary to classify the ion energy ranges. Ions having energy in the range 0.5–10 keV are called low energy ions, 10–500 keV are referred to as intermediate/medium energy ions, and beyond 500 keV are known as high energy ions [6].

## 1.2 Self-organized nanopatterning by ion irradiation

Back in the 1960s, Navez *et al.* studied the morphology of glass substrates bombarded with a 4 keV ion-beam [7]. During IBS process, the surface turned into periodically modulated ripple patterns with wavelengths in nanometer regime depending on the angle of incidence of the ion-beam. After more than five decades, the research interest in this novel phenomenon is still growing. This is because of the recently discovered promising technological applications of the patterned surfaces as well as for the continuing development in the theoretical understanding of ion-beam patterning. It is now understood that the evolution of the surface morphology during ion sputtering is a complex phenomenon and involves roughening and smoothing processes. In general, the shape and orientation of the structures are governed by ion angle of incidence. Two-dimensionally periodic nanoscale dot structures are observed for normal ion incidence [8] (or oblique ion incidence on a rotating substrate [9]), whereas obliquely incident ion irradiation leads to one-dimensionally periodic ripple structures [10]. Recent studies reveal that at normal incidence, however, the surface remains stable for monoatomic semiconductors [11]. Ion-induced ripple formation has been explored for different kinds of materials like semiconductors, insulators, metals, and polymers etc. [8,12-14].

Among various semiconductors, Si is a major material for technology and is available in high purity and abundance. That is why it is not unexpected that the ion-beam patterning studies are plentiful for this material. At room temperature, Si is readily amorphized during ion exposure [15]. The loss of crystal structure makes it an ideal material to be described by the continuum theory of ion erosion, which effectively ignores complex atomistic details of the processes. It may be mentioned that ion-induced pattern formation is extremely sensitive to various experimental parameters like ion -energy, -incident angle, -mass, -current density, -fluence, -flux, composition of the substrate, and substrate temperature. The effect of these parameters on low energy ion-beam induced pattern formation has been studied by many investigators

[5,11,16-18]. However, on many occasions, the experimental results are found to contradict the theoretical predictions [19]. The understanding of the processes involved are far from complete and requires further experimental explorations as well as theoretical formulation. In addition, the impurities present on the surface have been seen to drive pattern formation [20]. For example, the role of metallic impurities in pattern formation was addressed by Macko *et al.* by exposing Si(100) substrates to 2 keV Kr<sup>+</sup>-ion beam at an incident angle of 30° where sputter co-deposition of iron can take place [21]. They attributed their results to height fluctuations, local flux variation, and composition dependent sputtering. In another work, Zhang *et al.* explained the role of iron impurity on pattern formation for silicon by using 5 keV Xe-ions at normal incidence [22]. These experimental results clearly reflect that the presence of metal impurities enhances pattern formation process (sometimes unintentionally). While the dependence of patterning on such a large range of parameters makes the theoretical understanding a challenging task, they also open up ways to tune the surface features for specific applications.

The diversity of observed patterns stimulated the development of continuum theories [23-26] extending the concept of the curvature dependent sputtering yield or ion induced stress generation as leading destabilization mechanisms. Different theoretical formalisms have been adopted by the investigators to address the low energy pattern formation mechanism. In this context, the experimental studies by Madi *et al.* can be mentioned where a parametric phase diagram (which actually summarizes different patterns observed as a function of control parameters like angle of incidence and energy of the ion-beam) was presented [11]. In another note, Castro *et al.* explained their results using solid flow model [27]. It has been observed from these studies that silicon surface remains stable under argon-ion bombardment starting in the angular window of 0°-45° or 0°-52° whereas beyond this window, patterns start evolving.

These experiments suggest that the transition point from stable to unstable surface is not unique and requires systematic experimentation over the whole angular window ( $0^{\circ}$ - $85^{\circ}$ ).

The current theoretical models predict features of ion bombardment induced patterning such as linear and nonlinear modes of pattern evolution, influence of ion-beam shadowing, contributing factors like curvature-dependent sputtering, and ion induced mass redistribution. In this regard, low energy ion bombardment on solid surface provides an experimental platform to recognize the applicability of theoretical models or relevance of physical mechanisms in a particular experimental situation. This is extremely important for a complete theoretical understanding of the patterning process which is necessary to engineer the surface topography for novel technological applications.

Understanding ion induced pattern formation is not only fascinating from the fundamental physics point of view but the formed patterns may also offer a number of potential applications. It is observed that nanostructured surfaces with a high aspect ratio may serve as an antireflective surface due to their gradation of the refractive index [28-30]. Textured Si surfaces enhances the efficiency of solar cells [31-33]. Arrays of pillars oriented upstanding to the Si substrate were found to be an ideal material for enhancing the performance of thermoelectric generators [34], optoelectronic devices [35,36] as well as being useful for flat panel displays as field emitter arrays [37,38]. All these reports clearly demonstrate the manifold potential of patterned substrates in manipulating photovoltaic, optoelectronic, field emission, nanoscale magnetism, and plasmonics etc. In addition, high aspect ratio nanostructures (like Si nanocones) may give rise to improved photoluminescence property due to quantum confinement effect [39]. All these studies demonstrate the potential of a nanostructured surfaces towards various applications. Among various other techniques ion-induced nanopattern formation at surfaces offers several advantages and reveal promising applications in various field research. For instance, Ranjan *et al.* showed Ag nanoparticles on Si ripples are

capable of tuning the plasmon resonance while Martella *et al.* reported on the broadband light trapping property of self-organized nanopatterned Si substrates which can be effectively used for photon harvesting in ultra-thin crystalline solar cells [40,41]. Recently, tunability of magnetic anisotropy was demonstrated by Körner *et al.* [42]. Thus, it is obvious that a lot more can be done if the morphological anisotropy of the ion-beam patterned substrates can be judiciously used to tune the functional property of thin films.

### 1.3 Motivation

As mentioned above, ion-beam induced pattern formation is theoretically explained by taking into account two competing processes, viz. roughening due to curvature-dependent sputtering and surface relaxation processes like ion induced mass redistribution, ion induced effective diffusion or viscous flow. Recent experiments revealed that in case of a monatomic target like Si, the well-known Bradley-Harper (BH) theory alone cannot explain the existence of a critical angle (beyond which pattern formation takes place) [43]. In fact, the smoothing at angles below the critical angle was addressed by Carter and Vishnyakov (CV) [44]. Thus, till date, explanation of the angular dependence of pattern formation in case of Si relies mostly on these two basic mechanisms, viz. BH instability and mass redistribution or CV effect. In a later work, Madi *et al.* have shown that surface instabilities can be suppressed due to impact-induced mass redistribution phenomenon (rephrased as CV effect) [43, 44].

**Importance of Si as a target:** Silicon was selected as the target material for the present study because it is a mono-elemental target whose physical properties are well-known and is easily amorphizable by ion irradiation. Thus, it deserves to be an ideal system for exploring morphological evolution in conjunction with the theoretical models which are directly applicable to amorphous elemental target. Noble gas ion like argon was chosen as it is inert in nature and leaves the irradiated sample as ideal amorphous monoatomic system for theoretical

models. Further, the interaction of noble gas ions with Si is considered to be of fundamental interest in the field of ion implantation and related applications.

**Temporal evolution of ripples in linear regime:** Solid flow model was also introduced which deals with the idea of amorphous solid flowing due to ion impact [26,27]. The stress generated during ion bombardment eventually drives the solid to flow, resulting in nanoscale ripple development at the surface [26,27]. In fact, this is the first theory to predict the timescale (intrinsic timescale) beyond which nonlinear effects dominate the evolution of surface patterns. In the nonlinear regime, surface roughness does not follow the exponential growth and ripple coarsening may take place [23]. However, the potential of very recently developed solid flow model has not been exploited to its fullest. In particular, this model was not tested for very high oblique incidences ( $\theta=72.5^\circ$ ). In addition, this theory is based upon the ion induced stress gradient generation in solid which is very difficult to quantify from experiments. Thus, this necessitates the discovery of a new approach which can avoid this stress gradient term yet can calculate the exact timescale in which ripple evolves in linear regime.

**Angular dependence of pattern formation in nonlinear regime:** As pointed out by Madi *et al.* [43], the role of sputtering can be totally ignored and mass redistribution solely governs the mechanism of low energy ion induced pattern formation in Si. However, systematic experimentation is needed to address the role of sputtering in pattern formation. Moreover, in the past, even for similar ion-beam parameters and formation conditions, the type of pattern created suffered from the lack of lab-to-lab reproducibility. It is to be noted that apart from nonlinear effects, shadowing of the ion-beam by the surface features can also play a critical role in pattern formation at higher oblique angles of incidence. Thus, to come up with an adequate understanding of pattern formation, it is necessary to address those hidden factors in pattern formation on Si over a total angular window in the range of  $0^\circ$ - $85^\circ$ .

**Ripple to facet transition:** According to Carter, ripple structures can be transformed into triangular faceted structures under the influence of shadowing [45] of ion-beam surface features. Pattern formation at higher oblique incidence angles has not been studied in detail. In this regime, ion-beam shadowing may transform ripples into faceted morphology. In fact, there is no systematic fluence-dependent study of pattern evolution at higher oblique incidences which conclusively exhibit the transition from ripple to facets. Thus, a systematic investigation is required to explore the pattern formation at higher ion incidence angles.

**Role of substrate rotation:** Although studying ripple formation remains the main goal of ion beam pattern formation, ripple formation is unwanted in various techniques viz. secondary ion mass spectroscopy (SIMS), Auger electron spectroscopy (AES), and ion milling. The ion incidence angle  $\theta \neq 0$  for a typical SIMS or AES setup results in formation of ripples at the surfaces. This results in rapid degradation in depth resolution. As a way out to this problem Zalar first demonstrated that by rotating the sample with respect to its surface normal during sputtering one can avoid ripple formation [46]. According to Bradley's theory, nanoscale mound formation (instead of ripples) can take place if the in-plane symmetry is preserved by applying concurrent substrate rotation during oblique angle sputtering [47]. However, there is no such report which addresses the linear regime of pattern formation under concurrent substrate rotation over the full angular window of  $0^\circ$ - $85^\circ$ . In linear regime, the roughness should reduce under concurrent substrate rotation compared to the static substrate case. Another prediction of the theory is that the coarsening of mounds as a function of time should eventually get stopped due to higher order nonlinear effects. This phenomenon is known as the "interrupted coarsening". Till date there exists hardly any experimental proof of this prediction. Thus, it is exigent to validate these predictions with proper experimental evidences. In addition, temporal evolution study of the mounds under concurrent substrate rotation has to be

investigated systematically. All these aforementioned discussions clearly indicate that the complex physics involved in ion-beam patterning has not yet been entirely uncovered.

**Optical and field emission properties of nanostructured-Si:** In general, being an indirect band gap material, bulk-Si is not a good emitter of light. However, in nanoscale, due to quantum confinement effect, it emits light. It has been reported that sharp Si nanocones generate ultra-violet (UV) photoluminescence. In addition, high aspect ratio structures are capable of showing antireflection property due to graded refractive index effect [28]. Reduction of surface reflection is important for light harvesting in solar cells. Ion-beam induced nanopatterning process gives rise to various self-organized nanostructures (in the form of ripples or facets) at the surfaces in a single step. Thus, systematic study of optical properties (like photoluminescence and reflectance) would not only provide important information regarding the defects in the nanostructures but also help to understand the antireflection property of the material. These studies would open up new possibilities to couple the debatable photoluminescence and antireflection properties in a single frame work which will pave the way of employing Si-based materials in a more efficient way towards photovoltaic and optoelectronics research.

Field emission (FE) has drawn a lot of interest because of its possible applications as an efficient point electron source in electron microscopes, x-ray sources, flat panel displays, and microwave amplifiers. In particular, Si nanostructures suffer from the problem of oxidation which degrades its field emission quality. Thus, a new method is required where the oxide layer can be used as a protecting layer without much degradation in the FE property. This suggests that ion induced high aspect ratio structures might be the ideal candidate for this purpose.

**Patterned Si substrates as templates:** As specified above, since ion-beam nanopatterning is a technique for creating patterns over a large area and it is fast as well for creating various nanoscale surface patterns, it can be employed as templates for subsequent nanostructured thin

film deposition. For instance, transparent conducting oxides are always demanding due to their applications in solar cells, light emitting diodes, and display technology etc. At present, indium tin oxide (ITO) is commonly used as transparent electrodes, especially in large-area applications such as displays. However, due to the limited supply and high indium price alternative materials are sought for. In this regard, the discovery of *n*-type TCOs like Al-doped ZnO (AZO) has opened new scopes in different industrial areas such as opto- and nano-electronics, ceramics, and the photovoltaics [48,49]. In addition, as compared to passive electrodes, the transparent conductors can also be used as an active component. This has led to new applications as blue or ultra-violet (UV) light-emitting-diodes [50-52]. Different reports exist showing a dependence of excitonic energy on the dimension of ZnO nano-grains [53-55]. Thus, tailoring the optical properties by varying structure, size, and composition of a material is of utmost importance. As an alternative, optical properties can also be tuned by using a template for deposition of thin films where self-organized substrates lead to conformal growth [56-58]. In this context, understanding the role of anisotropic rippled-Si surfaces in achieving size-dependent optical properties of AZO nanostructured thin films will be of importance for potential applications in nanophotonics.

As mentioned earlier, the presence of high aspect ratio structures at surfaces leads to improved antireflection (AR) effect. This property of solids can be utilized to enhance the solar cell efficiency by increasing the light absorption in the active layer. The reduction of front surface reflection plays an important role in solar cells. In general, a silicon wafer without any AR structure, exhibit an average reflection more than 40% for visible light. Thus, a silicon solar cell based on this silicon substrate suffers from a large loss which in turn leads to a poor absorption of the incoming solar radiation. The textured structure and antireflection coating achieve the function of increased light-trapping by extending the length of the optical path of the incident rays in the solar cells which can increase the absorption [59, 60]. However, most

of the patterning processes involve conventional lithographic techniques [61] and hence, these are time consuming and involve multiple processing steps. On the other hand, low energy ion-beam sputtering has shown its potential as a single step and fast processing route to produce large area (size tunable), self-organized nanoscale patterned surfaces — compatible to the present semiconductor industry and thus, may be considered to be challenging to develop AR surfaces for photovoltaics in the form of heterojunction solar cells .

## 1.4 Outline of the thesis

This thesis presents studies on low energy Ar-ion induced pattern formation in case of Si and associated structural and compositional modifications. We attempt to understand our experimental observations in the framework of existing theoretical models. After optimizing the pattern formation mechanism, we explore the possibility of using high aspect ratio structures (nanofacets) towards modifying optical and electrical properties. In addition, we have shown the efficacy of rippled- and faceted-Si substrates as templates for conformal growth of Al-doped zinc oxide (AZO) overlayer. Modification in the optical and optoelectronic properties of AZO/rippled-Si and AZO/faceted-Si combinations are demonstrated as a function of AZO overlayer thickness. The thesis is organized in the following manner:

**Chapter 1:** In this chapter a brief review of the low energy ion induced pattern formation and related issues covered in the studies are presented. The introductory description also includes some applications of ion irradiation induced self-organized patterned surfaces. In this chapter, we have also described the motivation behind our study.

**Chapter 2:** This chapter describes the experimental techniques employed for carrying out the studies presented in this thesis.

**Chapter 3:** In this chapter, we first describe the statistical methods for classification and analysis of surfaces. Afterwards, a brief introduction to ion-solid interaction as related to the

issues covered in the studies presented in the thesis has been given. Then we briefly outlined the theoretical models developed to describe surface morphological evolution on amorphous solid surfaces. A brief description of the simulation methods used in our work is also given.

**Chapter 4:** This chapter describes the results of our detail experimental investigations on self-organized pattern formation on Si surface under low energy (<2keV) Ar-ion bombardment. We describe pattern formation in the angular window of  $0^{\circ}$ - $85^{\circ}$ . The temporal evolution of ripple morphology in the angular window of  $51^{\circ}$ - $72.5^{\circ}$  was explained in light of solid flow model. With the help of this model, we could also identify the linear and nonlinear regimes of ripple evolution. In addition, for the same angular window and beyond (up to  $85^{\circ}$ ), we describe the pattern evolution in nonlinear regime. It has been shown that the temporal evolution of morphology at higher oblique incidences ( $70^{\circ}$ - $72.5^{\circ}$ ) originates from the shadowing effect of the ion-beam, leading the ripples to undergo a transition to faceted nanostructures. At even higher fluences, coarsening of these facets are observed. We have also shown the effect of concurrent substrate rotation on pattern formation in Si in both linear and nonlinear regimes. Corresponding temporal evolution study at fixed angle of incidence revealed coarsening of mounds. All these observations are explained in light of the existing theoretical models.

**Chapter 5:** This chapter demonstrates a few applications of the faceted structures formed under ion-beam bombardment. For example, these structures are capable of showing tunable antireflection, photoluminescence, and field emission properties. Photoluminescence property is attributed to various defects and surface states present in facets whereas the improved antireflection property (in the range of 300-800 nm) is attributed to the graded refractive index effect. The antireflection effect can be used to enhance the photoluminescence intensity by orders of magnitude. Such nanofacets could be potentially useful as electron emitters. In this thesis, we have undertaken the case study of field emission from such self-organized faceted nanostructures. In doing so, we have used both bulk and local probe techniques. However, bulk

measurements cannot recognize the regions which generates field emission. To overcome this problem, we employed atomic force microscope-based local probe technique (DPTCM), which is similar to tunneling atomic force microscopy (TUNA). These measurements clearly show that the sidewalls of Si faceted nanostructures actually contribute to the field emission process instead of the apexes.

**Chapter 6:** In this chapter, we present the usage of nanostructured Si as templates for growth of ZnO:Al (AZO) thin films. In the first part, we show the conformal growth of AZO overlayer on rippled-Si and change in its optical property as a function of fluence. The role of quantum confinement has been pointed out to explain the observed blue shift in the near band excitonic peak. Next, we show the efficacy of AZO overlayers (30-90 nm) grown on ion-beam synthesized nanofaceted-Si for a further reduction in surface reflectance down to very low values. Tunable antireflection property is understood in light of depth-dependent refractive index of nanofaceted-Si and the AZO overlayers. It has been shown that the antireflection property helps increasing the fill factor of such textured AZO/Si heterostructures for an optimized AZO thickness. In addition, current-voltage (I-V) and capacitance-voltage (C-V) measurements were carried out to address the thickness dependent enhancement in photoresponsivity.

**Chapter 7:** In this chapter, we have summarized our studies presented in this thesis. Further, we have outlined the future scope of experimental studies based on our results and their importance towards a deeper understanding of the ion induced pattern formation and possible applications of generated patterns.

## Bibliography

1. R. Feynman, Caltech. Eng. Sci., 23 (1960) 22.
2. A. D. Maynard, R. J. Aitken, T. Butz, V. Colvin, K. Donaldson, G. Oberdorster, M. A. Philbert, J. Ryan, A. Seaton, V. Stone, S. S. Tinkle, L. Tran, N. J. Walker and D. Warheit, Nature, 444 (2006) 267.
3. B.D. Lucas, J-S Kim, C. Chin, and L. J. Guo, Adv. Mater. 20 (2008) 1129.
4. C. Portesi, S. Borini, G. Amato, E. Monticone, J. Appl. Phys. 99 (2006) 066115.
5. T. Som, D. Kanjilal, Nanofabrication by Ion-Beam Sputtering: Fundamentals and Applications, Singapore: Pan Stanford; 2012.
6. L. Hanley and S.B. Sinnott, Surf. Sci. 500 (2002) 500.
7. M. Navez, C. Sella, D. Chaperot, Comptes Rendus 254 (1962) 240.
8. S. Facsko, T. Dekorsy, C. Koerdt, C. Trappe, H. Kurz, A. Vogt, H.L. Hartnagel, Science 285 (1999) 1551.
9. F. Frost and R. Rauschenbach, Appl. Phys. A 77 (2003) 1.
10. A. Keller, S. Rossbach, S. Facsko, and W. Möller, Nanotechnol. 19 (2008) 135303.
11. C.S. Madi, B. Davidovitch, H.B. George, S.A. Norris, M.P. Brenner, and M.J. Aziz, Phys. Rev. Lett. 101 (2008) 246102.
12. G. W. Lewis, M. J. Nobes, G. Carter, J. L. Whitton, Nucl. Inst. Meth. Phys. Res. B 170 (1980) 363.
13. F. Vasiliu, I. A. Teodorescu, F. Glodeanu. J. Mater. Sci. 10 (1975) 399.
14. Q. Wei, J. Lian, S. Zhu, W. Li, K. Sun, and L. Wang, Chem. Phys. Lett. 452 (2008) 124.
15. T. Lohner, E. Kótai, N. Khánh, Z. Tóth, M. Fried, K. Vedam, N. Nguyen, L. Hanekamp, and A. van Silfhout, Nucl. Instrum. Methods Phys. Res., Sect. B 85 (1994) 335.

16. R. Gago, L. Vázquez, R. Cuerno, M. Varela, C. Ballesteros, and J. Albella, *Nanotechnology* 13 (2002) 304.
17. B. Ziberi, F. Frost, T. Höche, and B. Rauschenbach, *Vacuum* 81 (2006) 155.
18. T. Basu, J.R. Mohanty, and T. Som, *Appl. Surf. Sci.* 258 (2012) 9944.
19. R.M. Bradley and J.M.E. Harper, *J. Vac. Sci. Technol. A* 6 (1988) 2390.
20. A. Redondo-Cubero, R. Gago, F. Palomares, A. Mücklich, M. Vinnichenko, and L. Vázquez, *Phys. Rev. B* 86 (2012) 085436.
21. S. Macko, J. Grenzer, F. Frost, M. Engler, D. Hirsch, M. Fritzsche, A. Mücklich, T. Michely, *New J. Phys.* 14 (2012) 073003.
22. K Zhang, F. Rotter, M. Uhrmacher, C. Ronning, J. Krauser, and H. Hofsäss, *New J. Physics* 9 (2007) 29.
23. M. A. Makeev, R. Cuerno, and A. L. Barabási. *Nucl. Instrum. Methods Phys. Res., Sect. B* 197 (2002) 185.
24. M. Castro, R. Cuerno, L. Vázquez, and R. Gago. *Phys. Rev. Lett.* 94 (2005) 016102.
25. W. L. Chan, E. Chason, *J. Appl. Phys.* 101 (2007) 121301.
26. M. Castro, R. Cuerno, *Appl. Surf. Sci.* 258 (2012) 4171.
27. M. Castro, R. Gago, L. Vázquez, J. Muñoz-García, and R. Cuerno, *Phys. Rev. B* 86 (2012) 214107.
28. S.J. Wilson and M.C. Hutley, *Optical Acta* 29 (1982) 993.
29. D. Flamm, F. Frost, and D. Hirsch, *Appl. Surf. Sci.* 179 (2001) 95.
30. J-Q Xi, M. F. Schubert, J. K. Kim, E. F. Schubert, M. Chen, S-Y Lin, W. Liu, J. A. Smart, *Nat. Photonics* 1 (2007) 176.
31. C. H. Sun, P. Jiang, and B. Jiang, *Appl. Phys. Lett.* 92 (2008) 061112.
32. S. A. Boden and D. M. Bagnall, *Appl. Phys. Lett.* 93 (2008) 133108.

33. S.H. Hong, B. J. Bae, K. S. Han, E. J. Hong, H. Lee, and K. W. Choi, *Electron. Mater. Lett.* 5 (2009) 39.
34. Ü. Sökmen, A. Stranz, S. Fündling, S. Merzsch, R. Neumann, H.-H. Wehmann, E. Peiner, and A. Waag, *Microsyst. Technol.* 16 (2010) 863.
35. A. Wellner, R. E. Palmer, J. G. Zheng, C. J. Kiely, and K. W. Kolasinski. *J. Appl. Phys.* 91 (2002) 3294.
36. A. G. Nassiopoulos, S. Grigoropoulos, E. Gogolides, and D. Papadimitriou, *Appl. Phys. Lett.* 66 (1995) 1114.
37. P. D. Kichambare, F. G. Tarntair, L. C. Chen, K. H. Chen, and H. C. Cheng, *J. Vac. Sci. Technol. B* 18 (2000) 2722.
38. M. Hajra, C. E. Hunt, M. Ding, O. Auciello, J. Carlisle, and D. M. Gruen. *J. Appl. Phys.* 94, 4079 (2003).
39. W. H. Zheng, Jian-bai Xia, S. D. Lam, K. W. Cheah, M. R. Rakhshandehroo, and S. W. Pang, *Appl. Phys. Lett.* 74 (1999) 386.
40. M. Ranjan, S. Facsko, M. Fritzsche, S. Mukherjee, *Microelectron. Engg.* 102 (2013) 44.
41. C. Martella, D. Chiappe, P. Delli Veneri, L. V. Mercaldo, I. Usatii and F. Buatier de Mongeot, *Nanotechnology* 24 (2013) 225201.
42. M. Körner, K. Lenz, M. O. Liedke, T. Strache, A. Mücklich, A. Keller, S. Facsko, and J. Fassbender, *Phys. Rev. B* 80 (2009) 214401.
43. C. S. Madi, E. Anzenberg, K. F. Ludwig Jr., and M. J. Aziz, *Phys. Rev. Lett.* 106 (2011) 066101.
44. G. Carter and V. Vishnyakov, *Phys. Rev. B* 54 (1996) 17647.
45. G. Carter, *J. Appl. Phys.*, 85 (1999) 455.
46. A. Zalar, *Thin Solid Films* 124 (1985) 223.

47. R.M. Bradley, *Phys. Rev. E* 54 (1996) 6149.
48. A. B. Djurišić, A. M. C. Ng, X. Y. Chen, *Prog. Quant. Electron.* 34 (2010) 191.
49. Z. L. Wang, *Appl. Phys. A* 88 (2007) 7.
50. A. Sandhu, *Nature Photonics* 1 (2007) 38.
51. A. Tsukazaki et al., *Nature Materials* 4 (2005) 42.
52. B. Monemar, *Phys. Rev. B* 10 (1974) 676.
53. H. Zhao, W. Xiong, M. Z. Zhu, *Int. J. Mod. Phys. B* 21 (2007) 5237.
54. H. M. Cheng, K. F. Lin, H. C. Hsu, W. F. Hsieh, *Appl. Phys. Lett.* 88 (2006) 261909.
55. L. Dallali, S. Jaziri, J. El Haskouri, P. Amorós, *Superlattices and Microstructures* 46 (2009) 907.
56. T. W. H. Oates, *Appl. Surf. Sci.* 258 (2012) 9278.
57. Z. Zhou, F. Gao, D. Wayne Goodman, *Surf. Sci.* 604 (2010) L31.
58. J. J. S. Acuña, M. C. Marchi, F. Alvarez, *Thin Solid Films* 519 (2010) 214.
59. M. Otto, M. Kroll, T. Kasebier, S-M Lee, M. Putkonen, R. Salzer, P. T. Miclea, and R. B. Wehrspohn, *Adv. Mater.* 22 (2010) 5035
60. B. Hua, Q. Lin, Q. Zhang, and Z. Fan, *Nanoscale* 5 (2013) 6627.
61. L. Sainiemi, V. Jokinen, A. Shah, M. Shpak, S. Aura, P. Suvanto, S. Franssila, *Adv. Mat.* 23 (2011)122.

---

# CHAPTER 2

---

## **2. Experimental techniques and analysis methods**

The experimental studies presented in this thesis covers ion bombardment induced morphological, structural, compositional, and optical modifications of *p*-Si(100) surface. Ion bombardment was carried out using Ar ions extracted from a broad-beam electron cyclotron resonance (ECR)-based low energy ion source. Detail experiments were carried out by varying different ion-beam parameters, viz. ion energy, angle of incidence, or ion fluence. Ion-beam modified Si surfaces were investigated *ex-situ* by using atomic force microscopy (AFM), and scanning electron microscopy (SEM) and transmission electron microscopy (TEM). Luminescence property of ion-beam patterned Si was studied by photoluminescence (PL) spectroscopy whereas surface reflectance was measured by UV-Visible spectroscopy. In addition, patterned Si substrates were used as templates for growth of Al-doped ZnO (AZO) thin films by using pulsed dc magnetron sputtering technique. In addition to the above mentioned techniques used for characterization of Si surfaces, X-ray diffraction (XRD) studies were employed to check the crystallinity of the films whereas energy dispersive x-ray spectrometry (EDS) and x-ray photoelectron spectroscopy (XPS) were used for their compositional analyses. Further AZO/nanostructured-Si heterojunction properties were studied by using I-V, C-V, and photoresponsivity measurements. In this chapter, we briefly introduce the basic principles of these experimental techniques and describe the instruments.

### **2.1 Ion-beam induced surface nanostructuring setup (IBSN)**

#### **Low energy ion beam sputtering**

Experimental studies on the interaction of energetic particles with materials need a steady supply of well-focused contamination free ion-beam. The requirements over ion-beam parameters like ion-species, -current density, -energy, and -range depend upon specific applications and vary widely. Ion bombardment experiments, presented in this thesis, were carried out by using a low energy ECR-based, broad beam, filament-less ion etching setup (Tectra, Gen II, Germany) [1] named as ion-beam induced surface nanostructuring (IBSN) system. An ultra-high vacuum (UHV) compatible chamber (Prevac, Poland) equipped with a 5-axes sample manipulator was used to perform all the experiments [2]. The chamber base pressure was below  $5 \times 10^{-9}$  mbar and working pressure was maintained at around  $3 \times 10^{-4}$  mbar by using a differential pumping system. A photograph of the setup is shown in the Fig. 2.1. Parts of this experimental setup are briefly described below.

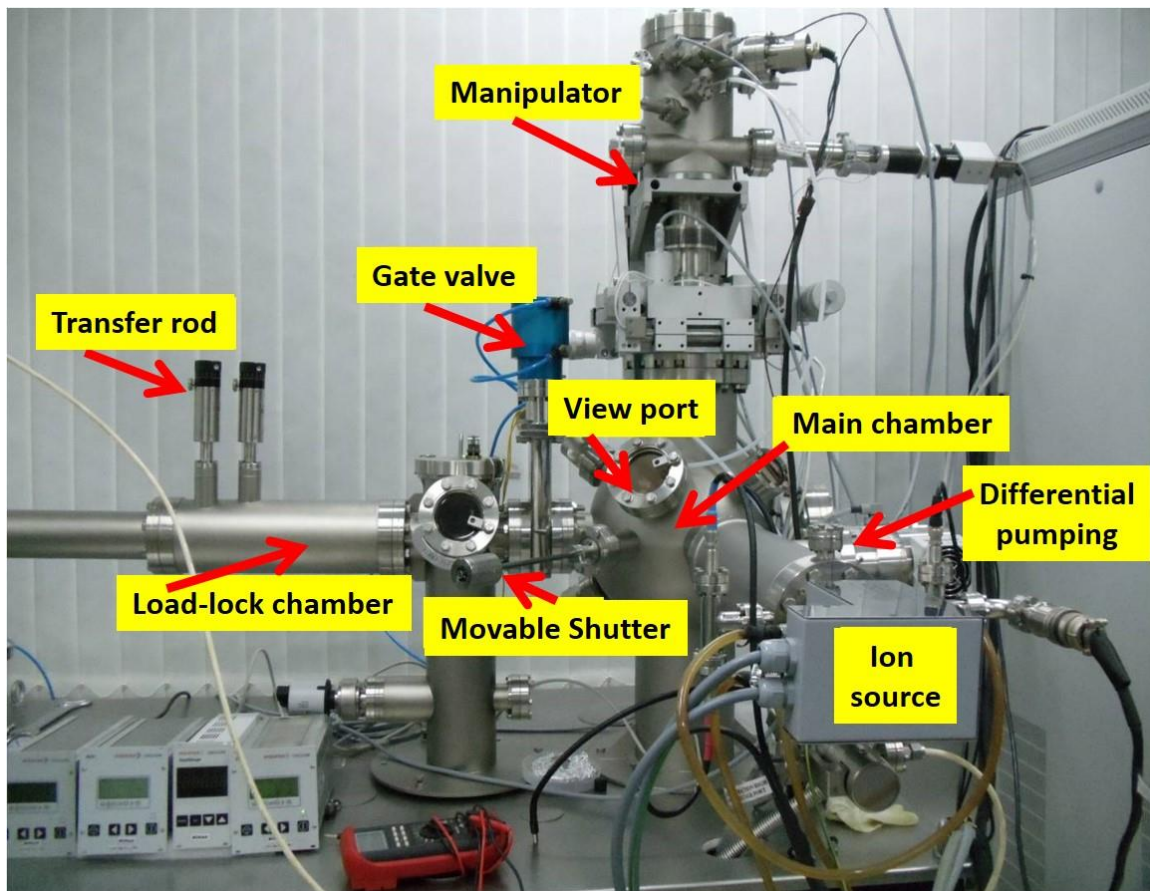


Figure 2.1: Ion-beam induced surface nanostructuring (IBSN) setup.

**ECR source:** The basic idea of an ECR ion source is microwave electron cyclotron resonance heating of electrons in a plasma and magnetic confinement of the ions created therein [3]. In general, to confine plasma, a special magnetic field configuration is required. This is achieved by superposition of the radial magnetic field ( $B$ ) of a permanent magnetic multipole and an axial magnetic mirror field (produced by a pair of solenoid coils). This geometry results in a minimum- $B$ -structure [4], i.e. an increase of magnetic field in all directions from the geometrical middle. In confined plasma, electron gyrate around the magnetic field lines with the cyclotron frequency

$$\omega_c = \frac{e}{m} B \quad (2.1)$$

For microwave based ECR source, injected (microwaves) can resonantly heat the electrons if the respective frequencies are equal. For an ECR ion source working at 2.45 GHz microwave frequency, Eq. 2.1 gives a corresponding resonant magnetic field of 0.088 T.

Passing the resonance region, an electron can gain 1-2 keV energy for further impact ionization processes. Ions, due to their heavy mass, are not accelerated and are confined by the space charge of the electrons. When electrons leave the plasma through the loss cone of the magnetic mirror, following ions can be extracted and subsequently separated with an analysing magnet. The detailed description of the ion source used for the studies presented in this thesis is described in the following paragraph.

#### **Ion source of IBSN setup:**

The ion source of IBSN setup is a low energy (50 eV-2 keV) ECR plasma source designed for the production of high current beam from any gaseous material. Figure 2.2 shows a cross section of a high vacuum version of the ion source. Plasma is generated in a quartz cup. The cup is attached to a UHV compatible base flange (NW63CF) and is surrounded by four water

cooled magnets of neodymium-iron-boron (outside vacuum) which produce ECR zones in a multicusp field. The magnetron operates at 2.45 GHz, and can be mounted either at the side or at the end plate. A metal rod is used as an antenna for near field coupling of the microwave to the plasma. The working gas is fed into the discharge cup via a

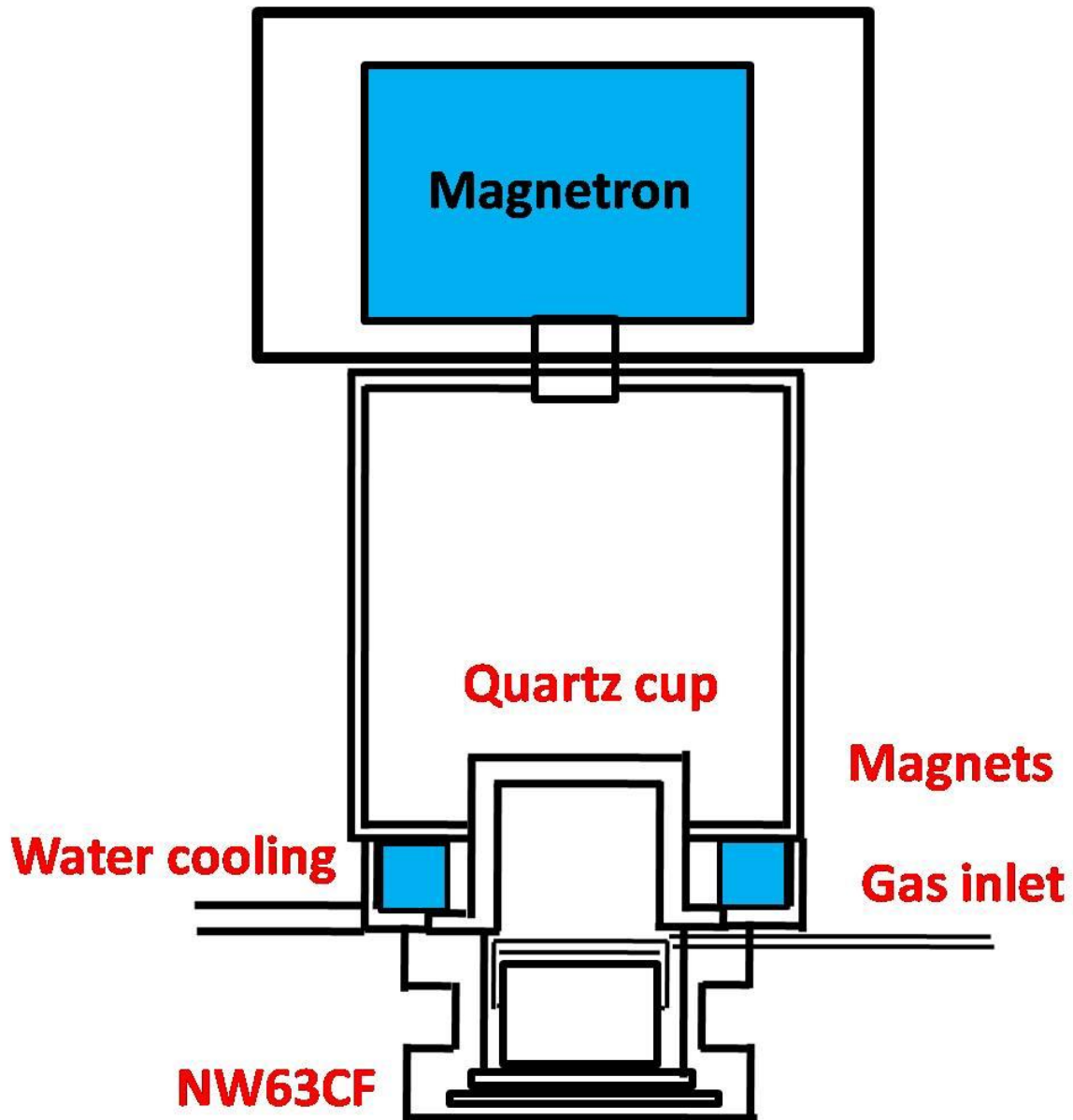


Figure 2.2: Cross sectional view of the low energy ion source in IBSN

distributor made up of a ceramic so as to prevent the plasma from “seeing” the metal at ground potential. The outside view of the source is shown in Fig. Fig. 2.3. Ions are extracted through multiple grid assemblies. In particular, the studies presented in this thesis are based on three

grid system containing 32 holes of diameter 3 mm each, which are collimated to form 32 einzel lenses.



Figure 2.3: The outside view of the ion Tectra-make Gen II ECR-based source

**Potential at the grids:**

Grid 1: Anode: The contact of the plasma, which is isolated from the ground in the plasma cup, with the anode shifts the potential of the plasma. Applying a voltage (say +500 V) will shift the plasma potential to +500 V (plus plasma potential). The sample is at ground potential. So the positive ions can be accelerated with about +500 V towards the sample.

Grid 2: Extractor: In this case, a negative voltage is needed to change this grid which controls the divergence of the beam. In addition, small negative field can reach through the anode into the positive plasma. This helps to extract more ions, because of a higher gradient and higher volume.

Grid 3: This grid is kept at ground potential. This is only useful for very low energies. It helps to slow down ions to fly through a field free space near the source.

**Modes of operation:** This ion source can be operated in four different modes which are described below.

**(a) Atom source:** The specially designed aperture plate inhibits ions from escaping from the plasma, yet allows reactive neutrals to escape and form the dominant beam fraction. The emitted particles are largely thermalized through multiple collisions on passing through the aperture.

**(b) Downstream plasma source:** With this aperture plate a larger proportion of the charged particles in the plasma are allowed to escape. There is no active extraction or acceleration of the charged particles but a considerably higher ion current reaches the sample in this mode as compared with the atom source above.

**(c) Hybrid source:** The beam optics in this mode combines the atom source aperture plate with electrodes providing active extraction of ions from the plasma. With no voltage applied to the electrodes the source functions like the atom source. With voltage applied to the electrodes, ions with controllable energy can be added to the atom beam.

**(d) Broad Beam Ion Source:** Dual or triple high conductance grid electrodes are used to produce the broad beam ion source mode. This mode was used for the ion irradiation experiments presented in this thesis.

### **Irradiation Chamber:**

The main irradiation chamber is made up of stainless steel (SS304) and is equipped with a 5-axes manipulator (Prevac, Poland) with X, Y, Z,  $\theta$ , and  $\varphi$  movements (Figure 2.1). A sample platen is attached with the manipulator on which substrates are mounted. The ion current in the target chamber is measured in front of the substrate holder by a retractable Faraday cup integrated in a movable shutter. By proper rotation of the sample platen using the manipulator, sample holder can be placed at any desired angle with respect to the ion-beam.

### **Vacuum system:**

The high vacuum in the irradiation chamber is maintained by a turbo molecular pump (Pfeiffer Vacuum, Germany) backed by a rotary pump (Pfeiffer Vacuum, Germany). The attached load-lock chamber can be separated from the main chamber using pneumatically controlled gate valves (Excel Instruments, India). To get a differential pumping arrangement, the source part of IBSN is equipped with a small turbo molecular pump (Pfeiffer Vacuum Germany) backed by a rotary. The vacuum in the main chamber is about  $5 \times 10^{-9}$  mbar while that in the load-lock chamber is  $1 \times 10^{-8}$  mbar.

## **2.2 DC Magnetron sputtering**

Sputter deposition is a physical vapour deposition (PVD) process where atoms are sputtered from a target material by collision with gas ions and gets deposited on a substrate surface. In this process, a plasma is created and positively charged ions from plasma are accelerated towards a negatively charged electrode or “target”. Upon striking the target, these ions have sufficient energy to dislodge the surface atoms of the target. The atoms which are getting ejected from the surface of the target will condense on surfaces that are placed in proximity to the magnetron sputtering cathode.

In addition, magnetron sputter deposition uses a closed magnetic field to trap electrons. As a result the efficiency of the initial ionization process gets enhanced. It also allows a plasma to be generated at lower pressures which reduces both background gas incorporation in the growing film and energy loss of the sputtered atom through gas collisions.

Arcing is a common source of numerous issues in magnetron sputtering. In contrast to the preferred uniform glow for stable sputtering, arcs are characterized as intense, localized concentrations of plasma supported by collective emission of electrons from the sputtered surface [7]. Multiple mechanisms promote the formation of arcs in sputtering process. Reactive sputtering of dielectrics is particularly problematic because of the formation of insulating regions that can promote severe arcing. It is well established in reactive sputtering that reverse-

voltage pulsing can dramatically reduce arcs in even the most arc-prone reactive processes [8]. Thus, properly chosen pulsing parameters are necessary to optimize the benefit, but once implemented, the result can be a significant reduction of the arc activity [9].

A schematic diagram of a dc magnetron sputtering process is shown in Fig 2.4.

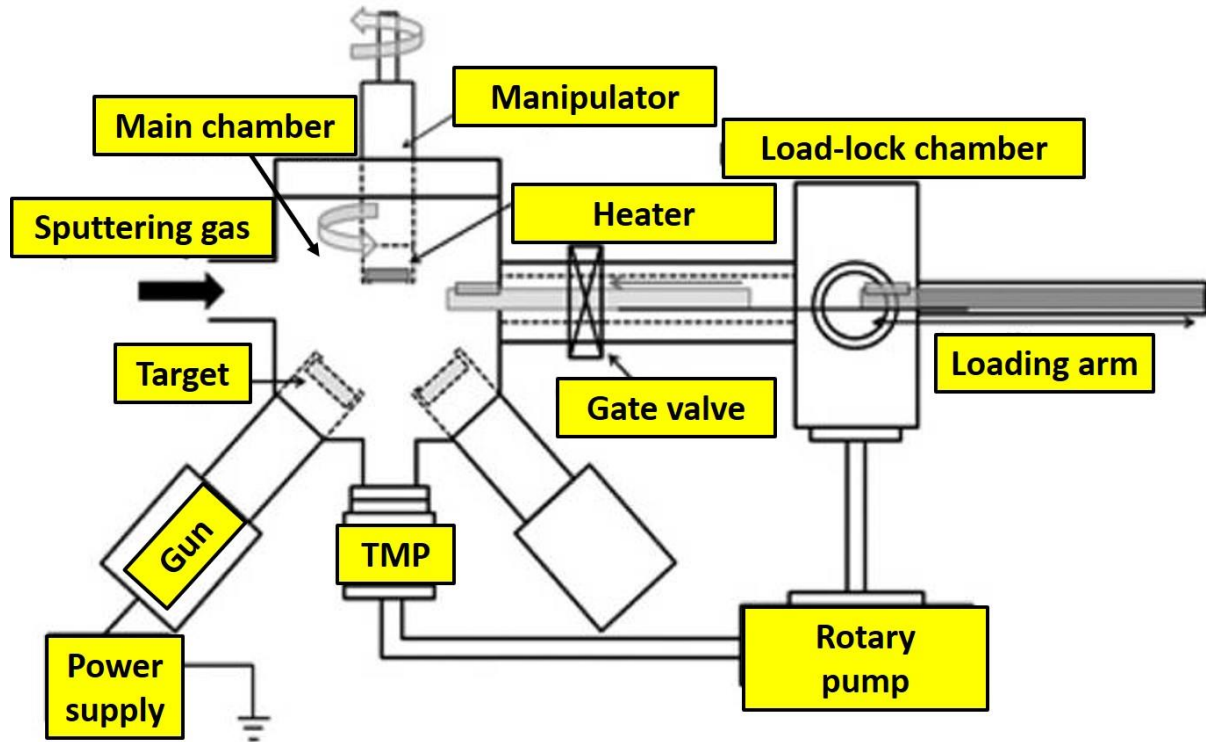


Figure 2.4: Schematic of the high vacuum pulsed dc magnetron sputtering setup

From the schematic, it is seen that a main deposition chamber coupled with a load-lock chamber is the heart of the constituting unit. Turbo molecular pump (Varian, USA) backed by a rotary pump are used to maintain the high vacuum condition. A small port is required to inject the sputtering gas into the main chamber. Generally, a sample manipulator is needed to align the substrate at different angles with respect to the incoming flux. This enables us to deposit films at a particular oblique angle other than normal incidence. More than one magnetron sputtering guns can be attached to the main chamber. These magnetron sputtering guns are equipped with the target material. The pulsed dc magnetron sputtering setup used for this thesis is shown in the Fig. 2.5. Different important parts of the setup are highlighted in yellow colour. The pulsed

dc magnetron sputtering setup (Fig. 2.5) has a spherical high vacuum chamber (Excel Instruments, India). Four 2" diameter magnetron sputtering guns (Excel Instruments, India) can be attached to the main chamber. These guns are equipped with chimneys to prevent the cross contamination between targets. In addition, the temperature of the target holders was kept below 19°C by using a continuous chilled-water flow.

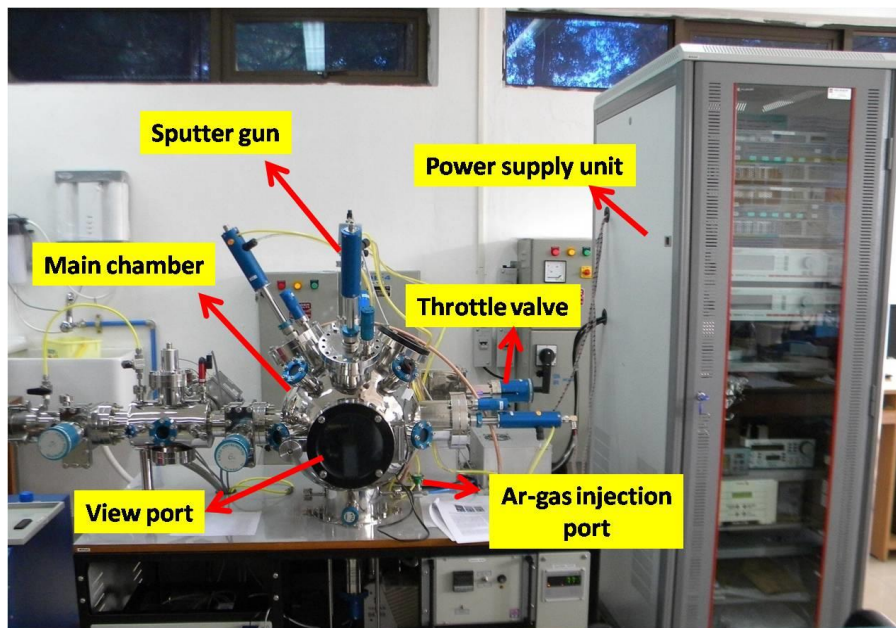


Figure 2.5: Pulsed dc sputtering set up at SUNAG laboratory

AZO films, used in the present thesis, were prepared by using setup at room temperature. The substrates (in the form of pristine- and nanopatterned-Si) were mounted on the top rotating substrate holder at a distance of 10 cm from the target. This substrate holder is equipped with a glancing angle deposition (GLAD) attachment. Prior to sputtering, a base vacuum pressure of  $3 \times 10^{-7}$  mbar was achieved. Then, Ar was introduced into the chamber at a flow rate of 30 sccm (standard cubic centimetres per minute) until it reached a working pressure of  $5 \times 10^{-3}$  mbar. A dc voltage (Pinnacle Plus, Advanced Energy, USA [10]) was applied between the target (cathode) and the substrate (anode) to generate the gaseous Ar plasma. Before each

deposition on substrate, pre-sputtering for a time duration of 5 min was conducted to remove the trapped impurities from the surface of the target. During this process a movable shutter was used to protect the substrate from getting contaminated.

The pulsed magnetron sputtering (PMS) process is an important development in the sputtering technique. However, the DC sputtering of fully dense, defect-free coatings of insulating materials, particularly oxides, is highly challenging. In fact, the process is hampered by low deposition rates and the occurrence of arc events. As the deposition process proceeds, areas on the target away from the main racetrack become covered with an insulating layer, as do the target earth shields. This coverage of the target with the reaction product is referred to as target poisoning. The poisoned layers charges up, until breakdown occurs in the form of an arc.

Arc events during reactive sputtering are a serious problem, because they can affect the structure, composition, and properties of the growing thin film and can also lead to damage of the magnetron power supply. In this regard, pulsing the magnetron discharge in the frequency range of 10-200 kHz, has been found to minimize arc events and stabilise the sputtering process. It may be noted that pulsed dc magnetron sputtering is not a fool proof technique to remove arc events. In order to solve this problem, low frequency ac dual magnetron sputtering may be employed.

### **2.3 Stylus profilometry**

Surface profilometry is one of the common techniques to measure the film thickness. A stylus is a small tool similar to a modern ball point pen. In a surface profilometer, a diamond stylus is moved across the surface to measure the vertical displacement corresponding to the feature studied. This process involves some mechanical and electronic devices in order to perform the conversion [11]. The sample is mounted on a stage which can move in X- and Y- direction. The measurement of the height or Z axis is done by the stylus in contact with the surface. The stylus is located at the end of a cantilever arm. The opposite end of the cantilever is counter-

balanced by a weight that is mounted in a screw system actuated by a motor; the motor can move the counter-weight closer or further from the pivoting centre of the cantilever, regulating the pressure of the tip. By dragging the stylus over the surface, the cantilever will move in Z-direction (up/down) and the force that the stylus impinges over the sample is controlled by the counter-weight system. The linear Z displacement is converted to an electric signal at the end. Thickness measurement of the deposited films was carried out by using a surface profilometer (Ambios XP-200, USA) (Fig. 2.6). The stylus is housed in an acoustic isolation hood to reduce vibrational noise during scanning and placed on a large vibration damped granite block. The vertical range of the profilometer is 400  $\mu\text{m}$  and its vertical resolution is 0.1 nm at a 10  $\mu\text{m}$  scan length, 1.5 nm at 100  $\mu\text{m}$  scan length, and 6.2 nm at 400  $\mu\text{m}$  scan length. The XP-200 profilometer's stylus is diamond coated one and has a tip radius of  $2.0 \pm 0.1 \mu\text{m}$  with an adjustable force range between 0.05 – 10 mg.



Figure 2.6: Stylus surface profilometer.

The XP-200 can also calculate surface roughness, waviness, and perform stress analyses on thin films. The film thickness is measured with respect to the substrate where a portion of the substrate is masked prior to deposition. This helps to get a reasonably good step height during thickness measurement.

Stylus profilometer has advantages of excellent measurement repeatability, thin transparent films can also be probed, long scan measurement up to 3 mm, fast and comparatively cheap. However, it suffers from problems like it is not appropriate for soft samples, resolution is very much tip dependent, and three-dimensional mapping of the surface is time consuming.

## **2.4 Atomic force microscopy (AFM)**

Scanning probe microscopy (SPM) [12] has a family of microscopy techniques for studying surface morphology. In the process of generating surface topography, a probe mechanically moves over the surface and records the probe-surface interaction as a function of position. This interaction can be manifested in different forms, e.g. tunnelling current, inter-atomic force, magnetic force, electrical force, and frictional force etc. which actually decides the mode of microscopy.

The most important among the SPM based techniques is the atomic force microscope (AFM). AFM is a microscopic technique which is applicable to all types of materials – insulators, semiconductors as well as conductors. This technique measures nanoscale variation in the surface topography by measuring the deflection of a tip (10-20 nm in diameter) attached to the end of a cantilever, as the tip is brought to a close proximity of the surface to be probed [13-17].

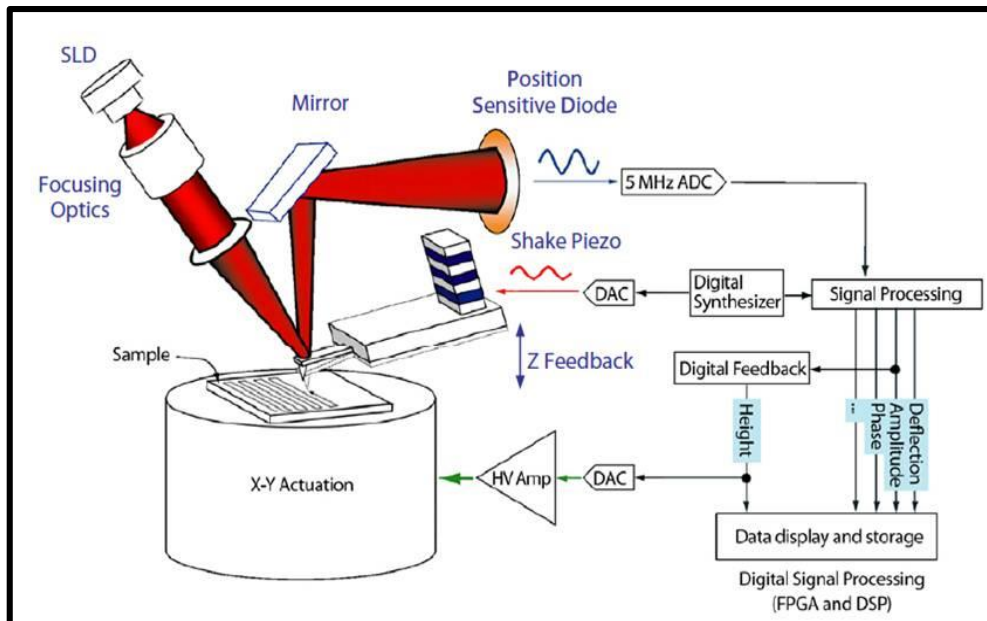


Figure 2.7: Schematic of AFM setup

A schematic diagram of the working principle of AFM is shown in Fig. 2.7. A laser beam is focused on the tip of a highly reflective cantilever head such that the laser beam is reflected on to the surface of a position-sensitive photo-detector [17]. The sample is scanned underneath the tip via a piezoelectric scanner made of PZT (Lead Zirconium Titanate). A feedback loop is used to maintain either a constant deflection (contact mode) or oscillatory amplitude (tapping mode) of the cantilever, as the tip is scanned over the sample surface. The force associated with the tip and the sample during scanning is the inter-atomic Van der Waals force. The dependence of this Van der Waals force upon the distance between the tip and the sample is shown in Fig. 2.8, where three regimes of tip-surface distance are labelled: the contact regime, the non-contact regime, and the tapping regime

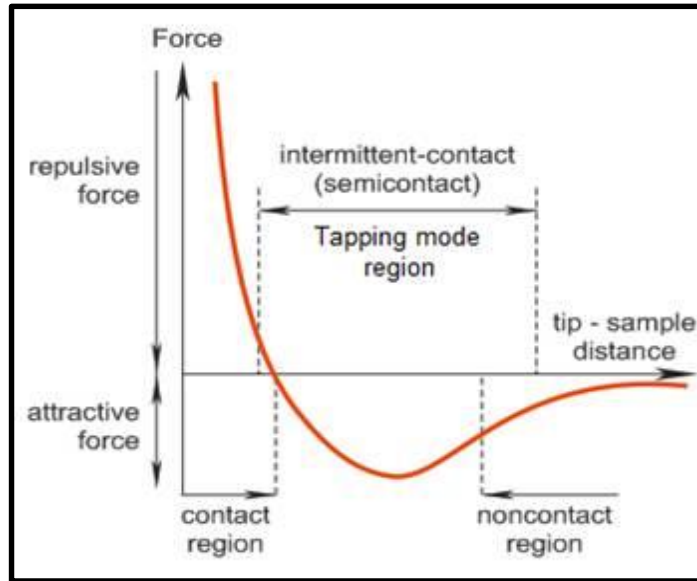


Figure 2.8: Van der Waal's force as a function of tip to surface distance

**Contact or repulsive mode:** In contact-AFM mode, also known as repulsive mode (due to the repulsive nature of the force in this regime), an AFM tip makes soft 'physical contact' with the sample by bringing the tip very close to a surface (a few angstroms). The tip is attached to the end of a cantilever with a low spring constant. As the scanner gently traces the tip across the sample (or the sample under the tip), the contact force causes the cantilever to bend to accommodate changes in the topography. This mode is usually used for hard crystalline surface because strong force involved may cause deformation of soft surfaces.

**Non-contact mode or attractive mode:** Non-contact mode AFM is one of several vibrating cantilever techniques in which an AFM cantilever vibrates near the surface of the sample keeping the tip-to-surface distance in the range of tens to hundreds of angstroms. The major advantage of the non-contact mode AFM is its truly non-invasive character.

**Tapping mode:** This mode is also known as intermittent-contact mode. In this case the vibrating cantilever is brought closer to the sample surface so that it just barely hits or 'taps' the sample. This mode is a compromise between the contact and the non-contact mode where the cantilever is made to oscillate with or near to the resonant frequency using a piezoelectric

crystal so that the tip remains very close to the sample for a short time and then goes far away for a short time. As the oscillating cantilever begins to contact the surface intermittently, the cantilever oscillation necessarily reduces due to energy loss caused by the tip in contacting the surface. The reduction in the oscillation amplitude is used to identify and measure the surface features. This mode allows one to scan soft adsorbates on a substrate with better resolution than in the non-contact mode but with a small interaction (and consequently less modification of the samples) between the tip and adsorbate as in the non-contact mode. Thus, this tapping mode overcomes certain problems associated with conventional AFM scanning method viz. friction, adhesion, electrostatic forces, and other difficulties.

### **AFM System and measurements**

All AFM images in this thesis were acquired with the help of an MFP-3D AFM from Asylum Research, USA in the tapping mode by using Si nitride tips [18,19]. The resonant frequency of the cantilevers is 300 kHz and the spring constant is 42 N/m. Special attention was given to prevent artefacts in the measurements. Among many advantages of this AFM, an important one is its large area-high precision facility because of which we could scan areas up to  $90 \times 90 \mu\text{m}^2$  with very high accuracy. Fig. 2.9 shows different parts of AFM.

A zoomed image of the main part of this AFM setup is also shown in Fig. 9 which shows the scanner, head, base, and thumbwheel. Initially, the head is used to manually bring the tip near the surface. In the next stage, close approach to the surface (separation between tip to sample remain 80 nm) is controlled by software to prevent the damage of tip. A XY-motorized sample stage attached with the AFM helps in precise positioning of a sample and checking large scale uniformity in surface morphology. For AFM image processing, WSxM [20], Gwyddion [21], and SPIP [22] were used. The SPIP (Scanning Probe Image Processor) software package has specialized tools for correcting and analyze SPM data.

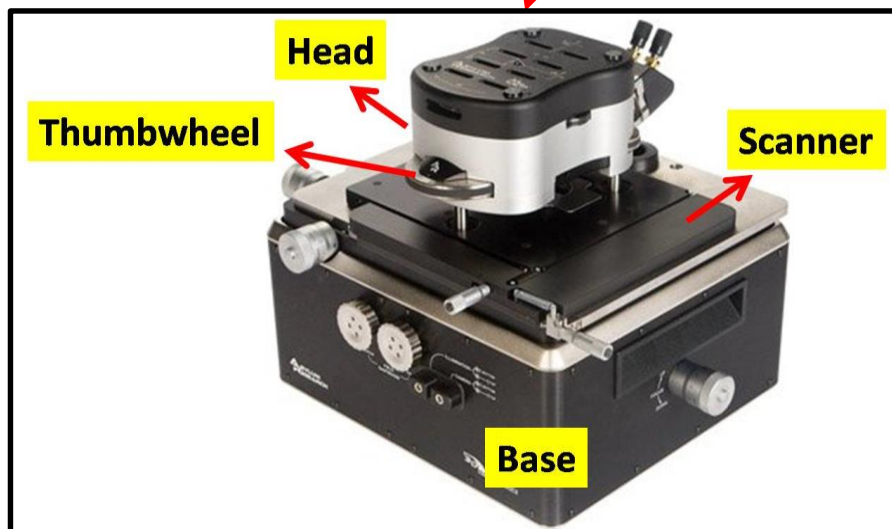


Figure 2.9: MFPD AFM setup

### Scanning Kelvin probe microscopy:

Scanning Kelvin probe microscopy (SKPM) is a technique that attempts to ascertain the potential difference between the probe tip and the sample. The data collected by this sample will represent a combination of three contributing factors: the work function difference, trapped charge, and any permanent or applied voltage between the tip and the sample.

The technique relies on an AC bias applied to the tip to produce an electric force on the cantilever that is proportional to the potential difference between the tip and the sample. There is no mechanically induced drive. The only oscillations that the probe will have will be induced by an applied AC bias. An AC bias applied between the tip and the sample produces an electrostatic force between the two. If they are modelled as a parallel plate capacitor, then the force between the two plates is proportional to the square of the applied voltage ( $V$ ):

$$F = \frac{1}{2} \frac{\partial C}{\partial Z} V^2. \quad (2.2)$$

The total potential difference between the probe and the sample is the sum of the applied AC bias ( $V_{ac}$ ), the potential difference we are trying to measure ( $V_{sp}$ ), and any DC voltage we wish to apply ( $V_{DC}$ ).

$$V = V_{sp} + V_{DC} + V_{ac} \sin(\omega t), \quad (2.3)$$

Where,  $\omega$  is the angular frequency of the applied AC signal.

If we substitute this into Eq. 2.2 and do some rearranging, we get:

$$F = \frac{1}{2} \frac{\partial C}{\partial Z} \left( [(V_{DC} - V_{sp}) + \frac{1}{2} V_{ac}^2] + 2[(V_{DC} - V_{sp}) V_{ac} \sin(\omega t)] - [\frac{1}{2} V_{ac}^2 \cos(2\omega t)] \right) \quad (2.4)$$

Note that there are three force terms here summed together. The first force is static, meaning it has no frequency dependence. The second occurs at the AC voltage drive frequency. The third force oscillates at twice the drive frequency. The most important term here as far as surface potential is concerned is the second, since this depends not on the square of the voltage, but rather on the potential difference between the tip and the sample, multiplied by the magnitude of the applied AC voltage. This means that if there is a potential difference between the tip and the sample, then when an AC voltage is applied, there will be an oscillatory force at the frequency of the drive and proportional to the magnitude of the applied voltage and to the potential difference.

The probes used are generally conductive or heavily-doped semiconductors. Insulating probes does not work on the MFP-3D, as the bias is applied to the tip. To implement this technique on the MFP-3D, a two pass technique is used. The first pass is used to determine the topography of the surface, and was done exactly like a standard tapping mode scan line. The second one is used to find the surface potential, and the tip is raised above the surface. To do this, a technique called '*nap<sup>TM</sup> mode*' is implemented. During a nap scan, the tip is raised over the surface on a point by point basis while the potential feedback loop is implemented.

### **Dual pass tunnelling current microscopy (DPTCM)**

Dual pass tunnelling current microscopy (DPTCM) is an AFM-based local probe technique to map the tunnelling current in ambient condition. In this process, tunnelling current is measured by using a dual pass technique (schematic shown in Fig. 2.10) in the first scan the tip operates in contact mode and maps the surface topography whereas in the second scan, the tip is lifted at a fixed height ( $z$ ) above the surface by following the topographic data of first scan (called lift mode). During the second scan the cantilever does not oscillate and a fixed DC voltage is applied to it with respect to the substrate. This in turn gives rise to a tunnelling current. We term this mode of MFP-3D AFM as *dual pass tunnelling current microscopy* (DPTCM). This process is similar to the tunnelling atomic force microscopy (TUNA) process is reported by Chatterjee *et al.* [23]. This technique not only enables us to track the height and morphological information of the surface but also gives the tunnelling current, simultaneously. In addition, this process can be used for highly rough samples as well. Moreover, this technique is not a conductive atomic force microscopy but here the tip moves in contact mode without any tip potential and hence, it would measure the tunnelling current instead of surface conductivity. The DPTCM studies presented in this thesis, were performed on ion bombarded nanostructured-Si surface using a Pt-coated conductive Si tip. The lift height was fixed at 20 nm from the surface.

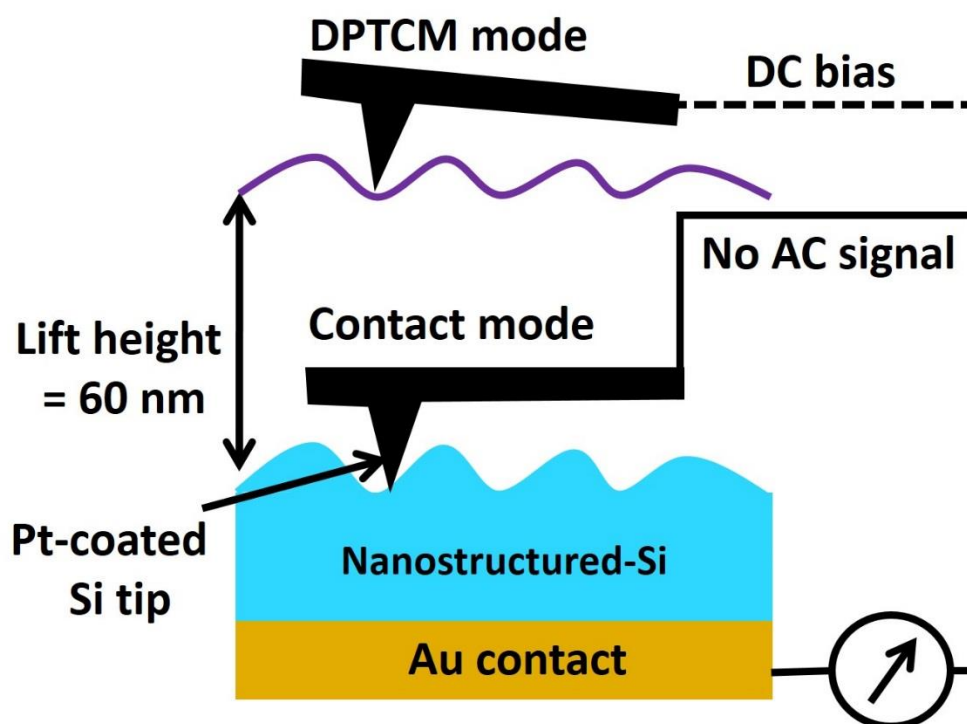


Figure 2.10: Schematic representation of DPTCM using MFP-3D AFM setup

The scanning speed of an AFM can pose some limitations. The relatively slow rate of scanning during AFM imaging often leads to thermal drift in an image, making the AFM microscope less suitable for measuring accurate distances between topographical features on an image. In the present thesis, most of the AFM images are captured with an optimized scan speed of 1 Hz.

Most of the analyses of the surface morphology were carried out using AFM measurements. AFM topographical images obtained from various sample surfaces were analysed using WSxM software. Different parameters viz. rms roughness, ripple amplitude and wavelength, structure height, lateral dimension, autocorrelation function, 2D FFT etc. were extracted from the topography images. However, there are other experimental techniques which may also be employed to calculate the parameters mentioned above. For example, roughness can be calculated from optical profilometry, ripple amplitude and wavelength from cross sectional TEM analysis, structure height and lateral dimension from SEM study etc. Although different

techniques exist, AFM gives the best statistically averaged out results corresponding to surface topography analysis.

## **2.5 Scanning electron microscopy (SEM)**

In scanning electron microscopy (SEM) [24-27] a finely focused electron beam is scanned in vacuum over the sample surface. The novelty of SEM lies in its capability of producing 10-100000 times magnified, three dimensional-like image of surface features of length scale from micrometer down to nanometer. In SEM, the sample needs to be conducting to prevent charging of the sample surface due to electron emission. In case of non-conducting samples, a very thin gold layer is coated over the sample surface or special beam conditions are applied such as low beam energy or high beam spot size and special detectors are used to prevent surface charging.

As the energetic electrons undergo a series of elastic and inelastic scattering events inside a material, different signals result from these interactions, viz. backscattering of electrons and production of characteristic x-rays, emission of secondary electron etc. In the most standard imaging mode secondary electrons are used. Secondary electrons produce topographic contrast with high resolution and large depth of field. The secondary electron coefficient depends strongly on the electron beam energy; at lower energies, they are generated closer to the surface and thus, they have higher escape possibility. At higher electron beam energies, the number of secondary electrons increases but they are excited deeper in the specimen. The secondary electron yield depends also on the surface gradient, increases with increasing tilt angle. Thus, more secondary electrons are produced from the tilted regions of the specimen, and this provides an important mechanism for the surface topography imaging.

A scanning electron microscope contains an electron column containing an electron gun and a demagnification system consisting of electromagnetic lenses for focussing of the electrons from the electron gun to a nanometer size spot on the sample mounted in the sample chamber

below the electron column. Detectors for electrons and x-rays emitted from the sample are also mounted inside the sample chamber and a computer interface is coupled with the detectors for displaying the image. In a field emission gun, the cathode is a very sharp tungsten tip attached to a hairpin shaped tungsten wire. High voltage bias applied on the cathode causes development of intense electric field around the tip which results in electron emission from the sharp tip. The source size of the electron beam can be of the order of 20 nm in field emission gun offering a better resolution in SEM. For the studies presented in this thesis, a Carl Zeiss-make SEM was used [28]. The microscope works with a probe current up to 100 nA and acceleration voltages from 0.2 to 30 kV.

## **2.6 Transmission electron microscopy (HRTEM)**

Transmission electron microscopes [29,30] are usually used to study sample microstructures, crystallinity aspect, etc. The ideal thickness of the sample may, in some cases, be of the order of 100 nm or even less [30] which transmits electron with relatively less energy loss. The power of the TEM relies on its better resolving power and production of diffraction data and images. The configuration of a transmission electron microscope (TEM) is shown schematically in Fig. 2.11. The electron gun at the top of the microscope produces a stream of energetic electrons. Electron guns with LaB<sub>6</sub> crystal filament is commonly used in TEMs. Electrons emerging from the electron gun are focused to a thin, almost parallel beam by a pair of condenser lenses. Some of the electrons in the beam which travel at relatively larger angles with respect to the optic axis is restricted from falling on the sample by a condenser aperture of controllable size placed below the condenser lenses. The sample to be examined is placed at the object plane of the objective lens of the TEM. To obtain a clearly visible image on the phosphor screen, the sample is required to be electron transparent, i.e., thin enough so that a large portion of the incident electron beam is transmitted through the sample. The thickness of any material that the electrons can penetrate through is dependent upon the energy of the incident beam and

elemental composition of the material. In general, it is necessary to thin a sample below 100 nm for observation in TEM and below 50 nm for high resolution TEM (HRTEM). The transmitted portion of the electron beam is focused by the objective lens. An electron diffraction pattern of the sample area illuminated by incident parallel beam of electrons is formed at the focal plane of the objective lens (called back focal plane). The image of the illuminated sample area is formed at the image plane (called the first image plane) of the objective lens as indicated in fig. 2.11. The electron diffraction pattern or the image formed at image plane is magnified on the viewing screen by the first and second intermediate lens and the projector lens assembly. In diffraction mode of operation, the first intermediate lens is adjusted in such a way that the back focal plane of the objective lens becomes the object plane of the first intermediate lens. In this case, an electron diffraction pattern is seen on the viewing screen which consists of a bright central spot on the optic axis and spots due to the diffracted electrons. An aperture of controllable size (called the selected area aperture) is placed at the first image plane. An area of interest can be selected from the sample image formed at first image plane by the selected area aperture. This selected area acts as a virtual source for the intermediate lens assembly so that only electron diffraction from this area can be observed in the viewing screen and is known as selected area diffraction (SAD) imaging. In imaging mode of operation of the TEM, a spot from the electron diffraction pattern can be chosen for imaging by another aperture placed above the SAD aperture which is called the objective aperture. To obtain an image of the sample, the first intermediate lens is adjusted so that the first image plane becomes its object plane. If the central spot on the optic axis is chosen for imaging by the objective aperture then the TEM image is called a bright field image. If any other diffraction spot is chosen for imaging then the image is called a dark field image. In this thesis, TEM measurements have been carried out using JEOL, UHR 2010 (at Institute of Physics,

Bhubaneswar) and field emission gun based 300 keV FEI Tecnai G2 S-Twin (at Saha Institute of Nuclear Physics, Kolkata) machines operating at 200 keV.

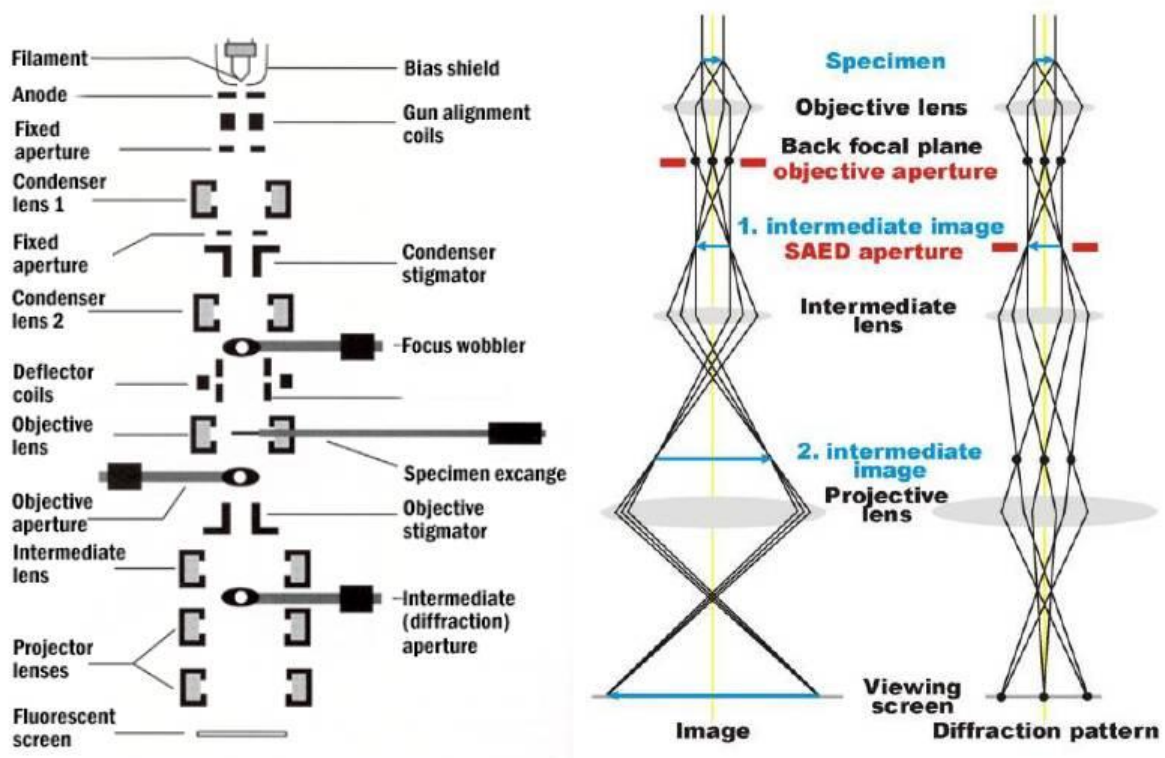


Figure 2.11: Schematic diagram of TEM parts, image formation and diffraction pattern formation process

In HRTEM the image formation is based on the phase contrast mode, which is the most difficult contrast mechanism to image in transmission electron microscopy, but it is also the mode that provides images with higher resolution. It is related to the phase lag in the electron wave front introduced by the passage of the electrons through the sample. The retarded phase will interfere with another wave, giving phase contrast.

It has been mentioned above that for observation of solid samples like ion bombarded Si wafers in TEM, thinning of the sample down to 50-100 nm is necessary for transmission of the electron beam through the sample. The sample thinning process involves several steps, especially in case of preparing sample for cross-sectional observation [31].

## 2.7 X-ray diffraction (XRD)

One of the most widely used techniques for evaluating the crystallinity of materials is x-ray diffraction (XRD). Since the wavelengths of the x-rays (1-100 Å) are similar in size to the interatomic spacing of the material, the waves diffract and scatter. The scattered waves contain information about the material's individual atoms and their arrangement. When a beam of monochromatic x-rays impinges on a sample most of the radiation scattered from atoms and interferes destructively with radiation scattered from other atoms. Hence, no signal is detected. However, when there is long range order in the atomic arrangement of a material, scattered x-rays interfere constructively. This condition of interference is defined by Bragg's law (Fig. 2.12):

$$2d \sin \theta = n\lambda, \quad (2.5)$$

Where  $\theta$  is half the angle between the diffracted beam and the original beam direction,  $\lambda$  is the wavelength of the x-rays and  $d$  is the inter-planar spacing between the planes that cause constructive reinforcement of the beam.

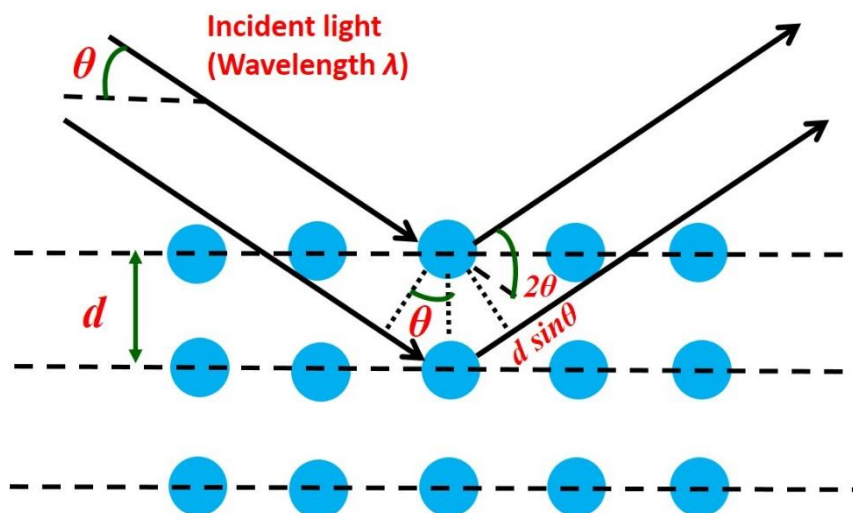


Figure 2.12: Schematic diagram of Bragg's reflection

The most commonly used geometry for thin films is a Brag-Brentano geometry, wherein an x-ray detector records the intensity of the diffracted beam and produces a characteristic diffraction spectra using  $\theta$ - $\theta$  geometry. The recorded characteristic spectra not only be used to determine overall material crystallinity, but also provide a quantitative means of measuring crystallite size by calculating the full width at half maximum (FWHM) of diffracted peaks. The average crystallite size is given by the Scherrer's formula [32]:

$$D = \frac{k\lambda}{\beta \cos \theta} \quad (2.6)$$

$D$  is the average size of the grains,  $\beta$  is the FWHM,  $\lambda$  is the wavelength of incident x-ray, and  $k=0.9$  has been chosen according to the literature. Additionally, relative strain in polycrystalline materials can be measured based on the shift in the central location of the reflection peak.

One of the most widely used techniques for evaluating the crystallinity of materials is x-ray diffraction (XRD). Since the wavelengths of the x-rays (1-100 Å) are similar in size to the interatomic spacing of the material, the waves diffract and scatter. The scattered waves contain information about the material's individual atoms and their arrangement.



Figure 2.13: XRD setup

A Bruker D8 Discover diffractometer [33] (Fig. 2.13) with Cu-K $\alpha$  radiation source was used for the studies presented in this thesis. The x-ray source was operated at a voltage of 40 kV. Göbel mirror attachment is used to produce a parallel beam of x-rays. Single bounce Ge (220) monochromator is used for high-resolution measurements.

## 2.8 Compositional analysis

Compositional analysis of sample were carried out using x-ray energy dispersive spectroscopy (EDS) and x-ray photoelectron spectroscopy (XPS). The basic principles and a brief descriptions of these two techniques are presented in the following paragraphs.

### 2.8.1 Energy dispersive x-ray spectrometry (EDS)

Energy dispersive x-ray spectrometry (EDS) is an analytical technique used for the elemental analysis or chemical characterization of a sample [34,35]. In case of EDS characteristic x-rays are emitted from a material due to energetic electron beam irradiation which are used to identify the elements present in the material and their relative amounts. An incident electron is inelastically scattered and knocks out a core electron. An electron from a higher orbital fills the empty state (hole) in lower (core) orbital. The energy difference between these two orbitals is released in the form of photons (when the core level electron of high enough atomic number is knocked out, the emitted photons have energy in the x-ray regime), whose energy is characterized for the transition in the respective target atom by following Mosley's law

$$\sqrt{\nu} = a (Z-b) \quad (2.7)$$

Where  $\nu$  is the characterized x-ray frequency,  $a$ ,  $b$  are constants, and  $Z$  is the atomic number of the atom. The emitted x-rays are detected by spectrally resolved (the number of counts in a given energy width of typically few eV/channel) with an appropriate energy dispersive detector, like Si(Li) or SDD (Si drifted detector). When an incident x-ray photon strikes the detector crystal its energy is absorbed by electrons in the valence band of the semiconductor and electrons are raised in the conduction band, creating holes in the valence band. A high bias voltage at the front and back face of the detector sweeps this electrons and holes producing a charge signal. The size of the charge signal is proportional to the energy of the incident x-ray photon. The charge signal is converted to a voltage signal by the field effect transistor (FET) circuit attached to the backside of the detector. The electronics in the pulsed processor is used for amplification of the x-ray signal from FET, analog to digital conversion of the data, and measurement of energy of the x-ray photons incident on the detector from the digital voltage signal. The output of the pulsed processor is read by the multichannel analyser inside the

control computer where each channel corresponds to a definite energy interval. For each measurement of x-ray energy by the pulsed processor, the count in the channel of the multichannel analyser corresponding to the x-ray energy is increased by one. The total number of counts at different channels are displayed as an x-ray spectrum. The resolution of the x-ray detector (given by the FWHM of the peak of a characteristic x-ray line) is 132 eV as measured for Mn- $K_{\alpha}$  line (5.9 keV). An EDX spectrum displays peaks corresponding to the energy levels for which the most x-rays had been received. Each of these peaks is unique to an atom, and therefore, corresponds to a single element. The higher the intensity of peak in a spectrum, the more concentrated the element is in the specimen. An EDX spectrum plot not only identifies the element corresponding to each of its peaks, but the type of x-ray to which it corresponds as well. For example, a peak corresponding to the amount of energy possessed by x-rays emitted by an electron in the L-shell going down to the K-shell is identified as a  $K_{\alpha}$  peak.

In this compositional analysis of selective samples were examined by X-Ray Energy Dispersive Spectroscopy (EDS) in the SEM coupled with an EDS arrangement (Carl Zeiss).

### **2.8.2 X-ray photoelectron spectroscopy (XPS)**

X-ray photoelectron spectroscopy (XPS) is a spectroscopic technique which quantitatively measures the elemental composition, chemical state, and charge state of elements present in a material. Since the discovery of photoelectric effect by Heinrich Rudolf Hertz in 1887, it has become the most interesting light-matter phenomenon which was successfully explained later in 1905 by Albert Einstein. Kai Siegbahn and his group in 1954 from Uppsala University (Sweden) developed and recorded the first high-energy-resolution XPS spectrum of the cleaved sodium chloride (NaCl) material [36]. XPS spectra are obtained by irradiating a material with a beam of X-rays while simultaneously measuring the kinetic energy and number of electrons that escape from the top 1 to 10 nm of the material being analyzed. XPS requires ultra-high vacuum (UHV) conditions.

When x-ray photons interact with a solid it leads to ionization and the emission of a core (inner shell) electron from the atoms of the solid. Because the energy of the incoming x-ray photon is known, the binding energy of the emitted electrons can be determined by

$$E_{\text{binding}} = E_{\text{photon}} - (E_{\text{kinetic}} + \phi) \quad (2.8)$$

$E_{\text{photon}}$  is the energy of the x-ray photon,  $E_{\text{kinetic}}$  is the kinetic energy of the electron and is measured by an electron analyzer.  $\phi$  is the work function of the material. These analyzers use electrostatic and/or magnetic lens units focused through apertures to effectively separate out electrons in a desired narrow band of energies from the wide range of energies contained in all other electrons entering the spectrometer.

For every element there will be a characteristic binding energy associated with each core atomic orbital. This gives rise to a characteristic set of peaks in the photoelectron spectrum at kinetic energies, determined by the photon energy and the respective binding energies. The presence of peaks at particular energies therefore, indicates the presence of a specific element in the sample under study. Intensity of the peaks is related to the concentration of the element within the sampled region.

In the present thesis, the XPS experiments were performed using a setup procured VG Instruments (the schematic of the system setup is shown in Fig. 2.14). The base pressure of the main chamber is maintained at  $1 \times 10^{-10}$  Torr. The load-lock chamber is equipped with low energy Ar ion gun. The XPS system is equipped with twin Mg/Al anodes, a hemispherical analyzer, and a channeltron unit. The dual anodes generate non-monochromatic X-ray emissions of energies 1253.6 eV for Mg- $K_{\alpha}$  and 1486.6 eV for the Al- $K_{\alpha}$  lines. Analyzer was operated with the pass energy of 200 eV for the large survey scans of 1–1000 eV, and 20 eV for the high-resolution scans. The instrumental resolution of the setup is 0.9 eV. The data were acquired at an angle of  $45^{\circ}$  between the sample normal and the analyzer axis. The final spectra were fitted using the VGX-900 software to get the binding energy positions of the elements.

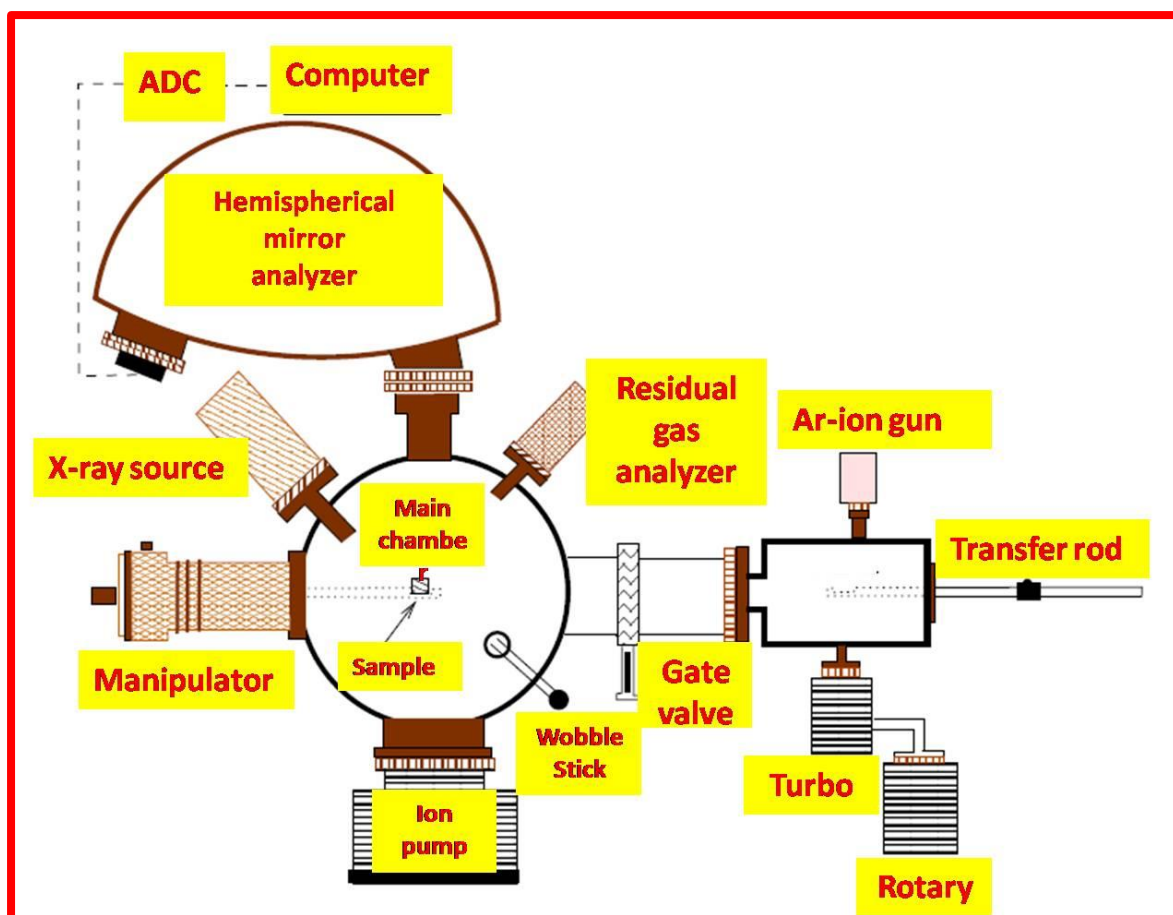


Figure 2.14: Schematic diagram of the XPS setup displaying different components

## 2.9 Optical studies

Reflectance measurements and photoluminescence studies were carried out for ion bombarded Si samples and AZO thin films grown on Si substrates. The working principles of these facilities are described below.

### 2.9.1 Reflectance

Reflectance is the amount of incident light that is reflected by a surface. Optical reflectance measurements were obtained using a Shimadzu UV 3101PC UV-visible-NIR spectrophotometer (Fig. 2.15) equipped with a specular reflectance measurement accessory. The spectral range that can be studied with this instrument is 200 to 3200 nm. However, in the present thesis, most of the spectra were collected over a wavelength range of 300–800 nm using

1 nm increment. The reflectance mode works in a specular reflection geometry arrangement with  $45^{\circ}$  incidence angle of light.



Figure 2.15: UV-Vis spectrophotometer

## 2.9.2 Photoluminescence

Emission of light from a material under optical excitation is known as photoluminescence (PL). PL is a useful non-destructive method for studying the band gap of semiconductor materials. When photons having energy greater than the band gap of a material is incident on the material, they are absorbed and as an outcome electronic excitation from valence band to conduction band take place. This creates holes in the valence band. Subsequently, electrons come down to the lowest level of the conduction band by nonradiative transition and then drop to the holes in the valence band. The energy difference in the electronic transition is radiated in the form of electromagnetic radiation. Thus, PL spectrum of a bulk semiconductor, in general, corresponds to its band gap. In low-dimensional systems, the gap between the valence band and the

conduction band increases due to the finite size of the systems. As a result, the frequency of the PL peak from these systems, corresponding to the transition of electron from the bottom of the conduction band to the top of the valence band, is shifted compared to that of the bulk materials. The characteristic change of the width of band gap with decrease in size of the nanostructures can thus, be studied from the shift in PL peak position. The PL studies presented in this thesis are based on the measurements by using a FLS 920 fluorescence spectrometer from Edinburgh Instruments, UK. The exciting radiation comes from a He-Cd 325 nm UV laser and is detected by a semiconductor detector having photomultiplier tube as attachment.

## **2.10 Electrical measurements**

The electrical properties of thin films, such as electrical conductivity and resistivity, are most commonly performed in the semiconductor industry using a four-point probe system. The four-point probe is often used on test structures throughout the semiconductor fabrication process to ensure and verify the condition of the device between the various processing steps. Two-point probe systems must take into account contact resistance and therefore, it makes the measurements much more difficult and erroneous.

### **2.10.1 Resistivity**

The resistivity of the films was determined by the four-probe method with the electrodes in the planar geometry. High conductivity silver paste was used for making contacts. The Ohmic nature of these contacts was confirmed with current-voltage ( $I$ - $V$ ) measurements which showed linear behaviour. The resistivity ( $\rho$ ) of the films was calculated applying Ohm's law, by using the relation  $\rho = RA/L$ . Here  $R$  is the resistance given by the slope of the current-voltage characteristic curves,  $A$  is the area of the film in the planar geometry given by the product of the film thickness and the width of the film,  $L$  is the spacing between the electrodes. The current voltage measurements were carried out using a Keithley source measure unit (Model 2410).

### 2.10.2 I-V characteristics

I-V characterization consists of basically applying a voltage between two probes in the sample and measuring the current that flows through the sample. I-V measurements were carried out using a Keithley 2410 source meter. Each source meter instrument is both a highly stable DC power source and a true instrument-grade 6½-digit multimeter. The power source characteristics include low noise, and precision. The result is a compact, single-channel, DC parametric tester. To do the characterization we used a computer program which scans voltage at constant rate up to maximum desired voltage.

### 2.10.3 C-V characteristics

Capacitance-voltage (C-V) profiling is used for characterized various semiconductor materials. In this technique, applied voltage is varied and corresponding capacitance (across a junction) is measured at plotted as a function of the voltage. Generally, a metal-semiconductor junction or a *p-n* junction were characterized using this technique where the formed depletion region (with its ionized charges) behaves like a capacitor. By varying the applied voltage one can vary the width of the depletion region. The dependence of the depletion width on the applied voltage provides information about the doping profile, defect densities, and junction barrier height etc. C-V measurements can be carried out using a DC or an AC signal.

In the present thesis, capacitance measurements are useful in determining the built-in voltage ( $V_{bi}$ ) as per the following equation mentioned below, where  $\epsilon_0$  is the permittivity of free space,  $K_s$  is the dielectric constant,  $A$  is the cross-sectional area,  $N_A$  is the acceptor concentration. Eq. 2.9 is the depletion capacitance equation for a metal-semiconductor, which is a good approximation and applicable for a highly doped *n*-AZO layer deposited onto a *p*-Si.

$$\frac{1}{C^2} = \frac{2(V_{bi} - V_A)}{qN_A K_s \epsilon_0 A^2} \quad (2.9)$$

In the ideal system, plotting  $1/C^2$  vs.  $V_A$ , the applied voltage, yields a straight line intercepting at  $1/C^2 = 0$  with the voltage axis. Following the above equation, the slope of this line is proportional to the carrier density and therefore, a straight line is indicative of a uniform doping distribution. Capacitance measurements, which are ideally frequency independent, indicate the capacitance of the space charge layer. It is however often the case that these plots are frequency dependent. Two types of plots are possible: curves that are parallel to each other and therefore having different built-in voltages and curves that have different slopes, converging to the same built-in voltage. The latter behaviour is attributed to the presence of surface irregularities and/or surface states in the semiconductor.

According to the equation, a nonlinear relationship between  $1/C^2$  and  $V$  are expected when deep levels are present and exposed and when their sites are ionized. Concentration levels increase in a nonlinear fashion as a result of bias changes. Nonlinearity in  $1/C^2$  vs.  $V$  curves is therefore, a direct result of the effect of deep level charge. The studies presented in this thesis were carried out using a precision LCR meter (HP 4284A).

#### 2.10.4 Photoresponsivity studies

In general, optoelectronic property of a heterojunction is categorized in two groups, namely, generation of photocurrents due to absorption of photons and the emission of photons as a result of electronic excitation in the heterojunction. In the thesis we concentrate on the former one. The current–voltage characteristic of a heterojunction gets changed under the presence of a light source. The modified expression can be written as [37]:

$$J = J_S \left[ \exp\left(\frac{qV}{K_B T}\right) - 1 \right] - J_R \quad (2.10)$$

Where  $J_R$  is the photocurrent density,  $J_S$  is the dark reverse saturation current density, and  $V$  is the applied voltage. In absence of recombination or generation of carriers,  $J_R$  is voltage

independent and is equal to the short-circuit photocurrent density  $J_{sc}$ . The open circuit voltage  $V_{oc}$  across the heterojunction ( $J=0$ ) can be expressed as:

$$V_{oc} = \frac{K_B T}{q} \ln \left[ 1 + \frac{J_R}{J_S} \right] \quad (2.11)$$

The saturation current ( $J_S$ ) depends on the heterojunction structure, while  $J_R$  depends on a geometrical dimension of the heterojunction.

The most commonly used mode of illumination for heterojunction is perpendicular illumination where the photons are incident on the front surface of the wide-band gap material and are perpendicular to the plane of the junction. In this case the high energy photons are absorbed in the wide band gap material while low energy photons penetrate through the wide band gap material and are absorbed in the narrowband gap material near the interface. This phenomenon is called window effect.

A heterojunction which responds to the incident photons is known as photon detectors. The photon detectors measure the rate of arrival of quanta and show a selective wavelength dependence of the response (in the form of current or voltage) per unit incident radiation power. Photovoltaic cell (solar cell) is a type of the photo detector where the energy of sun light is directly converted into electricity.

A solar cell under illumination is characterized by the following parameters: responsivity, short-circuit current, open-circuit voltage, the fill factor and the power conversion efficiency. In the following paragraphs these parameters are clarified [38].

### **Responsivity**

Responsivity ( $R_\lambda$ ) is defined as the ratio between the output electrical signals [voltage or current ( $I_{ph}$ )] to the incident radiation power ( $P_{in}$ ). The responsivity for monochromatic light of wavelength incident normally is given by [38]

$$R_\lambda = \frac{I_{ph}}{P_{in}} \quad (2.12)$$

### **Short–Circuit Current**

The short circuit current ( $I_{SC}$ ) is the current in illumination device at zero voltage bias. By the overlap between the absorption spectrum of the solar cell and the solar spectrum, the amount of current is determined, the intensity of the sunlight, the thickness of the active layer and the excitation charge. [39]

### **Open – Circuit Voltage**

The open-circuit voltage ( $V_{OC}$ ) is the voltage represents the bias we have to apply in our device in order to decimate the current generated by illumination of our device. So, at the  $V_{OC}$  point there is no external current that flows through the device under illumination ( $I= 0$  A) [39].

### **Fill Factor**

Another defining term in the overall behaviour of a solar cell is the fill factor ( $FF$ ). This is the ratio of the available power at the maximum power point ( $P_M$ ) divided by the open circuit voltage ( $V_{OC}$ ) and the short circuit current ( $I_{SC}$ )

$$FF = \frac{P_M}{V_{OC} \times I_{SC}} \quad (2.13)$$

### **Efficiency**

The operating regime of the solar cell is the range of bias, from 0 to  $V_{OC}$ , in which the cell delivers power. The cell power density ( $P$ ) is given by

$$P = JV \quad (2.14)$$

$P$  reaches maximum at the cell's operating point or maximum power point. This occurs at some voltage ( $V_{max}$ ) with a corresponding current density ( $J_{max}$ ).

The efficiency ( $\eta$ ) of the cell is the power density delivered at operating point of the incident light power as a fraction of the incident light power density is given by

$$\eta = \frac{J_{max} \times V_{max}}{P_{in}} \quad (2.15)$$

Alternatively,

$$\eta = \frac{J_{SC} \times V_{OC} \times FF}{P_{in}} \quad (2.16)$$

These four quantities:  $J_{SC}$ ,  $V_{OC}$ ,  $FF$ , and  $\eta$  are the key performance characteristics of a solar cell. All of these should be defined for particular illumination conditions.

The photovoltaic testing system (PTS, Sciencetech, Canada) [40], used for the present case, includes a 150 W Xe lamp and a monochromator to tune the light source. A schematic diagram is shown in Fig. 2.16 for better realization.

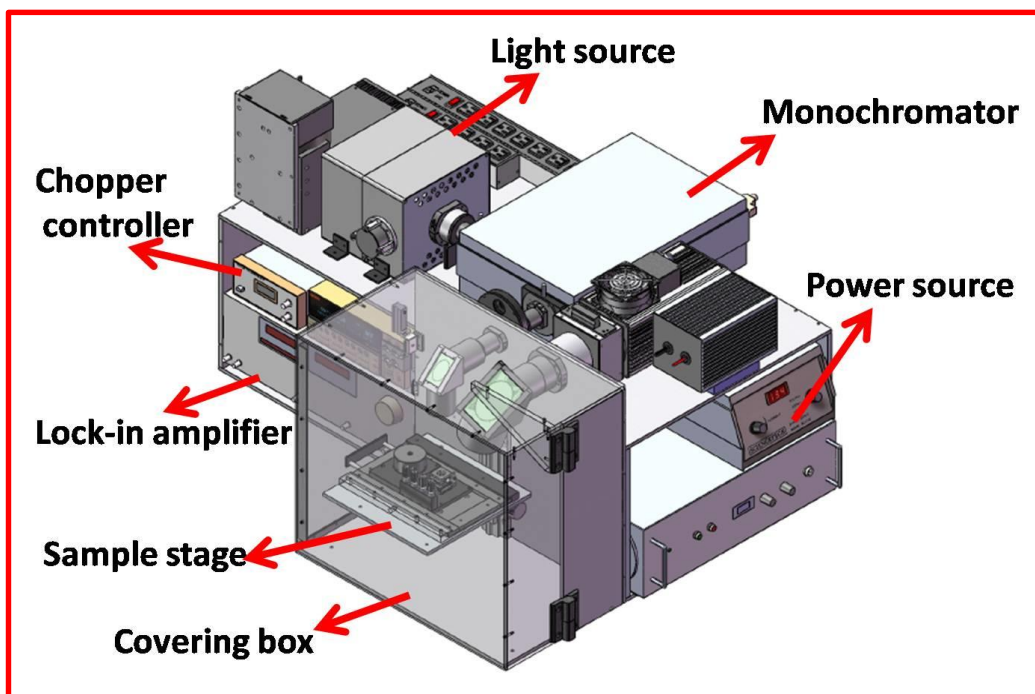


Figure 2.16: Schematic diagram of the Photoresponsivity measurement setup

A source meter was used as an active load permits operating the test cell at various load conditions, including short-circuit, compensating for a series resistor required to sense the current produced by the modulated monochromatic light. This sensed current plus a reference signal at the frequency of the light modulation are both fed into the precision lock-in amplifier to allow measurement of the photocurrent generated by the modulated monochromatic light.

PTS1 software provided by the company allows us to measure the spectral response (SR) and

*I-V* characteristic of the cell. It includes a SCIRUNSR *I-V*-Test measurement system, precision lock-in amplifier, and system software. The software controls the monochromator, source meter, and lock-in amplifier to automatically measure the *I-V* characteristics and SR versus wavelength, plotting the results on the screen and outputting calculated values, including  $V_{OC}$ ,  $I_{SC}$ ,  $P_{max}$ , fill factor ( $FF$ ), and the raw measurements to a standard file format. Key features of this instrument is listed below:

- Monochromator with automated order sorting filters
- Monochromatic probe light area adjustable from 2mm to 5mm diameter
- Monochromatic probe light power of 125 mW total (white light)
- Keithley 2400 Series source meter
- Bias voltage ranges from 0-200 V
- Calibrated reference detector
- Optical chopper and drive
- Stanford SR800 series lock-in amplifier
- Photocurrents measurable from 1 picoampere to 1 microampere
- Automated switching of lock-in input signals from reference detector to sample current measurement
- Target table with dual cell holder having 150 mm height adjustment

### **2.10.5 Field emission studies**

The field emission (FE) is a unique quantum mechanical effect, where electrons tunnel through a potential energy barrier at the solid-vacuum interface into the vacuum under an external electric field. The efficiency of this emission process is tens of millions of times higher than in other known emission process. This phenomenon occurs in high electric fields  $10^7$ - $10^8$ V-cm<sup>-1</sup>. In order to produce such high fields using reasonable potentials, the emitter is usually formed

into a tip with the apex radius of curvature ranging from tens of angstroms to several microns. The high electric field narrows the potential barrier (which can be described as the zero electric field work function energy,  $\Phi$ ) at the metal-vacuum interface so that the electrons undergo Fowler-Nordheim (F-N) tunnelling [41,42].

Generally, FE is defined by the Fowler-Nordheim (FN) equation which is defined as:

$$J = A \left( \frac{\beta^2 E^2}{\Phi} \right) \exp \left( \frac{-B\Phi^{3/2}}{\beta E} \right) \quad (2.17)$$

where  $J$  is the emission current density ( $\text{A m}^{-2}$ ),  $E$  is the mean electric field between the electrodes ( $\text{V } \mu\text{m}^{-1}$ ), and  $\Phi$  is the work function (eV). The constants are  $A=1.56 \times 10^{-10} \text{A V}^{-2} \text{eV}$  and  $B=6.83 \times 10^3 \text{V eV}^{-1.5} \mu\text{m}^{-1}$ . The enhancement factor,  $\beta$ , depends on tip-sample geometry which is 1 for a flat surface and higher for other geometries.

Field emission from semiconductors is a much more complicated process due to its low carrier concentration in bulk emitter compare to metal emitter. In the presence of external field, low carrier concentrations allow for field penetrating into the semiconductor, causing band bending and nonlinearity of current-voltage characteristics in F-N coordinates. The intercept of F-N plot,  $\ln(J/E^2)$  vs.  $1/E$  contains electron emission related information about effective emission area and field enhancement factor.

All the field emission studies presented in this thesis, were performed within a vacuum chamber at a base pressure of  $5 \times 10^{-7}$  mbar. Field emission measurements (presented in this thesis) were carried out using a standard two-electrode configuration with copper anode electrode and the sample was attached to the cathode plate with conductive copper tape (sheet resistance  $\sim 0.004 \Omega/\square$ ). Voltage was supplied to selective ion-bombarded Si samples with a Keithley 2410 source meter. The same source meter was used to measure corresponding field emission current as well.

## Bibliography

1. R. Anton, Th. Wiegner, W. Naumann, M. Leibmann, Chr. Klein, and Chr. Bradley, *Rev. Sci. Instrum.* 71 (2000) 1177.
2. [www.prevac.eu](http://www.prevac.eu)
3. *Handbook of Ion Source*, B. Wolf, ISBN 0-8493-2502-1, p136-146
4. D. P. Norton, M. E. Overberg, S. J. Pearton, K. Pruessner, J. D. Budai, L. A. Boatner, M. F. Chisholm, J. S. Lee, Z. G. Khim, Y. D. Park, and R. G. Wilson, *Appl. Phys. Lett.* 83(2003) 5488.
5. R.V. Stuart, *Vacuum technology, thin film, and sputtering*, Academic Press, Inc. (1985)
6. J.B. Webb, *Thin films for free atoms and particles*, Chapter 6, Academic Press, Inc. (1985)
7. A. Anders, *Thin solid Films* 502 (2006) 22.
8. P.J. Kelly, P.S. Henderson, R.D. Arnell, G. A. Roche, D. Carter, *J. Vac. Sci. Technol. A* 18 (2000) 6.
9. D. Carter, H. Walde, G. McDonough, G. Roche, *Society of Vacuum Coaters Conference Proceedings* (Apr. 2002).
10. [www.advanced-energy.com](http://www.advanced-energy.com).
11. D-H Lee and N-G Cho, *Meas. Sci. Technol.* 23 (2012) 105601.
12. G. Binnig, C.F. Quate, and Ch. Gerber, *Phys. Rev. Lett.* 56 (1986) 930.
13. Y. Seo and W. Jhe, *Rep. Prog. Phys.* 71 (2008) 016101.
14. G. J. Legget, "Scanning Tunneling Microscopy and Atomic Force Microscopy", in *Surface Analysis: The Principal Techniques*, edited by J C Vickerman (John Wiley & Sons, Chichester, 1997), pp. 393.
15. S. N. Magonov and N. A. Yerina, "Visualization of Nanostructures with Atomic Force

- Microscopy", in *Handbook of Microscopy for Nanotechnology*, edited by N Yao and Z L Wang (Springer, Berlin, 2005).
16. K. S. Birdi, *Scanning Probe Microscopes: Applications in Science and Technology*. (CRC Press, Boca Raton, 2003).
  17. Y. Sugawara, "Atomic Force Microscopy", in *Roadmap of Scanning Probe Microscopy*, edited by S. Morita (Springer, Berlin - Heidelberg, 2007).
  18. <http://www.oxford-instruments.com/products>
  19. <http://probe.olympus-global.com/en/>
  20. <http://www.nanotec.es/products/wsxm/>
  21. <http://gwyddion.net/>
  22. <http://www.imagemet.com/>
  23. V. Chatterjee, R. Harniman, P.W. May, and P.K. Barhai, *Appl. Phys. Lett.*104 (2014) 171907.
  24. D. K. Schroder, *Semiconductor material and device characterization*. (John Wiley & Sons, Inc., Hoboken, New Jersey, 2006), 3rd ed.
  25. B. G. Yacobi, D. B. Holt, and L. L. Kazmerski, "Scanning Electron Microscopy", in *Microanalysis of solids*, edited by B. G. Yacobi, D B Holt, and L. L. Kazmerski (Plenum Press, New York, 1994).
  26. P. S. Turner, C. E. Nockolds, and S. Bulcock, "Electron Microscope Techniques for Surface Characterization", in *Surface Analysis Methods in Materials Science*, edited by D J O'Connor, B A Sexton, and R St C Smart (Springer-Verlag, Berlin Heidelberg, 2003).
  27. H. Czichos, T. Saito, and L. Smith (eds), *Springer Handbook of Materials Measurement Methods*. (Springer-Verlag, Heidelberg, 2006).
  28. <http://www.zeiss.de>.

29. A. J. Garrat-Reed, "Transmission Electron Microscopy", in *Microanalysis of Solids*, edited by B. G. Yacobi, D. B. Holt, and L. L. Kazmerski (Plenum Press, New York, 1994).
30. N. Yao and Z. L. Wang (eds), *Handbook of microscopy for nanotechnology*. (Kluwer Academics Publishers, New York, 2005).
31. B. Satpati (Ph. D. Thesis, Institute of Physics, Bhubaneswar)
32. A.L. Patterson, *Phys. Rev.* 56 (1939) 978.
33. <http://www.bruker.com/products>
34. D. K. Schroder *Semiconductor material and device characterization*, second edition, A Wiley-interscience publication, New York, 1998.
35. P.E.J. Flewit and R.K. Wild, *Physical methods for material characterization*, second edition, IOP publishing, London, 2003.
36. K. Siegbahn, and K. I. Al. Edvarson, *Nuclear Physics* 1 (1956) 137.
37. B. Sharma and R. Purohit, First edition Vol. 5, (1974).
38. A. Tom, *Organic Bulk Heterojunction Solar Cells from Single Cell Towards FullFlexible Photovoltaic Module*, (2006).
39. Y. Liao, *Microwave Solid State Devices*, Chapter 9, p.p:11. (1984).
40. <http://sciencetech-inc.com/>
41. R. H. Flower and L. Nordheim, *Proceedings of the Royal Society of London. Series A* 119 (1928) 173.
42. P. A. Chatterton, *Proceedings of the Physical Society* 88 (1966) 231.

---

# CHAPTER 3

---

## 3. Theoretical Background

Self-organization of surfaces under ion bombardment has been extensively studied since its discovery [1]. The potential of ion-beams to create surface patterns rests on the simplicity by which large amounts of energy can be deposited near the surface of materials, thereby creating non-equilibrium, driven states of matter at the surface. In general, ion irradiation can lead to smoothening or roughening of surfaces depending upon the experimental conditions. However, till date, no single theory is able to capture the entire variety of patterns and their parameter space of formation. The materials, which get amorphized under ion-beam bombardment, are considered to be well describable in the frame work of continuum models [2] which describes the ion-bombarded surface at a length scale much higher than the atomic scale.

Theoretically, the roughness or smoothness of surface under ion exposure is described by fluctuations in surface height. In this chapter, we will first briefly introduce some basic parameters used to characterize a surface. Later on, we will present a short review of the theoretical models developed for understanding surface evolution under ion bombardment.

### 3.1 Statistical characterization of surfaces

In a continuum description, a surface can be described by a height function  $h(r) \equiv h(x,y)$  where the height is measured from a fixed reference frame and  $r = (x,y)$  is any point on the surface. The statistical quantities which are used to characterize the surface, are defined through the variation of  $h(r)$  over the surface as described below.

#### Average Surface Height

The average or mean surface height,  $\bar{h}$ , is the simplest characterization of a surface. It is defined as

$$\bar{h} = \frac{1}{L^2} \int_{-L/2}^{L/2} \int_{-L/2}^{L/2} h(x, y) dx dy, \quad (3.1)$$

where the surface height is measured over a surface area of dimension  $L \times L$ .

### RMS Roughness

This quantity determines the fluctuation in surface height with respect to the mean height. It is defined as

$$w = \frac{1}{l} \left[ \int_{-L/2}^{L/2} \int_{-L/2}^{L/2} [h(x, y) - \bar{h}]^2 dx dy \right]^{1/2} \quad (3.2)$$

### Correlation functions and correlation length

The connection or correlation of spatially separated surface points can be determined by the autocorrelation or height-height correlation function. The correlation length expresses the distance up to which height of two surface points can be considered to be correlated

**Autocorrelation:** The autocorrelation function  $R(r)$  is defined as,

$$R(r) = \frac{1}{w^2} \frac{1}{L^2} \int_{-L/2}^{L/2} \int_{-L/2}^{L/2} [(h(x, y) - \bar{h})(h(x+x', y+y') - \bar{h})] dx dy, \quad (3.3)$$

where,  $r$  is the spatial separation between two arbitrary surface points  $r_1 = (x, y)$  and  $r_2 = (x+x', y+y')$ . For a truly random rough surface,  $R(r)$  decays to zero with the increase of  $r$ . The decay rate depends on the randomness of the surface. The lateral correlation length ( $\zeta$ ) is defined as a length scale over which the magnitude of  $R(r)$  decreases to  $1/e$  of its value at  $r=0$ , i.e,  $R(\zeta) = (1/e) R(0)$ . If the distance  $r$  between two surface points is within lateral correlation length  $r < \zeta$ , the heights at these two points can be considered to be correlated. If the distance  $r$  between two points is greater than  $\zeta$  the height at these two points is considered to be independent of each other.

## Power spectrum

So far we have discussed the statistical properties of a rough surface in real space. Equivalent to real space characterization, a surface can also be characterized in reciprocal space by a function called the power spectrum or structure factor of the surface. Power spectrum,  $S(k)$ , is the square of the Fourier transformation of the surface height profile  $h(x,y)$  and expressed as

$$S(k) = \frac{1}{L^2} \left| \int_{-L/2}^{L/2} \int_{-L/2}^{L/2} [h(x+x', y+y') - h(x, y)] e^{-i(k_x x + k_y y)} dx dy \right|^2 \quad (3.4)$$

If the surface height fluctuation is periodic with a repetition length  $l$ , the periodicity will be reflected in the power spectrum  $S(k)$  as a peak at the wave number  $k = 2\pi/l$ .

## Measurement of ripple wavelength from AFM images

For our ripple patterned Si samples, the ripple wavelength has been determined from the autocorrelation of the AFM images. The autocorrelation image is the two-dimensional autocorrelation function as defined in Eq. 3.3. For the ripple patterned surfaces, the autocorrelation images show the bright strips on the two sides of a central line. The distance of the nearest bright region from the central bright region gives the wavelength of the ripple pattern [3].

## 3.2 Ion-Solid interaction

Ion bombardment of a solid surface results in a gamut of events [4,5]. A schematic of such events is presented in Fig. 3.1. These interactions are described below.

The major fraction of the incident ions penetrates through the target surface and enters inside the solid. While traveling through the bulk of the solid, the energetic ions slow down by transferring energy in elastic collisions with the target atoms and inelastic collisions with the target electrons. The energy transferred to these displaced target atoms are spent in the same process of collisions with other stationary target atoms and electrons, creating higher order

generations of mobile target atoms and electrons. Thus, this consecutive collision process results in a region within the target solid within which most of the atoms are mobile.

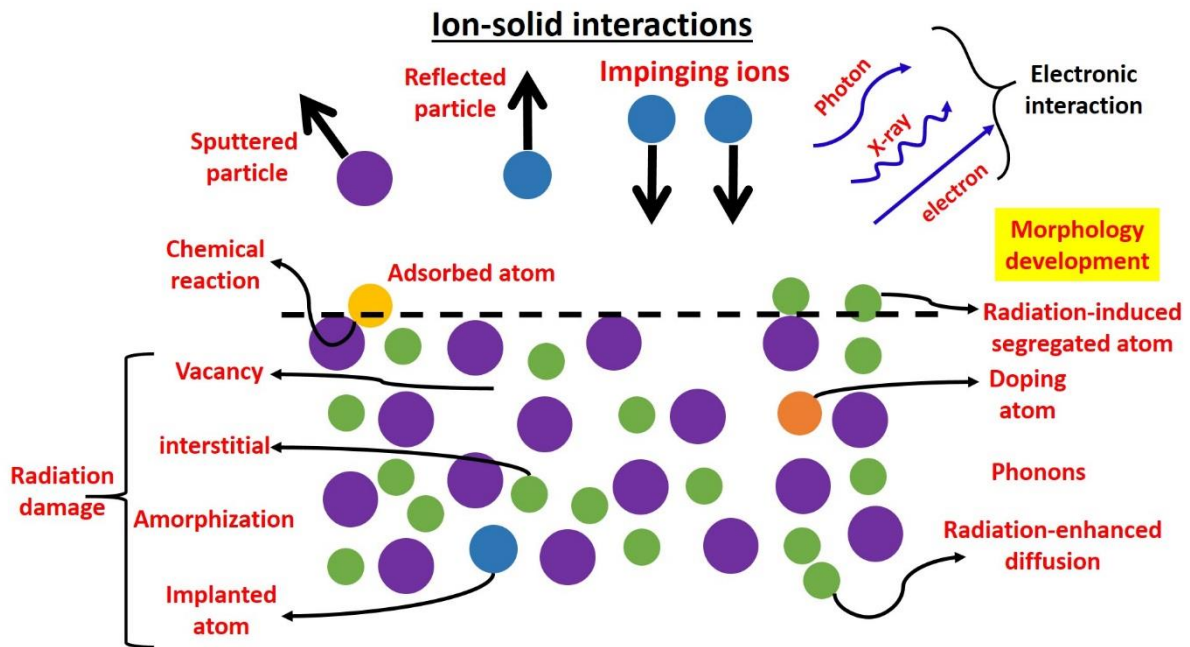


Figure 3.1: Interaction of energetic ions with solid target

This region is known as a collision cascade. If the target atoms located near the surface receive the energy required to overcome the surface potential energy barrier, from this collision cascade, atoms can be knocked out of the surface. This phenomenon of removal of atoms from the target surface is known as sputtering.

A small fraction of the incident ions, which undergo large angle scattering collision with the atoms of the target surface, are reflected back from surface. These atoms, called backscattered atoms, can be charged or neutral species.

Interaction of the energetic ions with the target electrons can give rise to secondary electron emission from surface, or emission of optical or x-ray photons.

The displacement of target atoms from their lattice sites causes the formation of highly disordered zones around the path of the incident ions. Disorder of the lattice structure introduced this way is termed as radiation damage. At sufficiently high doses, the individual disordered zones may overlap, and an amorphous layer may form.

### 3.2.1 Stopping of ions in matter

The interacting ion dissipates energy by elastic, nuclear collisions with the target atoms, known as *nuclear stopping*. This is the reason for defect generation in semiconductors and metals. They lead to the production of Frenkel pairs consisting of a vacancy and an interstitial atom. On the other hand, the second one, i.e. electronic stopping, leads to inelastic loss of energy by exciting the electrons of the target atoms and is known as electronic stopping.

The rate of energy loss of ions inside a target is expressed through the stopping power  $dE/dx$ , where  $dE$  is the energy lost by incident ions in traversing a distance  $dx$  measured from a reference frame parallel to the surface. The stopping power can be written as a summation of energy loss rates due to nuclear and electronic collisions as

$$\frac{dE}{dx} = \left( \frac{dE}{dx} \right)_n + \left( \frac{dE}{dx} \right)_e, \quad (3.5)$$

where  $\left( \frac{dE}{dx} \right)_n$  and  $\left( \frac{dE}{dx} \right)_e$  are the stopping powers due to nuclear and electronic energy loss, respectively. Energy loss rate is often expressed in terms of stopping crosssection  $S(E)$  defined as

$$S(E) = \frac{1}{N} \frac{dE}{dx} = \frac{1}{N} \left( \frac{dE}{dx} \right)_n + \frac{1}{N} \left( \frac{dE}{dx} \right)_e = S_n(E) + S_e(E) \quad (3.6)$$

where  $N$  is the atomic density of the target [6].

#### Nuclear Stopping

The interaction between an energetic ion and target atoms can be expressed in terms of the potential  $V(r)$  between them.  $V(r)$  can be written as

$$\begin{aligned} V(r) &= 0 && \text{for } r > r_0, \\ &= \frac{Z_1 Z_2 e^2}{r^2} \chi(r) && \text{for } a_0 < r < r_0. \end{aligned} \quad (3.7)$$

Here,  $r$ ,  $r_0$ , and  $a_0$  are the distance of separation of the incident ion and target atom, equilibrium distance of atoms in a solid, and Bohr radius of hydrogen atom, respectively.  $Z_1$  and  $Z_2$  are the atomic number of incident ion and target atom, respectively and  $e$  is the electronic charge.  $\chi(r)$  is a screening function which represents the electrostatic screening of nuclear charge by atomic electrons. In order to calculate the nuclear stopping, power law form of the interatomic potential  $V(r) \sim r^{-1}$  can be assumed where the screening function  $\chi(r)$  is approximated in power form as  $\chi(r/a_{TF}) = (k_s/s)(a_{TF}/r)^{s-1}$ , where  $s=1,2 \dots k_s$ , a numerical constant.  $a_{TF}$  is Thomas-Fermi screening radius defined as

$$a_{TF} = \frac{0.88534 a_0}{(Z_1^{1/2} + Z_2^{1/2})^2}, \quad (3.8)$$

in this power law form of interatomic potential, the nuclear stopping is given by [6],

$$S_n(E) = \frac{C_m E^{1-2m}}{1-m} \left[ \frac{4M_1 M_2}{(M_1 + M_2)^2} \right], \quad (3.9)$$

where

$$C_m = \frac{\pi}{2} \lambda_m a_{TF}^2 \left( \frac{Z_1 Z_2 e^2}{a_{TF}} \right)^{2m} \left( \frac{M_1}{M_2} \right)^m \quad (3.10)$$

Here,  $m=1/s$  and  $\lambda_m$  is a fitting variable has the functional form

$$\lambda_m = 2m \left( \frac{k_s \Gamma(1/2) \Gamma(1/2 + s)}{4\Gamma(s/2 + 1)} \right)^{2m}, \quad (3.11)$$

this stopping cross section can be shown in more compact form by defining reduced energy ( $\varepsilon$ ) and reduced length ( $\rho$ ) as:

$$S_n(\varepsilon) = \frac{d\varepsilon}{d\rho_L} = \frac{\lambda_m}{2(1-m)} \varepsilon^{1-2m}, \quad (3.12)$$

$$\text{where } \varepsilon = \frac{M_2}{M_1 + M_2} \cdot \frac{a_{TF}}{Z_1 Z_2 e^2} E; \quad \rho_L = 4\pi L N a_{TF}^2 \left[ \frac{M_1 M_2}{(M_1 + M_2)^2} \right], \quad (3.13)$$

the value of the exponent  $m$  depends upon the reduced energy ( $\varepsilon$ ) as

$$m=1/3 \quad \text{for } \varepsilon \leq 0.2 \quad (3.14)$$

$$m=1/2 \quad \text{for } 0.08 \leq \varepsilon \leq 2$$

$$m=1 \quad \text{for } \varepsilon > 2,$$

an approximation of screening function was given by Ziegler, Biersack and Littmark (ZBL) [7] for which the corresponding nuclear stopping is applicable to wider values of  $\varepsilon$ . Such higher values of  $\varepsilon$  corresponding to very high energy ion-beam are out of the scope of this thesis and not discussed here.

## Electronic Stopping

Electronic energy loss of an energetic ion inside a solid is dependent upon the velocity of the ions. For the ion velocity  $v < v_0 Z_1^{2/3}$ , where  $v_0$  is the Bohr velocity of atomic electron, electronic stopping cross section was derived by Lindhard and Scharff [6] as:

$$S_e(E) = 3.83 \frac{Z_1^{7/6} Z_2}{(Z_1^{2/3} + Z_2^{2/3})^{3/2}} \left( \frac{E}{M_1} \right)^{1/2} = K_L E^{1/2}, \quad (3.15)$$

other terms except energy are included in the constant  $K_L$ . In terms of reduced energy ( $\varepsilon$ ) and reduced length ( $\rho$ ) the above formula becomes

$$S_e(\varepsilon) = \left( \frac{d\varepsilon}{d\rho} \right)_e = \frac{Z_1^{2/3} Z_2^{2/3} \left( 1 + \frac{M_2}{M_1} \right)^{3/2}}{12.6 (Z_1^{2/3} + Z_2^{2/3})^{3/4} M_2^{1/2}} \varepsilon^{1/2} = k(\varepsilon)^{1/2} \quad (3.16)$$

In the high energy range where ion velocity  $v > v_0 Z_1^{2/3}$ , the influence of the incident ion can be regarded as a sudden, small perturbation to the target electrons. This interaction of high energy ion-beam with target electrons is out of the scope of this thesis and not discussed here.

Figure 3.2 shows a comparison of nuclear and electronic energy loss for Ar-ion irradiation in Si. In the low energy range (0.5-10 keV) total energy deposition rate follows the nuclear energy loss curve. In the medium energy range (10-500 keV) total energy curve starts to deviate from nuclear energy loss curve due to the increasing electronic energy loss of ions at higher energy. At high energies (above 1 MeV), where  $\varepsilon > 10$  (for nuclear energy loss) and  $v > v_0 Z_1^{2/3}$ , the electronic energy loss of ions become the dominant energy loss process.

Figure 3.2 shows a graph of the nuclear and electronic energy loss and their sum as function of ion energy for Ar<sup>+</sup>-ion irradiation of a Si target.

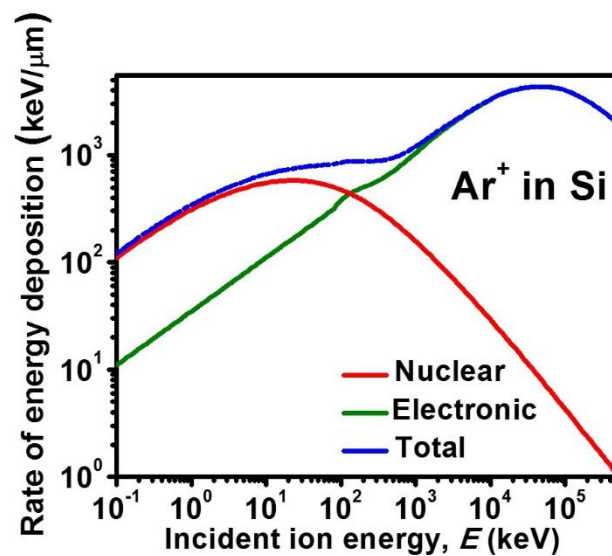


Figure 3.2: Rate of energy deposition,  $dE/dx$ , for Ar<sup>+</sup>-ions in Si. Nuclear, electronic and total energy losses are plotted as a function of incident ion energy ( $E$ ). The energy losses are calculated using SRIM 2012 Monte Carlo simulation code [8].

From Figure 3.2, it is clear that the stopping for argon in silicon is governed by the nuclear energy loss for ion energies ( $<10$  keV). During this process, target atoms are displaced from their original positions provided the transferred energy is larger than the displacement energy of a silicon atom which is of the order of 15 eV [9] and relevant effects like sputtering of surface atoms, generation and migration of point defects, amorphization of crystalline materials, and formation of surface layers with reduced viscosity relative to the bulk target etc. take place. The interplay of these processes lead to the evolution of nanostructures during irradiation. In the present thesis, with argon energies ranging between 500 and 1500 eV, the electronic stopping is only about 10% of the total stopping and is dominated by mostly nuclear energy loss. For higher ion energies ( $> 150$  keV in Figure 3.2), the energy loss is dominated by electronic stopping, due to electronic interactions between the ions and the target. The energy acquired by the electrons is subsequently transferred to the atomic lattice via electron-phonon coupling, resulting in local lattice temperatures that can exceed several thousand Kelvin [10] which induces a cylindrically-shaped molten region of few nanometers around the ion track. This process is commonly referred to as the thermal spike model [11,12] which can lead to structural modifications of the target such as amorphization and defect generation.

### **3.2.2 Ion range and straggling**

The direction of the trajectory of an energetic ion inside a solid keeps on changing from the point of entrance to its resting place due to collisions with the target atoms. A general three-dimensional presentation of the penetration of a projectile in a solid is shown in Fig. 3.3. In this schematic, an energetic projectile enters the surface at point  $(0,0,0)$ , at an angle  $\theta$  to the surface normal. The projectile comes to rest at point  $(x_s, y_s, z_s)$ . The actual distance travelled by the ion, i.e., the total path length is called the range  $R$  of the ion. The net penetration of the projectile into the material, measured along the initial ion trajectory, is called the projected range  $R_p$ . The net depth of penetration, the perpendicular distance of the ions resting place  $(x_s,$

$y_s, z_s$ ) from the surface, is  $z_s$ , which equals projected range only for normal incidence of the ion on the surface ( $\theta = 0$ ). The radial range  $R_r$  is the distance from the point of entrance to the point of ions resting place. In the context of ion-solid interaction, projected range,  $R_p$ , is often designated as range of the ions.

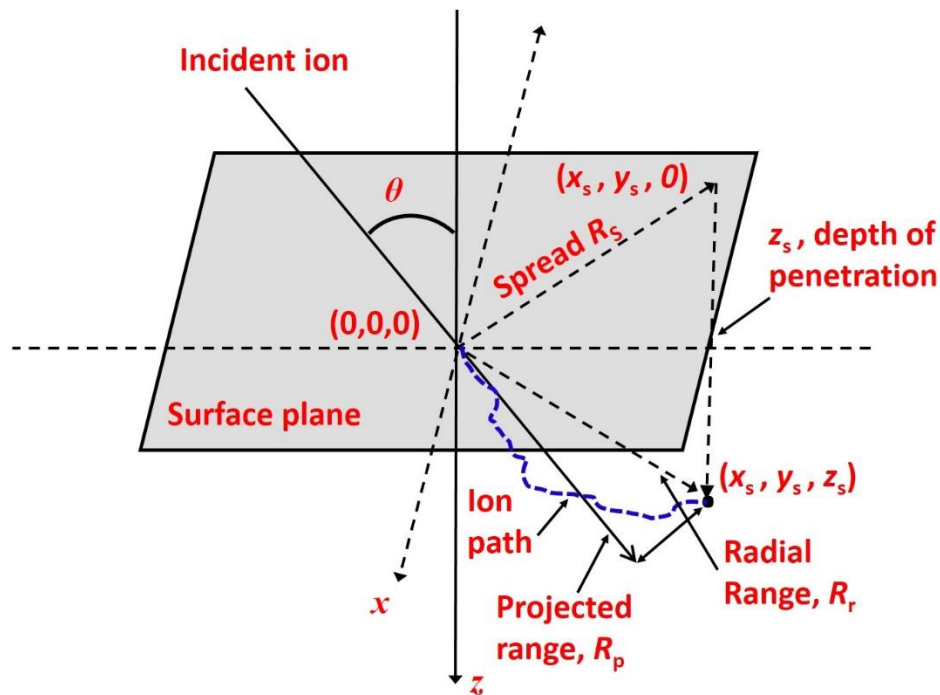


Figure 3.3: Schematic diagram for definition of penetration depth, spread, radial range, and projected range.

$R_s$  is called the lateral spread of ions from its impact point over the surface. Stopping of an ion in a target solid is a stochastic process. The collision sequence and subsequent ion deflection, and the total length of the ion trajectory inside the target varies from ion to ion. As a result, ions with same energy, incident with the same angle onto the target surface, do not necessarily come to rest at the same depth below the surface. Instead, a statistical distribution of the depths, to which ions penetrate, is observed. The distribution of the projected range is referred to as range distribution. At low ion doses and in the absence of crystal orientation effects, the range distribution of ions is roughly a gaussian. The average range is defined as the distance of peak

of the gaussian distribution from the surface. The width of this distribution is called “range straggling”. The average ion range ( $R$ ) can be expressed in term of incident ion energy ( $E_0$ ) [6] as:

$$R(E_0) = \left( \frac{1-m}{2m} \right) \frac{\gamma^{m-1}}{NC_m} E_0^{2m}, \quad (3.17)$$

Here,  $\gamma = 4M_1M_2/(M_1 + M_2)^2$ ,  $C_m$  and  $m$  are defined earlier.

### 3.2.3 Basics of sputtering

Sputtering is the removal of target atoms under ion bombardment. Sputtering is described quantitatively by the sputtering yield ( $Y$ ), no. of sputtered atoms per incident ion, defined as [6]

$$Y = \Lambda F_D = \frac{\alpha NS_n(E)}{E_B} \quad (3.18)$$

Here,  $\Lambda$  is a constant which depends on the properties of a material,  $F_D$  is the nuclear energy deposition per unit length,  $N$  and  $E_B$  are the target atomic density and surface binding energy, respectively, and  $\alpha$  is a correction factor that depends on the ratio of ion and solid atomic masses. Moreover, light-ion sputtering is independent of temperature, and heavy-ion sputtering is only influenced by temperature close to the target melting point [13]. The sputtering yield has its maximum value when the incident particle energy is somewhere in the medium energy regime. At higher energies, the particle penetrates deeper into the target and fewer surface atoms are removed, lowering the sputtering yield. When the mass equals the target mass, sputtering yield is maximized.

The sputtering yield,  $Y_E$ , at incident ions energy  $E$ , can be approximated by an empirical formula

$$Y_E = 0.42 \frac{\alpha_s Q_s S_n(E)}{E_B [1 + 0.35 E_B S_e(\varepsilon)]} \chi^{2.8}, \quad (3.19)$$

where  $\chi = 1 - (E_{th}/E)^{1/2}$ ,  $\alpha_s$  and  $Q_s$  are empirical parameters determined from experimental sputtering yield data, and  $E_{th}$  is the sputtering threshold.

The sputtering yield, in general, is an increasing function of ion angle of incidence,  $\theta$  (with respect to surface normal), except at very high angles where the reflection of ions from the surface becomes the dominating factor. An approximate relationship of the sputtering yield,  $Y_\theta$ , corresponding to ion angle of incidence  $\theta$ , to sputtering yield  $Y_0$  for normal ion incidence is given by

$$\frac{Y_\theta}{Y_0} = (\cos \theta)^{-f_s}, \quad (3.20)$$

$f_s$  is a function of  $M_2/M_1$  [6].

Experimentally obtained sputtering yield starts to deviate from the behavior predicted by Eq. 3.20 at higher incident angles. By carrying out a more detailed study, Yamamura *et al.* [14,15] put forward the following empirical relationship between  $Y_\theta$  and  $Y_0$

$$Y_\theta = Y_0 \left( \frac{1}{\cos \theta} \right)^f \exp \left[ -\Sigma \left( \frac{1}{\cos \theta} - 1 \right) \right], \quad (3.21)$$

where  $f$  is the function of energy,  $f = 1.85 \left[ 1 + 1.25 \left( \frac{1-\chi}{\chi} \right) \right]$ ,  $\Sigma = f \cos \theta_{opt}$ , where  $\theta_{opt}$  is the angle at which sputtering yield is found to be the maximum. Eq. 3.21 provides a more realistic description of sputtering yield compared to Eq. 3.20, especially at higher incident angles.

### 3.2.4 Numerical simulation of ion-solid interaction

Detailed simulation of ion-solid interactions over a large range of ion energies can be carried out using Monte-Carlo and molecular dynamics simulation codes available at present. These simulation codes offer a way of understanding the physical processes taking place in particular

experimental situations by providing details of ion stopping, resulting radiation damage, sputtering, ion and recoil distributions, etc. For the present study, the necessary simulations were performed using SRIM [8] and TRIDYN [16] codes.

**SRIM:** SRIM (Stopping and Range of Ions in Matter) is a simulation package based on the Monte Carlo code TRIM (Transport and Range of Ions in Matter). TRIM follows history or ion trajectories of a large number of individual ions or particles in a target. They all begin with a given energy, position, and direction. The particle is assumed to change direction as a result of binary nuclear collisions and moves in a straight path between two consecutive collisions. The energy of the particle is reduced as a result of nuclear and electronic (inelastic) collisions, and a trajectory is terminated either when the energy drops below a pre-specified value or when the particle position is outside the target. The target is considered amorphous with atoms at random locations and thus, the directional properties applicable for a crystalline material are ignored. This code calculates the final three-dimensional distribution of the ions and all kinetic phenomena associated with the ion's energy loss such as sputtering yield, target damage etc.

The applicability of TRIM is limited in the sense that the modification of the target composition due to ion implantation and erosion of the target surface due to sputtering is not taken into account during simulation. Therefore, the simulated results such as the distribution of implanted species conforms to experimentally obtained data mostly in the limit of low implantation fluence [ $\sim 10^{14}$  ions  $\text{cm}^{-2}$ ] since significant compositional modification of the target occurs at high fluences.

**TRIDYN:** TRIDYN uses the same Monte Carlo method as TRIM to simulate the interaction of energetic ions and target atoms. However, TRIDYN includes the dynamic change in the target during ion bombardment. TRIDYN provides reliable values of sputtering yield, modified target composition or implantation distribution at high fluences.

### 3.3 Continuum theories of ion-irradiated surface evolution

Continuum models describe the surface at a length scale much larger than the atomic scale. The solid surface is described by a surface height function  $h(x, y, t)$  measured from the laboratory coordinate whose  $x$ -,  $y$ -axes are parallel to the initial flat surface and  $z$ -axis is normal to the surface. The first successful theory to understand periodic pattern formation under ion bombardment was introduced by Bradley and Harper (BH) [17] based on Sigmund's [18] theory of ion sputtering of an amorphous solid surface.

For a slowly undulating surface, BH demonstrated the dependence of sputtering yield on local surface curvature which makes the surface unstable against development of sinusoidal modulations. Competition of the curvature-dependent sputter erosion process with the relaxation processes which tend to smooth out the surface results in growth of a range of sinusoidal perturbations on the surface. The fastest growing mode from these sinusoidal perturbations dominates over the other modes and is observed as ripple patterns on the bombarded surface. In the following, we introduce the continuum theories which describe ion-induced surface evolution

#### **Sigmund's Theory of sputtering**

If one considers only physical sputtering process, the ion bombardment of a solid surface will lead to increase in the surface roughness as a function of fluence. According to Sigmund, local variations in the sputtering rate may take place at solid surface when features are present at the surface. The feature dimension should be similar to the size of the zones where the ions deposit their energy. For an amorphous material, Sigmund proposed that the sputtering yield is proportional to the deposited energy in elastic collisions at the surface.

Sigmund [18] showed that, for energy range where the nuclear stopping of the ions is the dominant energy loss process, the spatial distribution of deposited energy by an ion inside an

amorphous solid can be approximated by a Gaussian distribution. The situation is schematically shown in Fig. 3.4. The average energy deposited, by the ion incident at the point P' (Fig. 3.4), due to nuclear collision in the bulk of the target is given by

$$E(r) = \frac{\varepsilon}{(2\pi)^{3/2} \sigma \mu^2} \exp \left[ -\frac{(z'+a)^2}{2\sigma^2} - \frac{x'^2 + y'^2}{2\mu^2} \right] , \quad (3.22)$$

where origin of the coordinate system  $r' = (x', y', z')$  is placed at the impact point P' of the ion and  $\varepsilon$  is the total energy deposited by the ion with  $a$  as the average depth of energy deposition. Here  $z'$  is measured along the direction of the incident ion trajectory, while  $x'$  and  $y'$  are measured perpendicular to the  $z'$  direction. The maximum energy deposition occurs at the point O, at a distance  $a$  below the surface and  $\sigma$  and  $\mu$  are the width of the Gaussian distribution in the direction parallel and perpendicular to the ion trajectory, as shown in Fig. 3.4. The rate of sputtering of atoms at any surface point P is expressed in terms of recession velocity,  $v$ , of the surface at P which is proportional to the total energy deposited at point P by all ions incident on the surface.

$$v = p \int_{\mathcal{R}} \phi(r') E(r') dr' \quad (3.23)$$

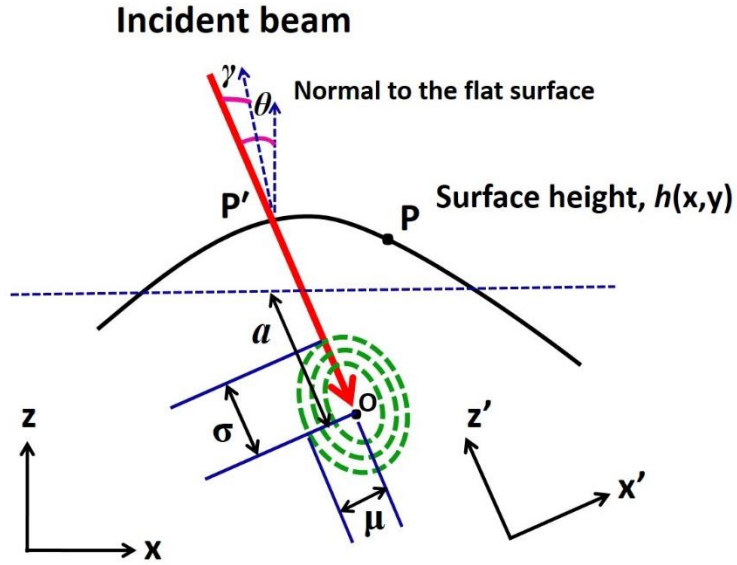


Figure 3.4: Schematic demonstration of Gaussian energy deposition of an incoming ion inside a target.  $\theta$ : global angle of incidence;  $\gamma$ : local angle of incidence.

The integral extends over the region  $\mathcal{R}$  within which the impact of ions contributes significantly to the total energy deposited at P.  $\phi(r')$  is the ion flux corrected for the difference between local angle of incidence  $\gamma$  and angle of incidence  $\theta$  with respect to flat surface normal ( $z$  direction) as shown in Fig. 3.4. The proportionality constant  $p$  is the characteristic of the substrate and depends on the atomic density of the substrate  $N$ , surface binding energy  $U_0$  and a constant  $C_0$  related to the square of radius of the effective potential of interaction between the incident ion and target atom.  $p$  is expressed as

$$p = \frac{3}{4\pi} \frac{1}{NU_0C_0} \quad (3.24)$$

Eq. 3.23 is important to calculate the curvature dependent sputter erosion rate and is discussed in the following section.

### 3.3.1 Bradley-Harper (BH) theory

Using Eq. 3.23, Bradley and Harper (BH) derived a linear partial differential equation to describe the dynamics of a slowly undulating surface for which the radius of curvature,  $R$ , at any surface point is much larger compared to the mean depth of energy deposition  $a$ . This small slope assumption allows approximating the height of the surface in the neighbourhood of the point P in Fig. 3.4 in the laboratory coordinate system  $(x, z)$  as

$$h(x) = -\frac{1}{2} \left( \frac{x^2}{R} \right), \quad (3.25)$$

Here  $R$  is the radius of curvature of the surface. Based on this small slope approximation, the curvature depends sputter erosion rate, evaluated from Eq. 3.23, is given by

$$v(\theta, R) \cong \frac{pEfa}{\sqrt{2\pi\sigma\mu}} B_1^{-1/2} \exp\left(-\frac{a^2}{2\sigma^2} + \frac{A^2}{2B_1}\right) \left[ \cos\theta + \Gamma_1(\theta) \frac{a}{R} \right], \quad (3.26)$$

The parameters  $A$ ,  $B_1$ , and  $\Gamma_1$  are functions of angle of incidence  $\theta$ , incident ion flux  $f$ ,  $a$ ,  $\sigma$ , and  $\mu$ . Let us now consider the limit of a flat surface,  $R=\infty$ . The sputtering yield in this case is  $Y_0(\theta) = Nv(\theta, R=\infty)/f \cos\theta$ , where  $N$  is the number of atoms per unit volume in the amorphous solid. From Eq. 3.26 we can write that

$$Y_0(\theta) = \frac{pEfa}{\sqrt{2\pi\sigma\mu}} B_1^{-1/2} \exp\left(-\frac{a^2}{2\sigma^2}\right) \exp\left(\frac{A^2}{2B_1}\right), \quad (3.27)$$

For  $\sigma > \mu$ ,  $A$  and  $B_1$  is known to be an increasing function of the angle of incidence  $\theta$ , meaning  $Y_0(\theta)$  is also an increasing function of angle of incidence  $\theta$ . In reality, however, sputtering yield begins to decrease after a critical angle  $\theta$  when reflection of ions becomes important.

Using Eqs. 3.26 and 3.27 one can write

$$v(\theta, R) \cong \frac{f}{N} Y_0(\theta) \left[ \cos\theta + \Gamma_1(\theta) \frac{a}{R} \right], \quad (3.28)$$

In Eq. 3.28 the term  $\Gamma_1(\theta)a/R$  contains the curvature dependence of erosion velocity. The parameter  $\Gamma_1(\theta)$  is negative for normal incidence of the ion-beam ( $\theta=0$ ). The radius of curvature

$R$  is negative in a trough and positive in a crest. According to Eq. 3.28, therefore, velocity of erosion is greater in surface troughs than the crests, meaning the valleys of any surface perturbation will be eroded faster than the peaks under ion bombardment. Thus, sputtering increases the amplitude of the perturbation and so leads to an instability.

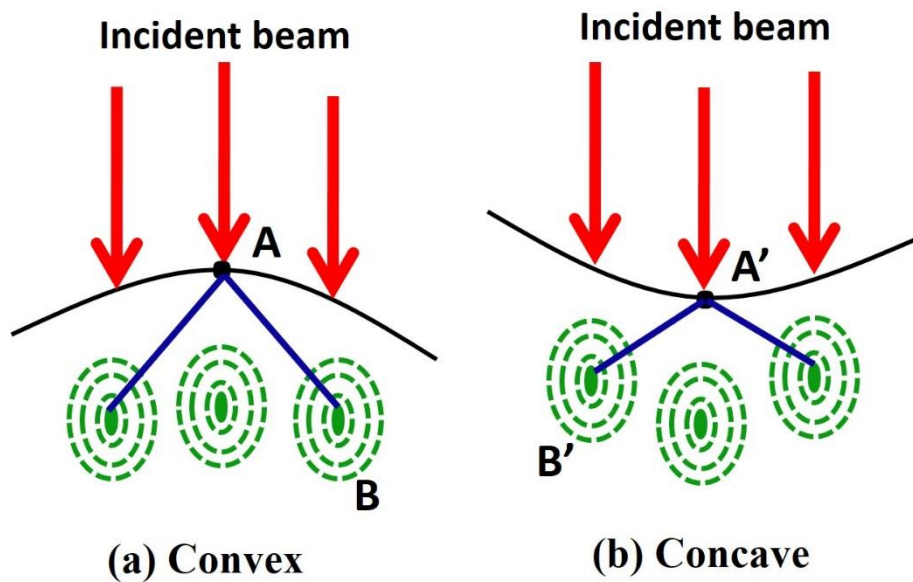


Figure 3.5: Schematic illustration of the origin of the surface instability induced by ion beam erosion of non-planar surfaces.  $\theta$ : global angle of incidence;  $\gamma$ : local angle of incidence.

The reason of enhanced sputtering at troughs compared to crests discussed above is shown in the schematic diagrams of Fig. 3.5. The Gaussian distribution of the energy deposited by the incident ion is centered at point O for both the convex (Fig 3.5a) and concave (Fig 3.5b) surface. Due to geometry of convex and concave surfaces, the distance OP is smaller in case of convex surface compared to the concave one. Therefore, the energy deposited at point P is greater for the convex (Fig 3.5a) surface, leading to a greater erosion of the valleys compared to the hills. In BH theory this curvature-dependent erosion rate induced surface roughening competes with surface smoothing processes, which leads to the formation of periodically modulated structures like ripples. This theory predicts that below a critical angle  $\theta_c$ , ripples are oriented parallel to the projection of ion-beam on the surface and beyond that they get rotated by  $90^\circ$ . For a better

realization, a schematic of parallel-mode ripples are shown in the Fig. 3.6. From this figure it is clear that ripple wave-vector is parallel to the projection of the ion-beam onto the surface. When angle of incidence of the ion-beam is close to grazing, however, the reflection of the ion-beam becomes an important factor and BH model becomes inappropriate to describe surface morphology.

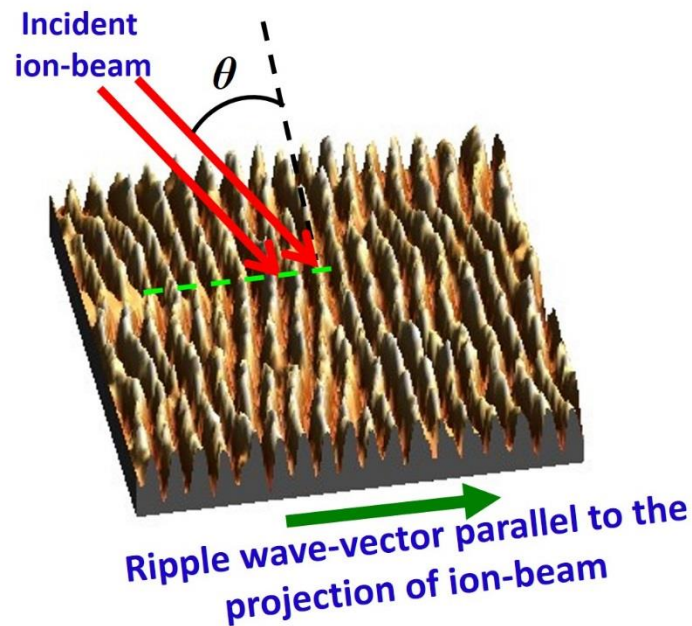


Figure 3.6: Schematic illustration of the parallel-mode ripples

### 3.3.2 Carter-Vishniakov Theory

BH theory predicts formation of periodic ripple patterns for any off-normal incidence of the ion-beam. Experimental observations, however, demonstrates formation of ripples beyond a critical angle of incidence which varies between  $45^{\circ}$ - $55^{\circ}$ . In addition to the curvature-dependent sputtering theory of ripple formation introduced by BH, Carter and Vishniakov (CV) [19] considered the ion induced lateral mass redistribution as the reason behind the formation of these modulated topography. The analysis of CV shows that the impact of an energetic ion at a surface point leads to a displacement of the generated recoils, on the average,

in a direction parallel to the initial direction of the incident beam. The average displacement of the target atoms has a component parallel to the surface in the direction of projection of the ion-beam onto the surface for off-normal incidence of the beam.

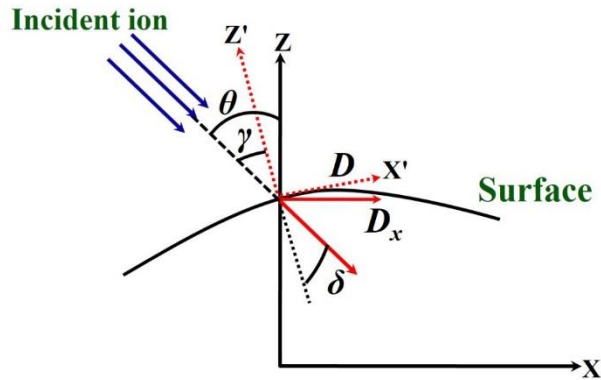


Figure 3.7: Schematic diagram of the laboratory coordinate frame ( $x, z$ ) along with the local coordinate frame ( $x', z'$ ) to represent the CV mechanism. The local normal to the surface is represented by the unit vector  $z'$  which also the one axis of local coordinate frame.

To demonstrate the CV mechanism, a schematic diagram is presented as Fig. 3.7. In this figure, the incident ion lies in the  $XZ$  plane of the laboratory coordinate frame which is parallel to the initial flat surface. The local coordinate system is defined with respect to the incident ion-beam with  $z'$ -axis parallel to the incident beam direction and  $x'$ -axis is perpendicular to it. In Fig. 3.7 the incident ion makes an angle  $\theta$  and  $\gamma$  with the  $z$ -axis and  $z'$ -axis, respectively.

$(\theta - \gamma) = \tan^{-1}(\partial h / \partial x) \approx \partial h / \partial x$  is considered to be the local misorientation of the surface. The quantity  $\delta$  is the recoil displacement vector defined as  $\delta = f(E)d$  where  $f(E)$  is the total number of generated recoil atoms and  $d$  is the mean recoil displacement distance (the average movement of the recoils parallel to the incident ion-beam direction).  $D$  and  $D_x$  are the projection of  $\delta$  on the surface and the  $x$ -axis, respectively. Under the present geometry

$v_n = -\cos(\theta - \gamma) \left( \frac{\partial h}{\partial t} \right)$  is defined to be the normal component of the surface velocity. With this

information following identities are obtained [20]:

$$|D| = \delta \sin(\gamma); \quad D_x = \delta \sin(\gamma) \cos(\gamma) \quad (3.29)$$

The projection of the ion flux along the  $x$ -axis becomes  $J_x = J \cos(\gamma) / \cos(\theta - \gamma)$ . Therefore, net generated recoil displacement due to ion flux in the  $x$ -direction is  $J_x \times D_x$ . The equation of motion follows from the continuity equation [21]:

$$\frac{\partial h}{\partial t} = -\frac{1}{N} \frac{\partial}{\partial x} (J_x D_x) = \frac{J \delta a \cos 2\theta}{N} \frac{\partial^2 h}{\partial x^2} \quad (3.30)$$

The recoil displacement generated by the ion flux as given by Eq. 3.30 also contributes to the growth of surface height. Eq. 3.30 was first introduced by CV [19] and later elaborated by Madi *et al.* [20]. Hence, the effective surface tension term (coefficient of  $\frac{\partial^2 h}{\partial x^2}$  term) which causes sinusoidal perturbations to grow on the surface becomes:

$$v_x = \frac{Ja}{N} [\delta \cos 2\theta + Y_0(\theta) \Gamma_1(\theta)] \quad (3.31)$$

Eq. 3.31 includes the contribution of both the recoil displacement and the sputters erosion as given by BH, where,  $N$  is atomic density of the target. In Eq. 3.31 the magnitude of  $\delta$  exceeds the sputtering yield  $Y(\theta)$  by two orders of magnitude or more due to number of recoils generated,  $[f(E)]$ , and the energy deposition depth  $a$  similarly exceeds the mean recoil displacement distance  $d$ . It is therefore, probable that the coefficients of the angle-dependent terms in Eq. 3.31 will be similar.

For normal ( $\theta=0^\circ$ ) and near-normal incidences, Eq. 3.31 becomes positive and smoothing dominates over roughening at all wave vectors. As  $\theta$  increases, the roughening term will assume an increasing importance and for some critical angle ( $\theta=\theta_c$ ), Eq. 3.31 becomes negative and roughening will dominate at all wave vectors. The above scenarios explain both why ripple pattern appears to be suppressed for near-normal ion incidences and also drives its own instability at higher angles.

### 3.3.3 Relaxation mechanisms

Relaxation processes tend to smooth out any surface features formed by ion bombardment. A range of relaxation mechanisms have been proposed to explain various experimental observations. Determination of the relaxation mechanisms which are dominant in particular experimental conditions involving various amorphous or crystalline substrates, surface temperatures, and ion-beam parameters still remains the subject of extensive research. In this section, we briefly discuss various relaxation processes which may be operative under specific experimental conditions during the ion irradiation.

#### A. Thermal Diffusion

This is the only type of diffusion considered in BH theory. Patterns on any amorphous surface are smoothed out due to mass transport driven by the gradient in chemical potential. For a simplified description of the process, we consider a surface profile  $h(x,y)$  where the variation in surface profile occurs only in the  $x$ -direction. Chemical potential,  $G$ , per atom increases with transfer of atom from a point of zero curvature to a point of curvature  $R$  and can be expressed as  $G = R\gamma\Omega$ , where  $\gamma$  is surface free energy per unit area and  $\Omega$  is atomic volume. Thus, the gradient of surface curvature produces a drift in surface atoms with a surface current [22, 23] given by

$$j = \frac{D_s \gamma \Omega \nu}{kT} \frac{\partial R}{\partial s}, \quad (3.32)$$

where  $D_s$  is surface diffusivity,  $\nu$  is number of atoms per unit area,  $k$  is Boltzmann constant, and  $s$  is the arc length along the profile.  $D_s$  has an Arrhenius type behavior with temperature  $D_s \sim e^{-\Delta E/kt}$  where  $\Delta E$  is the activation energy for surface diffusion. The surface divergence of  $j$  gives an increase in number of atoms per unit area per unit time, which can be converted to variation in surface height by multiplying with atomic volume ( $\Omega$ ):

$$\frac{\partial h}{\partial t} = -\Omega \frac{\partial j}{\partial s} = \frac{D_s \gamma \Omega \nu}{kT} \frac{\partial^2 R}{\partial s^2} \quad (3.33)$$

Using small slope approximation,  $R \sim -\frac{\partial^2 h}{\partial x^2}$  and  $\partial s \sim \partial x$ , Eq. 3.33 reduces to:

$$\frac{\partial h}{\partial t} = -D^T \frac{\partial^4 h}{\partial x^4} = -D^T \nabla^4 h \quad (3.34)$$

where,  $D^T = \frac{D_s \gamma \Omega v}{kT}$  is the surface diffusion constant. Eq. 3.34 can be readily extended for a two-dimensionally varying surface to give:

$$\frac{\partial h}{\partial t} = -D^T \left( \frac{\partial^4 h}{\partial x^4} + \frac{\partial^4 h}{\partial y^4} \right) \quad (3.35)$$

### B. Effective Surface Diffusion (ESD)

Makeev *et al.* [24] introduced ion induced effective surface diffusion (ESD) as relaxation mechanism. ESD is reminiscent to surface diffusion but does not imply mass transport along the surface. In fact, it mimics the smoothening of the surface due to surface diffusion and therefore, is called ion induced effective surface diffusion (ESD) terms. The ESD [24] involves preferential erosion of the surface where surface hills are eroded faster than the valleys. If the system is viewed from a coordinate frame moving together with the average height of the surface, this preferential erosion appears as a re-organization of the surface, corresponding to a surface diffusion like mechanism. ESD leads to relaxations which are different along  $x$ - and  $y$ -direction, implying anisotropy in diffusion on the surface. The importance of ESD is that it is independent of temperature and thus can be effective at low temperature where thermal diffusion is negligible.

### C. Ion induced Viscous Flow

The ion induced viscous flow (IVF), proposed by Umbach, Headrick, and Chang, consider surface-confined viscous flow driven by surface tension as the dominant smoothing mechanism which can occur in case of materials with a disordered surface layer with reduced viscosity [30]. The coefficient of viscous flow is given by

$$D_{xx} = D_{yy} = D_{IVF} = \frac{\gamma d^3}{\eta_s} \quad (3.36)$$

Here,  $\eta_s$  is ion-enhanced surface viscosity and  $\gamma$  is surface free energy per unit (both are assumed to be constant and isotropic). The parameter  $d$  is the depth of the damaged layer, which is taken to be equal to the ion penetration depth  $d$ . Although viscous flow can be effective in amorphous materials, the approach of the IVF can be extended to crystalline substrates where a thin damaged surface layer is created by irradiation [26]. If IVF is considered as the smoothing mechanism, the ripple wavelength becomes an increasing function of ion energy and substrate temperature and independent of ion flux, which successfully describes the characteristics of ripple formation on SiO<sub>2</sub>. Furthermore, molecule dynamic (MD) simulations by Mayr *et al.* have emphasized important roles of flow of point defects and of thermal-spike induced local melting in ion-induced viscous flow in the 0.1-1 keV range [27].

### **3.3.4 Solid flow model**

In the theoretical models of ion-bombarded surface described so far, effective surface tension which leads to instability of the surface against growth of modulation is caused by sputter erosion (BH theory) or mass redistribution (CV theory). In the fluence range where the periodic surface patterns appear, the ion bombardment can also results in amorphization of target materials. Viscous flow of material in the amorphous layer can occur under ion bombardment due to the stress generated by irradiation. Castro *et al.* [28] put forward a model which demonstrates the formation of periodic surface patterns due to this viscous mass flow in the amorphous layer.

In the low and medium energy range, nuclear energy is the dominant energy loss process. Incident ions generate vacancies and interstitials in the subsurface layer, which can diffuse at different rates, annihilate by recombination or form clusters. As observed from Molecular Dynamics (MD) simulations, the overall effect of these processes is threefold: amorphization of target, development of stress, and displacement of the mean position of atoms inside the

material. Moreover, experimental studies on Si reveal that the thickness of the generated amorphous layer, becomes stationary after a fluence of  $10^{14}$  ions  $\text{cm}^{-2}$ .

The solid flow model put forward by Castro *et al.* [29], is based on the fact that, as a consequence of the impact of the ions and the subsequent release of energy within the target, defects are created inside the material. These events occur in a few picoseconds after the impact. Partial relaxation of the defects leads to sputtering of target atoms and generation of a residual stress which is confined to a thin amorphous layer that builds up beneath the surface and that reaches a stationary thickness after the very early times of irradiation. This ion-induced (compressive) stress is characterized by a slow time relaxation that involves highly viscous flow of the amorphous layer, which is assumed to be incompressible. This amorphous layer is treated as a fluid flowing under stress.

A body force  $b \equiv \nabla \cdot T^S$  acting in the bulk of the fluid layer is defined from the conservation laws of mass and momentum for fluid. Here,  $T$  is the stress tensor. This force can be splitted into amplitude,  $f_E$ , and an angular contribution  $\Psi$ , which is a function of the local angle of incidence. Mathematically,  $b = f_E \Psi(\theta - \gamma)$  where  $\gamma$  is the local slope of the surface and  $\theta$  is the angle of incidence of the ion-beam. The amplitude  $f_E$  contains the coarse-grained information about the effect of the residual stress created in the target, due to ion-induced mass redistribution, and has dimensions of a gradient of stress. Using proper boundary conditions, Castro *et al.*, specified the evolution for two important boundaries of the system: the amorphous-vacuum interface (the free surface),  $h^{(a)}$ , and amorphous-crystalline interface,  $h^{(c)}$ . Kinematic condition at each interface leads to evolution equations for both  $h^{(a)}$  and  $h^{(c)}$  as

$$\frac{dh^{(c)}}{dt} - w = j_{am} \quad (3.37)$$

$$\frac{dh^{(a)}}{dt} - w = j_{er} \quad (3.38)$$

where  $w$  is the vertical component of the velocity field of the fluidized layer. The terms  $j_{am}$  and  $j_{er}$  stand for the rates of amorphization and erosion, respectively.

With the help of Eqs. 3.37 and 3.38, a real part of the dispersion relation (i.e. amplification rate of wave vector,  $q$ ) for this viscous fluid were obtained is given by

$$\omega_q = -[f_E d^3 \phi(\theta) q^2 + \alpha d^3 q^4] / 3\mu \quad (3.39)$$

where  $\phi(\theta) = \frac{\partial}{\partial \theta} (\Psi(\theta) \sin \theta)$ ,  $d$  is the average thickness of the amorphous layer,  $\mu$  is (ion-induced) viscosity, and  $\sigma$  is the interface surface tension. The parameter  $f_E$  can be understood as the gradient of residual stress induced by the ions across the amorphous layer, whose angular dependence is described through the function  $\Psi(\theta)$ . Since this angular function needs to be prescribed, we take  $\Psi(\theta) = \cos \theta$  as the simplest geometrically motivated choice that shows a good agreement. In this formalism the thickness of amorphous layer is assumed to be much less than the characteristic wavelength of the ripple pattern. The characteristic wavelength given by

$$l_c = 2\pi \left( \frac{2\sigma}{-f_E \partial_\theta (\Psi(\theta) \sin \theta)} \right)^{1/2} \quad (3.40)$$

Here,  $\sigma$  is the surface tension of target and  $\Psi(\theta) = \cos \theta$  is the angular contribution. Thus, the term  $\partial_\theta (\Psi(\theta) \sin \theta)$  in the denominator of Eq. 3.40 becomes  $\equiv \phi(\theta) = \cos 2\theta$ . It can be observed from Eq. 3.40 that for  $\theta < 45^\circ$ , the denominator is negative. This imply that the periodic ripples should start to appear for angle of incidence  $> 45^\circ$ .

One of the predictions obtained from Eq. 3.39 is that it allows one to find the characteristic time scale  $\tau$  for the exponential growth of the pattern amplitude occurring at short times where the linear approximation holds. Indeed, under conditions for pattern formation and within the linear approximation, there is a single Fourier mode  $q^*$  whose amplitude dominates all other

modes exponentially in time, leading to the formation of ripple morphology with Thus, this timescale is defined as the intrinsic timescale and can be expressed as follows:

$$\tau(\theta, E) = 2\pi / \omega_q^* \sim \frac{\mu}{f_E^2 d^3 \phi^2(\theta)} \quad (3.41)$$

This equation predicts the smallest time scale associated with ripple formation in linear regime, i.e. the surface roughness should grow exponentially as a function of time. However, this exponential behaviour will eventually be interrupted by various nonlinear mechanisms at sufficiently long times. Hence, the time duration of the validity of the linear approximation is also safely characterized by  $\tau$ . In particular, the above formula implies that such duration depends on system parameters, such as average flux, energy, and angle of incidence.

The potential of this model is that it enables one to calculate the intrinsic timescale for any other angle and energy  $(\theta, E)$  for a given pair of angle and energy reference values,  $(\theta_{ref}, E_{ref})$ .

The relation can be written in the following form:

$$\tau(\theta, E) = \tau(\theta_{ref}, E_{ref}) \frac{J_{exp}(\theta_{ref}, E_{ref}) E_{ref}^{-7/3+2m} \phi^2(\theta_{ref})}{J(\theta, E) E^{-7/3+2m} \phi^2(\theta)} \quad (3.42)$$

where  $J_{exp}(\theta_{ref}, E_{ref}) = J_{exp}(E) \cos \theta$  is the flux used in a particular experiment for energy  $E$  and angle  $\theta$ , with  $J_{exp}(E)$  being the flux at normal incidence and  $m$  can be assumed to be in the range 1/3-1/2.

### 3.3.5 Effect of concurrent substrate rotation

The orientation of the nanostructures formed is determined by the direction of the ion-beam. If the sample is rotated around its surface normal during irradiation, the anisotropy due the oblique incidence of ion-beam is eliminated. It is observed that under certain conditions, the rotation during ion bombardment may suppress pattern formation, enhancing smoothening of

surfaces [30]. Nevertheless, in many cases the rotation does not suppress patterning; it only decreases its rate [31] of roughening.

Bradley proposed a formalism where one can address the concurrent substrate rotation during ion-beam irradiation [31]. In this theory, the unperturbed steady-state solution is assumed to be  $h=h_0-v_0t$ , where  $h_0$  is the initial height of the interface and  $v_0>0$ , is the speed of the surface. However, a real surface, is not perfectly flat initially and hence,  $h$  can be written in the following form:  $h=h_0-v_0t+u$ , where  $u\equiv u(x,y,t)$ . Including only the lowest order nonlinearities, the equation of motion becomes

$$u_t = v_0' u_x + A_1 u_{xx} + A_2 u_{yy} - B \nabla^2 \nabla^2 u + \frac{1}{2} \lambda_1 u_x^2 + \frac{1}{2} \lambda_2 u_y^2, \quad (3.43)$$

where the subscripts denote the partial derivatives like  $u_t = \partial u / \partial t$  and  $u_x = \partial u / \partial x$  etc.  $A_1$ ,  $A_2$ ,  $\lambda_1$  and  $\lambda_2$  are constants, and  $B$  is the surface self-diffusivity. In Eq. 3.43 the first term on the right-hand side accounts for the angular dependence of the sputter yield, the second and third terms arise because the sputter yield depends on the surface curvature, and the fourth term accounts for the effect of surface self-diffusion. The final two terms make Eq. 3.43 nonlinear and have an important effect once the surface width has become sufficiently large. Eq. 3.43 is the anisotropic Kuramoto-Sivashinsky equation [32]:

We know from BH theory that for

1.  $A_1, A_2 > 0$ , the surface remains flat
2.  $A_1 < 0$  and  $A_1 < A_2$ , parallel-mode ripples develop
3.  $A_2 < 0$  and  $A_2 < A_1$ , perpendicular-mode ripples emerge

Now, under concurrent substrate rotation, if the angular speed ( $\omega$ ) is sufficiently large, the equation of motion becomes

$$u_t = A \nabla^2 u - B \nabla^2 \nabla^2 u + \frac{1}{2} \lambda (\nabla u)^2, \quad (3.44)$$

where  $A = \frac{1}{2}(A_1 + A_2)$  and  $\lambda = \frac{1}{2}(\lambda_1 + \lambda_2)$ .

If  $A > 0$ , surface remains flat. On the other hand, if  $A < 0$ , Eq. 3.44 becomes the Kuramoto-Sivashinsky equation and the surface becomes unstable and mound-like structures may appear at the surface. At long times, the surface consists of an irregular array of mounds and it exhibits a spatio-temporal chaos.

According to Bradley's theory, at early times when the system evolves in linear regime, the nonlinear terms in Eqs. 3.43 and 3.44 can be neglected. Without sample rotation, the ripple growth rate is

$$\sigma = |A_1|^2 / 4B \quad \text{for } \theta_1 < \theta < \theta_c \quad (3.45)$$

$$\sigma = |A_2|^2 / 4B \quad \text{for } \theta_c < \theta < \theta_2 \quad (3.46)$$

More generally,

$$\sigma_{nr} = \max(|A_1|^2, |A_2|^2) / 4B \quad \text{for } \theta_1 < \theta < \theta_2 \quad (3.47)$$

With concurrent sample rotation, the mound growth rate is

$$\sigma_r = |A|^2 / 4B \quad \text{for } \theta'_1 < \theta < \theta'_2 \quad (3.48)$$

For  $\theta'_1 < \theta < \theta_c$ ,  $A_1 < 0$  and  $A_1 < A_2$ . Therefore,  $A_1 < A < 0$ . On the other hand,  $A_2 < 0$  and  $A_2 < A_1$ . Thus,  $A_2 < A < 0$ . In the first case,  $|A_1|^2 > |A|^2$  and in the second,  $|A_2|^2 > |A|^2$ . Combining both,

$$\max(|A_1|^2, |A_2|^2) > |A|^2 \quad (3.49)$$

Hence, from Eqs. 3.47 and 3.48, we see that

$$\sigma_{nr} \geq \sigma_r \quad \text{for } \theta'_1 < \theta < \theta'_2 \quad (3.50)$$

Physically, this means that the amplitude of the mounds formed with sample rotation grows more slowly than the amplitude of the ripples formed without sample rotation. It may be noted that this has been shown to be valid only in the linear regime, before nonlinear effects becomes important.

Now the question is: What happens when  $\omega$  is large and when it is small. It may be mentioned that when beam is not rotated, ripple amplitude should be proportional to  $B/A^2$ . Thus, when  $\omega \ll B/A^2$ , the orientation of the ripples will slowly rotate. However Eq. 3.44 is applicable when  $\omega \gg B/A^2$ . If ripple topographies are never observed at this rotation rates, one can assume that  $\omega \gg B/A^2$  for the remainder of this thesis.

In addition, if one appends next-to-lowest order nonlinearity, then the Eq. 3.44 takes the following form:

$$u_t = A\nabla^2 u - B\nabla^2 \nabla^2 u + \frac{1}{2} \lambda (\nabla u)^2 - \frac{1}{2} A \nabla^2 (\nabla u)^2 \quad (3.51)$$

This nonlinearity is discussed by García *et al.* [33] Simulation of this equation reveal that one the mounds form, they coarsen for a time but then stop growing. This is called “interrupted coarsening”. However, this behaviour is yet to be observed for Si.

### 3.4 Shadowing effect

Under off-normal incidence of the ion-beam on surface, the BH model predicts an exponential increase in the amplitude of the developed ripple patterns on surface with sputtering time. The development of surface slope due to the exponential increase in ripple amplitude can result in, apart from the initiation of nonlinear effects, a situation where the ion-beam can be restricted from falling on the upstream face of a ripple by the preceding ripple peak. This phenomenon, called *shadowing effect*, becomes a factor of utmost importance in determining the evolution of ripple patterns when angle of ion incidence is close to grazing or even at lower angle of ion incidence in case of relatively high amplitude ripple pattern evolution induced, e.g., by medium energy ion bombardment. The effect of shadowing on ripple pattern evolution can be understood from the geometrical argument introduced by Carter [34].

A schematic diagram for illustrating Carter's argument is presented in Fig. 3.8. In Carter's model [34], any fluctuation in regular sinusoidal ripple patterns with wave vector aligned parallel to the projection of the ion-beam onto the surface is ignored in and thus, only a two-dimensional section in the  $xz$  plane through the surface can be considered as shown in Fig. 3.8.

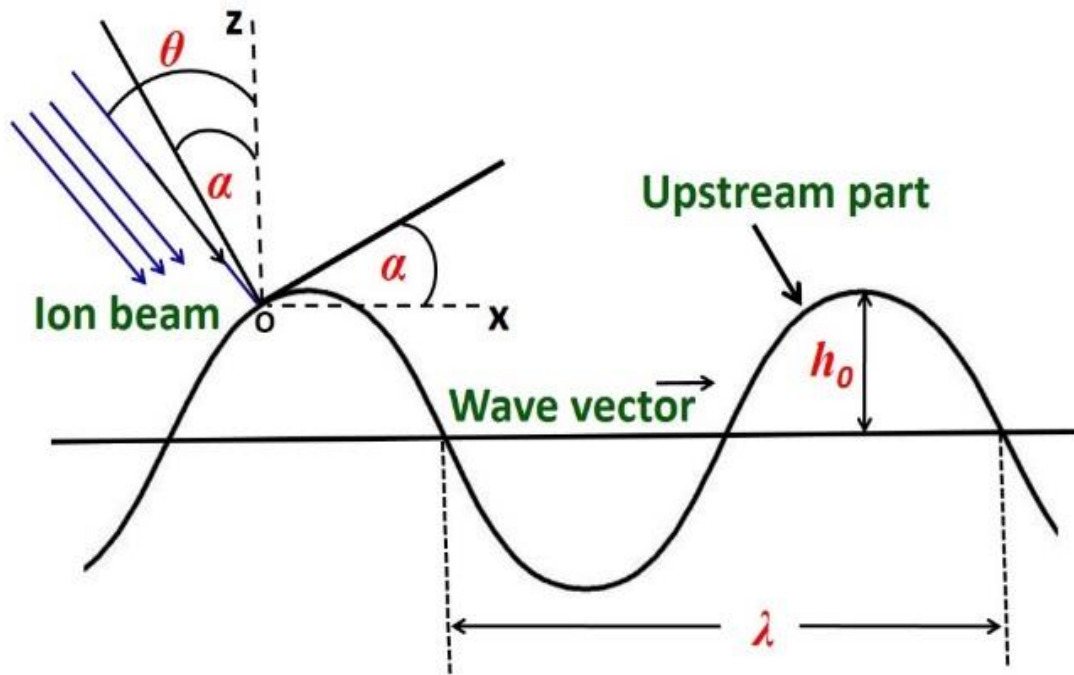


Figure 3.8: Illustration of geometry of ion bombardment on a sinusoidal profile.

This surface profile can be described by  $h = h_0 \cos(2\pi x/\lambda)$  where  $h$  is the ripple amplitude and  $\lambda$  is the ripple wavelength. The ion-beam is incident on the surface at an angle  $\theta$  to the normal to the mean surface plane (the  $Oz$  axis). Over an incremental surface length  $ds$ , at the point  $O$  on the surface, the gradient of the surface slope is given by  $\tan \alpha = \partial h / \partial x$ . It is evident that  $\alpha$  is also the angle between the local surface normal and the  $Oz$ -axis. As the ratio of the ripple amplitude and ripple wavelength  $h_0/\lambda$  increase, the maximum gradient of the sinusoidal ripple pattern  $2\pi x/\lambda$  becomes too large and, as a consequence, the local angle of incidence of the incident ion-beam ( $\theta - \alpha$ ) decreases, ultimately reaching a limiting condition when the incident ion-beam is parallel to the back slope of the ripple pattern. For any further increment in  $h_0/\lambda$  ratio, part of the upstream face of the ripples is 'blocked' or 'shadowed' from the incident ion-

beam by the preceding peak in the waveform. The limiting value of the ratio  $h_0/\lambda$  for shadowing not to occur is given by

$$\tan\left(\frac{\pi}{2} - \theta\right) \geq \frac{2\pi h_0}{\lambda} \quad (3.52)$$

which places an upper limit on the ratio  $h_0/\lambda$  for any angle of ion incidence  $\theta$ . If this ratio is exceeded then the valleys will not be eroded but the ripple crests will be. Although the dynamics of the subsequent changes in surface morphology is difficult to describe theoretically it is reasonable to expect that a transformation to a sawtooth-like waveform will gradually evolve for prolonged ion sputtering [34].

#### **Fractional change in sputter erosion rate due to ripple evolution:**

Figure 3.8 shows a schematic diagram of a regular sinusoidal ripple pattern with wave vector aligned parallel to the projection of the incident ion-flux of density  $J$ . Ion-flux is incident in the  $xOz$  plane at an angle  $\theta$  with respect to normal of the mean surface plane (the  $Oz$  axis) and over an incremental surface length  $ds$  at any arbitrary point on the surface. Gradient of the surface,  $\partial h/\partial x$ , is given by  $\tan \alpha = \left(\frac{\partial h}{\partial x}\right)$  where  $\alpha$  is the angle between the local surface normal and the  $Oz$  direction. The rate of erosion of the surface element, at the arbitrary point under consideration, in the  $Oz$  direction is given by

$$\left(\frac{\partial h}{\partial t}\right) = (J/N)Y(\theta - \alpha)\cos(\theta - \alpha)\sec \alpha \quad (3.53)$$

where  $Y(\theta - \alpha)$  is the sputtering yield for local ion incidence angle and  $N$  is the target atomic density. Under the assumption that the local surface gradient is small everywhere, one can expand Eq. 3.53 to first order as follows:

$$-\left(\frac{\partial h}{\partial t}\right) = (J/N)\left[Y(\theta)\cos\theta - \left(\frac{\partial h}{\partial x}\right)\frac{\partial}{\partial\theta}\{Y(\theta)\cos\theta\}\right] \quad (3.54)$$

Following Carter, the surface can be approximated as follows [34]:

$$h = h_0 \cos(2\pi x/\lambda) \quad (3.55)$$

where  $h_0$  is the ripple amplitude and  $\lambda$  is the wavelength. Using this expression in Eq. 3.54 and integrating over a complete wavelength where  $x=0 \rightarrow \lambda$ , the total rate of erosion (averaged over a wavelength),  $R$ , is given by

$$R = (J/N) Y(\theta) \cos\theta \quad (3.56)$$

Bradley and Harper showed that in addition to gradient dependence of sputtering yield, for surface radii of curvature comparable to or larger than dimensions of the atomic collision cascade which generates sputtering, it is also a linear function of the second spatial derivative of the height profile. Carter extended this linear dependence of sputtering yield to higher order of derivatives of the height profile and thus  $R$  can be expressed as:

$$R' = (J/N) Y(\theta) \cos\theta + (J/N) \sec\theta \cdot (1/\lambda) \cdot \int_0^\lambda dx \left[ a(\theta) \left( \frac{\partial h}{\partial x} \right)^2 + b(\theta) \left( \frac{\partial h}{\partial x} \right)^4 + \dots \right] \quad (3.57)$$

Where 
$$a(\theta) = Y_{2\theta} (\cos\theta/2!) - Y_\theta \sin\theta \quad (3.58)$$

$$b(\theta) = Y_{4\theta} (\cos\theta/4!) - Y_{3\theta} (\sin\theta/3!) - Y_{2\theta} (\cos\theta/3) + Y_{2\theta} (\sin\theta/3)$$

$$Y_{n\theta} = \frac{\partial^n Y}{\partial \theta^n}$$

Performing the integral and letting  $F = [R' - (J/N)Y(\theta)\cos\theta] / (J/N)Y(\theta)\cos\theta$ , the fractional change in sputter erosion rate (with respect to a plane surface) can be expressed as follows:

$$F = [\sec\theta/Y(\theta)] [2\pi^2 a(\theta)(h_0/\lambda)^2 + 6\pi^4 b(\theta)(h_0/\lambda)^4 + \dots] \quad (3.59)$$

Thus, fractional sputtering yield becomes a polynomial function of even powers of  $h_0/\lambda$ .

## Bibliography

1. T. Som and D. Kanjial, *Nanopatterning by Ion-beam Sputtering: Fundamentals and Applications* (Panstanford, Singapore, 2013).
2. E. Chason, W.L. Chan, *J. Phys. Condens. Matt.* 21 (2009) 224016

3. Y. Zhao, G.-C. Wang, T.-M. Lu, M. De Graef, and T. Lucatorto, *Characterization of Amorphous and Crystalline Rough Surface-Principles and Applications*. Vol. 37. 2000: Access Online via Elsevier.
4. H. Gnaser, *Low-energy Ion Irradiation of Solid Surfaces* (Springer-Verlag, Berlin-Heidelberg, 1999).
5. R. Hellborg, H. J. Whitlow, and Y. Zhang (eds), *Ion-beams in Nanoscience and Technology*. (Springer-Verlag, Berlin-Heidelberg, 2009).
6. M. Nastasi, J.W. Mayer, and J.K. Hirvonen, *Ion-solid interactions: Fundamentals and Applications* (Cambridge University Press, Cambridge, 1996).
7. J.F. Ziegler and J.P. Biersack, *The Stopping and Range of Ions in Matter* (Springer, New York, 1985).
8. J.F. Ziegler, J.P. Biersack, and K. Littmark, *The stopping and Range of Ions in Matter* (Pergamon, New York, 1985) See also "<http://www.srim.org/>".
9. L.A. Christel, J.F. Gibbons, and T.W. Sigmon, *J. Appl. Phys.* 52 (1981) 7143.
10. M. Toulemonde *et al.*, *Nucl. Instr. Meth. Phys. Res. B* 116 (1996) 1.
11. H. Trinkaus and A.I. Ryazanov, *Phys. Rev. Lett.* 74 (1995) 5072.
12. H. Trinkaus, *Nucl. Instr. Meth. Phys. Res. B.* 107 (1996) 155.
13. R. Behrisch and H.H. Andersen, *Sputtering by particle bombardment*. Vol. 1. 1981: Springer.
14. Y. Yamamura, Y. Itikawa, and N. Itoh, Report IPPJ-AM-26, Institute of Plasma Physics, Nagoya University (1983).
15. Y. Yamamura, C. Mössner, and H. Oechsner, *Radiat. Eff.* 103 (1987) 25.
16. W. Möller and W. Eckstein, *Nucl. Instrum. Methods Phys. Res. B* 2 (1984) 814.
17. R.M. Bradley and J.M.E. Harper, *J. Vac. Sci. Technol. A* 6 (1988) 2390.
18. P. Sigmund, *Phys. Rev.* 184 (1969) 383.

19. G. Carter and V. Vishnyakov, *Phys. Rev. B* 54 (1996) 17647.
20. C.S. Madi, *Linear Stability and Instability Patterns in Ion Bombarded Silicon Surfaces*.  
(Ph. D. Thesis, Harvard University, 2011).
21. A.-L. Barabási and H.E. Stanley, *Fractal Concepts in Surface Growth* (Cambridge University Press, Cambridge, 1995).
22. C. Herring, *J. Appl. Phys.* 21 (1950) 301.
23. W.W. Mullins, *J. Appl. Phys.* 30 (1959) 77.
24. M.A. Makeev and A.-L. Barabási, *Appl. Phys. Lett.* 71 (1997) 2800.
25. C.C. Umbach, R.L. Headrick, and K.-C. Chang, *Phys. Rev. Lett.* 87 (2001) 246104.
26. F. Frost, A. Schindler, and F. Bigl, *Phys. Rev. Lett.* 85 (2000) 4116.
27. S. Mayr, Y. Ashkenazy, K. Albe, and R. Averback, *Phys. Rev. Lett.* 90 (2003) 055505.
28. M. Castro and R. Cuerno, *Appl. Surf. Sci.* 258 (2012) 4171.
29. M. Castro, R. Gago, L. Vázquez, J. Muñoz-García, and R. Cuerno, *Phys. Rev. B* 86 (2012) 214107.
30. A. Zalar, *Thin Solid Films* 124 (1985) 223.
31. E.-H. Cirlin, J. J. Vajo, R. E. Doty, and T. C. Hasenberg, *J. Vac. Sci. Technol. A* 9 (1991) 1395.
32. R. M. Bradley, *Phys. Rev. E*, 54 (1996) 6149.
33. J. M. García, R. Cuerno, and M. Castro, *J. Phys. Condens. Matter* 21 (2009) 224020.
34. G. Carter, *J. Appl. Phys.* 85 (1999) 455.

---

## CHAPTER 4

---

### **4. Evolution of morphology on Si surface under low energy Ar<sup>+</sup>-ion irradiation**

#### **4.1 Introduction**

It is well-known that ion-beam sputtering (IBS) leads to formation of spontaneously arising patterns of corrugations, holes, and dots [1-2] at the surfaces of different materials viz. metals, semiconductors, and insulators [3-8]. In fact, patterned substrates, mostly in the form of ripples, are being used as templates to grow and tune magnetic and plasmonic properties of thin films by using their morphological anisotropy [9-12]. However, in spite of its potential applications, complete control over tailoring IBS induced self-organized patterns with desired properties is yet to be achieved. One of the major reasons behind this has been the lack of complete understanding of the mechanisms that govern the pattern formation. This is partly due to the huge time-scale separation among different processes that influence the system, which complicates the unambiguous identification of the main underlying physical mechanisms.

Ripple formation is known to result from off-normal ion bombardment of materials. In the linear stability analysis (as mentioned in chapter 3) of Bradley and Harper (BH) theory, patterns originate from destabilizing (roughening) effect in which the erosion rate is enhanced at regions of high concave curvature and the stabilizing (smoothing) effect of surface diffusion [13]. This theory explains many experimental observations (like ripple formation, ripple rotation, growth of ripple amplitude etc.) although some significant contradictions with experimental results also exists. For instance, one of the important predictions of BH theory is that a flat surface is always unstable under ion erosion. In contrast, experimental studies on Si and SiO<sub>2</sub> [14-17] show the existence of flat surfaces, up to incident angles of 50° or 40°, respectively,

from where ripple formation starts. Such a sharp boundary between a flat (stable) and a rippled (unstable) silicon surface was identified by Madi *et al.* as bifurcation in control parameter (incident angle,  $\theta$  and ion energy,  $E$ ) space [18]. Later on, Madi *et al.* [18] concluded that stability at low angles and topographical instability at high angles can be explained by taking into account the effects of ion impact-induced prompt atomic redistribution [calculated from Carter-Vishnyakov (CV) theory] [14] and that the erosive component (calculated from BH theory) is essentially irrelevant.

As mentioned in chapter 3, Castro *et al.* [19] put forward an alternative approach of ion induced solid flow model to explain formation of ripple patterns beyond a threshold angle. This theory is based on the continuum description of the surface flow that is driven by surface confined stress-induced viscous flow of a thin amorphous layer that forms during ion bombardment. It has been pointed out by the same authors that both the mass redistribution and the viscous flow descriptions agree with the experiments with respect to the transition from flat to rippled surface at a particular incidence angle and the dependence of the pattern wavelength on incident angle of ions [20]. However, molecular dynamics (MD) based calculations cannot probe the required timescales associated with pattern evolution whereas the solid flow model offers the advantage of time-dependent (dynamic) evolution of ripple patterns [16,21,22].

The solid flow model is based on the assumption that due to the impact of the ions and the subsequent release of energy within the target, defects are created inside the material. These events occur within a few picoseconds after the impact. Relaxation of some amount of defects leads to sputtering of target atoms which is associated with the generation of a residual stress that is confined within a thin amorphous layer that builds up beneath the surface [23] and reaches a stationary value. This ion-induced (compressive) stress is manifested as a highly viscous flow of the incompressible amorphous layer. Using a hydrodynamic description of the solid flow with a linear approximation in perturbations around a flat target profile, Castro and

Cuerno [24] obtained a real part for the linear dispersion relation (i.e. amplification rate of wave-vector,  $\vec{q}$ ) given by:

$$\omega_q = -[f_E d^3 \phi(\theta) q^2 + \sigma d^3 q^4] / 3\mu \quad (4.1)$$

where  $\phi(\theta) = \frac{\partial}{\partial \theta} (\Psi(\theta) \sin \theta)$ ,  $d$  is the average thickness of the amorphous layer,  $\mu$  is (ion-induced) viscosity, and  $\sigma$  is the interface surface tension. The parameter  $f_E$  can be understood as the gradient of residual stress induced by ions across the amorphous layer, whose angular dependence is described through the function  $\Psi(\theta)$ . Since this angular function needs to be prescribed, we take  $\Psi(\theta) = \cos \theta$  as the simplest geometrically motivated choice that shows a good agreement [24]. According to the solid flow model [19], the smallest timescale associated with ripple formation in the linear regime can be written as:

$$\tau(\theta, E) \sim \frac{\mu}{f_E^2 d^3 \phi^2(\theta)} \quad (4.2)$$

The most general prediction that can be obtained from this theory is that it allows finding the characteristic scale for the exponential growth of the pattern amplitude occurring at short times where linear approximation holds. For a given pair of angle and energy reference values,  $(\theta_{ref}, E_{ref})$ , one can extrapolate the value of the intrinsic timescale,  $\tau$ , for any other pair  $(\theta, E)$  through the relation:

$$\tau(\theta, E) = \tau(\theta_{ref}, E_{ref}) \frac{J_{exp}(\theta_{ref}, E_{ref}) E_{ref}^{-7/3+2m} \phi^2(\theta_{ref})}{J(\theta, E) E^{-7/3+2m} \phi^2(\theta)} \quad (4.3)$$

where  $J_{exp}(\theta_{ref}, E_{ref}) = J_{exp}(E) \cos \theta$  is the flux used in a particular experiment for energy  $E$  and angle  $\theta$ , with  $J_{exp}(E)$  being the flux at normal incidence and  $m$  can be assumed to be in the range 1/3-1/2 [19].

In case of solid flow model, based on detailed binary-collision simulations, it is assumed that the generated stress depends on the ion energy ( $<2$  keV) [25,26]. However, there is no direct measurement which quantifies ion induced stress. Thus, it is a good strategy if the parameter,  $f_E$ , can be avoided while calculating the intrinsic timescale at any angle. In order to do so, we experimentally determined the intrinsic timescale (for a reference ion incidence angle) up to which the growth of roughness follows an exponential behaviour and the ripple wavelengths remained constant. This intrinsic timescale was utilized to verify the validity of solid flow model at other ion incidence angles.

Using this model, we identified the hitherto unexplored angular window in which the solid flow model may be invoked to explain 500 eV Ar-ion induced ripple formation. Since, in general, it is observed that the ion incidence angle (in our case  $51^\circ$ ) at which transition from flat to rippled surface takes place remains constant at different energies (in the range of 0.25-1.5 keV) [18,20,22], we have chosen an Ar-ion energy of 0.5 keV as a representative one and tested the applicability of the solid flow model on silicon over an angular window of  $51^\circ$  to  $72.5^\circ$  – wherever parallel-mode ripple patterns evolve. We found out the experimental timescale at an arbitrary angle of incidence – the reference angle ( $60^\circ$ ) – up to which the system evolved linearly. This time was used to predict the intrinsic timescale (by invoking the solid flow model) for other ion incidence angles and subsequently systematic experiments were carried out to check their proximities at each of those angles. These angles included the transition point of flat to rippled surface and beyond which parallel-mode ripples disappear. We also show that the temporal evolution of ripples at all these angles remains in the linear regime although the nonlinear regime sets in quickly at higher incidence angles.

Identification of the linear regime of pattern formation can be precisely done only with the help of the solid flow model. However, it may be mentioned that on the experimentally front, the major drawbacks have been the lack of adequate experimental data, in particular, at higher

oblique angles of incidence, and the reproducibility of observed patterns. These give rise to the necessity of performing systematic experiments over a large angular window to develop a better understanding and to learn how to control and manipulate the surface patterns by ion irradiation. As mentioned above, usually, parallel-mode ripples (i.e. wave-vector parallel to the projected ion-beam) are formed and reported beyond an incident angle ( $\theta$ ) of  $50^\circ$  [27,28]. If one considers the full angular window (i.e.  $\theta= 0^\circ$  to  $85^\circ$ ), reports are available on ripple formation up to an oblique incidence of  $\sim 70^\circ$  [27,29,30]. Thus, there is hardly any systematic study on Ar-ion induced pattern formation on Si in the angular window  $70^\circ \leq \theta \leq 80^\circ$  which would have helped unfolding the underlying processes leading to a transition from parallel- to perpendicular-mode ripples. In the studies presented in the thesis, evolution of surface topography on Si(100) substrates is investigated under low energy ion bombardment over an angular window of  $63^\circ$ - $83^\circ$ . This gives rise to evolution of a gamut of unusual patterns which were not reported earlier (those formed at higher oblique incident angles, viz.  $70^\circ$ - $78^\circ$ ). Through these intermediate patterns parallel-mode ripples are seen to undergo a transition to perpendicular-mode ripples at an incident angle of  $80^\circ$ . In case of an even higher angle of incidence surface smoothening is observed. At this point the origin of these unusual structures was not clear. We have made an attempt to correlate the roughness evolution plot to the sputtering yield plots as a function of ion incidence angle. However, this does not solve the problem of explaining unusual patterns observed in the angular window of  $70^\circ$ - $72.5^\circ$ . To understand the pattern formation mechanism at these two angles, fluence-dependent studies were carried out at  $\theta=70^\circ$  and  $72.5^\circ$  by keeping all other parameters same. In doing so, it was observed that with increasing fluence parallel-mode ripples gets transformed into protruded mounds/faceted structures. In addressing the mechanism of the observed transition, variation in the erosion rate of a nonplanar surface is calculated by using the theoretical model of Carter [31]. It is seen that beyond threshold values of the amplitude to wavelength ratio, inter-peak

shadowing of incident ion-flux can lead to a transition from ripples to faceted structures. The coarsening behaviour of faceted structures with increasing fluence is explained in light of Hauffe's mechanism based on reflection of primary ions [32]. In addition, Carter's theory was also employed to calculate fractional change in sputtering yield for ripples and faceted structures (where we have replaced the amplitude to wavelength ratio by amplitude to base-width ratio for the latter ones) to correlate the surface roughness to the sputtering yield.

It may be pointed out that ripples are being utilized as a template for depositing thin films to modify their functional properties [11,33,34], albeit ripple formation is unwanted in various techniques, viz. secondary ion mass spectroscopy (SIMS), Auger electron spectroscopy (AES), and ion milling. The ion incidence angle  $\theta \neq 0^\circ$  for a typical SIMS or AES set up results in formation of ripples at the surfaces. This results in rapid degradation in depth resolution. As a way out to this problem Zalar first demonstrated that by rotating the sample with respect to its surface normal during sputtering one can avoid ripple formation [35]. It may be noted that sample rotation does not always become fruitful in suppressing surface roughening. Sometimes sample rotation during ion erosion roughens the surface but at a slower rate [36,37]. Smoothing of the surface under sample rotation is explained by Bradley and Cirlin [38]. According to Bradley's theory, during sample rotation, smoothing effect due to bulk viscous flow and surface self-diffusion can be predominant over the roughening effect of the curvature-dependent sputter yield and generate a smooth surface [38]. Carter extended this approach to examine the evolution of surface roughness with continuous irradiation under concurrent substrate rotation [39]. In this frame work, the surface height evolution is described by taking into account curvature-dependent roughening [13] and different surface relaxation processes namely, viscous relaxation [40], sputtering relaxation [41], ballistic collisional drift, and diffusion relaxation [42] along with statistical fluctuations. For a semiconducting material, ion irradiation causes defects in the amorphous layer (created during early stage of sputtering)

which subsequently relaxes and leads to a viscous flow. In addition, ion impact generates internal fluxes of moving recoils that transports both parallel and normal with respect to the surface. This movement has a drift component and diffusion-like-component. Furthermore, thermally activated diffusion is also important when experiments are performed at higher temperatures. However, sample can still get roughened during concurrent ion sputtering and sample rotation if the viscosity of the sample is too high. Bradley explained this behaviour by taking into account the sign of a parameter characterizing the curvature dependence of the sputtering yield [41].

In the last part of this chapter, we demonstrate the effect of sample rotation during ion-beam irradiation towards tuning the surface roughness. Si(100) substrates were exposed to argon ions at different incident angles with respect to the surface normal. It is observed that under substrate rotation, flat surface remains flat whereas mound-like structures formed at oblique incidence angles (where ripple morphology prevails without substrate rotation). In addition, a detailed quantitative atomic force microscopy (AFM) measurements are presented for different sputtering times at two incident angles viz. ( $67^\circ$  and  $60^\circ$ ) under sample rotation with a constant angular speed ( $\omega$ ) during ion-beam erosion to address the temporal evolution of mounds under substrate rotation. Moreover, to check the effect of angular speed variation, the substrates were rotated at different angular velocities for a particular fluence. The results are explained in light of existing models based on ion-matter interaction.

## 4.2 Experimental

The substrates used in the experiments were sliced into small pieces from a *p*-type Si(100) wafer (B-doped, resistivity 0.01-0.02  $\Omega$  cm). The UHV-compatible experimental chamber was used which is equipped with a 5-axes sample manipulator and an electron cyclotron resonance (ECR) based broad beam, filament-less ion source (more details are available in chapter 2).

The chamber base pressure was below  $5 \times 10^{-9}$  mbar and the working pressure was maintained at  $2.5 \times 10^{-4}$  mbar by using a differential pumping unit. Silicon samples were fixed on a sample holder which was covered with a sacrificial silicon wafer of the same lot to ensure a low-impurity environment. The beam diameter and the ion flux were measured to be 3 cm and  $1.3 \times 10^{14}$  ions  $\text{cm}^{-2} \text{s}^{-1}$ , respectively. The experiments to identify the linear regime of pattern formation, were performed at this fixed flux and exposure times in the range of 1 to 120 min for four incidence angles, viz.  $51^\circ$ ,  $60^\circ$ ,  $65^\circ$ , and  $72.5^\circ$ . In addition, Argon-ion energy was chosen to be 500 eV since it lacks a systematic study at this energy for higher oblique incident angles under consideration. The current density was measured to be  $21 \mu\text{A cm}^{-2}$  (except for  $65^\circ$  where the current density was fixed at  $28 \mu\text{A cm}^{-2}$ ). The experiments were performed at a fixed fluence of  $5 \times 10^{17}$  ions  $\text{cm}^{-2}$  for the entire angular window of  $63^\circ$ - $83^\circ$ . In addition, measurements were carried out to study flux- and fluence-dependent evolution of surface morphology in case of selective angles.

To observe the ripple to facet transition, experiments were performed for fluences in the range of  $1$ - $20 \times 10^{17}$  ions  $\text{cm}^{-2}$  and at two different ion incidence angles, namely  $70^\circ$  and  $72.5^\circ$  (with respect to the surface normal). According to TRIDYN simulation [43], although the sputtering yield maxima is close to  $70^\circ$ , for the sake of completion, we also performed measurements at  $72.5^\circ$  which is not far off from the sputtering yield maxima and at this higher angle the shadowing effect is expected to be more prominent.

Following Ar-ion exposure the samples were imaged by *ex-situ* atomic force microscopy (described in chapter 2). Root mean square (rms) surface roughness,  $w$ , and two-dimensional (2D) autocorrelation function were calculated for all AFM images by using the WSxM software [44]. Wavelength of ripple patterns was calculated from the respective autocorrelation functions. For faceted structures, instead of wavelength, we considered the average base-width value which were calculated from a large number of line profiles drawn on the respective AFM

images. In addition, x-ray photoelectron spectroscopic measurements were performed on Ar-ion bombarded Si samples which did not show the presence of any impurity above their respective detection limits.

For addressing the effect of concurrent substrate rotation during ion-beam irradiation, 500 eV Argon-ion energy was chosen and due to the lack of any systematic study at this energy for higher oblique incident angles under substrate rotation during ion-beam irradiation. A thorough angle-dependent study was performed with a substrate rotational speed of  $0.5^\circ \text{ s}^{-1}$  at  $67^\circ$ . Most of the experiments were performed for different angles of incidence by properly choosing the rotational speed and the time of erosion so that the system evolves in the linear regime. For  $67^\circ$ , six different angular speeds (in the range of  $8 \times 10^{-3}$ - $44 \times 10^{-3}$  rad/s) were chosen to realize the effect of rotational speed variation. Moreover, experiments were carried out to study time evolution of patterns for the incident angles of  $67^\circ$  and  $60^\circ$ .

## **4.3 Results and discussion**

### **4.3.1 Temporal evolution of ripple patterns**

Figure 4.1 presents a high-resolution cross-sectional TEM image of a silicon sample which was exposed to argon ions at  $60^\circ$  for the duration of 11 min. The presence of ion-induced surface corrugation in the form of ripples (wavelength,  $\lambda \sim 30$  nm) is clearly seen from Fig. 4.1. In addition, a thin amorphous silicon layer at the top is also evident which forms during ion bombardment and subsequently acts as a highly viscous and incompressible medium. This meets one of the pre-requisites for invoking solid flow model in the present case. To further justify the use of solid flow model, we performed systematic experiments at  $60^\circ$  which was chosen to be the reference angle.

Figure 4.2 shows the roughness evolution plot for silicon following argon ion bombardment (up to 11 min). The insets show selective AFM images for three different exposure times, viz.

1, 5, and 11 min. The exponential fit ensures that the temporal evolution of ripples remains in the linear regime up to 11 min.

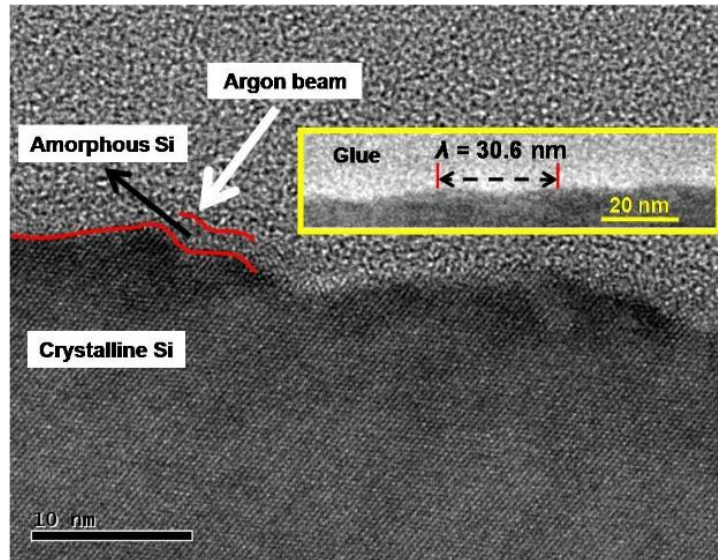


Figure 4.1: Cross-sectional TEM image corresponding to ion incidence angle of  $60^\circ$  where the amorphous layer is marked by the red line. The inset shows slightly zoomed out version of the same sample.

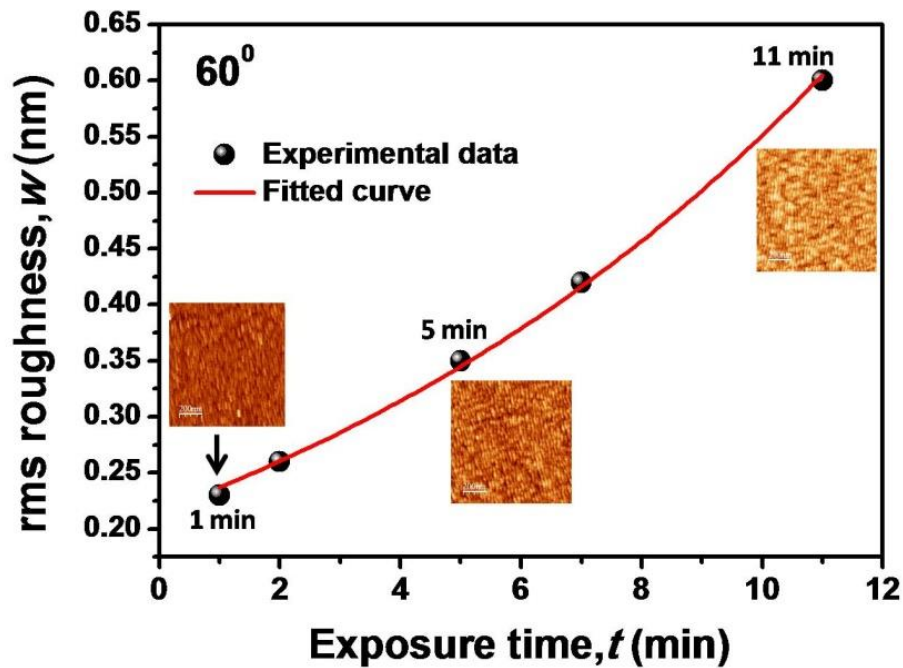


Figure 4.2: Roughness evolution plot corresponding to incidence angle of  $60^\circ$ . The inset shows the AFM topographic images corresponding to exposure times of 1, 5.5, and 11 min, respectively.

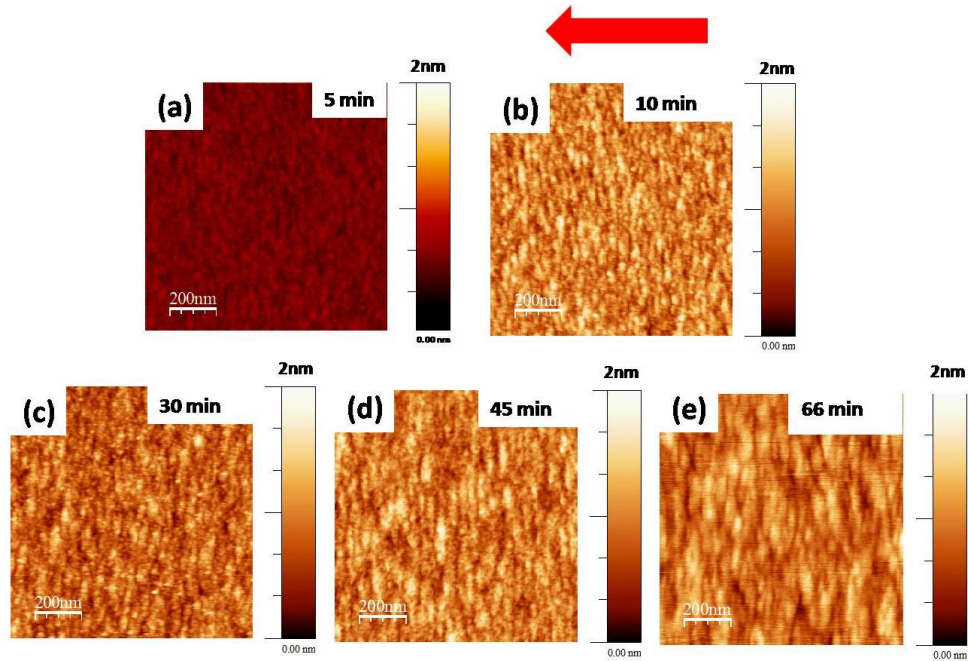


Figure 4.3: AFM micrographs of *p*-Si(100): Exposed at an incidence angle of  $51^\circ$  for different times starting from 5 to 66 min. The arrow indicates the direction of the incoming ion beam.

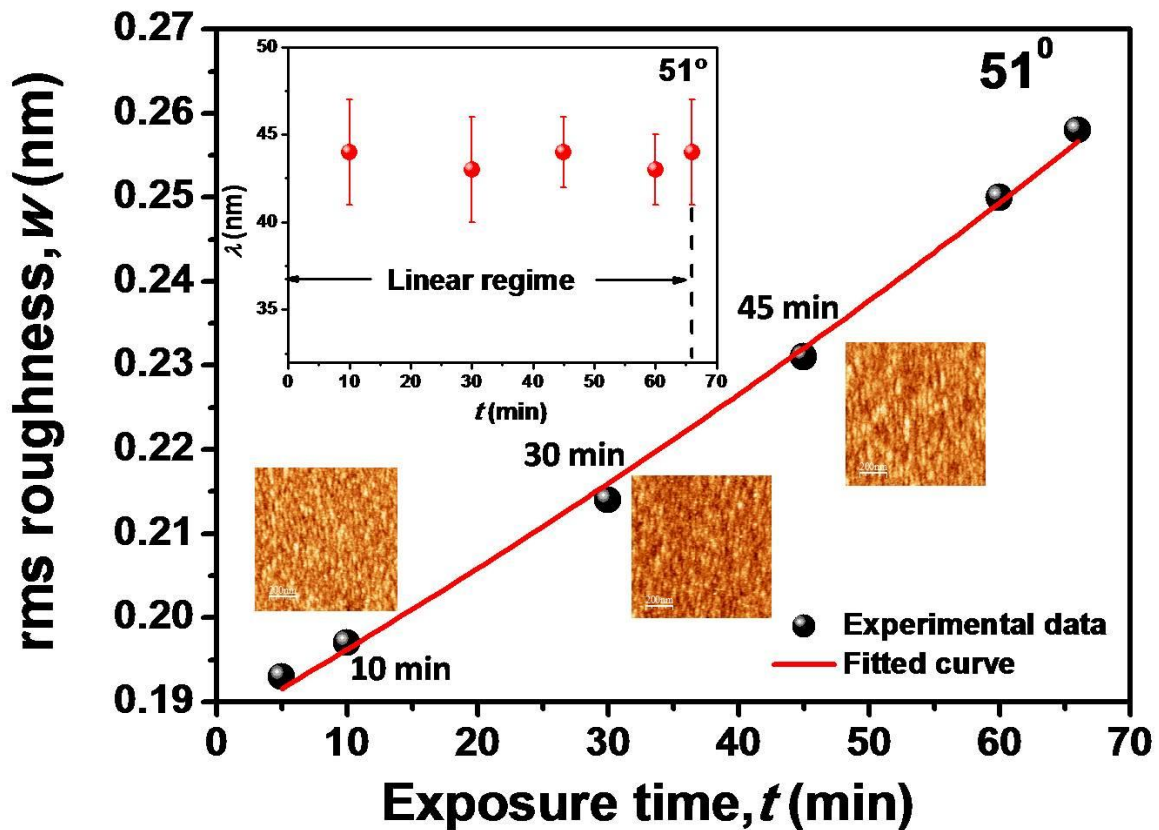


Figure 4.4: Variation in roughness with exposure time for the incidence angle of  $51^\circ$  where the exponential fit is well realized. The inset shows the plot for wavelength versus exposure time at  $51^\circ$ .

However, beyond 11 min of erosion time (i.e. the intrinsic timescale for  $60^\circ$ ) the rms roughness does not follow the exponential growth behaviour any more (further discussed in the later part of this section). This is in accordance with the solid flow model as described above (Chapter 3) and thus, we identify this threshold time (11 min) as the reference intrinsic timescale ( $\tau$ ) to test the applicability of solid flow model at other incidence angles, viz.  $51^\circ$  (the transition point from flat to parallel-mode rippled surface),  $65^\circ$ , and  $72.5^\circ$  (beyond which the parallel-mode ripples disappear).

In the present study, we performed our experiments at a constant flux and energy which simplify Eq. 4.3 further. This leads to the estimated intrinsic timescale,  $\tau(\theta, E)$  (=64 min), at  $\theta=51^\circ$ . A systematic time evolution study (starting from 1 to 66 min of exposure to argon ion beam) was carried out at this angle and the AFM images are presented in Figs. 4.3(a)-(e). These micrographs involve very small roughness values and hence, lack the typically coherent look of ripple patterns observed at other angles.

Corresponding roughness evolution plot is shown in Fig. 4.4 where a clear exponential growth of the rms roughness is observed up to an irradiation time of 66 min which is very close to the time predicted by the solid flow model (64 min). Beyond this time, an increase in the roughness takes place although the exponential behaviour is not followed any more. The validity of the linear regime is further confirmed from the wavelength versus exposure time plot where the wavelengths remain constant (average value of 43 nm) up to an exposure time of 66 min (inset, Fig. 4.4).

To verify the applicability of this theory far from the stable to rippled surface transitional point, we chose  $65^\circ$  as one of our test angles. For this angle, the intrinsic timescale calculated by using Eq. 4.2 turned out to be 5 min.

Accordingly, early stage evolution of ripple pattern was studied and the results are presented in Fig. 4.5 which shows time-dependent roughness evolution.

The insets in this figure show morphological evolution in the form of selective AFM images. The roughness evolution data get fitted well by an exponential curve up to 4.5 min which can be identified as the point of transition from the linear to the non-linear regime. In addition, the ripple wavelengths remain constant ( $\lambda \sim 23$  nm) up to this time. This clarifies the relevance of the solid flow model at an incidence angle greater than the reference angle ( $60^\circ$ ).

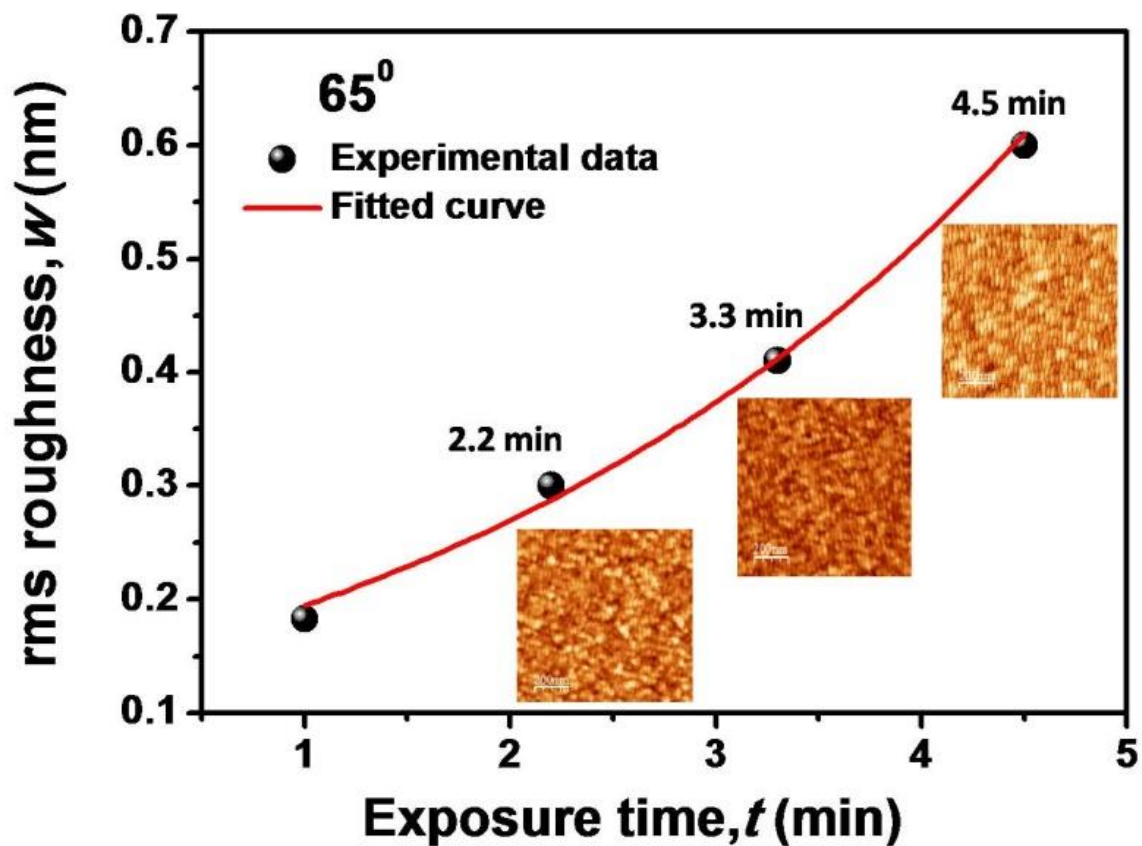


Figure 4.5: Temporal evolution of surface roughness at  $\theta=65^\circ$ . Images corresponding to 2.2, 3.3, and 4.4 min of exposure times are shown as insets for a realization of the corresponding surface morphology.

Likewise, an exponential growth in roughness is also observed for ripples, formed by irradiation at an incidence angle of  $72.5^\circ$ , till 2.5 min which is little earlier than the intrinsic time scale predicted by the solid flow model (3.8 min). A comparison between the predicted ( $\tau_{pre}$ ) and the experimentally measured ( $\tau_{ob}$ ) timescales for transition from the linear (ripple wavelength remains constant) to the nonlinear (ripple coarsening) regime is depicted in Table 4.1.

It is clearly seen that with increasing ion incidence angle, the said transition takes place at a shorter timescale. In addition,  $\tau_{ob}$  deviates from  $\tau_{pre}$  corresponding to some incidence angles which is not well understood at this point. It may be mentioned that evolution of parallel-mode ripples, under the present experimental conditions and at higher energies do not occur beyond this angle and hence the solid flow model could be successfully tested for  $51^\circ \leq \theta \leq 72.5^\circ$ .

**Table 4.1**

Predicted ( $\tau_{pre}$ ) and experimentally measured ( $\tau_{ob}$ ) timescales for transition from the linear to the non-linear regime at different ion incidence angles.

Angle of incidence ( $^\circ$ )	$\tau_{ob}$ (min)	$\tau_{pre}$ (min)
51	66	64
60	11	11
65	4.5	5.0
72.5	2.5	3.8

In order to address the temporal evolution of roughness beyond the linear regime, experiments were carried out for long durations over the entire angular window (i.e.  $\theta=51^\circ$  to  $72.5^\circ$ ) where ripple formation takes place and the results are summarized in Fig. 4.6.

These plots clearly demonstrate that the exponential growth behaviour of roughness does not hold true beyond the intrinsic timescales (as discussed above) where ripple formation remains in the linear regime. According to Castro *et al.* [19], nonlinear effects can originate from ion induced stress [24] or from purely erosive effects [45] due to prolonged sputtering although they are not included in the scope of the solid flow model. However, a more generalized nonlinear theory — lubrication theory — which is beyond the scope of the present study, has already been invoked which can access the nonlinear regime of ripple evolution [46].

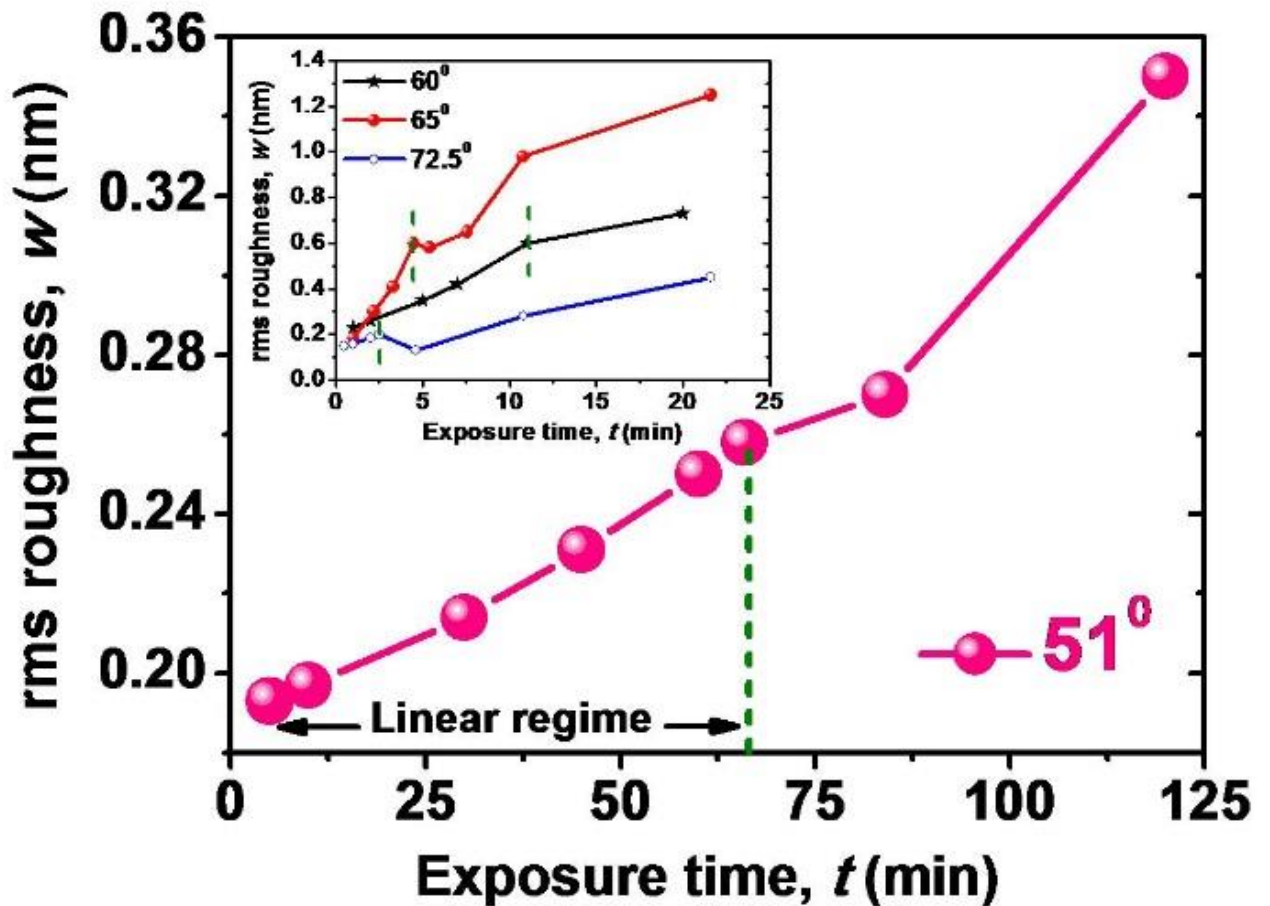


Figure 4.6: Complete temporal evolution of surface roughness at all incidence angles. The dashed lines indicate the time beyond which the nonlinear effects start under the solid flow model where the exponential growth of roughness does not occur anymore.

### 4.3.2 Role of ion incidence angle on pattern formation

Figures 4.7(a-h) present the AFM topographic images of silicon surface before and after exposure to argon ions at different oblique incident angles. Fig. 4.7(a) depicts AFM image of the pristine sample which has a smooth surface ( $w=0.09$  nm). From Fig. 4.7(b) it is observed that ripple morphology evolves at  $65^\circ$ . Estimations using WSxM software show that ripples have wavelength of 38 nm, height of 3 nm, and rms surface roughness of 1.7 nm. Careful measurements reveal that the ripple wavelength is independent of ion flux. Fig. 4.7(c) represents the morphology corresponding to an incident angle of  $67^\circ$  where parallel-mode ripples (wavelength of 60 nm, height of 3 nm, and rms roughness of 2.6 nm) are formed. In

addition, mounds (average dimension of 65 nm) appear on top of the ripples. Formation of such parallel-mode ripples is consistent with literature [23, 29].

Starting from this point (i.e. at  $67^\circ$ ), where mounds on ripples are observed, unusual patterns evolve at higher incident angles which were hardly seen earlier. Fig. 4.7(d) presents the AFM image corresponding to an oblique incidence of  $70^\circ$  where mounds are observed instead of parallel-mode ripples. These mounds have an average dimension of 88 nm and the corresponding surface roughness is 5.7 nm. There is a mild signature that these mounds may be protruded in the direction of ion-beam projection on the sample surface. For the incident angle of  $72.5^\circ$ , cone-like structures are observed where their apexes point towards the direction of ion beam [Fig. 4.7(e)]. The calculated surface roughness, mean value of the apex angle, and the base dimension are 7.8 nm,  $34.8^\circ$ , and 110 nm, respectively.

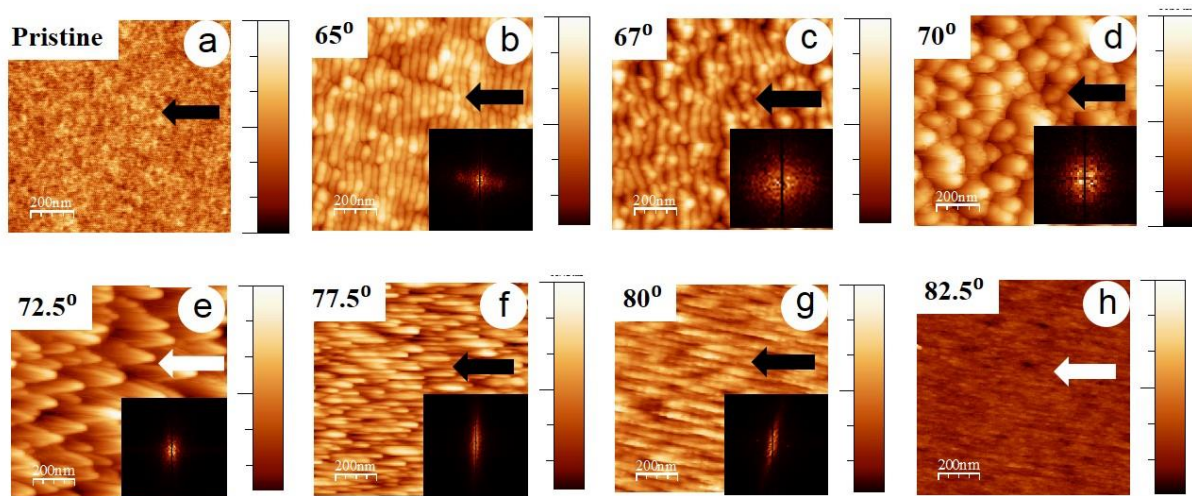


Figure 4.7: AFM images of Si(100): (a) Pristine and exposed to 500 eV  $\text{Ar}^+$ -ions to the fluence of  $5 \times 10^{17}$  ions  $\text{cm}^{-2}$  at incident angles of (b)  $65^\circ$ , (c)  $67^\circ$ , (d)  $70^\circ$ , (e)  $72.5^\circ$ , (f)  $77.5^\circ$ , (g)  $80^\circ$ , and (h)  $82.5^\circ$ . Corresponding height scales in (a)-(h) are 1 nm, 15 nm, 23 nm, 37 nm, 51 nm, 19 nm, 3 nm, and 2 nm, respectively. Arrows indicate projection of the ion beam on the surface. Insets show the 2D FFT obtained from the corresponding images.

Upon increasing the angle of incidence to  $77.5^\circ$  elongated structures are formed which resemble more like nano-needles. These needle-like structures (having an average length of 200 nm) lie parallel to the projection of ion beam onto the surface [Fig. 4.7(f)].

Further, increasing the ion incidence angle to  $80^\circ$ , perpendicular-mode ripples (of wavelength 65 nm and rms surface roughness of 0.4 nm) are formed [Fig. 4.7(g)]. Thus, it is clear that parallel-mode ripples undergo a transition to perpendicular-mode ripples at this angle. However, the transition from parallel- to perpendicular-mode ripples is not sharp since it undergoes a series of unusual pattern formation at intermediate angles. At  $82.5^\circ$ , a smooth surface is observed [Fig. 4.7(h)] whose roughness is comparable to the pristine surface. Formation of such ultra-smooth surfaces under nearly similar experimental conditions was reported earlier even at  $85^\circ$  [28]. The insets corresponding to AFM images shown in Figs. 4.7(b)-(h) represent the respective 2D FFT. For instance, the FFT corresponding to the incident angle of  $65^\circ$  depicts the obvious presence of a characteristic wavelength, which gets weakened in case of incident angle of  $67^\circ$ . On the other hand, starting from  $70^\circ$  to  $80^\circ$ , FFTs show signature of topographical anisotropy.

From the above discussion it is observed that due to 500 eV Ar-ion bombardment many different patterns evolve over the entire angular window being considered under the present study. However, for the angular window of  $0^\circ$ - $50^\circ$ , surface remains stable under ion bombardment whereas parallel-mode ripples emerge at  $51^\circ$  incidence angle (demonstrated in Fig. 4.8). It may be mentioned that formation of ion-induced self-organized nanostructures is generally caused due to the interplay between roughening caused due to sputter erosion and smoothening due to surface diffusion [13,47]. However, no single theory is adequate to explain all kinds of observed experimental features. This fortifies the need to invoke possible multiple physical effects to explain our observed patterns at different incident angles.

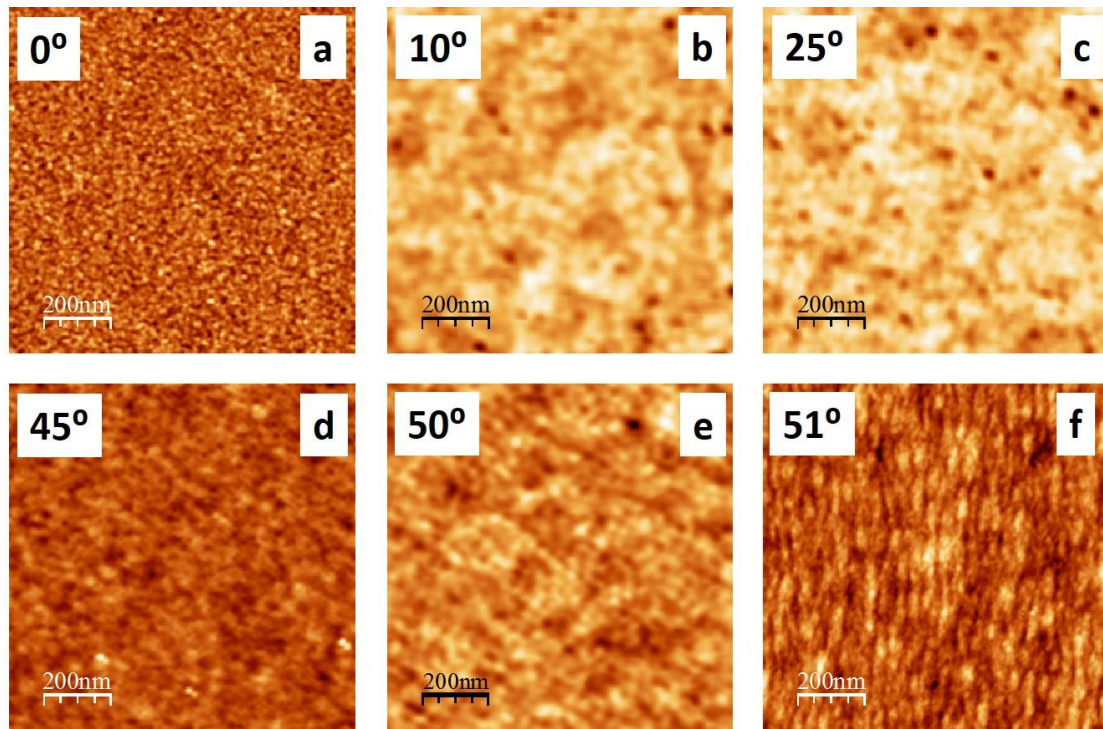


Figure 4.8: AFM images of Si(100) exposed to 500 eV Ar<sup>+</sup>-ions to the fluence of  $5 \times 10^{17}$  ions cm<sup>-2</sup> at incident angles of (a) 0°, (b) 10°, (c) 25°, (d) 45°, (e) 50°, and (f) 51°. Corresponding height scales in (a)-(f) are 1 nm, 1 nm, 1 nm, 1 nm, 1 nm, and 2 nm, respectively.

Let us first examine the role of sputtering on the origin of pattern formation observed in our case. In order to do this, an attempt has been made to correlate the evolution of surface roughness with sputtering. Fig. 4.9(a) shows the evolution of surface roughness [obtained from AFM images shown in Figs. 4.7(b)-(h)] at different incident angles. We also performed TRIDYN simulation [43] to calculate sputtering yield for 500 eV Ar-ions (for the fluence of  $5 \times 10^{17}$  ions cm<sup>-2</sup>) corresponding to different angles. Figure 4.9(b) shows the variation in sputtering yield with incident angle. From these figures it is seen that the roughness value peaks at 72.5° whereas the sputtering yield is maximum at ~70°. Thus, it is expected that sputtering will play a role for unusual pattern formation in our case.

The evolution of mounds/faceted structures at 70° and 72.5° angles of incidence will be discussed in the next section. It may be mentioned that the elongated needle-like structures

seen at  $77.5^\circ$  can be attributed to shadowing effect which is expected to cause an increase in erosion of surface protrusions compared to depressions [28,47].

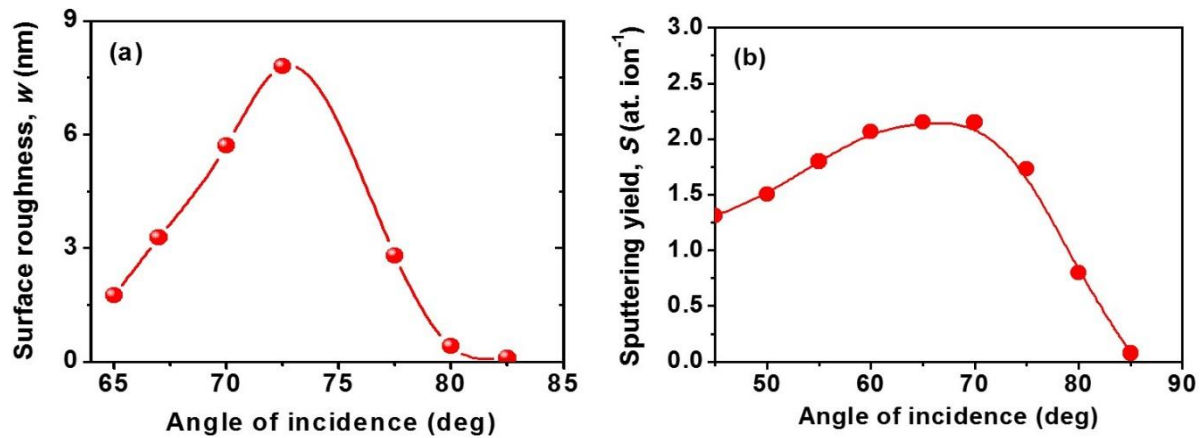


Figure 4.9: (a) Evolution of rms surface roughness corresponding to different angle of incidence. (b) Plot of sputtering yield versus angle of incidence obtained from TRIDYN simulation performed for 500 eV  $\text{Ar}^+$ -ions to the fluence of  $5 \times 10^{17}$  ions  $\text{cm}^{-2}$ .

The same mechanism should be operative at  $80^\circ$  where the surface evolves with a relatively low rms roughness. Such a low surface roughness may be attributed to a reduced sputtering yield at  $80^\circ$  [Fig. 4.9(b)]. For an even higher glancing angle of incidence (viz.  $82.5^\circ$ ), the observed smoothing of the surface can be explained in terms of extremely low sputtering yield where most of the ions would get reflected rather than contributing to sputtering [28].

### 4.3.3 Role of shadowing: Ripple to facet transition

Figures 4.10(a)–(g) present AFM topographic images obtained from silicon samples before and after exposure to argon-ion incidence angle  $70^\circ$  at different fluences. Fig. 4.10(a) presents AFM image of the pristine sample which shows a smooth surface (rms surface roughness = 0.09 nm). Figs. 4.10(b) and (c) show signature of corrugated surfaces formed at low fluences, namely  $1 \times 10^{17}$  and  $2 \times 10^{17}$  ions  $\text{cm}^{-2}$ , respectively. However, small mound-like entities also start appearing on the corrugated surface at the latter fluence.

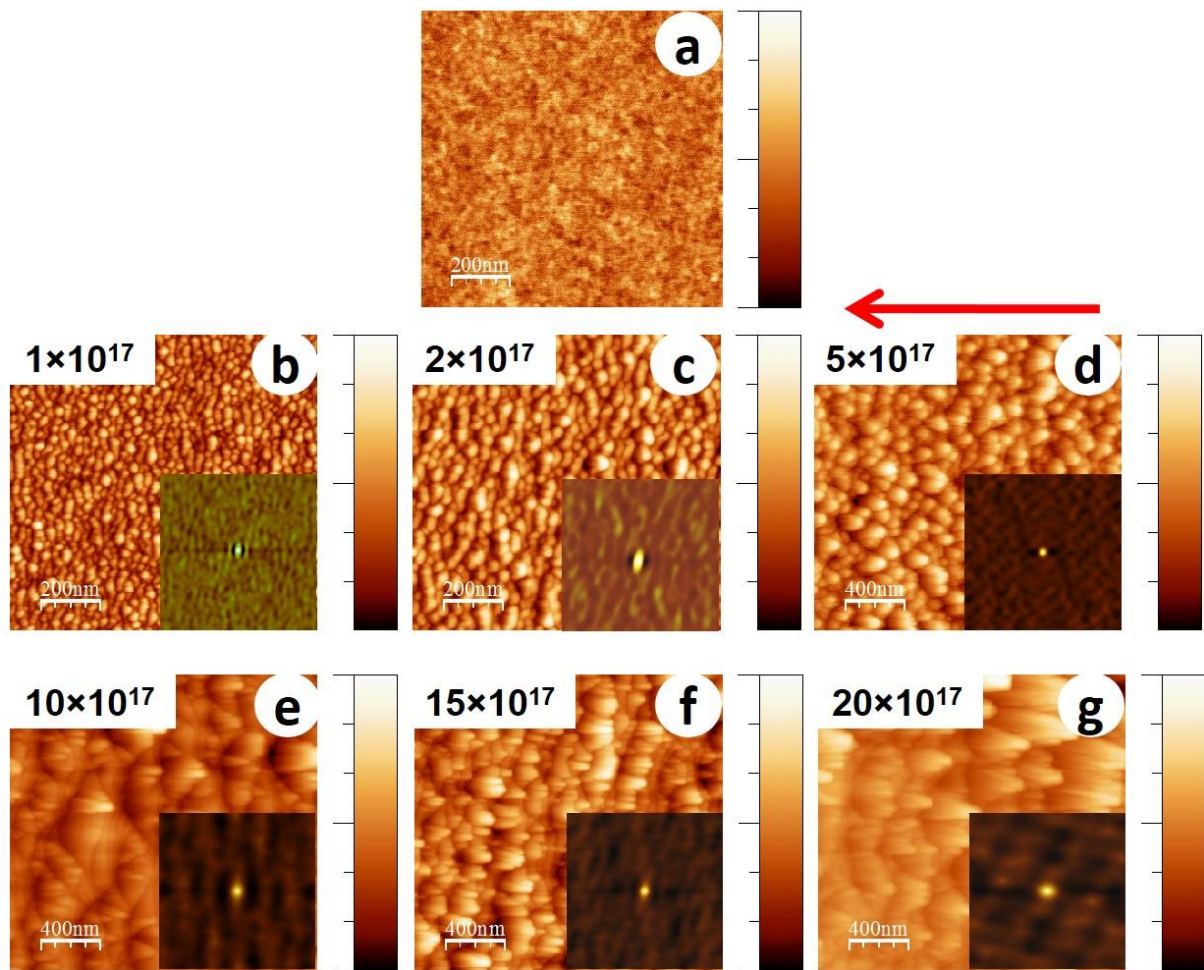


Figure 4.10: AFM images of (a) pristine-Si and those exposed to 500 eV Ar<sup>+</sup>-ions at an incidence angle of 70° to various fluences: (b) 1×10<sup>17</sup> ions cm<sup>-2</sup>, (c) 2×10<sup>17</sup> ions cm<sup>-2</sup>, (d) 5×10<sup>17</sup> ions cm<sup>-2</sup>, (e) 10×10<sup>17</sup> ions cm<sup>-2</sup>, (f) 15×10<sup>17</sup> ions cm<sup>-2</sup>, and (g) 20×10<sup>17</sup> ions cm<sup>-2</sup>, respectively. The corresponding height scales for (a)-(g) are: 1 nm, 4.3 nm, 9.9 nm, 39.5nm, 60.9 nm, 85.7 nm, and 182.2 nm. For better clarity (a)-(c) represent images acquired over a scan area of 1μm×1μm whereas (d)-(g) are of scan area 2μm×2μm. Insets show the 2D autocorrelation functions for corresponding images.

Figs. 4.10(d)-(g) depict AFM images where mound formation becomes predominant (at the fluence of 5×10<sup>17</sup> ions cm<sup>-2</sup>) which transform into faceted structures corresponding to the fluence of 10×10<sup>17</sup> ions cm<sup>-2</sup> and grow further at even higher fluences.

Figures 4.11(a)-(f) show AFM topographic images corresponding to incidence angle of 72.5° where presence of ripple morphology is clear up to a fluence of 1×10<sup>17</sup> ions cm<sup>-2</sup>. Beyond this fluence, ripples disappear and small mounds as well as faceted structures evolve (which grow further with increasing fluence) which is evident from Figs. 4.11(b)-(f).

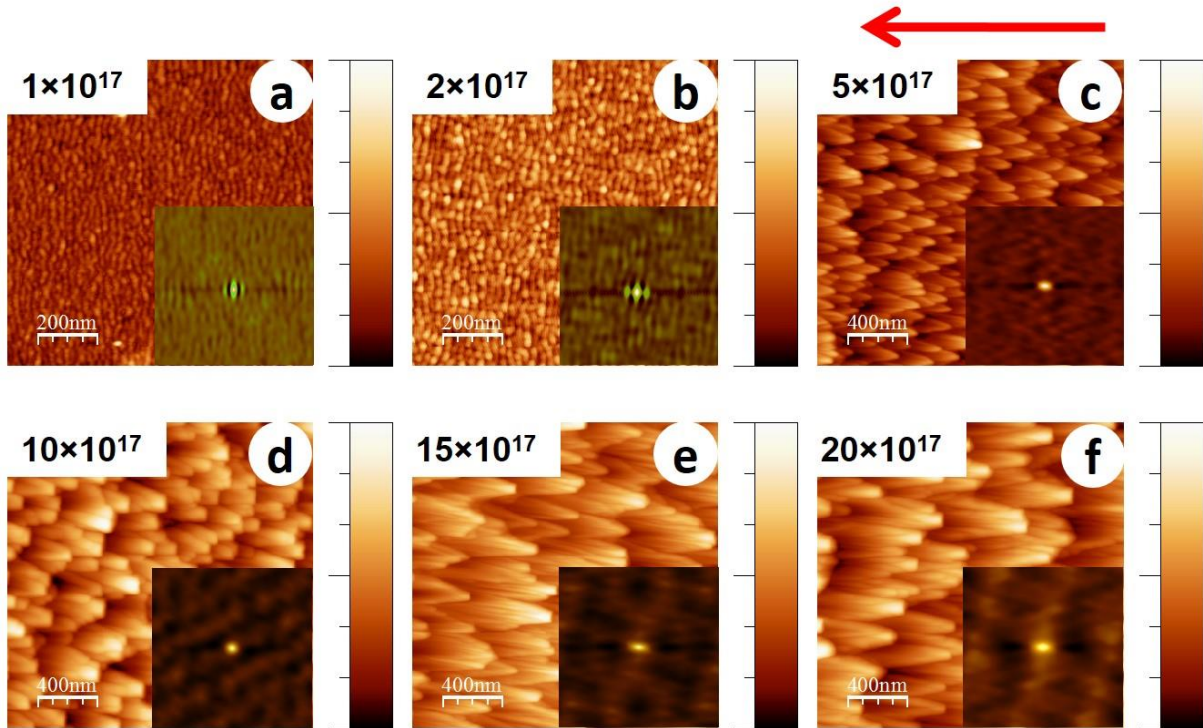


Figure 4.11: AFM images of silicon exposed to 500 eV  $\text{Ar}^+$ -ions at  $72.5^\circ$  incidence angle at fluences of (a)  $1 \times 10^{17}$  ions  $\text{cm}^{-2}$ , (b)  $2 \times 10^{17}$  ions  $\text{cm}^{-2}$ , (c)  $5 \times 10^{17}$  ions  $\text{cm}^{-2}$ , (d)  $1 \times 10^{18}$  ions  $\text{cm}^{-2}$ , (e)  $1.5 \times 10^{18}$  ions  $\text{cm}^{-2}$ , and (f)  $2 \times 10^{18}$  ions  $\text{cm}^{-2}$ , respectively. The corresponding height scales for (a)-(f) are: 4 nm, 4 nm, 74 nm, 86 nm, 154nm, and 165 nm. For better clarity (a) & (b) have scan size of  $1 \mu\text{m} \times 1 \mu\text{m}$  whereas (c)-(f) have scan size of  $2 \mu\text{m} \times 2 \mu\text{m}$ . Insets show the 2D autocorrelation functions for corresponding images.

The insets of all the images shown in Figs. 4.10 and 4.11 represent corresponding 2D autocorrelation functions. In Fig. 4.10, ripple anisotropy is clearly observed at the fluence of  $1 \times 10^{17}$  ions  $\text{cm}^{-2}$  whereas the same in Fig. 4.11 is clear up to the fluence of  $2 \times 10^{17}$  ions  $\text{cm}^{-2}$ . The average values (calculated from the AFM images shown in Figs. 4.10 and 4.11) of ripple wavelength, feature height, and base-width of mounds/facets are listed in Table 4.2 for different fluence values. An increasing trend in height and base-width of mounds/facets is observed for both angles of incidence with increasing Ar-ion fluence albeit the effect is more prominent at  $72.5^\circ$ . The aspect ratio of the feature is one of the crucial parameters in understanding the variation of the feature size as a function of ion fluence. In the present thesis, the variation of average structure height has been depicted as a function of ion fluence. We have calculated the

aspect ratio of faceted structures formed at  $70^\circ$  and  $72.5^\circ$  incidence angles. Table-4.2 depicts the aspect ratio of facets at different fluences corresponding to the above two incident angle

**Table 4.2**

Calculated values of ripple wavelength ( $\lambda$ ), average feature height ( $h$ ), and average base-width of the faceted structures formed under 500 eV Ar<sup>+</sup>-ions bombardment at different fluences at different angles of incidence.

Angle of incidence	Fluence (ions cm <sup>-2</sup> )	$\lambda$ (nm)	Average feature height (nm)	Average base-width (nm)	Aspect ratio
70°	1×10 <sup>17</sup>	34	2	--	--
	2×10 <sup>17</sup>	57	5	--	--
	5×10 <sup>17</sup>	--	16	131	0.122
	1×10 <sup>18</sup>	--	22	152	0.145
	1.5×10 <sup>18</sup>	--	30	199	0.151
	2×10 <sup>18</sup>	--	56	357	0.157
72.5°	1×10 <sup>17</sup>	26	1	--	--
	2×10 <sup>17</sup>	27	2	--	--
	5×10 <sup>17</sup>	--	28	237	0.118
	1×10 <sup>18</sup>	--	50	363	0.137
	1.5×10 <sup>18</sup>	--	78	486	0.166
	2×10 <sup>18</sup>	--	90	525	0.171

To explain the transition from a rippled surface to faceted structures we invoke the shadowing condition stated in Eq. 3.56. Let us first consider the case of  $70^\circ$  and the fluence of  $1 \times 10^{17}$  ions cm<sup>-2</sup> where the calculated value of  $2\pi h_0/\lambda$  turns out to be 0.369 whereas  $\tan(\pi/2 - \theta)$  is 0.364. Thus,  $2\pi h_0/\lambda$  is slightly above the limiting condition which indicates shadowing effect to start playing a role at this fluence itself. In the case of  $2 \times 10^{17}$  ions cm<sup>-2</sup>, the shadowing effect becomes more prominent since  $2\pi h_0/\lambda$  turns out to be 0.551. As a result, crests of the ripples should undergo more erosion compared to troughs and hence there is a likelihood of

mounds/facets to evolve. This explains the observation of mounds at this fluence. Similar behaviour is observed in case of  $72.5^\circ$ . For instance, in the case of  $1 \times 10^{17}$  ions  $\text{cm}^{-2}$ ,  $2\pi h_0/\lambda$  equals to 0.242 while  $\tan(\pi/2 - \theta)$  turns out to be 0.315. Thus, the condition for no shadowing, i.e.  $\tan(\pi/2 - \theta) \geq 2\pi h_0/\lambda$  gets satisfied here and ripples are expected to be seen. The observation of sinusoidal ripples in Fig. 4.10(a) supports this theoretical prediction. On the other hand, shadowing sets in at the fluence of  $2 \times 10^{17}$  ions  $\text{cm}^{-2}$  since in this case  $\tan(\pi/2 - \theta)$  becomes smaller than  $2\pi h_0/\lambda$  ( $=0.465$ ). This leads to formation of small mound-like entities (in the form of broken ripples) appearing on the corrugated surface.

For further investigation on the role of shadowing effect in morphological evolution we extracted line profiles of the observed structures along the direction of incident ion-beam onto the surface as shown by the arrow marks on the respective AFM images. Line profiles obtained from Figs. 4.10(b) & (c) and Figs. 4.11(a) & (b) are shown in Figs. 4.12 and 4.13, respectively. It is observed from Figs. 4.12(b) and 4.13(b) that at the beginning of shadowing transition the line profiles are still sinusoidal in nature. As discussed above, beyond shadowing transition one would expect signature of saw-tooth like waveform. The fact that for both incidence angles saw-tooth like waveform is not yet formed may be attributed to early stage of shadowing where  $h_0/\lambda$  ratios are very close to the limiting values or little above. To check this, line profiles obtained from Figs. 4.10(d) & 4.11(c) (corresponding to a higher fluence of  $5 \times 10^{17}$  ions  $\text{cm}^{-2}$ ) are shown in Figs. 4.12(c) & 4.13(c) which clearly show a transition to saw-tooth like waveform. This is due to the fact that  $h_0/\lambda$  ratios (in both cases) are well beyond the respective shadowing limits (0.767 and 0.741, respectively). Thus, we can infer that the effect of ion-beam shadowing plays a dominant role in the transition from rippled surfaces to faceted structures and is expectedly more prominent for the higher incidence angle as is evident from the above discussion. We now go on to explain the coarsening behaviour of faceted structures (as is evident from Table 1) at higher fluences ( $>5 \times 10^{17}$  ions  $\text{cm}^{-2}$ ) by using the mechanism

proposed by Hauffe [32]. In this framework, the intensity of reflected ions impinging on an arbitrary area on a facet depends on the dimensions of the reflecting adjoining facets. According to  $V_n \sim jY$  where  $j$  is the ion density on the surface element (which also contains the reflected ions),  $Y$  is the sputtering yield, and  $V_n$  is the displacement velocity of a surface element in the direction of its normal, it is clear that the displacement velocity will be higher for the larger facet.

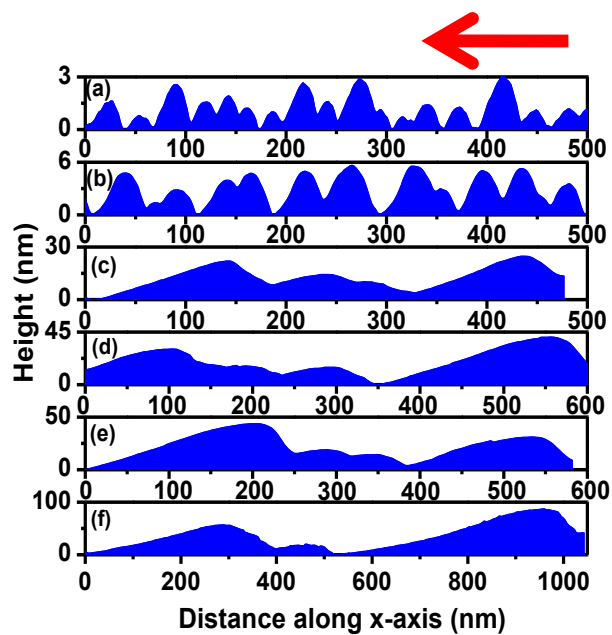


Figure 4.12: Line profiles extracted from the AFM images of ion exposed samples at  $70^\circ$  for various fluences: (a)  $1 \times 10^{17}$ , (b)  $2 \times 10^{17}$ , (c)  $5 \times 10^{17}$ , (d)  $10 \times 10^{17}$ , (e)  $15 \times 10^{17}$ , and (f)  $20 \times 10^{17}$  ions  $\text{cm}^{-2}$ , respectively. Arrow indicates the direction of ion-beam onto the surface.

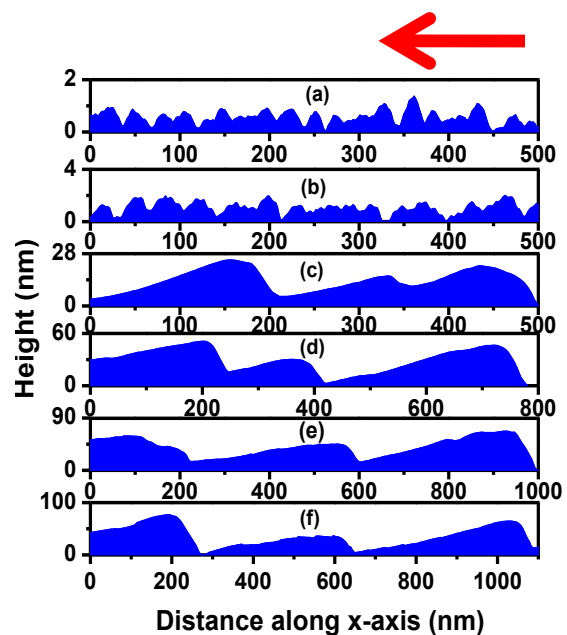


Figure 4.13: Line profiles extracted from the AFM images of ion exposed samples at  $72.5^\circ$  for different ion fluences: (a)  $1 \times 10^{17}$ , (b)  $2 \times 10^{17}$ , (c)  $5 \times 10^{17}$ , (d)  $10 \times 10^{17}$ , (e)  $15 \times 10^{17}$ , and (f)  $20 \times 10^{17}$  ions  $\text{cm}^{-2}$ , respectively. Arrow indicates the direction of ion-beam onto the surface.

This does not require a particular form of spatial distribution of reflected ions albeit it is necessary that the reflected ions should fall on the neighbouring facets. Accordingly, a smaller facet will disappear into the next bigger one and form an even bigger facet. This corroborates well with the cross-sectional line profiles corresponding to faceted structures shown in Figs.

4.12(d)-(f) and Figs. 4.13(d)-(f) which reveal clear enhancements in lateral dimension and height of the faceted structures with increasing ion fluence.

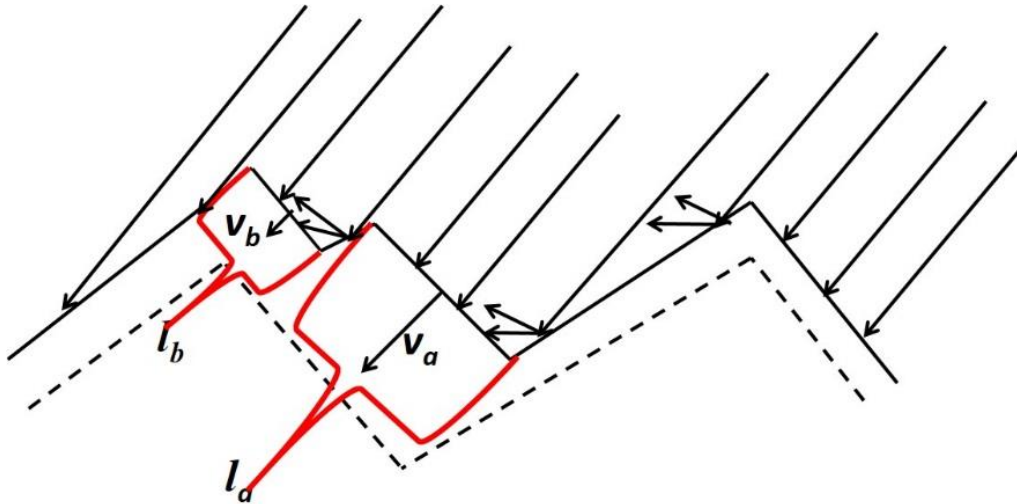


Figure 4.14: Schematic diagram depicting the mechanism responsible for coarsening of faceted structures at  $72.5^\circ$  (as a representative one). Arrows indicate the incident ion-beam.

Formation of faceted structures and their coarsening behaviour discussed above are beyond the scope of linear stability analysis of BH theory because of the presence of ion-beam shadowing and possible slope-dependent nonlinear effect. In the linear regime, based on Sigmund's theory of sputtering [47], BH theory takes into account a competition between curvature dependent sputtering and surface diffusion. Sputtering is treated as a surface roughening mechanism in this theory and hence, it is always useful to study the temporal evolution of surface roughness under ion-beam erosion to address pattern formation. Fig. 4.15 presents the roughness spectrum (i.e. variation in surface roughness with ripple wavelength/facet base-width) for both the angles under consideration. In both cases we observe an increase in roughness with increasing feature (ripple/facet) dimension. Under this frame work, we examine the role of sputtering by using Eq. 3.63 which is solved by assuming the dependence:  $Y(\theta)=Y(0) \sec\theta$  [48]. Although this form is known to be reasonable for not too large values of  $\theta$ , in our case this approximation simplifies the sputtering yield calculation and explains our results qualitatively.

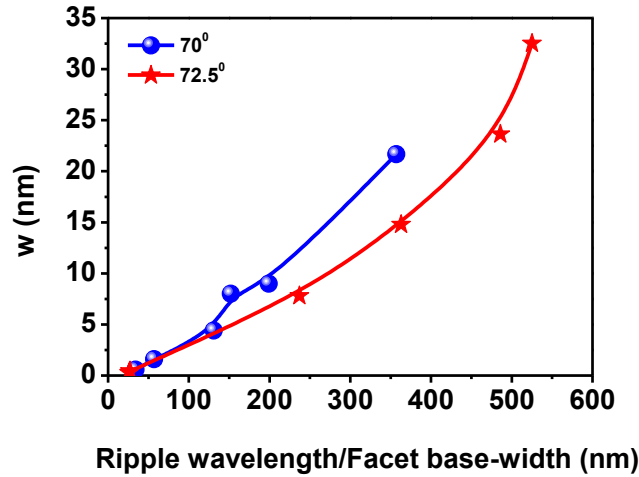


Figure 4.15: Variation in rms surface roughness, ' $w$ ' with lateral feature dimension corresponding to both angles of incidence.

The variation in fractional change of the sputter erosion rate,  $F$ , with ripple wavelength/facet base-width is shown in Fig. 4.16 for both the angles under consideration. It is observed from Fig. 4.16 that  $F$  follows nearly the similar trend as observed in the case of surface roughness (although a slight mismatch is observed in case of 70°). Therefore, results shown in Figs. 4.15 and 4.16 can be considered to be well correlated and confirm our claim that evolution of faceted structures at higher angles of incidence may also be driven by significant contribution from the sputter erosion induced roughening phenomenon.

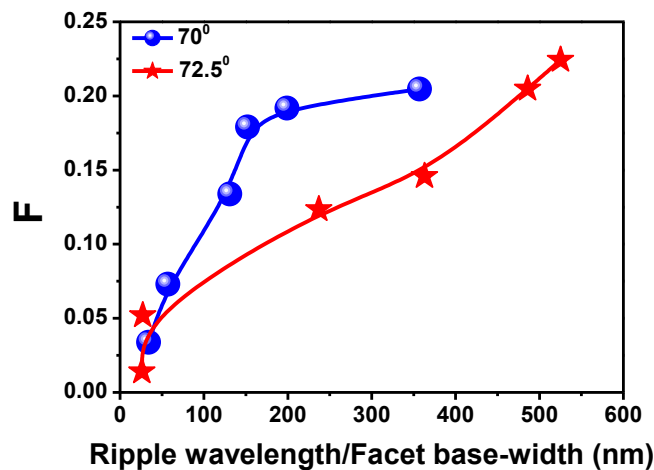


Figure 4.16: Variation in fractional change of the sputter erosion rate, ' $F$ ' with lateral feature dimension corresponding to both angles of incidence.

### 4.3.4 Evolution of morphology under substrate rotation

An example of the evolution of surface morphology (along with the pristine silicon) at different incidence angles under continuous substrate rotation is depicted in Fig. 4.17(a)-(f). Figure 4.17(a) shows presence of smooth surface (rms roughness=0.1 nm) in case of ion exposed silicon substrate at  $40^\circ$  at a fixed fluence of  $5 \times 10^{17}$  ions  $\text{cm}^{-2}$  under continuous azimuthal rotation (rotational speed  $0.5^\circ \text{ s}^{-1}$ ). Figs. 4.17(b-d) show nanoscale mound formation at three different oblique angles of incidence, namely  $60^\circ$ ,  $67^\circ$ , and  $70^\circ$ , respectively. It may be mentioned that our previous experiments show presence of ripples and mounds at these particular angles without any substrate rotation [15].

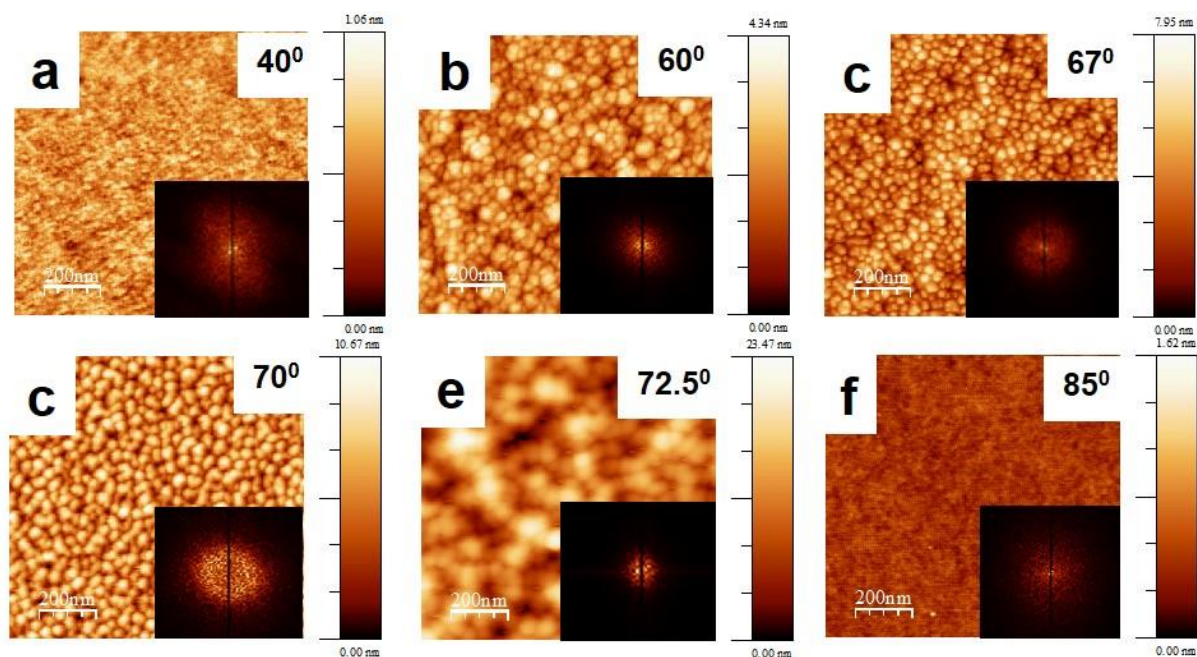


Figure 4.17: AFM images of (a) Pristine-Si and exposed Si to 500 eV argon ions at a fluence of  $5 \times 10^{17}$  ions  $\text{cm}^{-2}$  at different angles under continuous substrate rotation in the angular range of  $40^\circ$ - $85^\circ$ . Corresponding height scales in (a-f) are 1 nm, 1 nm, 4 nm, 8 nm, 10 nm, and 2 nm, respectively. Insets show 2D FFT obtained from the corresponding images. (g) Shows angular dependence of surface roughness for both static and rotating samples. The reduction in surface roughness is very clear in case of rotating samples.

Figure 4.17(e) reveals the presence of bigger mounds (diameter~80 nm) at 72.5° incidence angle whereas smooth surface in Fig. 4.17(f) is observed due to ion bombardment at 85° incidence angle with substrate rotation. Thus, in comparison to our earlier results [15], it is observed that flat surface remains flat whereas ripple patterns get transformed into mounds- by losing their spatial anisotropy [as confirmed from the inset of Figs. 4.17(a)-(e) where the respective 2D FFT shows the absence of any satellite peak]. As seen in earlier cases, ripple formation can be avoided using a rotating substrate albeit our results end up in mound formation instead of a smooth surface. Corresponding rms roughness evolution plots are shown in the Fig. 4.18 as a function of incidence angle of the ion-beam with and without substrate rotation. It is clear from this image that there is a significant reduction in the roughness values using the concurrent substrate rotation. The maximum decrease occurred in case of 72.5° where  $w$  goes down below 2 nm from 5.7 nm under substrate rotation.

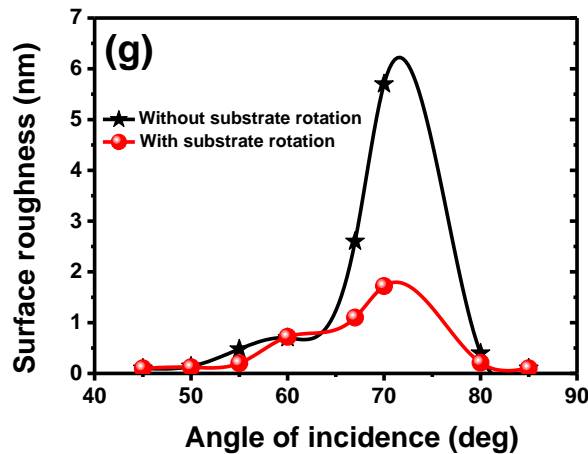


Figure 4.18: Roughness evolution plot as a function of ion incidence angle (shown later). Solid lines are guide to the eyes.

The mound size is observed to increase with angle of incidence (e.g. in case of 60°, 67°, and 70° mound dimensions are 28, 32, and 38 nm, respectively). At a much higher oblique angle of incidence, effect of substrate rotation again becomes trivial which is evident from Fig.

4.17(f) where a flat surface emerges at  $80^\circ$  incidence angle. Thus, following the roughness evolution plot, one can infer that under concurrent substrate rotation, with increasing angle of incidence, silicon surface evolves from flat surface to intermediate mounded surface (rougher surface) to flat surface.

In Fig. 4.19, we compile our observations into a phase diagram of patterns formed (or lacked thereof) versus control parameter like angle of incidence under two experimental conditions, viz. with and without concurrent substrate rotation. To the best of our knowledge, this would be the first study of this kind which addresses temporal evolution of silicon surface under both static and rotating substrate condition. From this phase diagram, it is clear that the surface remains stable up to  $\theta = 51^\circ$  whereas parallel-mode ripples undergo a transition to mounds under substrate rotation. At high  $\theta (=80^\circ)$ , again stable surface merges.

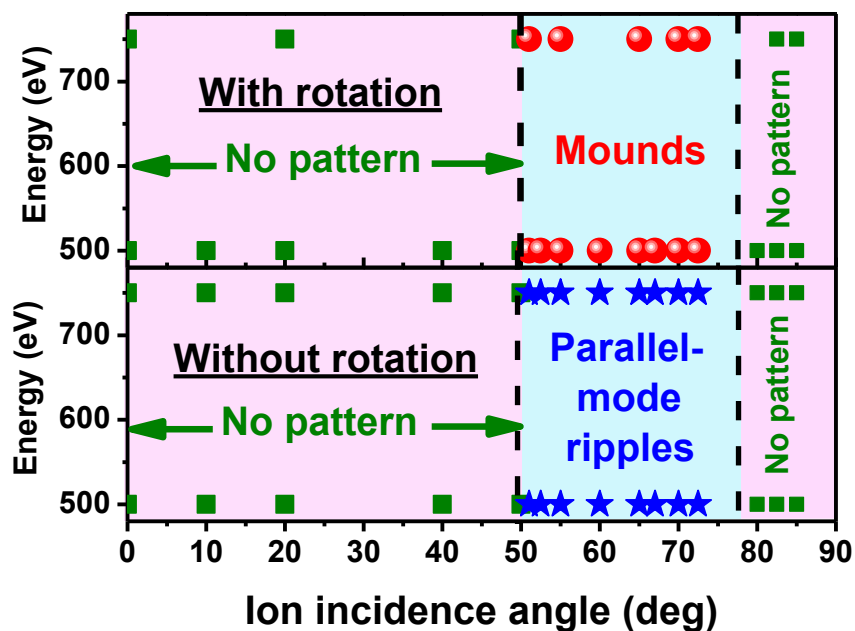


Figure 4.19: Phase diagram for different patterns versus control parameters like ion incidence angle ( $\theta$ ) and ion-beam energy ( $E$ ). Both phase diagram are in the linear regime corresponding to the respective angle of incidence.

To understand the observations mentioned above, we first consider the situation without any substrate rotation. Let the unperturbed steady-state solution be  $h=h_0-v_0t$ , where  $h_0$  and  $v_0>0$  are constants. For a surface that is not flat,  $h=h_0-v_0t+u$ , where  $u=u(x,y,t)$  and including only the lowest order nonlinearities, the equation of motion becomes

$$u_t = v_0 u_x + A_1 u_{xx} + A_2 u_{yy} - B \nabla^2 \nabla^2 u + \frac{1}{2} \lambda_1 u_x^2 + \frac{1}{2} \lambda_2 u_y^2, \quad (3.64)$$

where the subscripts denote the partial derivatives like  $u_t = \partial u / \partial t$  etc.

We know from BH theory:

1. For  $A_1, A_2 > 0$ , the surface remains flat,
2. For  $A_1 < 0$  and  $A_1 < A_2$ , parallel-mode ripples develop, and
3. For  $A_2 < 0$  and  $A_2 < A_1$ , perpendicular-mode ripples emerge.

Now, under concurrent substrate rotation, if the angular speed is sufficiently large, the equation of motion becomes [41]:

$$u_t = A \nabla^2 u - B \nabla^2 \nabla^2 u + \frac{1}{2} \lambda (\nabla u)^2 \quad (3.65)$$

$$\text{where } A = \frac{1}{2} (A_1 + A_2) \text{ and } \lambda = \frac{1}{2} (\lambda_1 + \lambda_2)$$

If  $A > 0$ , the surface remains flat. If  $A < 0$ , on the other hand, Eq. 3.65 is the Kuramoto-Sivashinsky equation and the surface becomes unstable. At long times, the surface consists of an irregular array of mounds and it exhibits a spatio-temporal chaos. These theoretical predictions match well (qualitatively) with our experimental results shown in Fig. 4.16 where the presence of irregular mounds are observed within the angular range of  $51^\circ$ - $72.5^\circ$ . The plot shown in Fig. 4.16(g) does not clearly identify the linear and nonlinear regimes. Thus, it would be difficult to draw any conclusion out of this plot. However, this problem can be overcome by performing the experiments in the linear regime. According to Bradley's theory, at early

times when the system evolves in the linear regime, the nonlinear terms in Eqs. (1) and (2) can be neglected and the rms roughness should be

$$\sigma_{nr} \geq \sigma_r \quad (3.66)$$

where,  $\sigma_{nr}$  and  $\sigma_r$  are roughness values for both without and with substrate rotation.

Physically, this means that the amplitude of the mounds formed with sample rotation grows more slowly than the amplitude of the ripples formed without sample rotation.

To verify the prediction mentioned in Eq. (3.66), we performed similar angle-dependent experiments by selecting a proper timescale where the pattern formation can be described by taking into account linear approximation only (the nonlinear term in Eq. 3.65 can be ignored).

To find out the timescale, we took help of the solid flow model and calculated the upper limit of intrinsic time scale of pattern evolution. In this process, we observed that 5 min would be a safe time scale to remain in the linear regime for the angular window of  $55^\circ$ - $67^\circ$  whereas 2 min should be the appropriate one for the angular window of  $70^\circ$ - $72.5^\circ$ . Thus, we carried out experiments within the angular range of  $55^\circ$ - $67^\circ$  with and without substrate rotation. It may be mentioned that particularly for this case, we chose the rotational speed to be  $6^\circ/s$  or  $0.104 \text{ rad/s}$  so that we can safely use the linear extension of Eq. 3.65. From Fig. 4.20, it is obvious that rms roughness decreases as we switch on the substrate rotation. The above mentioned experiments clearly demonstrate the validity of prediction mentioned in Eq. 3.66.

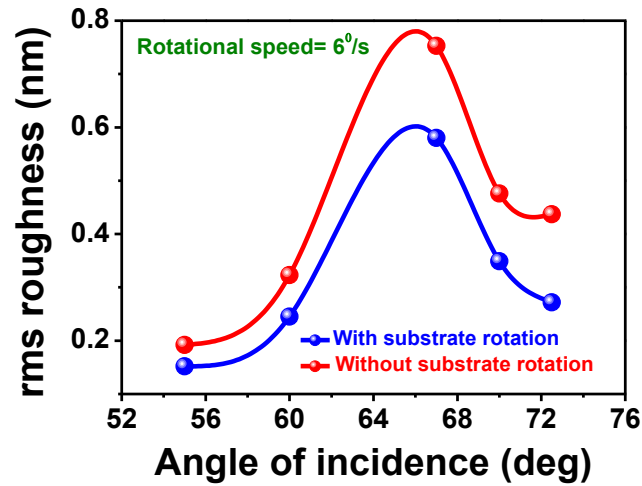


Figure 4.20: Roughness evolution plot in linear regime as a function of ion incidence angle.

#### Temporal evolution of mounds:

Temporal evolution of the mounds under continuous substrate rotation is summarized in Figs. 4.21(a-d) at  $67^\circ$  incidence angle. Fig. 4.21(a) shows the morphology corresponding to an exposure time of 11 min where smaller dimensional mounds are visible. With increasing the sputtering time up to 110min, mounds grow in dimension.

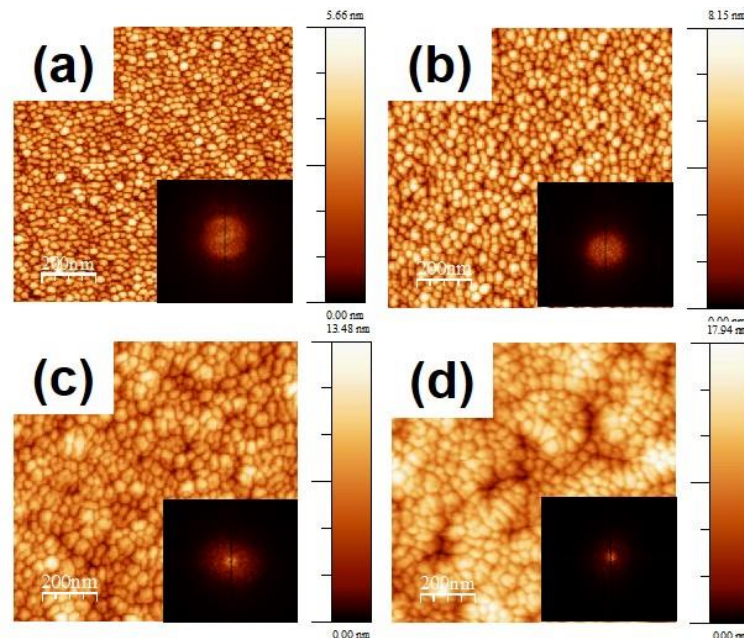


Figure 4.21: AFM images showing temporal evolution of mounds corresponding to different times (fluences) namely (a) 11 min, (b) 22 min, (c) 54 min, and (d) 108 min at an incidence angle of  $67^\circ$ . Corresponding height scales in (a-d) are 6 nm, 8 nm, 8 nm, and 13 nm, respectively. Insets show 2D FFT obtained from the corresponding images.

The inset of the respective images does not show any anisotropy from the 2D FFT (no satellite peak is observed). This behaviour can be well realized from Figs. 4.22 (a) and (b) where one can see that the growth of mounds is proportional to the square root of the sputtering time. This is followed by an increase in rms roughness in a linear fashion as a function of sputtering time. It can be mentioned here that Frost *et al.* observed coarsening of mounds (followed by an increase in rms roughness) with increasing sputtering time in case rotating InP substrates under argon-ion bombardment [49]. This behaviour of mound coarsening is not consistent with the equations (e.g. KS equation or Eq. 3.65) that describe topographical evolution due to sputtering. Frost *et al.* attributed their results to the preferential sputtering of phosphorous which leads to indium enrichment and agglomeration at the surface. On the contrary, for a silicon surface the possibility of preferential sputtering is totally ruled out.

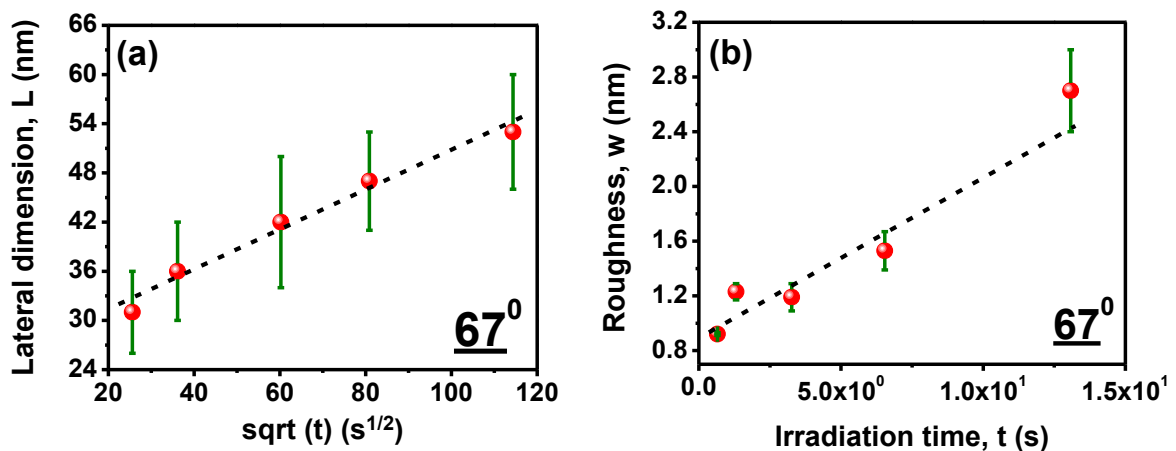


Figure 4.22: (a) Variation in the lateral dimension of mounds as a function of square root of the sputtering time. (b) rms roughness plot as a function of sputtering time at 67° angle of incidence. Dashed lines are for guide to the eyes.

Hence, to account for the results shown in Fig. 4.22, we must go beyond Eq. 3.65. In particular, the next-to-lowest order nonlinearity must be appended to Eq. 3.65. This nonlinearity is

discussed by García *et al.* [50]. According to them, the more refined equation of motion should be

$$u_t = A\nabla^2 u - B\nabla^2 \nabla^2 u + \frac{1}{2} \lambda (\nabla u)^2 - \frac{1}{2} \mu \nabla^2 (\nabla u)^2 \quad (3.72)$$

Simulation of this equation reveals that once the mounds form, they get coarsened for a certain amount of time but then stop growing. This is called “interrupted coarsening”. In the present experiments, we have observed the coarsening, but the arrest of coarsening is not. To observe this arrest, one should go to even higher fluences.

In order to do so, we chose 60° incidence angle and carried out similar temporal evolution study. The results are presented in Figs 4.23 (a) and (b).

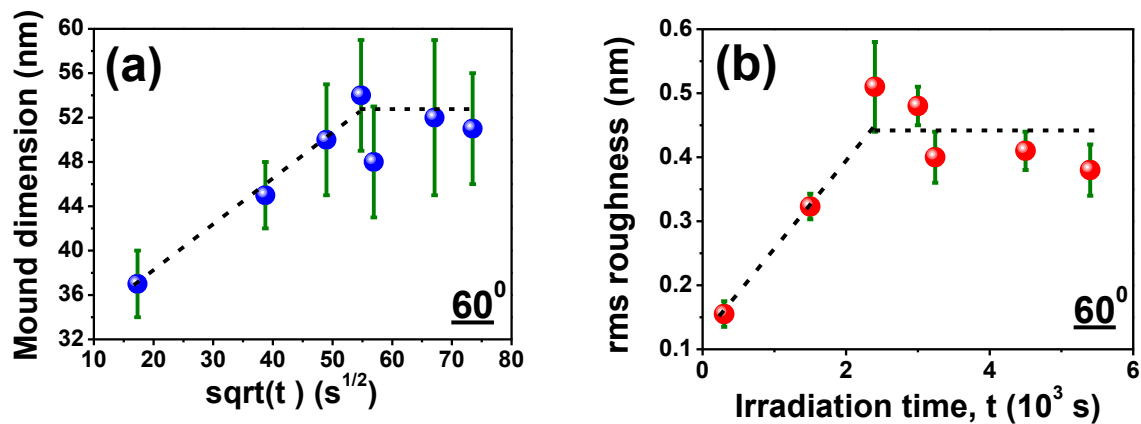


Figure 4.23: (a) Variation of the lateral dimension of the mounds as a function of square root of the sputtering time. (b) rms roughness plot as a function of sputtering time at 60° angle of incidence. Dashed lines are for guide to the eyes.

These two figures clearly show that the arrest of coarsening takes place faster in case of 60° angle of incidence and supports all the prediction by García *et al.* [50].

### Rotational speed variation

The effect of rotational speed variation on the formation of nanostructures has not been studied to a great extent [51] in case of sputtering process. Thus, to explore the consequence of rotational speed variation, we exposed silicon wafers to 500 eV argon ion-beam at an oblique incidence of 67° with rotational speed varying in the range of  $8 \times 10^{-2}$ – $44 \times 10^{-2}$  rad s<sup>-1</sup> at a

constant fluence of  $5 \times 10^7$  ions  $\text{cm}^{-2}$  (selective images are shown in Fig. 4.24). Corresponding roughness evolution plots as a function of rotational speed are shown in Fig. 4.25(a) while Figs. 4.25(b) and (c) depict the variation in the mound size and the mound amplitude as a function of rotational speed ( $\omega$ ), respectively. It is observed that with increasing  $\omega$ , roughness and mound height show an increasing trend up to a speed of  $35 \times 10^{-2}$   $\text{rad s}^{-1}$  whereas beyond this it gets saturated (within our present experimental domain). On the other hand, mound dimension remains constant as a function of substrate rotational speed [Fig. 4.25 (b)]. It can be mentioned that recently, Chowdhury *et al.* showed a non-monotonic increase in the rms roughness as function of  $\omega$  over a wide range of variation (0-25 rpm) [51].

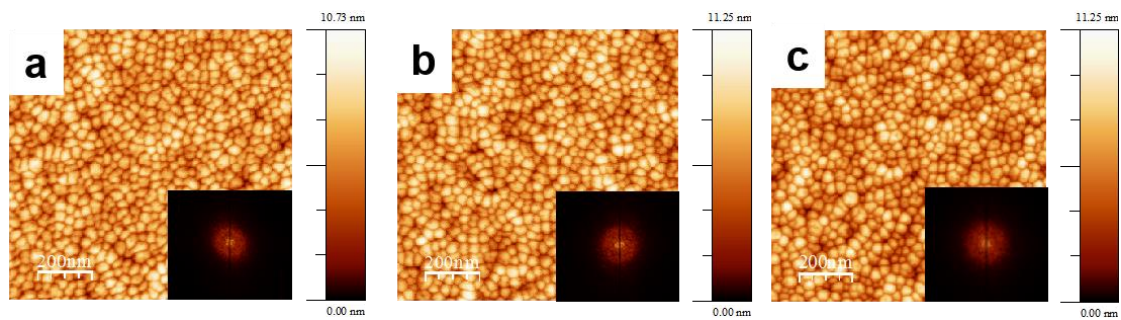


Figure 4.24: AFM images showing the effect of rotational speed variation corresponding to different angular speeds, namely (a) 17.4, (b) 26.2, and (c) 43.6  $\text{rad s}^{-1}$  at an incidence angle  $67^\circ$ . Corresponding height scale in (a-c) is 11 nm. Insets show 2D FFT obtained from the corresponding images.

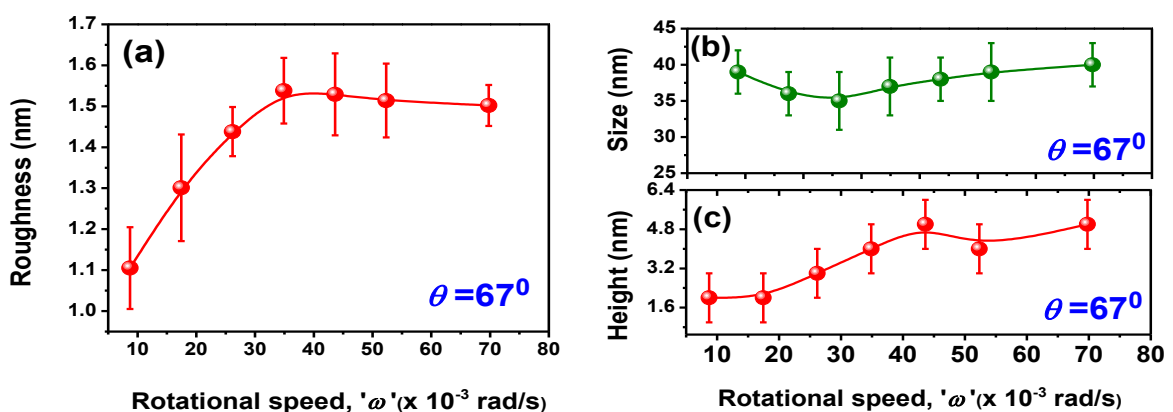


Figure 4.25: (a) rms roughness versus rotational speed variation plot for  $67^\circ$  and at a fixed fluence of  $5 \times 10^{17}$  ions  $\text{cm}^{-2}$  incidence angle. (b) and (c) show corresponding mound dimension and height versus rotational speed plots, respectively.

According to Yasserli et al., one should observe non-monotonic dependence of the rms roughness upon the rotational speed ( $\omega$ ) [52]. However, we restricted ourselves within the range of 0.083-1.33 rpm (due to the instrumental limit) and also observe a non-monotonic nature in roughness values.

## 4.4 Conclusions

In this chapter, experimental results were presented to understand low energy ion induced ripple formation in the framework of ion induced solid flow model over an angular range of ( $51^\circ$ - $72.5^\circ$ ). The present experimental results show the existence of an intrinsic timescale (where ripple evolution is in the linear regime) and beyond which the nonlinear effects dominate (e.g. ripple coarsening starts). It is observed that the experimentally determined intrinsic timescale for all angles matches quite closely with those predicted by the solid flow model and in general, it decays faster with increasing ion incidence angle. In addition, angle-dependent studies at higher fluences reveal that the transition from parallel-to perpendicular-mode ripples is not a sharp one but undergoes a series of unusual pattern formation (viz. mounds, facet/cone-like, and needle-like structures) at intermediate angles. We find that facet formation is a very special case where parallel-mode ripples are formed at lower fluences and subsequently undergo a transition to mounds/faceted structures. This transition from ripples to mounds and/or faceted structures is explained geometrically which takes into account the inter-peak shadowing effect. With increasing ion fluence, faceted nanostructures undergo coarsening, i.e. they grow bigger in both lateral dimension and height. The coarsening behaviour is explained by invoking Hauffe's mechanism which is based on reflection of primary ions on facets. In addition, the effect of concurrent substrate rotation during ion bombardment is also investigated. It is found that, in the linear regime, substrate rotation leads to a reduction in surface roughness compared to the static case, which was supported by the theoretical predictions. Angle-dependent study reveals that a flat surface remains flat whereas

ripples transform into mounds under concurrent substrate rotation. Our results qualitatively support a nonlinear theory proposed by Bradley on surface roughening under substrate rotation. Temporal evolution of mounds show arrest of the coarsening behaviour which has been explained by appending next-to-lowest order nonlinearity in the nonlinear equation proposed by García *et al.* [50].

## Bibliography

1. R. Gago, L. Vázquez, O. Plantevin, T.H. Metzger, J.M. García, R. Cuerno, M. Castro, *Appl. Phys. Lett.* 89 (2006) 233101
2. H. Hansen, A. Redinger, S. Messlinger, G. Stoian, J. Krug, T. Michely, *Phys. Rev. Lett.* 102 (2009) 146103
3. R. Gago, L. Vázquez, O. Plantevin, T.H. Metzger, J.M. García, R. Cuerno, M. Castro, *Appl. Phys. Lett.* 89 (2006) 233101.
4. S. Facsko, T. Dekorsy, C. Koerdt, C. Trappe, H. Kurz, A. Vogt, H.L. Hartnagel, *Science* 285 (1999) 1551
5. B. Ziberi, M. Cornejo, F. Frost, B. Rauschenbach, *J. Phys.: Cond. Mat.* 21 (2009) 224003.
6. A. Keller, S. Roßbach, S. Facsko, W. Möller, *Nanotechnology* 19 (2008) 135303.
7. P.F.A. Alkemade, *Phys. Rev. Lett.* 96 (2006) 107602.
8. R.L. Headrick, H. Zhou, *J. Phys.: Cond. Mat.* 21 (2009) 224005.
9. J. Fassbender, T. Strache, M.O. Liedke, D. Markó, S. Wintz, K. Lenz, A. Keller, S. Facsko, I. Mönch, J. McCord, *N. J. Phys.* 11 (2009) 125002.
10. M. O. Liedke, M. Körner, K. Lenz, F. Grossmann, S. Facsko, J. Fassbender, *Appl. Phys. Lett.* 100 (2012) 242205; M. Körner, K. Lenz, R. A. Gallardo, M. Fritzsche, A.

- Mücklich, S. Facsko, J. Lindner, P. Landeros, J. Fassbender, *Phys. Rev. B* 88 (2013) 054405.
11. M. Ranjan, T.W.H. Oates, S. Facsko, W. Möller, *Opt. Lett.* 35 (2010) 2576.
  12. C. Martella, D. Chiappe, P. D. Veneri, L. V. Mercaldo, I. Usatii, F. B. de Mongeot, *Nanotechnology* 24 (2013) 225201.
  13. R. M. Bradely, J. M. E. Harper, *J. Vac. Sci. Technol. A* 6 (1988) 2390.
  14. G. Carter, V. Vishnyakov, *Phys. Rev. B* 54 (1996) 17647.
  15. T. Basu, J. R. Mohanty, T. Som, *Appl. Surf. Sci.* 258 (2012) 9944.
  16. C. S. Madi, E. Anzenberg, K. F. Ludwig, Jr., M. J. Aziz, *Phys. Rev. Lett.* 106 (2011).
  17. A. Keller, S. Facsko, W. Möller, *Nanotechnology* 21 (2009) 495305.
  18. C. S. Madi, B. Davidovitch, H. B. George, S. A. Norris, M. P. Brenner, and M. J. Aziz, *Phys. Rev. Lett.* 101 (2008) 246102.
  19. M. Castro, R. Gago, L. Vázquez, J. Muñoz-García, R. Cuerno, *Phys. Rev. B* 86 (2012) 214107.
  20. R. Cuerno, M. Castro, J. Muñoz-García, R. Gago, L. Vázquez, *Nucl. Instrum. Meth. B* 269 (2011) 894.
  21. S. A. Norris, J. Samela, L. Bukonte, M. Backman, F. Djurabekova, K. Nordlund, C. S. Madi, M. P. Brenner, M. J. Aziz, *Nat. Commun.* 2:276 (2011) 1.
  22. C. S. Madi, M. J. Aziz, *Appl. Surf. Sci.* 258 (2012) 4112.
  23. N. Kalyanasundaram, M. C. Moore, J. B. Freund, H. T. Johnson, *Acta Mater.* 54 (2006) 483.
  24. M. Castro, R. Cuerno, *Appl. Surf. Sci.* 258 (2012) 4171.
  25. B. Abendroth, H. Jäger, W. Möller, M. Bilek, *Appl. Phys. Lett.* 90 (2007) 181910.
  26. C. A. Davis, *Thin Solid Films* 226 (1993) 30.

27. C.S. Madi, B. Davidovitch, H.B. George, S.A. Norris, M.P. Brenner, M.J. Aziz, Phys. Rev. Lett. 101 (2008) 246102; C.S. Madi, E. Anzenberg, K.F. Ludwig Jr., M.J. Aziz Phys. Rev. Lett. 106 (2011) 066101
28. B. Ziberi, F. Frost, B. Rauschenbach, J. Vac. Sci. Technol. A 24 (2006) 1344.
29. A. Keller, S. Roßbach, S. Facsko, W. Möller, Nanotechnology 19 (2008)135303.
30. P.F.A. Alkemade, Z.X. Jiang, J. Vac. Sci. Technol. B 19 (2001) 1699.
31. G. Carter, J. Appl. Phy. 85 (1999) 455.
32. W. Hauffe, Physica Status Solidi (a) 35 (1976) K93.
33. T. W. H. Oates, M. Ranjan, S. Facsko, and H. Arwin, Opt. Exp. 19 (2011) 3.
34. M. O. Liedke, M. Körner, K. Lenz, F. Grossmann, S. Facsko, and J. Fassbender, Appl. Phys. Lett. 100 (2012) 242405.
35. A. Zalar, Thin Solid Films 124 (1985) 223.
36. E.-H. Cirlin, J. J. Vajo, R. E. Doty, and T. C. Hasenberg, J. Vac. Sci. Technol. A 9, 1395 (1991).
37. E.-H. Cirlin, J. J. Vajo, and T. C. Hasenberg, J. Vac. Sci. Technol. B 12 (1994) 269.
38. R. M. Bradley and E.-H. Cirlin, Appl. Phys. Lett. 68 (1996) 3722.
39. G. Carter, Vacuum 49 (1998) 285.
40. W. W. Mullins, J, Appl. Phys., 30 (1959) 77.
41. R. M. Bradley, Phys. Rev. E, 54 (1996) 6149.
42. G. Carter, V. Vishnyakov, Phys. Rev. B 54 (1996) 647.
43. W. Möller and W. Eckstein, Nucl. Instrum. Meth. B 2 (1984) 814.
44. <http://www.nanotec.es/products/wsxm/index.php>.
45. M. Castro, R. Cuerno, L. Vázquez, R. Gago, Phys. Rev. Lett. 94 (2005) 016102.
46. A. Oron, S. H. Davis, S. G. Bankoff, Rev. Mod. Phys. 69 (1997) 931

47. B. Ziberi, M. Cornejo, F. Frost, B. Rauschenbach, J. Phys.: Condens. Matter 21 (2009) 224003.
48. P. Sigmund, Phys. Rev. 184 (1969) 383.
49. F. Frost, A. Schindler, F. Bigl, Phys. Rev. Lett., 85 (2000) 4116.
50. J. M. García, R. Cuerno, and M. Castro, J. Phys. Condens, Matt. 21 (2009) 224020.
51. D. Chowdhury, D. Ghose, and B. Satpati, Mater. Sci. Eng. B 179 (2014) 1.
52. T. Yasserli and R. Kree, Nucl. Instrum. Meth. Phys. Res. B 268 (2010) 2496.

---

## CHAPTER 5

---

### **5. Tunable optoelectronic properties of nano-patterned-Si surfaces**

In this chapter, we have demonstrated the usage of nanopatterned-Si surfaces towards tuning antireflection (AR) and photoluminescence (PL) properties. In particular, nanofaceted-Si surfaces were used to study corresponding AR and PL properties. Furthermore, as a case study, Si nanofacets were employed to study field emission properties.

#### **5.1 Tailoring room temperature photoluminescence of antireflective Si nanofacets**

##### **5.1.1 Introduction**

Silicon nanostructures have drawn a lot of attention in recent years because of its unusual quantum confinement (QC) properties which yields unique structural, optical, and electronic behaviours [1], viz. single electron devices [2], sensors [3], and cold cathodes for field-emission displays [4]. In bulk silicon, direct inter-band transitions are not allowed by the momentum conservation law and to make this happen, phonon absorption is required [5]. An alternative way to overcome this difficulty is to modify the electron dispersion equations for valence and conduction bands by controlling the size of Si nanostructures [6]. Besides QC-mediated photoluminescence (PL), Si-O defect states (generally exist at the surface of Si nanoclusters or at the Si/SiO<sub>x</sub> interface) also take part in radiative emission, as reported earlier [7-9]. Although the origin of PL emission from silicon nanostructures is a much debatable topic, silicon based UV-emitting materials always draw special attention since optical data

storage devices often need light sources with shorter wavelengths, preferably in the UV range, for improving the storage density.

Over the last two decades, different types of Si-based nanocrystalline materials were prepared which exhibit PL comparable to porous silicon [10]. Although most of these studies are based on luminescence in the visible range, few studies exist where blue and UV light emission from Si nanostructures are addressed [11,12]. Despite much progress in the fabrication and luminescence property of Si nanostructures, one of the key challenges is to improve the emission efficiency which is largely dependent on the absorbed photons. Different approaches are followed to improve light extraction ratio (which in turn enhances the luminescence efficiency) by using photonic crystal structures, surface plasmon polariton etc. [13-15]. However, these processes are complex and involve multiple fabrication steps. On the other hand, an alternative way to enhance absorption of light and in turn achieve higher emission efficiency is to use textured/rough surfaces which are effective to reduce reflection loss, leading to an improved light extraction ratio [16,17]. In fact, for a planar surface, a large difference in the refractive index between Si and air causes enhanced Fresnel reflection of the incident light from air to the substrate. This makes a diminishing intensity of the incident light available for absorption, leading to a large optical loss. In contrast, this loss gets minimized for textured surfaces – inspired by biomimetic moth-eye structures – where the surface micro/nano-structures lead to a gradual change in the effective refractive index between air and the substrate [18]. Recently, successful attempts have been made to fabricate light emitting diodes based on nanostructured surfaces where light extraction efficiency is seen to be enhanced [19-21].

In this work, we emphasize on the importance of antireflection (AR) property of nanofaceted-Si surfaces, fabricated by low energy argon ions, to achieve tunable photoluminescence at room temperature (RT). Si surfaces having nanofacets of different

heights were prepared at various ion fluences and two different angles of incidence, viz.  $70^\circ$  and  $72.5^\circ$ . In both cases, the observed PL intensity from these nanostructures increases with ion fluence whereas an opposite trend is noticed for surface reflectance. Origin of such PL emission from the faceted-Si substrates is attributed to argon-ion activated  $E'$  centres and Si-O related states present at the interface of Si/SiO<sub>x</sub>. In particular, the observed PL peak at 368 nm has been correlated to the -SiO<sub>3</sub> group where the presence of different oxides at the surface has been confirmed by x-ray photoelectron spectroscopic (XPS) studies. Enhancement in the PL intensity has further been ascribed to the improved light absorption (i.e. reduction in surface reflectance) due to the presence of silicon nanofacets at the surface.

### 5.1.2 Experimental

Silicon samples, used in the present experiments, were sliced out ( $1 \times 1 \text{ cm}^2$ ) from a *p*-type Si(100) wafer. A UHV-compatible experimental chamber, equipped with an electron cyclotron resonance based broad beam ion source, was used to prepare nanofaceted structures on Si surfaces. The chamber base pressure was below  $5 \times 10^{-9}$  mbar and the working pressure was maintained at  $3 \times 10^{-4}$  mbar. Substrates were fixed on the sample platen of a 5-axes manipulator which was first covered by a sacrificial Si wafer (taken from the same lot of the substrate) to ensure a low impurity environment. Samples were exposed to 500 eV Ar-ions at two incidence angles, viz.  $\theta=70^\circ$  and  $72.5^\circ$  (with respect to the surface normal) at RT. The beam diameter was measured to be 3 cm which corresponds to a fixed ion flux of  $1.3 \times 10^{14}$  ions  $\text{cm}^{-2} \text{ s}^{-1}$  (corresponding to a target current of 160  $\mu\text{A}$ ) in a plane normal to the ion-beam direction. Experiments were carried out for fluences ranging from  $5 \times 10^{17}$  to  $2 \times 10^{18}$  ions  $\text{cm}^{-2}$ .

Following Ar-ion exposure, the samples were imaged by *ex-situ* atomic force microscopy. All the AFM images were analyzed by using the WSxM software [22]. In addition, microstructural study was performed by using high-resolution transmission electron

microscopy (HRTEM). The surface chemical property was studied by x-ray photoelectron spectroscopy (XPS) using Mg- $K_{\alpha}$  radiation source ( $h\nu = 1254$  eV). Optical reflectance studies were carried out by using a UV-Vis-NIR spectrophotometer at  $45^{\circ}$  incidence in the wavelength range of 300-800 nm. Room temperature PL measurements were performed at RT by steady state fluorescence spectrometer equipped with a 325 nm He-Cd laser.

### 5.1.3 Results and discussion

Figure 5.1(a) and (b) represents three-dimensional (3D) AFM topographic images obtained from samples after exposure to Ar-ions at  $\theta=70^{\circ}$  and  $72.5^{\circ}$  at the highest ion fluence of  $2 \times 10^{18}$  ions  $\text{cm}^{-2}$ . It is observed that nanofaceted structures (conical) evolve up to  $2 \times 10^{18}$  ions  $\text{cm}^{-2}$ . Similar morphological evolution takes place for lower fluences as well (images not shown). Formation of such faceted morphology is observed only over this limited angular window [23]. Figure 5.1(c) depicts the evolution of average facet heights as a function of ion fluence at  $\theta=70^{\circ}$  and  $72.5^{\circ}$  where an increasing trend is observed for both cases. Such nanofaceted structures evolve due to a transition from ripple (which are formed at fluences below  $5 \times 10^{17}$  ions  $\text{cm}^{-2}$ ).<sup>23</sup> As a matter of fact, with an increase in the ratio of ripple height ( $h_0$ ) to ripple wavelength ( $\lambda$ ), the local angle of incidence along the ripple pattern eventually become so large that the upstream part of the ripple gets shadowed from the incoming ion-flux by the preceding peak. Thus, the limiting condition to avoid such shadowing of incident beam is [24]:

$$\tan(\pi/2 - \theta) \geq 2\pi(h_0/\lambda)$$

where  $\theta$  is the angle of incidence. According to this condition, if the ratio ( $h_0/\lambda$ ) exceeds a threshold value, troughs of a sinusoid will not be eroded further but instead erosion will take place at the crest. This in turn can give rise to a faceted structure [23].

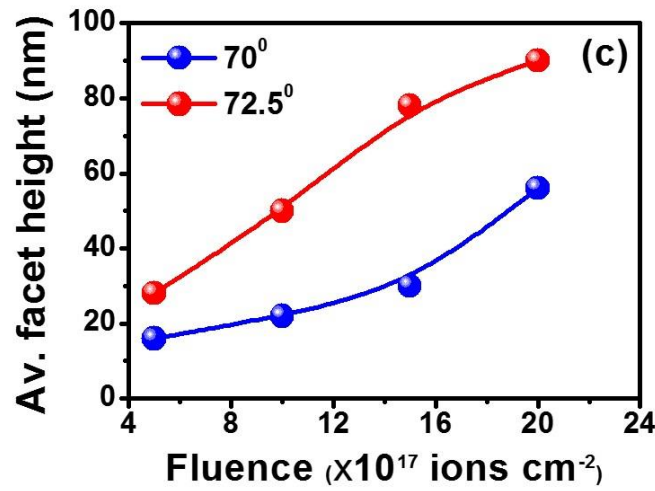
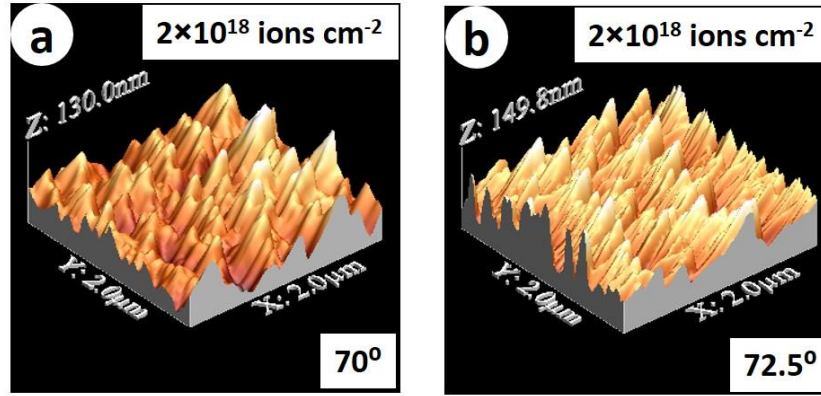


Figure 5.1: Three-dimensional AFM micrographs corresponding to samples exposed to ion fluence of  $2 \times 10^{18} \text{ cm}^{-2}$  at incidence angle of  $70^\circ$  (a) and  $72.5^\circ$  (b). Figure 1(c) depicts the evolution of average facet heights as a function of ion fluence at  $\theta = 70^\circ$  and  $72.5^\circ$ .

In the present case, beyond the fluence of  $2 \times 10^{17} \text{ ions cm}^{-2}$ , the condition of shadowing sets in and thus, it is expected to get faceted nanostructures as mentioned above. In addition, with increasing fluence, faceted nanostructures demonstrate coarsening behaviour. The observed facet coarsening is attributed to a mechanism based on reflection of primary ions from facets [23,25]. Recently, Engler *et al.* also reported formation of similar kind of faceted nanostructures on Si surface by using 2 keV Kr-ions at comparable fluences [26] and quantified the obtained faceted nanostructures in terms of facet height and slope distribution. It was demonstrated that with increasing ion fluence, the facet angle did not show any meaningful change. It may be mentioned that, we also observed the similar trend for facet angle as a

function of ion-fluence (the upstream facet angle becomes constant at  $9^\circ$  for both  $\theta = 70^\circ$  and  $72.5^\circ$ ) by using the SPIP software [27].

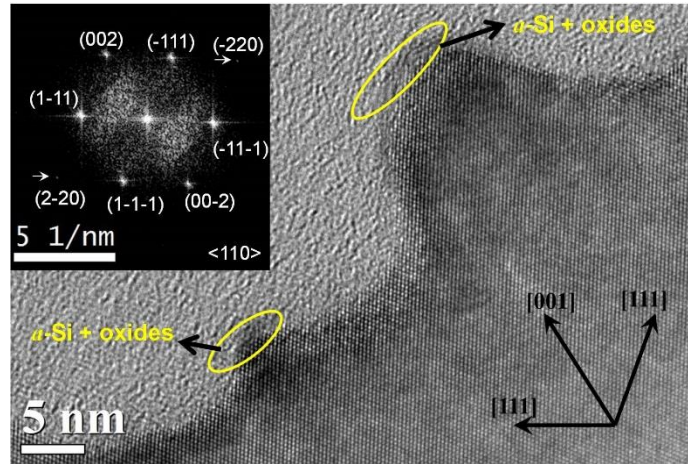


Figure 5.2: XTEM image showing silicon facets fabricated by using 500 eV Ar-ions to the fluence of  $5 \times 10^{17} \text{ cm}^{-2}$ . The black circles depict the zones where *a*-Si and native oxides are present. Inset shows the FFT of the same image which reveals presence of different crystallographic planes.

Microstructural investigations were also carried out by cross sectional transmission electron microscopy (XTEM). Figure 5.2 depicts a high-resolution XTEM image of such a faceted surface which shows the clear presence of lattice fringes, indicating the formation of crystalline facets. A careful observation reveals the presence of amorphous patches (marked by yellow loops) around the apex of the facets, albeit they are absent along both the sidewalls. This was confirmed by looking at a large number of frames. These patches may result from either ion induced amorphization of Si or the presence of native oxides.

In order to understand the fluence-dependent change in surface chemical properties, XPS studies were carried out for selective samples. Figures 5.3(a)-(c) show the Si *2p* spectra of pristine- and nanofaceted-Si samples exposed to the fluences of  $5 \times 10^{17}$  and  $2 \times 10^{18}$  ions  $\text{cm}^{-2}$  (for  $\theta = 72.5^\circ$ ).

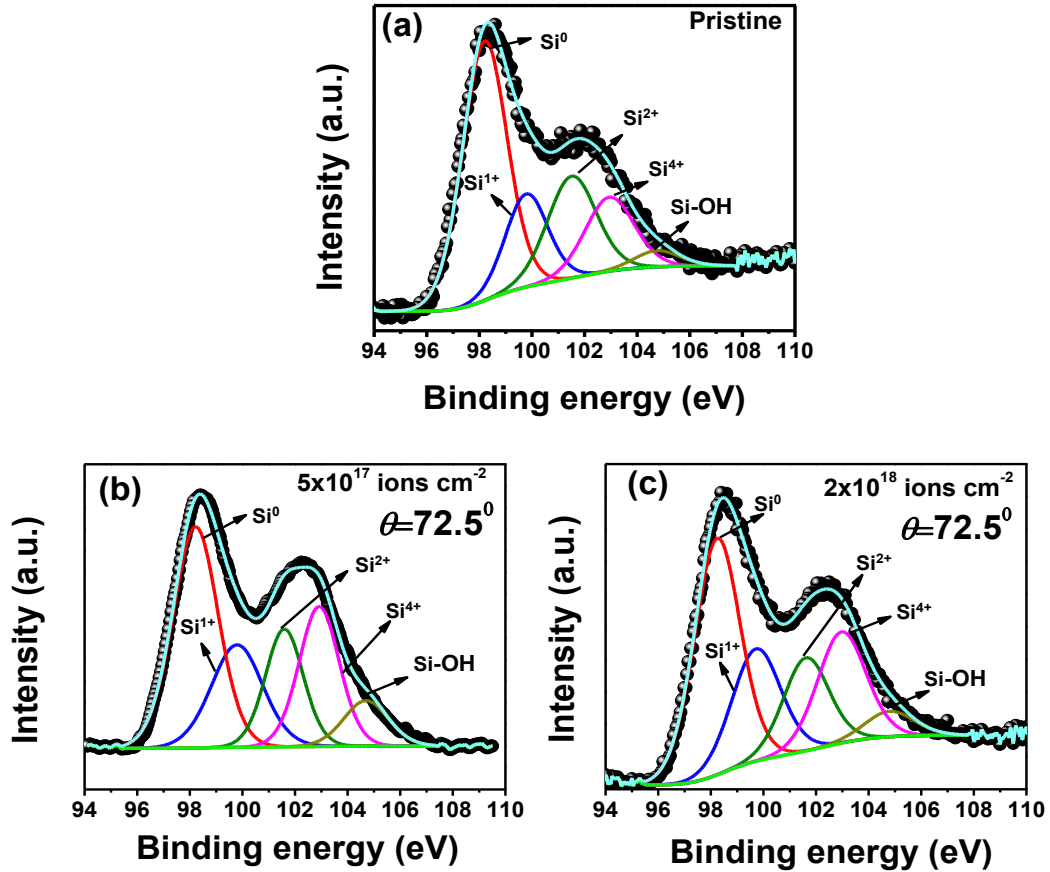


Figure 5.3:  $2p$  core level Si XPS spectra taken from (a) Pristine-Si and samples exposed to ion fluences of (b)  $5 \times 10^{17}$ , (c)  $2 \times 10^{18} \text{ cm}^{-2}$ , respectively.

The Si  $2p$  core level spectrum, corresponding to the pristine sample, shows the presence of silicon oxides ( $\text{Si}^{1+}$  in the form of  $\text{SiO}_3$  and  $\text{Si}^{3+}$  in the form of  $\text{Si}_2\text{O}_3$ ) along with some proportions of  $\text{SiO}_2$  and Si-OH. The Si  $2p$  spectrum corresponding to the fluence of  $5 \times 10^{17} \text{ cm}^{-2}$  was deconvoluted into five peaks located at  $98.25 \pm 0.15$ ,  $99.77 \pm 0.15$ ,  $101.59 \pm 0.15$ ,  $102.97 \pm 0.15$ , and  $104.76 \pm 0.15 \text{ eV}$  which are assigned to Si,  $\text{SiO}_3$ ,  $\text{Si}_2\text{O}_3$ ,  $\text{SiO}_2$ , and Si-OH bonds, respectively [28]. On the other hand,  $\text{O}1s$  core level spectrum for the said fluence shows bonding with  $\text{SiO}_x$  and  $\text{H}_2\text{O}$ . For the highest fluence of  $2 \times 10^{18} \text{ ions cm}^{-2}$ , a similar trend is observed although Si concentration is little higher compared to that at the lowest fluence case. Relative amount of the respective components in the pristine and irradiated samples, determined from XPS analyses, are listed in Table 5.1. The survey spectra (not shown) at all fluences did not reveal the presence of any Fe signal from nanofaceted samples. This is

expected for the chosen experimental geometry where a sacrificial Si wafer was used to cover the entire sample platen (as described in the experimental section and Ref. 25) to avoid having impurity-induced nanostructure formation at such a glancing incidence angle. Similar results are obtained for  $\theta=70^\circ$  (spectra not shown) as well. Thus, the amorphous patches at the facet apexes mostly consist of native oxide layer ( $\text{SiO}_x$ ) which matches well with the prediction made on the basis of XTEM image shown in Fig. 5.2.

**Table 5.1:** Chemical compositional analyses using XPS

Sample	Binding energy (eV)	Chemical composition	Concentration (%)
Pristine-Si	98.2	$\text{Si}^0$ , Si elemental	46.58
	99.78	$\text{Si}^{1+}$ , $\text{SiO}_3$	15.92
	101.51	$\text{Si}^{2+}$ , $\text{Si}_2\text{O}_3$	19.98
	102.94	$\text{Si}^{4+}$ , $\text{SiO}_2$	14.61
	104.76	Si-OH	2.91
Si irradiated with $5 \times 10^{17} \text{Ar}^+ \text{cm}^{-2}$ at $72.5^\circ$	98.22	$\text{Si}^0$ , Si elemental	36.58
	99.79	$\text{Si}^{1+}$ , $\text{SiO}_3$	19.19
	101.59	$\text{Si}^{2+}$ , $\text{Si}_2\text{O}_3$	16.31
	102.92	$\text{Si}^{4+}$ , $\text{SiO}_2$	20.51
	104.7	Si-OH	7.41
Si irradiated with $2 \times 10^{18} \text{Ar}^+ \text{cm}^{-2}$ at $72.5^\circ$	98.24	$\text{Si}^0$ , Si elemental	39.85
	99.72	$\text{Si}^{1+}$ , $\text{SiO}_3$	20.22
	101.62	$\text{Si}^{2+}$ , $\text{Si}_2\text{O}_3$	15.6
	102.97	$\text{Si}^{4+}$ , $\text{SiO}_2$	19.74
	104.79	Si-OH	4.59

Figure 5.4(a) presents the change in surface reflectance with increasing ion fluence in the range of  $5 \times 10^{17}$ - $2 \times 10^{18}$  ions  $\text{cm}^{-2}$  for  $\theta=72.5^\circ$ . It is observed that the reflectance decreases with increasing fluence. For instance, the reflectance at 550 nm reaches the values of 40% (for  $5 \times 10^{17}$  ions  $\text{cm}^{-2}$ ), 38% (for  $1 \times 10^{18}$  ions  $\text{cm}^{-2}$ ), and 26% (for  $2 \times 10^{18}$  ions  $\text{cm}^{-2}$ ). A similar trend is observed (reflectance reduces up to 31% for the fluence  $2 \times 10^{18}$  ions  $\text{cm}^{-2}$ ) in case of  $\theta=70^\circ$  incidence angle (spectra not shown). Thus, it can be inferred that argon-ion induced topographically modulated Si surfaces (having faceted nanostructures) can manifest variable degree of AR property which is dependent on angle of incidence of ions and fluence.

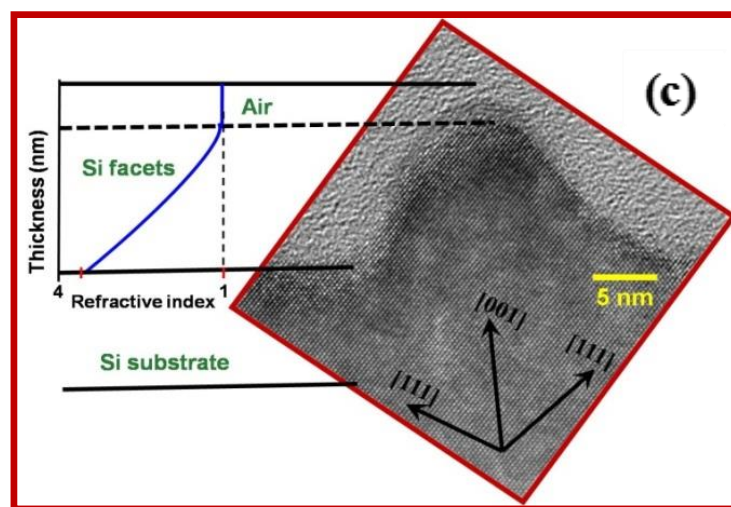
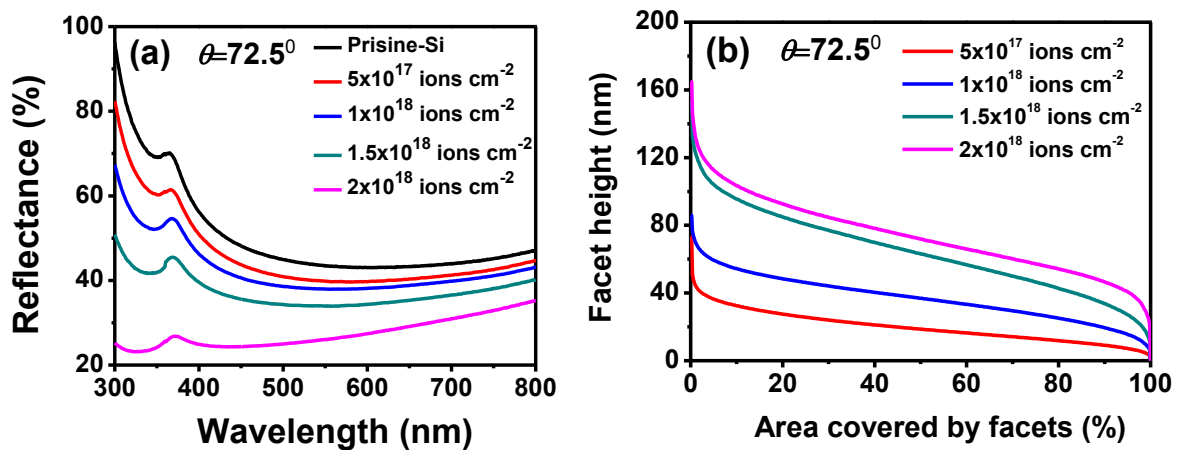


Figure 5.4:(a) Reflectance study corresponding to Pristine-Si and samples exposed to four different ion fluences, viz.  $5 \times 10^{17}$ ,  $1 \times 10^{18}$ ,  $1.5 \times 10^{18}$ , and  $2 \times 10^{18}$   $\text{cm}^{-2}$  for incidence angle of  $72.5^\circ$ , (b) facet height versus percentage area covered by the faceted structures extracted by using SPIP software from the respective AFM images shown in Fig. 1, and (c) schematic of the refractive index profile from air to Si substrate due to the presence of a facet.

In order to correlate the change in AR property with the surface morphology observed at two different  $\theta$ -values and Ar-ion fluences, we used SPIP software [27] to calculate the percentage area covered by the Si faceted structures with respect to air and plot it against the corresponding facet height at different fluences [Fig. 5.4(b)]. This shows an increasing trend in the surface height with decreasing percentage area covered by the facets. Thus, in our case, a faceted surface has a gradually varying Si-fraction from top (100% air: 0% Si) to bottom (0% air: 100% Si). This is further supported by the plots shown in Fig. 5.1(c) where facet height increases as

a function of ion fluence. Since a gradual change in facet height leads to the gradual variation in percentage area covered by the facets from top (100% air: 0% Si) to bottom (0% air: 100% Si), the observed AR property of nanofaceted-Si substrates can be understood in terms of well-known graded refractive index effect [29]. Corresponding schematic diagram of the refractive index profile from air to Si substrate due to the presence of a facet is shown in Fig. 5.4(c) where the presence of small amount (as compared to total facet) of amorphous-Si and native oxides at the apex was neglected. This gradual variation in refractive index can effectively eliminate the reflected light across a wide spectrum [29]. In the present case, with increasing sputtering time, facet dimensions become larger [as observed from Fig. 5.1(c)] which improves the antireflection over a wide spectral range.

The PL spectra of Si-nanofacets are presented in Fig. 5.5. In case of  $\theta=72.5^\circ$ , PL intensity is the weakest for the lowest fluence whereas it becomes the strongest at the highest fluence. It is observed that several PL peaks are located in the energy range of 3.39-2.67 eV (365-465 nm). Figure 5.5 illustrates that for the fluence of  $5 \times 10^{17}$  ions  $\text{cm}^{-2}$ , a small shoulder appears at 373.5 nm along with a clear peak at 371 nm. With increasing fluence up to  $2 \times 10^{18}$  ions  $\text{cm}^{-2}$ , a blue shift ( $\sim 2.5$  nm) is observed which is accompanied by the appearance of a less intense peak is detected at 396 nm. The inset of Fig. 5.5 shows the PL spectrum of a pristine-Si sample where no other PL peak is observed except a small hump at around 370 nm. This indicates that the origin of 371 nm PL band, in our case (including pristine-Si), may be related to the native oxide layer formed on top of the crystalline-Si. For UV light emission from Si-based nanostructures, two possible mechanisms are proposed. One is based on quantum size effect, which says that the excitation occurs between the quantized levels of nanocrystallites and the recombination happens either directly between the same levels or at the nanocrystalline surface/interface states after a relaxation process [30-33]. The other possibility is the presence of Si-O related species which governs the whole excitation and recombination processes [34-38].

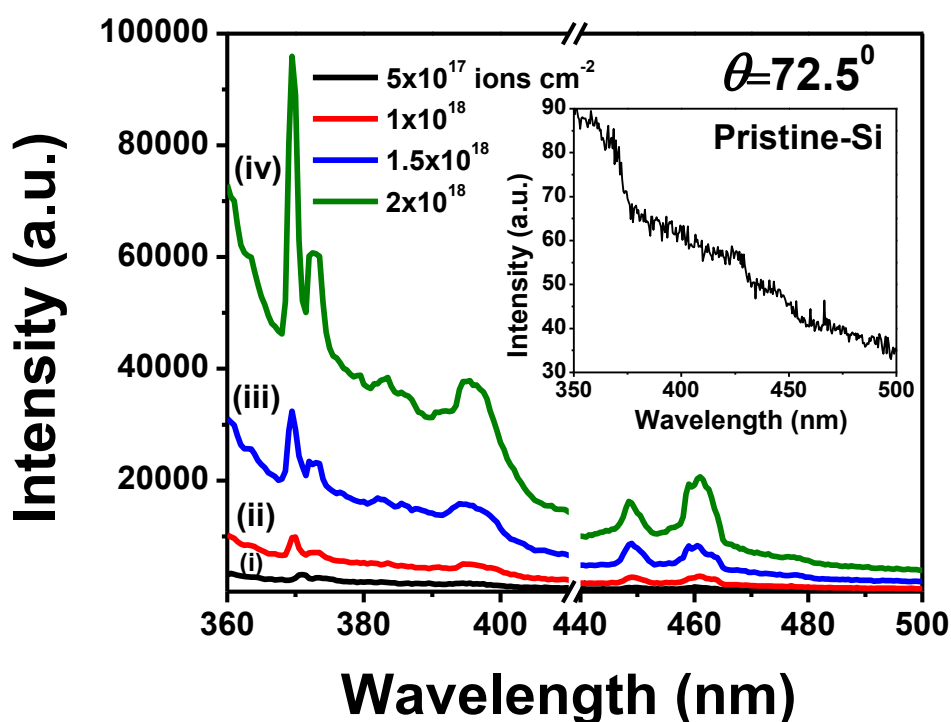


Figure 5.5: PL spectra plotted against wavelength for ion incidence angle of  $72.5^\circ$  and for fluences of (i)  $5 \times 10^{17}$ , (ii)  $1 \times 10^{18}$ , (iii)  $1.5 \times 10^{18}$ , and (iv)  $2 \times 10^{18}$  ions  $\text{cm}^{-2}$ , respectively. Inset shows the PL spectrum corresponding to Pristine-Si.

To understand the origin of light emission from silicon nanostructures, we first explore the possibility of nanostructure-driven quantum confinement effect in silicon. For example, the model described by Zheng *et al.* [12] calculates the electronic states and optical transition matrix elements of Si quantum tips in a large energy range which yields transitions in the energy range of 2-4 eV. In another work, Adachi *et al.* reported UV PL emission at RT from porous silicon where they have attributed the results to the reduction in the  $E_1$  critical point from two-dimension (2D) to zero-dimension (0D) due to quantum size effect [39]. As compared to silicon quantum tips or nanocrystals in case of faceted silicon, the apexes have the dimension in the range of 3-10 nm (Fig. 5.2) and they grow in the (001) direction. Thus, apparently, quantum confinement may play a role for the observed PL emission in the present case. In that case, one would expect a broad PL band due to a large distribution of the quantum tips and sizes. However, neither broadening nor blue shift of the PL peak in the UV region is

observed in our case and hence, the possibility of quantum confinement in the present study may be ruled out. Thus, in our case Si-O related defects seem to be more important for generating light emission. The UV PL band at 365 nm (in our case  $370\pm 2$  nm) was attributed to the hole-trapped  $E'$  centres ( $O_3\equiv Si$ ) by Kim *et al.* [40]. In this study, XPS measurements reveal the presence of  $E'$  centres in the form of  $O_3\equiv Si$  for both pristine and ion-irradiated samples and the corresponding concentrations are given in Table 5.1. Although  $SiO_3$  (concentration 18.76%) is present in pristine-Si, it does not give rise to any strong 368 nm PL. On the other hand, one can strengthen this emission by exposing to 500 eV Ar-ions. Thus, it can be inferred that the  $E'$  centres become more active due to the presence of Si nanofacets formed under argon-ion exposure because of the increased surface-to-volume ratio of the nanofacets. The small peak that appears at  $\sim 373$  nm shows the similar behaviour and should be related to the same mechanism stated above.

Let us now try to explain the origin of the 396 nm emission from nanofaceted-Si structures. UV emission from porous silicon was reported earlier by Kanjilal *et al.* [41] where they reported on the 396 nm PL band and explained it on the basis of QC-luminescence centre model [42]. In addition, the role of fluorine related defects was also addressed. In the present case, we do not observe any fluorine related peak from XPS analysis which indicates that the observed emission at 396 nm should be related to the luminescence centres present in the vicinity of the silicon nanostructures. As mentioned by Qin *et al.* [42], there is a possibility of lack of non-radiative recombination centres inside the nanoscale objects of Si and therefore, radiative recombination takes place through the luminescence centres present outside Si nanostructures. According to this, the light emission takes place in two steps: Firstly, photo-excitation takes place inside Si nanostructures and subsequently the excited electrons and holes tunnel into the surrounding  $SiO_x$  layers [42]. Secondly, the electrons and holes recombine radiatively via luminescence centres (LCs) in the neighbourhood. The aforementioned

discussion is also true in the present case, showing the PL signal at 396 nm for an excitation wavelength of 325 nm. As discerned from the XTEM image and XPS studies, the apexes of the faceted nanostructures are rich in SiO<sub>x</sub>. Thus, the neutral oxygen vacancy sites located in the peripheral SiO<sub>x</sub> (on the top of the Si facets) can work as the LCs and give rise to the near-UV emission. Another possible explanation would be the formation of interconnects with the crystalline-Si nanostructures due to the diffusion of oxygen atoms. Kanemitsu *et al.* [43] reported that in case of oxidized porous silicon, amorphous SiO<sub>2</sub> layer on crystalline-Si core may give rise to PL emission in the range of 310-413 nm. Actually, at the interface of SiO<sub>2</sub>/Si, electronic states are created due to the presence of the amorphous layer. With increasing temperature, oxygen atoms can diffuse into the crystalline layer and subsequently form bridges or interconnected silicon atoms. According to Kanemitsu *et al.*, the inter-connected Si structure has a direct band gap of 3-4 eV which can give rise to blue light emission. Due to a large mismatch in the band gaps between interface and the outer surface, carriers may get confined in the Si-core. The same group reported that the corresponding blue emission decayed with a time constant of 650 ps [43]. Following this argument, we propose here that ion-exposure provides sufficient energy to oxygen atoms at the surface to inter-diffuse in the silicon matrix and to form bridges which give rise to the 396 nm emission line (in case of all ion-irradiated samples). To validate our claim further, time-resolved PL measurements were performed at an excitation wavelength of 375 nm by using a pulsed diode laser corresponding to the peak observed at 396 nm. The time constant turns out to be 347 ps which is close to the value obtained in case of porous silicon [43]. Thus, in the present case, it is difficult to point out the dominant mechanism (for UV PL emission) between these two.

Apart from the above-mentioned PL bands, appearance of twin peaks in the blue (449 and 460 nm) region is observed explicitly in case of argon-ion irradiated Si samples. It may be mentioned that the PL band at 468 nm PL band is thoroughly studied in case of silica glass and

ion implanted silicon [44-46]. This blue emission generally corresponds to the photo-absorption of neutral oxygen vacancies ( $O_3\equiv Si-Si\equiv O_3$ ) and diamagnetic radiative recombination centres [47]. Thus, oxygen vacancies can play a crucial role in generating blue light emission. Origin of oxygen vacancies in Si are governed by different factors. For instance, Friebele and Griscom showed that oxygen vacancies are generated from the energetic electrons in the ionization cascade during irradiation process [48]. In another study, Devine *et al.* discussed oxygen vacancy generation process during ion bombardment [49]. Absorption of photons of energy higher than the band gap of  $SiO_2$  generates electron-hole pairs, a substantial portion of which gets converted to excitons. These excitons become the so-called self-trapped excitons when they get localized within the material by defects in the material. The radiative recombination of self-trapped excitons can produce blue (2.7 eV) PL emission [49]. Following the above discussion, oxygen vacancies generated during Ar-ion irradiation process might be acting as trap centres for photo-generated excitons in  $SiO_2$  (as evident from XPS analysis). These trapped excitons subsequently recombine to give rise to PL bands at 449 and 460 nm.

The key result in the present case is the observation of drastic enhancement in overall PL intensity (at RT) as a function of ion-fluence. We explored the possibility of correlating this behaviour to the improved antireflection/enhanced absorption property of the nanofaceted-Si. This seems more plausible in our case as XPS analyses (Fig. 5.3) do not reveal much difference in the concentration of chemical species in the pristine and ion-irradiated Si samples. Thus, it is clear that the observed enhancement in the PL intensity is not due to the variation in the concentration of different defect states but something else. It has been reported that light extraction from Si-based materials can be enhanced by making use of textured surfaces which show enhanced luminescent property by surface roughening process [21]. As discussed above, the surface reflectance is significantly suppressed by using nanopatterned structures (Fig. 5.4), the light emission should effectively increase due to the antireflection effect over a wide

spectral range. Since the reflection of incident light in the UV region also reduces [as observed from Fig. 5.4(a)], the more incident light can be absorbed in the Si nanofacets to excite much more electron-hole pairs leading to a stronger emission. It may be noted that the excitation wavelength (325 nm) is in the UV region and from the reflectance measurements [Fig. 5.4(a)], we observe a significant improvement in the AR property as a function of ion fluence, in the UV region as well. Thus, the excitation light (He-Cd laser, 325 nm) gets benefitted from this antireflection property and maximum increment in the emission intensity is observed in the spectral range of 360-380 nm. Thus, the improved AR property of nanofaceted-Si contributes to the significant enhancement in the PL intensity particularly in the UV region.

#### **5.1.4 Conclusions**

In conclusion, anion-fluence dependent tunable room temperature PL emission is demonstrated from nanofaceted-Si structures produced by 500 eV argon ion bombardment at oblique incidences. Origin of this UV PL emission is explained by taking into account argon-ion activated  $E'$  centres and Si-O related states present at the interface of Si/SiO<sub>x</sub> nanofacets. On the other hand, emission in the blue region corresponds to the self-trapped excitons localized at the argon-ion induced oxygen vacancies at the surface of crystalline nanofacets. The enhancement in the overall PL intensity is attributed to the decrease in surface reflectance as a function of fluence due to the presence of textured surfaces (decorated with nanofacets). Thus, our experimental results show that the intensities of light emission of Si-based devices can be improved by using nanoscale textured surfaces. The present study indicates that silicon nanofacets might be a good candidate both as a functional silicon nanostructure and as a template for assembling silicon-based nanocomposites in fabricating optoelectronic nanodevices.

## 5.2 Field emission from nanofaceted-Si: Role of native oxide

### 5.2.1 Introduction

Contemporary technological research is based on the ability to manipulate the smallest unit of matter, i.e. atom in a precise way in order to obtain an exceptional performance. In doing so, engineering in nanoscale plays a critical role in today's technology due to its structural dependency on physical properties. For instance, the electron transport mechanisms show different behaviour in case of three-dimensional (3D), two-dimensional (2D), and one-dimensional (1D) structures [50-52]. Taking this into consideration, it may be mentioned that electron tunnelling is highly influenced by the physical and geometrical properties of a nanomaterial [53-57]. In general, electrons from solids get emitted in vacuum under the thermal excitation (i.e. thermionic emission) or by applying an electric field [i.e. field emission (FE)]. However, most of the thermionic emission-based devices suffer from the problems of stability issues and heating effects [58]. Therefore, for room temperature operation, cold cathode emitters have emerged as promising candidates. Materials with high aspect ratios such as nanotubes, nanowires, and nanorods demonstrate excellent electron emission characteristics [59-61]. The enhanced electric field at the tips reduces the potential barrier at the metal-vacuum interface, which can be described as the zero electric field work function energy,  $\phi$ , so that electrons can tunnel from the solid into vacuum, enabling the Fowler-Nordheim (FN) tunnelling [62,63]. . Generally, FE is defined by the Fowler-Nordheim (FN) equation defined as [62]:

$$J = A \left( \frac{\beta^2 E^2}{\phi} \right) \exp \left( \frac{-B \phi^{3/2}}{\beta E} \right) \quad (1)$$

where  $J$  is the emission current density ( $\text{A m}^{-2}$ ),  $E$  is the mean electric field between the electrodes ( $\text{V } \mu\text{m}^{-1}$ ), and  $\phi$  is the work function (eV). The constants are  $A=1.56 \times 10^{-10} \text{ A V}^{-2} \text{ eV}$  and  $B=6.83 \times 10^3 \text{ V eV}^{-1.5} \mu\text{m}^{-1}$ . The enhancement factor,  $\beta$ , depends on tip-sample geometry

which is 1 for a flat surface and higher for other geometries. It may be mentioned that FE-based devices have potential applications in flat panel display, microwave power amplifiers, electron microscopes as well as gas and mass sensors [57,64,65].

Among various field emitters, Si-based ones are extremely important for micro- and nano-electronics due to their low mass and volume with very low power requirements [66]. In addition, nowadays, Si-based field emitters are being used as neutralizers to reduce space craft charging which occurs as a side-effect during propulsion [67]. Hence, numerous studies have been directed towards the preparation of Si nanowires, nanobelts, nanoribbons, and nanotubes, and utilization of such nanostructures in miniaturized electronic devices which also show considerable FE property [68,69]. Si-based field emitters are fabricated by various catalyst or lithographic methods. For instance, silicon nanowires were grown on carbon cloth via the vapor-liquid-solid reaction using gold as catalyst which yielded a very low turn-on field of  $0.7 \text{ V } \mu\text{m}^{-1}$  [70]. On the other hand, Si nanotip array, formed by porous alumina mask, demonstrates a turn on field of  $8.5 \text{ V } \mu\text{m}^{-1}$  whereas for Si nanotubes, synthesized by template replication and chemical vapor deposition, the turn-on field value becomes  $5.1 \text{ V } \mu\text{m}^{-1}$  [71,72]. Although these results are exciting, such methods of fabrication have their own disadvantages, e.g. template-based lithographic techniques are expensive and template removal is difficult. On the other hand, in catalyst driven processes, metal particles may play the role of electron or hole traps in Si which leads to various contamination related problems [61].

This indicates that for commercial usage of Si as a field emitter, a single step large area fabrication process is required and those rely on self-organization of nanostructures are of special interest. However, under the exposure to ambient, these nanostructures are prone to get oxidized due to the formation of a native  $\text{SiO}_x$  layer (dielectric) at RT [73]. This creates an additional tunnelling barrier for electrons, resulting in a drastic reduction of the field emission properties. On the other hand,  $\text{SiO}_2$  is an important candidate in micro- and nano-electronics

industry and helps Si surface to get rid of contamination related problems as well. Therefore, understanding the role of a native oxide layer in FE property of Si nanostructures is of utmost importance. In this context, it is a great challenge to develop a new method where Si nanostructures can be fabricated with a native oxide capping layer without much of a degradation in their FE property.

In the present study, we report on the FE from low energy ion-beam fabricated nanofaceted-Si structures [23]. Bulk measurements show an impressive turn-on field of  $4.7 \text{ V } \mu\text{m}^{-1}$  and excellent stability. However, bulk FE bulk measurements cannot specifically identify the region of FE and hence, we have employed combined atomic force microscopy-based local tunnelling current and scanning Kelvin probe microscopy (SKPM) measurements to understand the local FE properties of such Si nanofacets. In fact, tunnelling current mapping conclusively shows that the valleys and the sidewalls of nanofaceted structures/nanofacets contribute more to the field emission process compared to their apexes. In addition, cross sectional transmission electron microscopy (XTEM) reveals that the apexes of the nanofacets are covered with native oxide whereas the side walls and valleys are crystalline. This presence of native oxide at apexes will increase the local work function and in turn reduce the electron tunnelling probability. This observation corroborates well with SKPM based studies.

### **5.2.2 Experimental**

Silicon samples, used in the present experiments, were sliced out ( $1 \times 1 \text{ cm}^2$ ) from a *p*-type Si(100) wafer. A UHV-compatible experimental chamber, equipped with an electron cyclotron resonance based broad beam ion source, was used in this case. The chamber base pressure was below  $5 \times 10^{-9}$  mbar and the working pressure was maintained at  $3 \times 10^{-4}$  mbar. Samples were fixed on a sample holder which was covered by a sacrificial Si wafer (taken from the same lot of the substrate) to ensure a low impurity environment. Samples were exposed to 500 eV Ar-ions at an oblique incidence of  $72.5^\circ$  incidence angle (with respect to the surface normal) and

at an optimized fluence of  $3 \times 10^{18}$  ions  $\text{cm}^{-2}$  at RT. The beam diameter was measured to be 3  $\mu\text{m}$  which corresponds to a fixed ion flux of  $1.3 \times 10^{14}$  ions  $\text{cm}^{-2} \text{s}^{-1}$  (corresponding to a target current of 160  $\mu\text{A}$ ) in a plane normal to the ion-beam direction.

Surface morphology and local electrical properties of nanofaceted was examined *ex-situ* by atomic force microscopy in different modes using conductive tips (AC240TM, Electric-Lever, Olympus) and with a resonance frequency of 70 kHz. Further, dual pass tunnelling current microscopy (DPTCM) [equivalent to tunnelling atomic force microscopy (TUNA)] and SKPM studies were performed using a user-defined lift height of 20 nm from the surface [74]. It may be mentioned that AFM and SKPM measurements were accomplished with optimized drive amplitudes, frequencies, set points, and scan speeds. Moreover, AFM image analyses were carried out by employing WSxM and SPIP softwares [22,32]. In addition, microstructural study was performed by using high-resolution transmission electron microscopy (HRTEM).

Field emission measurements were carried out at RT in high vacuum ( $3 \times 10^{-7}$  mbar) condition by using a two-electrode configuration with a copper anode and the sample was attached to the cathode plate with conductive copper tape (sheet resistance  $\sim 0.004 \Omega/\square$ ). To ensure a stable emission, 10 cycles with external bias were applied before recording each data set.

### 5.2.3 Results and discussion

Figure 5.6(a) shows the current density as a function of the applied electric field for the Si nanofacets. The turn-on field (the field at which a sharp increment in current density is observed) was  $4.7 \text{ V } \mu\text{m}^{-1}$ . The pristine-Si did not show any emission up to 1000 V, (our measurement limit). The observed threshold emission is similar to the case of Si nanotube arrays where the value comes around  $5.1 \mu\text{m}^{-1}$  [72]. Fig. 5.6 (b) shows  $1/E$  vs  $\ln(J/E^2)$  plot which can be fitted linearly, indicating that FN mechanism is operative for the observed FE. The enhancement factor,  $\beta$ , is calculated from the slopes of the fitted lines which turns out to

be  $\sim 1104$ , assuming the work function of nanofaceted-Si to be 4.8 eV [75]. We find that the enhancement factor turns out to be little low compared to the existing reports [71, 72] whereas the threshold field value is among the best reported ones in case of Si nanostructures.

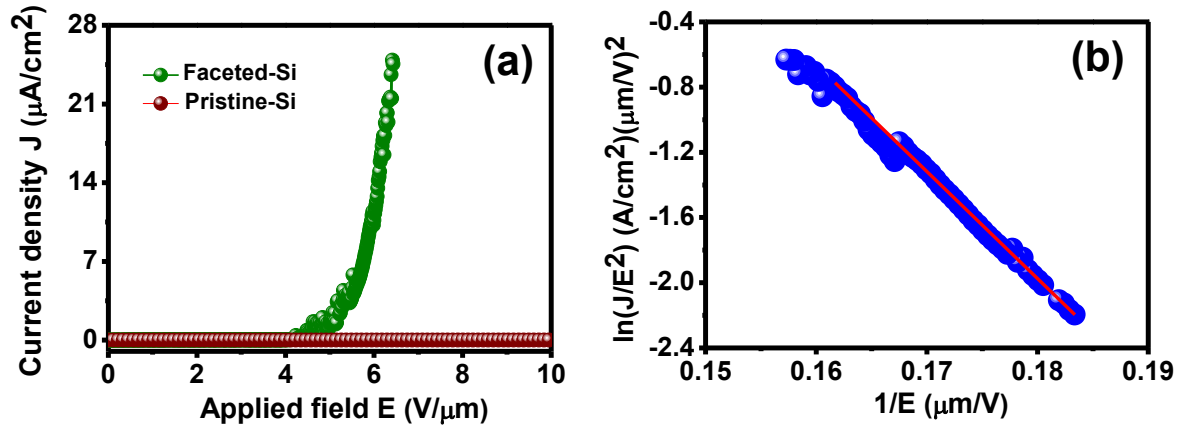


Figure 5.6: (a) Field emission current density as a function of the applied electric field for the nanofaceted-Si (green) and pristine-Si nanotube (brown), (b) Fowler-Nordheim plot for the nanofacets. The straight line drawn is for guide to the eye.

The efficient field emission performance of nanostructured-Si is generally ascribed to the enhanced aspect ratio and sharp apexes of the structures. However, the bulk measurements cannot specifically identify the regions of a faceted structure which gives rise to FE. To overcome this problem, we employed AFM-based local probe technique to map the tunnelling current. In fact, tunnelling current is measured by using a dual pass technique [schematic shown in Fig. 5.7(a)] which is similar to the tunnelling atomic force microscopy (TUNA) process reported by Chatterjee *et al.* [74].

Advances in scanning tunnelling microscopy (STM) and AFM over the past few years have seen the development of this conducting-AFM/STM combination into a highly sensitive technique called tunnelling current microscopy [74]. This allows a tunnelling current to be obtained from a sharpened tip attached to a cantilever, while simultaneously the tip traverses across the sample surface tracking height and morphological information. Whilst standard STM requires sample surfaces to be smooth on the nanometer scale, the physical tracking of topography in tunnelling current microscopy means that samples with a surface rms roughness

of several microns can be investigated over scan areas up to hundreds of square microns. This allows a wider picture of the overall morphology to be obtained. Physical tracking also means that, unlike the constant-current mode of STM, the height data collected via deflection of the cantilever beam avoids possible artefacts introduced by variations in the conductivity of the sample surface. Here, for the present study, we call it dual pass tunnelling current microscopy (DPTCM) (details are described in chapter 3). Microstructural investigation was carried out by using cross sectional transmission electron microscopy (XTEM) on faceted substrates. Figure 5.7(b) depicts a high-resolution XTEM image of representative a faceted surface (formed at a lower fluence value of  $5 \times 10^{17}$  ions  $\text{cm}^{-2}$ ) which shows the clear presence of lattice fringes, indicating the formation of crystalline facets. A careful observation reveals the presence of amorphous patches (marked by yellow dashed lines) around the apex of the facets, albeit they are absent at the valleys, i.e. between two facets. These patches may result from the presence of mostly native oxides (as confirmed from the XPS study and discussed in the section 5.1.3). Fig. 5.7(c) shows the surface topography image recorded during tunnelling current measurements, which clearly shows the apexes and valleys of nanofacets. Several scans (from various places) with different scan directions were performed to confirm the true electron emission sites. Figure 5.7(d) shows one of the maps of tunnelling current (FE) which clearly indicates (shown by green lines) that the apexes are not actually contributing to the FE process (in contrary to the present notion), rather sidewalls and the valleys of nanofacets are the preferential sites [marked by blue and green lines in Figs. 5.7 (c) and (d)] for electron emission for a tip voltage of 10 V (maximum voltage limit of the used AFM). In order to confirm that the measured tunnelling current was a true reflection of the emission properties of the surface and not simply an artefact of surface topology, scans were repeated in four different directions to check that the data from each scan were all in good agreement. Thus, the local tunnelling current measurements indicate that higher tip voltage is required to tunnel the electron from

apexes. In fact, this result shows the presence of trap states at the apex in the form of native silicon oxide which may lead to the suppression of FE from the apexes as observed from Fig. 5.7(b).

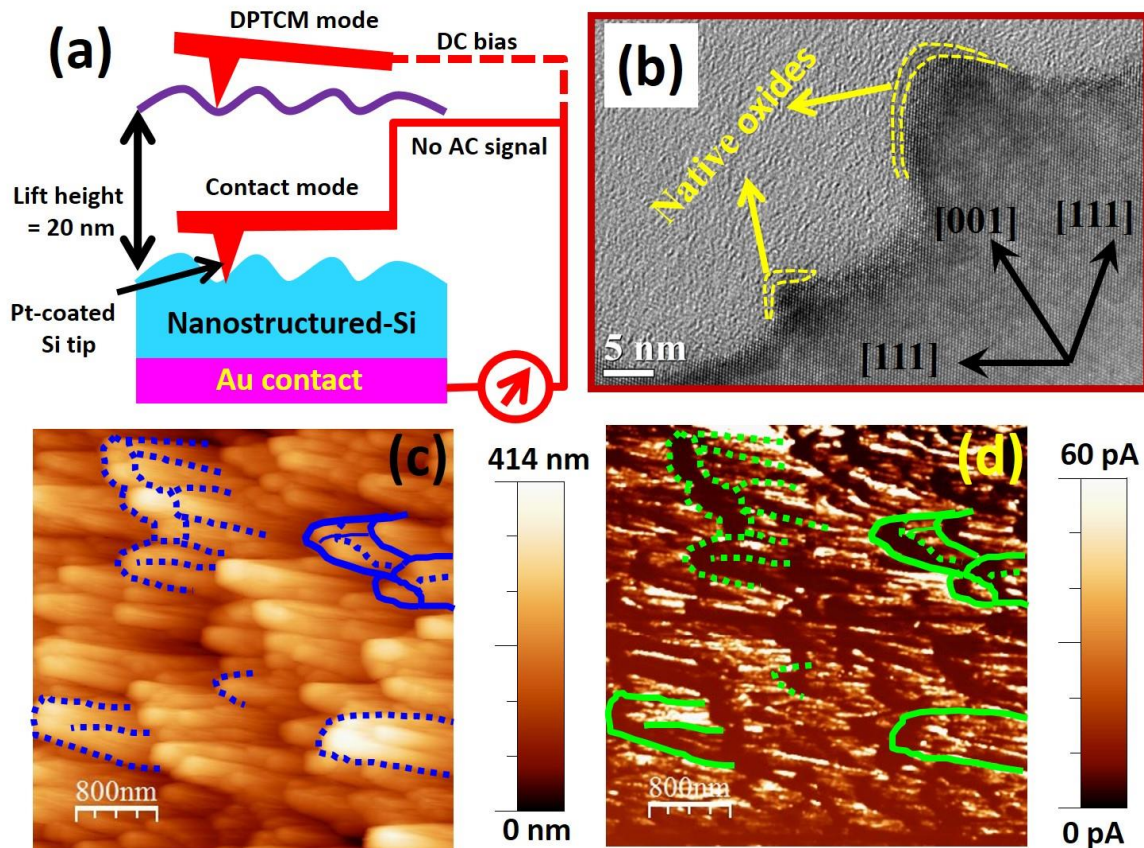


Figure 5.7: (a) Schematic of the DPTCM measurement using dual pass mode. (b) XTEM image showing silicon facets fabricated by using 500 eV Ar-ions to the fluence of  $5 \times 10^{17} \text{ cm}^{-2}$ . The yellow lines depict the zones where native oxides are present. (c) Topographical image of nanofaceted-Si surface in contact mode. Corresponding height scale is 0 to 414 nm. (d) Map of tunnelling current measurements showing clear contrast difference in the valley and apex. Corresponding height scale is 0 to 60 pA. Blue and green lines in (c) and (d) are for guide to eyes.

It may be mentioned that the growth of oxide layer on Si nanostructures is of great importance although the mechanism of oxidation is not well understood till date. Presently, various reports exist where the oxidation of Si nanostructures has been addressed. For instance, Büttner *et al.* reported on the retarded oxidation of Si nanowires due to increased stress at the Si/SiO<sub>2</sub> interface [69]. This stress value depends on the curvature of the nanostructures. As mentioned by Büttner *et al.*, due to smaller curvature of the surface, oxidation of planar Si is

faster and follows the common Deal-Grove theory [76,77], whereas for nanowires, the increased curvature of the surface leads to a retarded oxidation effect. In another note, experimental and simulation studies show that the rounded Si shapes that appear after oxidation are caused by stress induced reduction of oxide viscosity [80]. These reports clearly indicate that the oxidation of Si nanostructures can be significantly different compared to planar geometry. Thus, in the present work, the presence of native oxide only at the apexes may be attributed to the inhomogeneous strain and stress distribution for a non-planar geometry (leading to a different curvature compared to the planar geometry) of the nanofacets.

Generally, field emission, a quantum mechanical tunnelling of electrons, from the surface of a semiconductor depends on the work function of the materials. In the present case, the presence of native oxide at the apexes should influence the field emission mechanism. Thus, to understand the role of native oxide, we used scanning Kelvin probe microscopy (SKPM). In fact, SKPM measures the constant potential difference ( $V_{CPD}$ ) between tip and sample which can be written as:  $V_{CPD} = (\phi_{tip} - \phi_{sample})/q$ , where  $\phi_{tip}$  and  $\phi_{sample}$  are the work functions of the tip and sample, respectively [79] while  $q$  is the electronic charge. Thus, to find out the work function, SKPM measurements were carried out at various points of a particular nanofacet. Fig. 5.8(a) shows the topographic image of a Si nanofacet from which a clear difference in the height contrast at apex and valley is observed. On the other hand, Fig 5.8(b) shows the corresponding SKPM image. A clear difference in the contrast of the apex and the valleys is seen which actually signifies the spatial variation of the work function over the surface. However, due to inhomogeneous nature of the native oxide formed on Si nanofacets, this image cannot be converted directly into work function mapping. Thus, we measured  $V_{CPD}$  values at different points of a single facet as shown in the topographic image for a better realization of the apex point and the valley [Fig. 5.8(a)] and correlate with the corresponding SKPM image. For instance, we found out the respective work functions values from the locations marked by

(i), (ii), (iii), and (iv). By taking in to account the work function of the tip (Si coated with Pt/Ir) is  $\sim 4.85$  eV [80], the measured work function at points (i), (ii), (iii), and (iv) are found to be 4.75, 4.78, 4.71, and 4.73 eV, respectively.

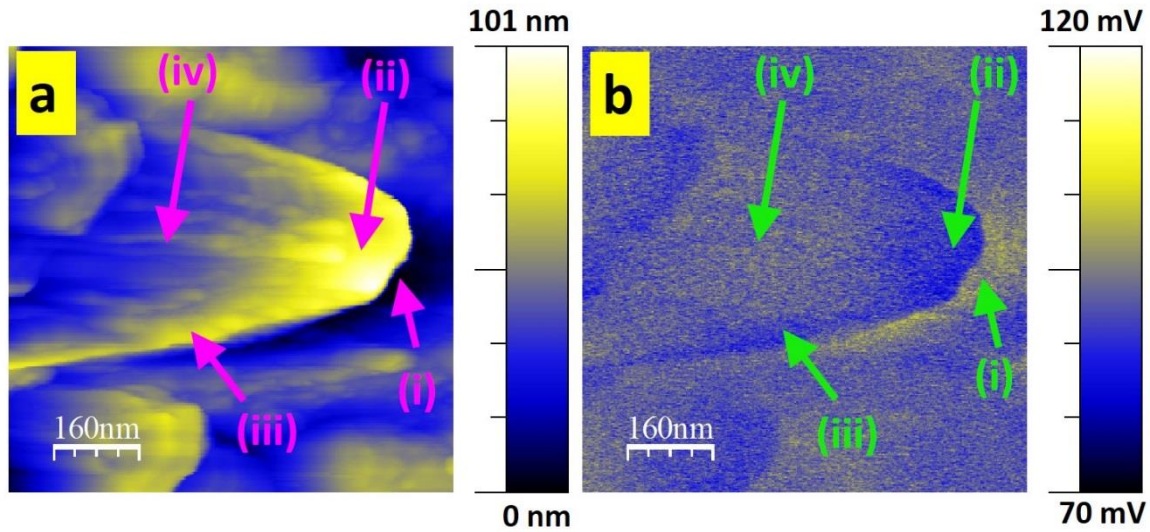


Figure 5.8: (a) topography image of a single nanofacet having a height scale of 101 nm. (b) SKPM image of nanofaceted-Si surface depicting variation of work function over the surface. Corresponding height scale is 70 to 120 mV. (i), (ii), (iii), and (iv) are the regions from where corresponding work functions are calculated.

It is observed that the nanofaceted-Si apex has higher work function ( $\sim 50$  meV) compared to those of valleys [the difference between points (ii) and (iv) in the topography]. This is due to presence of native oxide layer at the apexes of the nanofacets. It may be mentioned that the work function of the apex shows a mismatch with respect to the pure  $\text{SiO}_2$  work function which may be due to its very low thickness [81]. Thus, SKPM measurements further supports the observation of suppression of field emission from the apexes of the nanofacets due to high degree of variation in the work function values from apex to valleys.

#### 5.2.4 Conclusions

In conclusion, the possibility of using self-assembled nanofaceted-Si substrates as stable field emission cathodes has been demonstrated. It has been shown that these Si nanofacets yield an impressive turn on field of  $4.7$  V/ $\mu\text{m}$ . Local probe based DPTCM technique unfolds that the

valleys and the sidewalls of nanofaceted-Si contribute more to the field emission process compared to the apexes. This can be attributed to the formation of a native oxide layer at the apex of the facets. The presence of native oxide at the apexes may result from the inhomogeneous stress distribution over nonplanar geometry. This corroborates well with the XTEM and SKPM studies. Actually, native oxide layer leads to the variation in the work function from tip to the valley of the facets, observed from the SKPM measurements, causing a suppression of the electron emission from the apexes. Our experimental findings demonstrate a novel way to address the field emission in a very local scale by using local probe based microscopic techniques.

## **Bibliography**

1. J. M. Garguilo, F.A.M. Koeck, R. J. Nemanich, X. C. Xiao, J. A. Carlisle, and O. Auciello, *Phys. Rev. B* 72 (2005) 165404.
2. S. Fujita, K. Uchida, S. Yasuda, R. Ohba, and T. Tanamoto, *Nanotechnol.* 3 (2003) 309.
3. M. W. Shao, Y. Y. Shan, N. B. Wong, and S. T. Lee, *Adv. Funct. Mater.* 15 (2005) 1478.
4. M. Kanechika, N. Sugimoto, and Y. Mitsushima, *J. Appl. Phys.* 98 (2005) 054907.
5. R. Tsu and K. Daneshvar, *ECS Trans.* 2(2007) 1.
6. A. P. Alivisatos, *Science* 271 (1996) 933.
7. N. Daldosso, M. Luppi, S. Ossicini, E. Degoli, R. Magri, G. Dalba, P. Fornasini, R. Grisenti, F. Rocca, L. Pavesi, S. Boninelli, F. Priolo, C. Spinella, and F. Iacona, *Phys. Rev. B* 68 (2003) 085327.
8. G-R Lin, C-J Lin, C-K Lin, L-J Chou, and Y-L Chueh, *J. Appl. Phys.* 97 (2005) 094306.
9. F. Iacona, G. Franzò, and C. Spinella, *J. Appl. Phys.* 87 (2000) 1295.
10. X. Wen, L.V. Dao, and P. Hannaford, *J. Phys. D: Appl. Phys.* 40 (2007) 3573.
11. G. Sahu, H. P. Lenka, D.P. Mahapatra, B. Rout, and M. P. Das, *Nanotechnol.* 3 (2012) 025002.

12. W. H. Zheng, Jian-bai Xia, S. D. Lam, K. W. Cheah, M. R. Rakhshandehroo, and S. W. Pang, *Appl. Phys. Lett.* 74 (1999) 386.
13. Y. Mochizuki, M. Fujii, S. Hayashi, T. Tsuruoka, and K. Akamatsu, *J. Appl. Phys.* 106 (2009) 013517.
14. J. Goffard, D. Gérard, P. Miska, A-L Baudrion, R. Deturche, and J. Plain, *Sci. Rep.* 3 (2013) 2672.
15. B. Kim, C. Cho, J. Mun, M. Kwon, T. Park, J. S. Kim, C. C. Byeon, J. Lee, and S. Park, *Adv. Mater.* 20 (2008) 3100.
16. M. Hsieh, C. Wang, L. Chen, T. Lin, M. Ke, Y. Cheng, Y. Yu, C. Chen, D. Yeh, C. Lu, C. Huang, C. Yang, and J. Huang, *IEEE Electron Device Lett.* 29 (2008) 658.
17. P. Lalanne, and G. M. Morris, *Nanotechnol.* 8 (1997) 53.
18. Y-F. Huang, S. Chattopadhyay, Y-J. Jen, C-Y. Peng, T-A. Liu, Y-K. Hsu, C-L. Pan, H-C. Lo, C-H. Hsu, Y-H. Chang, C-S. Lee, K-H. Chen, and L-C. Chen, *Nat. Nanotechnol.* 2 (2007) 770.
19. A. O. Altun, S. Jeon, J. Shim, J-H. Jeong, D-G. Choi, K-D. Kim, J-H. Choi, S-W. Lee, E-S. Lee, and H-D. Park, *Org. Electron.* 11 (2010) 711.
20. A. C. Tamboli, K. C. McGroddy, and E. L. Hu, *Phys. Status Solidi C6* (2009) S807.
21. Y. Liu, J. Xu, H. Sun, S. Sun, W. Xu, L. Xu, and K. Chen, *Opt. Exp.* 19 (2011) 3347.
22. <http://www.nanotec.es/products/wsxm/index.php>
23. T. Basu, D. P. Datta, and T. Som, *Nanoscale Res. Lett.* 8 (2013) 289.
24. G. Carter, *J. Appl. Phys.* 85 (1999) 455.
25. W. Hauffe, *Physica Status Solidi (a)* 35 (1976) K93.
26. M. Engler, S. Macko, F. Frost, and T. Michely, *Phys. Rev. B* 89 (2014) 245412.
27. <http://www.imagemet.com/index.php?main=products>
28. F. G. Bell and L. Ley, *Phys. Rev. B* 37 (1988) 8384.

29. W. H. Southwell, *Opt. Lett.* 11 (1983) 584.
30. D. J. Lockwood, Z. J. Lu, and J-M Baribeau, *Phys. Rev. Lett.* 76 (1996) 539.
31. E. Edelberg, S. Bergh, R. Naone, M. Hall, and E. S. Aydil, *Appl. Phys. Lett.* 68 (1996) 1415.
32. S. Tong, X. Liu, and X. Bao, *Appl. Phys. Lett.* 66 (1995) 469.
33. X.-N. Liu, S. Tong, L.-C. Wang, G.-X. Chen, and X.-M. Bao, *J. Appl. Phys.* 78 (1995) 6193.
34. L. Skuja, *J. Non-Cryst. Solids* 149 (1992) 77.
35. L. Lucovsky, *Philos. Mag.* 39 (1979) 513.
36. C. M. Gee and M. Kastner, *Phys. Rev. Lett.* 42 (1979) 1765.
37. D. L. Griscom, *J. Non-Cryst. Solids* 73 (1985) 51.
38. E. P. O'Reilly and J. Robertson, *Phys. Rev. B* 27 (1983) 3780.
39. S. Adachi, T. Miyazaki, K. Inoue, and S. Sodezawa, *Jap. J. Appl. Phys.* 46 (2007) 4028.
40. K. Kim, M. S. Suh, T. S. Kim, C. J. Youn, E. K. Suh, Y. J. Shin, K. B. Lee, and H. J. Lee, *Appl. Phys. Lett.* 69 (1996) 1908.
41. A. Kanjilal, M. Song, K. Furuya, and B. Mallik, *J. Phys. D: Appl. Phys.* 40 (2007) 5044.
42. C.G. Qin and Y. Q. Jia, *Solid State Commun.* 86 (1993) 559.
43. Y. Kanemitsu, T. Futagi, T. Matsumoto, and H. Mimura, *Phys. Rev. B* 49 (1994) 14732.
44. R. Tohmon, Y. Shimogaichi, H. Mizuno, Y. Ohko, K. Nagasawa, and Y. Hama, *Phys. Rev. Lett.* 62 (1989) 1388.
45. H. Nishikawa, T. Shiroyama, R. Nakamura, Y. Ohki, K. Nagasawa, and Y. Hama, *Phys. Rev. B* 45(1992) 586.
46. H. Z. Song and X. M. Bao, *Phys. Rev. B* 55 (1997) 6988.
47. C. G. Siu, X. L. Wu, and X. M. Bao, *Appl. Phys. Lett.* 74 (1999) 1812.

48. E. J. Friebele and D. L. Griscom, in *Treatise on Materials Science and Technology*, edited by M. Tomozawa and R. H. Doremus (Academic, New York, 1979), Vol. 17, p. 257.
49. R. A. B. Devine, *Appl. Phys. Lett.* 43 (1983) 1056.
50. S. Nandy, G. Goncalves, J.V. Pinto, T. Busani, V. Figueiredo, L. Pereira, R.F. Paiva Martins, E. Fortunato, *Nanoscale* 5 (2013) 11699.
51. L.-J. Pegg, and R. A. Hatton, *ACS Nano* 6 (2012) 4722.
52. J. A. Anta, *Science* 17 (2012) 124.
53. H. Shi, K. Yu, F. Sun, and Z. Zhu, *Cryst. Eng. Commun.* 14 (2012) 278.
54. K. Yu, Y.S. Zhang, F. Xu, Q. Li, Z.Q. Zhu, Q. Wan, *Appl. Phys. Lett.* 88 (2006) 153123.
55. J. Liang and G. Zhang, *ACS Appl. Mater. Int.* 4 (2012) 6053.
56. Y. Guo and W. Guo, *J. Phys. Chem. C* 117 (2012) 692.
57. S.W. Joo and A.N. Banerjee, *J. Appl. Phys.* 107 (2010) 114317.
58. C. Gu, X. Jiang, W. Lu, J. Li, and S. Mantl, *Sci. Rep.* 2 (2012) 746.
59. F.M. Ross, J. Tersoff, and M.C. Reuter, *Phys. Rev. Lett.* 95 (2005) 146104.
60. J.B. Hannon, S. Kodambaka, F.M. Ross, and R.M. Tromp, *Nature* 440 (2006) 69.
61. X. Fang, Y. Bando, U. K. Gautam, C. Ye, and D. Golberg, *J. Mater. Chem.* 18 (2008) 509.
62. R. H. Fowler and L. Nordheim, *Proc. R. Soc. London, Ser. A* 119 (1928)173.
63. P.A. Chatterton, *Proc. Phys. Soc.* 88 (1966) 231.
64. I. Chakraborty, S. Chatterjee, and P. Ayyub, *Appl. Phys. Lett.* 99 (2011) 143106.
65. D. Ye, S. Moussa, J.D. Ferguson, A.A. Baski, and M.S. El-Shall, *Nano Lett.* 12 (2012) 1265.
66. X.S. Fang, Y. Bando, C.H. Ye, G.Z. Shen, U.K. Gautam, C.C. Tang, and D. Golberg, *Chem. Commun.* 40 (2007) 4093.
67. K.L. Aplin, C.M. Collingwoodand, and B.J. Kent, *J. Phys. D: Appl. Phys.* 37 (2004) 2009.
68. J.D. Holmes, K.P. Johnston, R.C. Doty, and B.A. Korgel, *Science*, 2000, 287, 1471.

69. G. Audoit, T. Ni Mhuircheartaigh, S.M. Lipson, M.A. Morris, W.J. Blau, and J. D. Holmes, *J. Mater. Chem.*, 2005, 15, 4809.
70. B.Q. Zeng, G.Y. Xiong, S. Chen, W.Z. Wang, and Z. F. Ren, *Appl. Phys. Lett.* 90 (2007) 033112.
71. G.S. Huang, X.L. Wu, Y.C. Cheng, X.F. Li, S.H. Luo, T. Feng and P.K. Chu, *Nanotechnology*, 17 (2006) 5573.
72. C. Mu, Y.X. Yu, W. Liao, X.S. Zhao, D.S. Xu, X.H. Chen, and D.P. Yu, *Appl. Phys. Lett.* 87 (2005) 113104.
73. J.D. Ryckman, R.A. Reed, R.A. Weller, D.M. Fleetwood, and S.M. Weiss, *J. Appl. Phys.* 108 (2010) 113528.
74. V. Chatterjee, R. Harniman, P.W. May, and P.K. Barhai, *Appl. Phys. Lett.* 104 (2014) 171907.
75. A. Novikov, *Solid-State Electron.* 54 (2010) 8.
76. C. C. Büttner and M. Zacharias, *Appl. Phys. Lett.* 89 (2006) 263106.
77. T. Watanabe and I. Ohdomari, *J. Electrochem. Soc.* 154 (2007) G270.
78. M. Uematsu, H. Kageshima, K. Shiraishi, M. Nagase, S. Horiguchi, and Y. Takahashi, *Solid-State Electron.* 48 (2004) 1073.
79. C. Maragliano, S. Lilliu, M. S. Dahlem, M. Chiesa<sup>1</sup>, T. Souier, and M. Stefancich, *Sci. Rep.* 4 (2013) 4203.
80. Y. Lv, J. Cui, Z. M. Jiang, and X. Yang, *Nanoscale Res. Lett.* 7 (2012) 659.
81. L. Yan, C. Punckt, I. A. Aksay, W. Mertin, and G. Bacher, *Nano Lett.* 11 (2011) 3543.

---

## CHAPTER 6

---

### **6. Nanopatterned-Si surfaces: Templates for growth of Al-doped ZnO (AZO)**

Our experimental studies on potential of nanopatterned Si as templates for growth of thin films with improved properties is described in the present chapter. Aluminium-doped ZnO (AZO) films were grown on ripple and nanofaceted-Si templates using magnetron sputtering. While the AZO films grown on rippled-Si show modification in photoluminescence (PL), the AZO films on nanofaceted-Si show antireflection and photovoltaic properties which are tunable through facet dimension.

#### **6.1 Growth of AZO on rippled-Si**

##### **6.1.1 Introduction**

Over the last two decades, zinc oxide has been thoroughly investigated in different industrial areas such as opto- and nano-electronics, ceramics, and photovoltaics [1,2]. Doping of Group III elements, and in particular Al, enhances the conductivity and makes it behave like a transparent conducting oxide (TCO) material. The TCOs are becoming increasingly important to improve the quality as well as efficiency of display panel and solar energy conversion devices [3]. In addition, ultra-violet (UV) light emitting diode based on ZnO are being applied in UV curing, counterfeit detection, and medical instrumentation [4] due to their outstanding properties, viz. wide band gap (3.37 eV at room temperature), high absorption in the UV range, and higher excitonic binding energy (60 meV) [5], compared to other materials having similar applications (e.g. GaN having an excitonic binding energy of 28 meV) [6].

Nowadays, ZnO related research for optoelectronics is growing and is focused on

improving the ZnO excitonic emission in the blue-UV region, taking advantages of its high excitonic binding energy and efficient radiative recombination even at room temperature (RT) [7,8]. Photoluminescence (PL) in the UV region is caused by free electron-hole recombination phenomena in the near band-edge. In the visible region, PL is due to the presence of chemical and structural defects such as oxygen and zinc vacancies and oxygen and zinc interstitials [9]. Free excitons are bound electron-hole pairs that can move together through the crystal<sup>10</sup> and are useful in optoelectronics and photovoltaics [11-13]. On the other hand, materials having excitons bound to structural defects can be used as laser media [14,15]. Different reports exist showing a dependence of excitonic energy on the dimension of ZnO nano-objects [16,17]. One of these reports indicates confinement effects in polycrystalline ZnO-based films with grain size as the confined dimension [19]. Thus, tailoring the optical properties by varying structure, size, and composition of a material is of utmost importance. As an alternative, optical properties can also be tuned by using a template for deposition of thin films where self-organized substrates lead to conformal growth [20-22].

Recently, the efficacy of low energy ion-beam fabricated self-organized nanoscale ripple-patterned substrates has been demonstrated as templates to grow Ag nanoparticle arrays [20,22,23]. We have studied the conformal growth of Al-doped ZnO (AZO) overlayers on ion-beam synthesized nanofaceted-Si templates, leading to tunable antireflection property for improved solar cell performance [24]. In that case, height of the nanofacets was comparable to the wavelength of incident light. On the other hand, the vertical dimension of low energy ion-beam induced ripples (i.e. ripple amplitude) are orders of magnitude smaller compared to light wavelengths and hence, the growth of AZO overlayers on rippled-Si substrates should manifest very different optical properties. Thus, understanding the role of anisotropic rippled-Si templates in achieving size-dependent optical properties of AZO nanostructured thin films will be of importance for potential applications in nanophotonics.

In this paper, we report on growth of self-organized AZO thin films on rippled-Si templates to address morphological anisotropy-driven thickness-dependent tuning of their optical properties. As a comparative study, we also present our experimental results on AZO overlayers of same thicknesses simultaneously grown on pristine-Si substrates. Atomic force microscopy (AFM)-based morphological studies reveal the signature of conformal growth, giving rise to chain-like structures of AZO on rippled-Si templates (up to a thickness of 15 nm). On the other hand, growth of only granular AZO overlayers is observed on pristine-Si substrates. Photoluminescence (PL) study was performed at RT on both type of substrates to study thickness-dependent excitonic response. For instance, 10-nm-thick AZO film grown on rippled-Si shows a blue shift (6 nm) in the free excitonic peak (with respect to the same thickness grown on pristine-Si) which diminishes with increasing film thickness. The observed thickness-dependent blue shift is attributed to quantum confinement effect, originating from the AZO grain size and their spatial arrangement governed by underlying substrates having morphological anisotropy.

### 6.1.2 Experimental

For fabrication of rippled-Si templates, a *p*-type Si(100) wafer was sliced into small pieces (1 cm×1 cm) and these pieces were exposed to 500 eV Ar<sup>+</sup>-ions at an oblique incidence of 63° (with respect to the substrate surface normal). A fixed ion fluence of 5×10<sup>17</sup> ions cm<sup>-2</sup> was used corresponding to the ion flux of 1.3×10<sup>14</sup> ions cm<sup>-2</sup>s<sup>-1</sup>. Details of the experimental geometry is described elsewhere [25]. The ion-exposed substrates were subsequently transferred to a deposition chamber for growth of AZO films by using pulsed dc magnetron sputtering technique. Commercially available 99.99% pure (Testbourne, UK) ZnO:Al<sub>2</sub>O<sub>3</sub> (2 wt.%) target (5.08 cm diameter and 0.64 cm thick) was used for growth of AZO overlayers in a vacuum chamber with a base pressure of 3×10<sup>-7</sup> mbar. Ultra-pure (99.999%) argon gas was injected into the chamber with a flow rate of 30 sccm to maintain a working pressure of 5×10<sup>-3</sup> mbar

during sputtering. A pulsed dc power of 100 W (frequency = 150 kHz and reverse time = 0.4  $\mu$ s) was supplied (Advanced Energy, Pinnacle Plus) to the AZO target where the target-to-substrate distance was fixed at 10 cm. The deposition was carried out at an optimized angle of  $50^\circ$  with respect to the target normal [26]. Two sets of AZO films having thicknesses of 10, 15, and 30 nm were deposited simultaneously on pristine- (named as P1, P2, and P3, respectively) and rippled-Si (named as R1, R2, and R3, respectively) substrates with an average deposition rate of 5 nm  $\text{min}^{-1}$ . For AZO growth on rippled-Si templates, projection of the incoming flux was ascertained to be parallel to the direction of the ripple wave-vector (Fig. 6.1). The corresponding thicknesses were measured by using a surface profilometer (Ambios, XP-200).

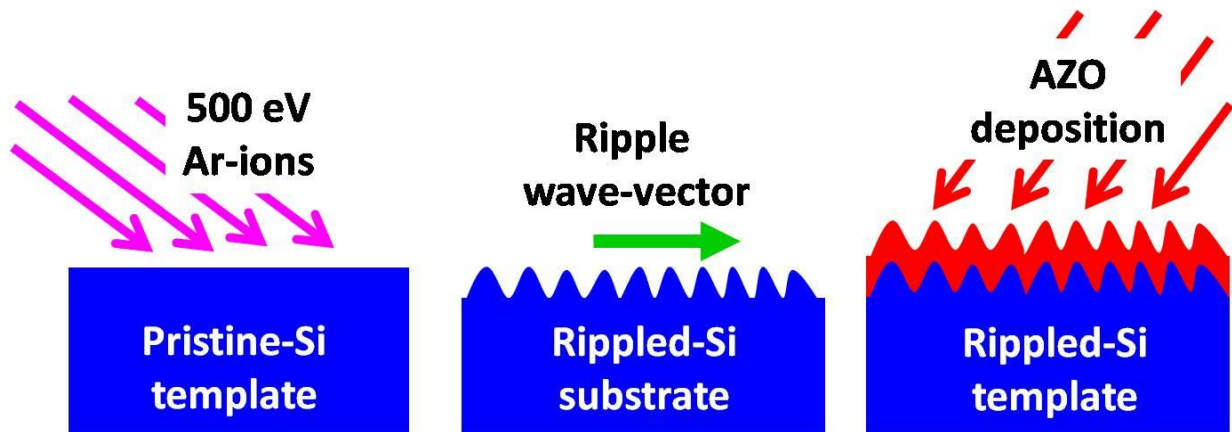


Figure 6.1 Schematic of the ion-beam fabrication of rippled-Si and its further usage as a template for growth of AZO films. The projection of incoming flux during deposition was kept same as that of the ion-beam projection onto pristine-Si surface for fabrication of ripples.

Phase identification and crystalline orientation were investigated by x-ray diffraction (XRD) (Bruker, D8 Advance) measurements, using a  $\text{Cu-K}\alpha$  radiation ( $\lambda=0.154$  nm) over a  $2\theta$  scan range of  $20^\circ$ – $60^\circ$ . Surface morphology was examined by *ex-situ* atomic force microscopy (Asylum Research, MFP3D) in tapping mode. For each sample, several images were taken from different regions to check the uniformity and to estimate the average grain size and root mean square (rms) roughness. AFM images were analyzed by using WSxM and Gwyddion softwares [27,28]. Cross sectional transmission electron microscopy (field emission gun based 300 keV

FEI Tecnai G2 S-Twin) studies were performed on selective samples for microstructural analysis. Optical properties of the deposited films were studied by using a photoluminescence spectrometer (Perkin Elmer, LS-55), having a Xe-lamp with excitation wavelength of 325 nm at RT. The compositional analyses of AZO overlayers were carried out by using x-ray photoelectron spectroscopy (VG Instrument).

### 6.1.3 Results and discussion

Figures 6.2(a)-(h) show AFM micrographs of rippled- and pristine-Si substrates before and after the growth of AZO overlayers of different thicknesses, viz. 10 nm, 15 nm, and 30 nm. Profilometric measurements show that the films are highly uniform in thickness (within 1 nm). From Fig. 6.2(a), we observe that the ripples have wavelength of  $28\pm 1$  nm and amplitude of 3 nm. Figures 6.2(b)-(d) depict the morphologies of R1, R2, R3 where corresponding two-dimensional (2D) fast Fourier transforms (FFT) are shown in the insets. These clearly illustrate the presence of anisotropy in the  $x$ -direction up to an AZO thickness of 15 nm. It may be pointed out that in Figs. 6.2(b) and (c), signature of the rippled templates after AZO growth is still visible. Thus, we can infer that the film morphologies have a bearing on the underlying ripple morphology up to the thickness of 15 nm and beyond that a granular morphology evolves [Fig. 6.2(d)]. On the other hand, films deposited on pristine-Si [Figs. 6.2(f)-(h)] substrates show only isotropic growth (as confirmed from 2D FFTs presented as insets on the respective AFM images) having granular morphologies.

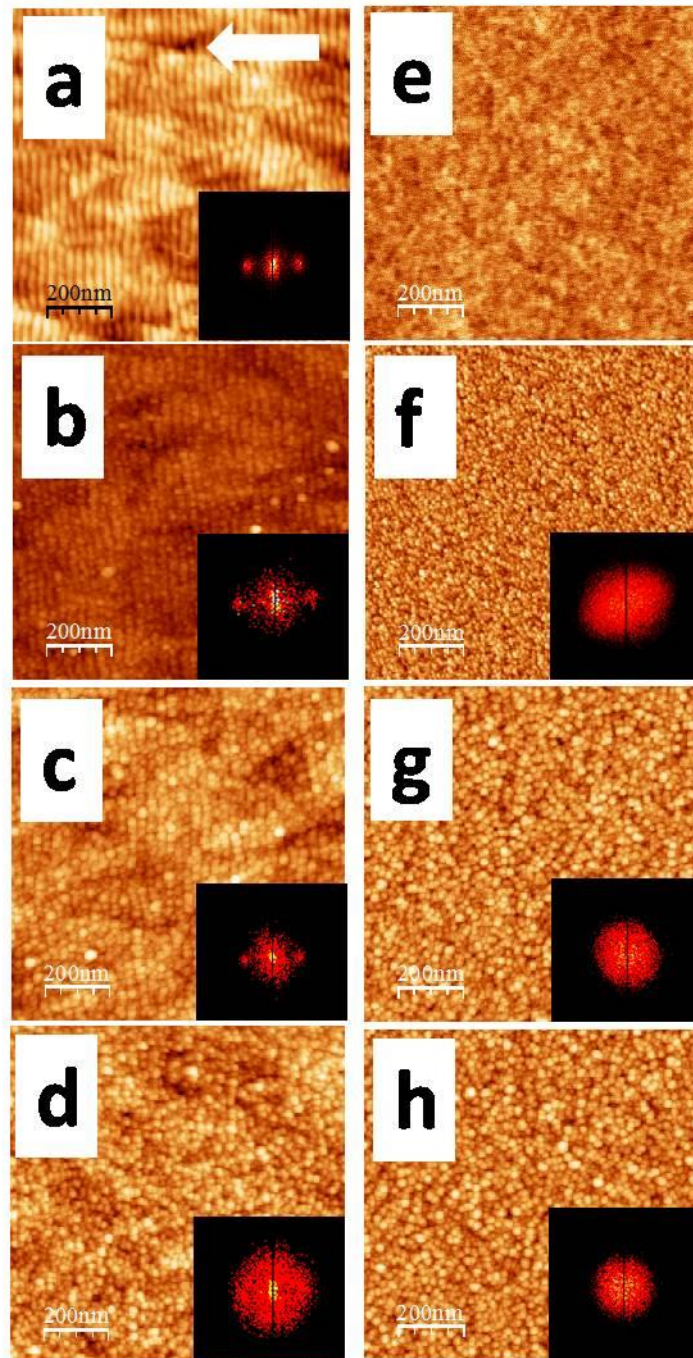


Figure 6.2: AFM images: (a) rippled-Si, (b) R1, (c) R2, (d) R3, (e) pristine-Si, (f) P1, (g) P2, and (h) P3. Insets are 2D FFT of the respective images. The white arrow in (a) indicates the projection of argon ion-beam onto the pristine-Si substrate. The height scales in (a)-(h) are: 6 nm, 9 nm, 10 nm, 12 nm, 1 nm, 6 nm, 8 nm, and 9 nm, respectively.

Various parameters, extracted from the AFM images, are summarized in Table 6.1. It is observed that rms roughness increases with thickness for films grown on both pristine- and rippled-Si substrates.

**Table 6.1: Various parameters extracted from AFM analyses**

Sample	rms roughness (nm)	Wavelength (nm)	Av. Grain size (nm)
Rippled-Si	0.76	$28 \pm 1$	--
Pristine-Si	0.098	--	--
R1	1.10	$28 \pm 1$	$15 \pm 2$
P1	0.60	--	$20 \pm 2$
R2	1.124	$28 \pm 1$	$25 \pm 2$
P2	0.64	--	$27 \pm 2$
R3	1.39	--	$28 \pm 2$
P3	1.03	--	$30 \pm 2$

Figure 6.3 shows XRD patterns obtained from samples R3 and P3 where the (002) reflection corresponding to hexagonal wurtzite structure is observed, implying the films are preferentially oriented along the *c*-axis. It may be mentioned that for lower film thicknesses (<30 nm), XRD signals were not strong enough and hence, corresponding microstructural analyses of those films were carried out using cross-sectional transmission electron microscopy (XTEM) in a selective manner.

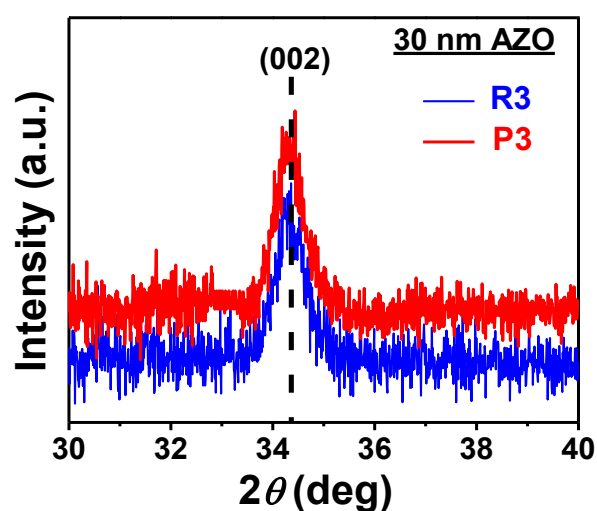


Figure 6.3: XRD spectra corresponding to 30 nm-thick AZO overlayers: R3 and P3.

Figure 6.4 presents XTEM data corresponding to the sample R2. The undulated nature (with wavelength of 28.8 nm) of the interface is evident from this XTEM image. Figure 6.4(a) reveals that the AZO overlayer of 15.9 nm thickness grows conformally (indicated by dashed yellow line) on the rippled-Si substrate covered with a thin native oxide layer. In addition, the columnar growth of AZO overlayer is obvious from this image [Fig. 6.4(b)] [26]. The presence of lattice fringes in the high-resolution TEM (HRTEM) image [Fig. 6.4(b)] indicates the high quality of the conformally grown AZO film. The calculated  $d$ -spacing from the zoomed portion of the HRTEM image [Fig. 6.4(c)] turns out to be 0.26 nm which matches well with the  $d_{002}$  of wurtzite ZnO [29]. Thus, the XTEM data corroborates well with our XRD data corresponding to 30 nm-thick films described above.

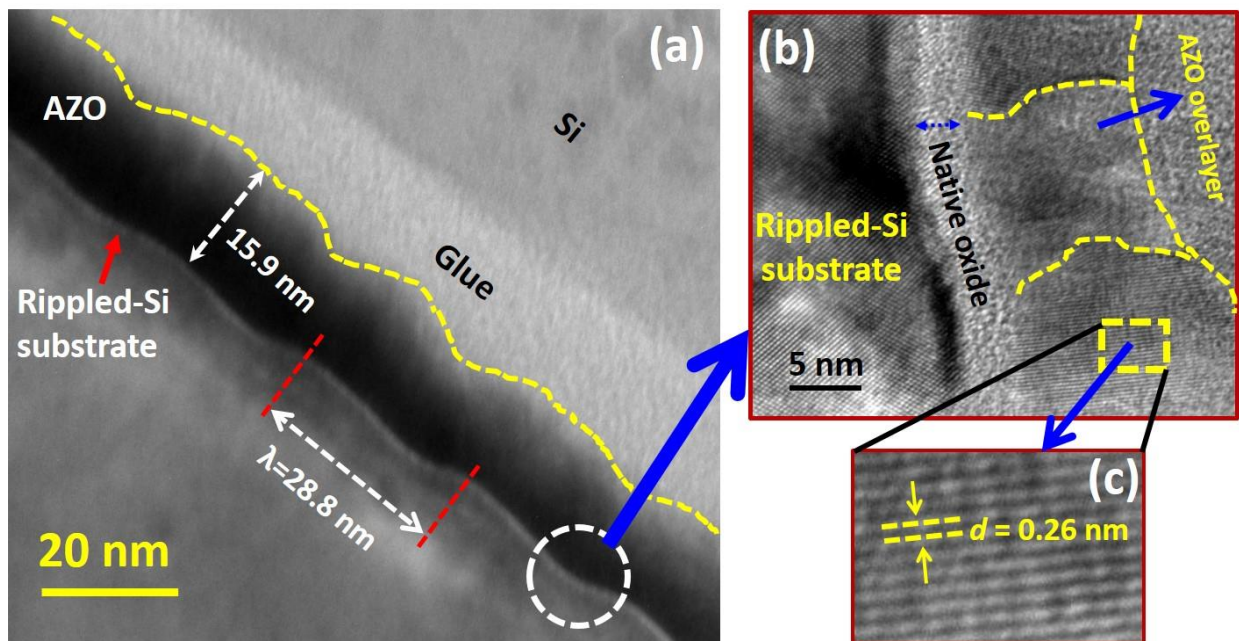


Figure 6.4: (a)-(c) present XTEM micrographs corresponding to R2: (a) Low-magnification image, showing a uniform and conformal growth of AZO on the native oxide covered rippled-Si substrate, (b) HRTEM image obtained from the marked region on (a), showing the interface regions of native oxide covered rippled-Si substrate and AZO overlayer, where columnar growth of AZO film is demonstrated by dashed yellow lines on the same. (c) HRTEM image taken from the marked region on (b), which shows lattice fringes.

Compositional analyses of AZO films were carried out by x-ray photoelectron spectroscopy (XPS) measurements. The survey spectra (not shown) of all samples do not reveal the presence of any undesirable species (impurity). Figures 6.5(a)-(d) depict Zn 2*p* and O 1*s* core level spectra corresponding to two AZO films deposited on rippled-Si. In particular, Figs. 6.5(a) and (b) correspond to sample R1 while 6.5(c) and (d) represent R2. In order to maintain the clarity, we have not presented the XPS spectra corresponding to the sample R3. Details of the XPS analyses for all AZO films deposited on rippled-Si substrates are summarized in Table 6.2. It is observed that XPS spectra of the Zn 2*p*<sub>3/2</sub> and Zn 2*p*<sub>1/2</sub> levels are nearly centered at binding energy values of around 1021.4 eV and 1044.5 eV, respectively, corresponding to Zn atoms at regular sites of an AZO lattice. The difference in the binding energies of Zn 2*p*<sub>3/2</sub> and Zn 2*p*<sub>1/2</sub> is found to be 23.1 eV, which is a characteristic value of AZO [30,31]. On the other hand, individual O1*s* peak is deconvoluted to have three distinct curves centered at binding energies around 530, 531.4, and 532.1 eV. The lowest binding energy curve at 530 eV is attributed to O atoms at regular lattice site (O<sub>L</sub>). In other words, the intensity of this peak is a measure of the amount of oxygen atoms in a fully oxidized stoichiometric surrounding [30,32]. The intermediate binding energy of 531.4 eV is associated with O atoms in the oxygen deficient regions (O<sub>v</sub>) within the AZO matrix and the peak corresponding to the binding energy of 532.1 eV is attributed to the presence of interstitial O atoms (O<sub>i</sub>) or non-stoichiometric oxygen, belonging to either of the species such as adsorbed H<sub>2</sub>O or O<sub>2</sub> on the surface of AZO films [30,32].

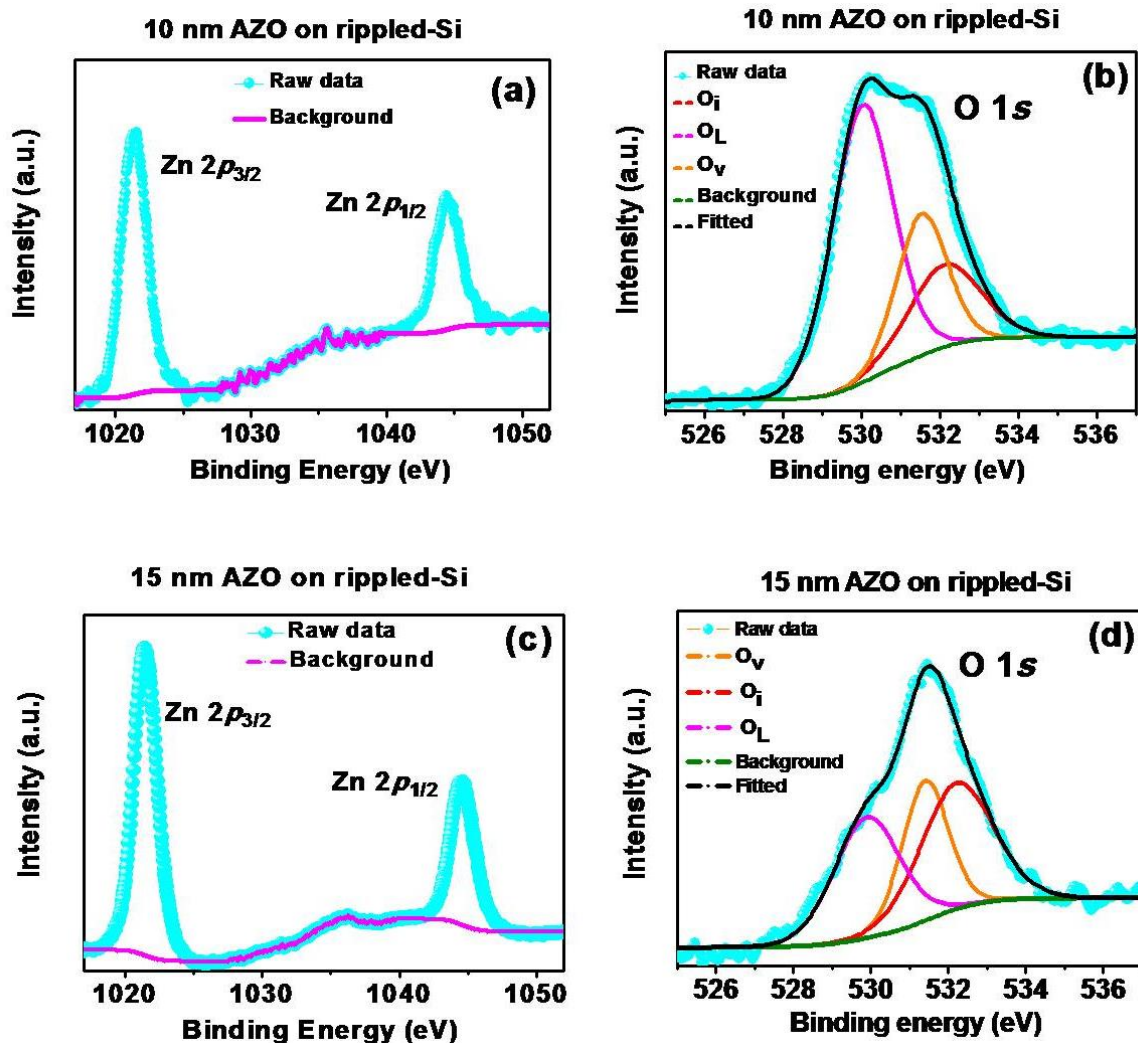


Figure 6.5: Core-level Zn2*p* and O1*s* spectra of AZO films having thicknesses of 10 nm [(a)-(b)] and 15 nm [(c)-(d)] grown on rippled-Si templates.

It is observed from Table 6.2 that, with increasing AZO thickness, the concentration of interstitial O ( $O_i$ ) increases and reaches its maximum (63.23%) for the 30 nm-thick film. On the other hand, the concentration of  $O_v$  shows a random behaviour for film thickness greater than 15 nm, although its origin is not clear to us at this point. It may be mentioned that XPS analyses of samples P1, P2, and P3 (which show granular morphologies) yield similar results and hence, are not presented here. Another crucial observation is that simultaneously the concentration of regular oxygen atoms at regular lattice sites reduces from 56.27% to 20.41% as a function of AZO film thickness.

**Table 6.2: Results of XPS analyses for AZO films grown on rippled-Si templates**

Sample	Binding energy (eV)	Composition	Relative percentage
R1 (O1s)	529.9	O <sub>1s</sub> , O <sub>L</sub>	56.27
	531.4	O <sub>1s</sub> , O <sub>v</sub>	23.92
	532.2	O <sub>1s</sub> , O <sub>i</sub>	19.81
R2 (O1s)	530.03	O <sub>1s</sub> , O <sub>L</sub>	33.80
	531.53	O <sub>1s</sub> , O <sub>v</sub>	27.41
	532.11	O <sub>1s</sub> , O <sub>i</sub>	38.79
R3 (O1s)	530.05	O <sub>1s</sub> , O <sub>L</sub>	20.41
	531.5	O <sub>1s</sub> , O <sub>v</sub>	16.36
	532.1	O <sub>1s</sub> , O <sub>i</sub>	63.23

PL spectra collected at RT for films deposited on both pristine- and rippled-Si templates are shown in Fig. 6.6. All the samples exhibit complex PL spectra with several bands, covering both UV and visible ranges (350-500 nm). The peak in the UV region corresponds to the free excitonic emission, which is also referred to as the near band-edge emission. This excitonic peak is located around 376 nm in all AZO films deposited on pristine-Si substrates. It is observed that for both type of substrates, intensity of the excitonic peak reduces with increasing film thickness and a broad band in the visible region starts dominating for the whole spectra (corresponding to the highest thickness of 30 nm). It is generally accepted that the signal in the visible range arises from excitons that are bound to acceptor and donor defects (bound excitons) [33,34]. As a matter of fact, these bound excitons are trapped by the intrinsic defects in the films which correspond to various energy states for deep level emission. This corroborates well with our XPS studies, confirming the presence of defects like O<sub>v</sub> and O<sub>i</sub> which are known to cause emission in the visible region [35].

It is well-known that ZnO is a polar compound and hence, its thin polar films [36-38] can easily adsorb radical species. The XPS results support this polarity effect in case of AZO films

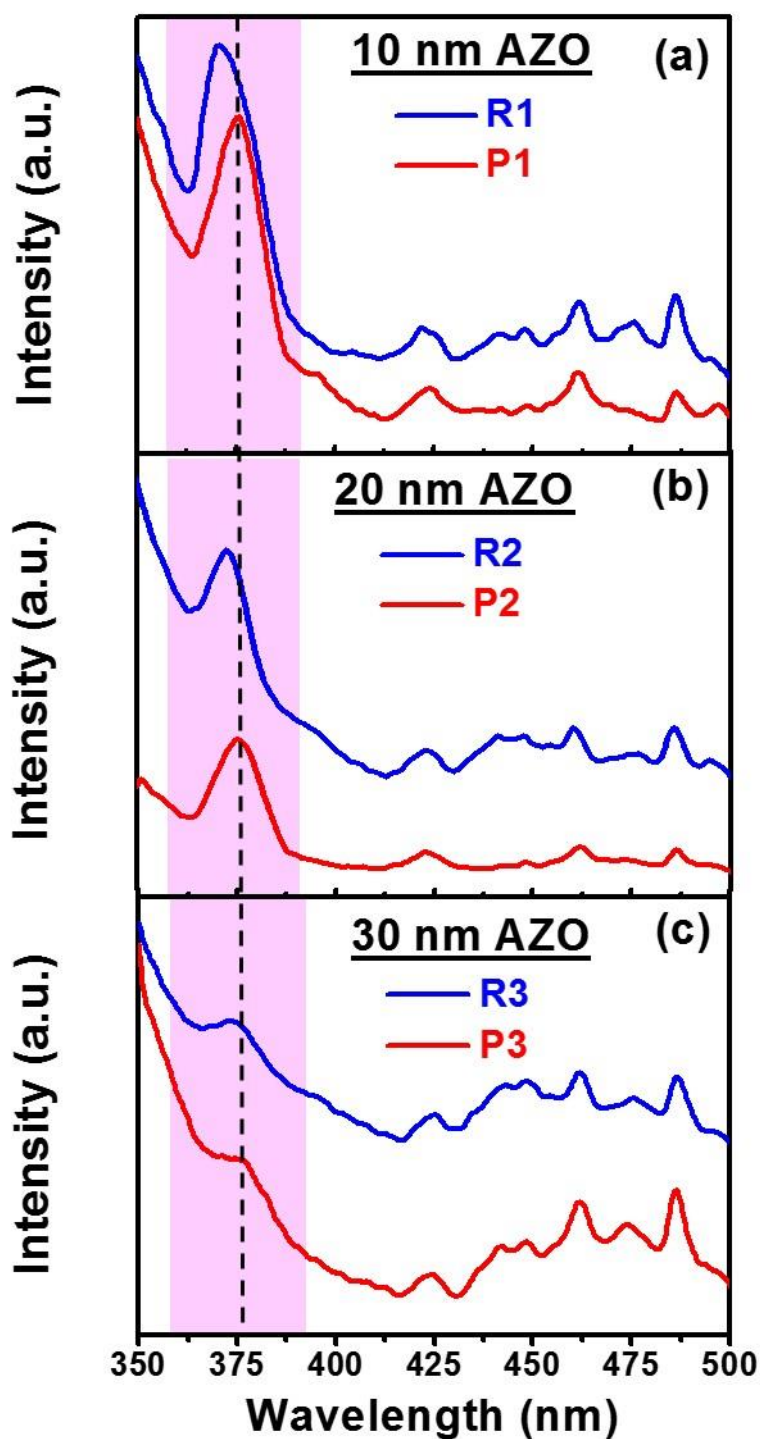


Figure 6.6: PL spectra of AZO films recorded at room temperature: (a) 10 nm, (b) 15 nm, and (c) 30 nm-thick films on pristine- and rippled-Si substrates.

as well, since adsorbed OH species are identified from the  $O1s$  (at around 532.1 eV binding energy) spectra. The free excitonic emission is known to be suppressed in the presence of these adsorbed species [39]. Thus, reduction in the intensity of the excitonic emission line, with

increasing AZO thickness, can be attributed to the higher amount of adsorbed radical species at the surface of AZO films.

Another key observation from our PL studies is the blue shift in case of AZO samples deposited on rippled-Si substrates (viz. R1 and R2) with respect to those of similar thicknesses deposited on pristine-Si substrates (viz. P1 and P2). For instance, R1 shows the maximum shift of 6 nm with respect to its counterpart, P1. On the other hand, for R2, the excitonic peak shift reduces to 3 nm (with respect to P2), whereas R3 shows hardly any blue shift.

In order to understand such a PL behaviour in case of R1, R2, and R3 (compared to P1, P2, and P3, respectively), we have presented the AFM phase contrast image of sample R1 in the inset of Fig. 6.7. It is known that, in general, an AFM phase image gives a better resolution [40] and it is possible to detect very small features which may otherwise remain hidden in the normal topographic images. A careful observation of the inset in Fig. 6.7 reveals that bigger grains of R1 are comprised of very small grains (marked by green peripheral lines) having an average size of ~15 nm and they are arranged conformally with respect to the underlying rippled-Si substrate. However, this conformal nature of AZO grains disappears for 30 nm-thick film (as discussed earlier).

In a recent paper, Nie *et al.* mentioned that due to the quantum confinement effect, smaller mean grain size of films leads to increased excitonic peak energy [19]. The present experimental results indicate that not only the size of the grains are important to cause confinement of the free excitons, but also their spatial arrangement is equally important. According to Nie *et al.*, the band gap energy of the confined nanostructures can be expressed as  $E_g(\text{eV}) = E_{g,\text{bulk}} + A/D^2$ , where  $E_{g,\text{bulk}}$  is the band gap for the bulk material,  $A$  is the quantum confinement constant, and  $D$  is the grain size. Here we consider,  $E_{g,\text{bulk}} = 3.37$  eV,  $A = 6.8$ , and  $D = 15$  nm (corresponding to R1) [19]. Putting these values in the above expression, one obtains  $E_g$  to be 3.4 eV which is very close to the value corresponding to the excitonic peak appearing

at 370 nm (or 3.35 eV) for R1. On the other hand, for R2, the average grain size turns out to be 25 nm. Thus, using the above relation,  $E_g$  turns out to be 3.38 eV, whereas the experimental excitonic peak appears at 3.33 eV. These calculations demonstrate a probable free excitonic confinement in case of chain-like AZO structures grown anisotropically on rippled-Si. In contrast, for a 30 nm-thick AZO film grown on rippled-Si (i.e. R3), albeit the average grain size is ~28 nm, we do not see any aligned chain-like features as well as any meaningful blue shift of the excitonic peak ( $E_g=3.37$  eV). This may be attributed to the fact that this value is greater than the upper limit of the critical grain size up to which quantum confinement effect was observed for ZnO [19].

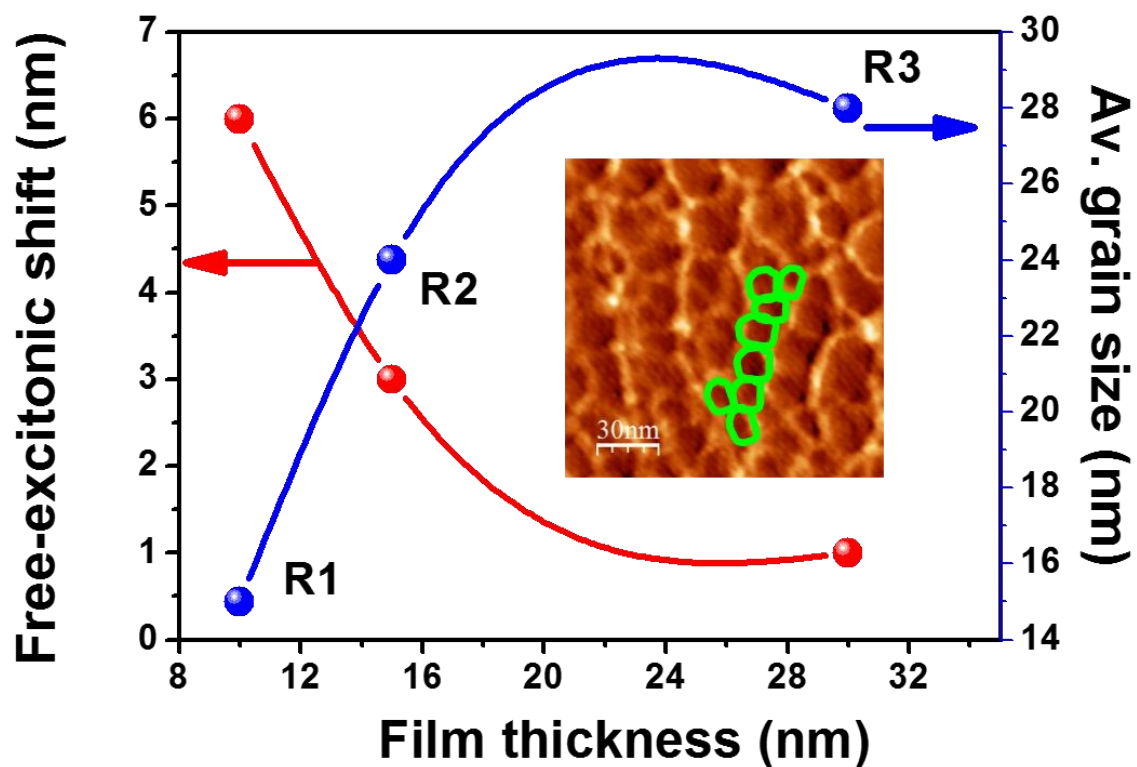


Figure 6.7: Variations in free excitonic shift and average grain size of R1, R2, and R3 as a function of thickness. The inset shows AFM phase contrast image of R1, where the presence of smaller grains are evident (marked by green closed loops). The range of the scale bar in this case is  $-3^\circ$  to  $+12^\circ$ . The solid lines are guide to the eyes.

Fig. 6.7 presents the variations in the excitonic peak shift and the average grain size (for AZO films grown on rippled-Si templates) as a function of AZO thickness, which show opposite

trends. Although there is a slight mismatch between the experimental and theoretically calculated values of  $E_g$  for R1, R2, and R3, the observed trend in blue shift matches well with Fig. 6.7. It may be mentioned that for all AZO films grown on pristine-Si substrates (i.e. P1, P2, and P3), the excitonic peak appears at 376 nm (or 3.297 eV), indicating the absence of any blue shift for these granular films (showing an isotropic morphology). For instance, for a 10 nm-thick AZO film grown on pristine-Si (i.e. P1), the average grain size turns out to be ~20 nm but still no blue shift is observed (with respect to P2) [Figs. 6.6(a) and (b)]. Further, no PL signal is observed from as-prepared rippled-Si substrates as well. Thus, our investigations suggest that the undulated Si substrates underneath, having morphological anisotropy, help excitons to get spatially confined by forming chain-like structures.

#### **6.1.4 Conclusions**

In summary, we have shown the use of self-organized nanoscale rippled-Si substrates as a potential template to grow AZO thin films and modify their thickness-dependent optical properties. Free excitonic emission of AZO thin films, deposited by pulsed dc magnetron sputtering, with varying thicknesses (10, 15, and 30 nm), is investigated for pristine- and rippled-Si substrates. Films deposited on pristine-Si substrates are granular in nature, whereas AZO films of thicknesses 10 and 15 nm, grown on rippled-Si substrates, give rise to the formation of self-organized chain-like structures. On the other hand, for 30 nm-thick film grown on rippled-Si template, the chain-like morphology disappears and instead a randomly arranged granular morphology evolves. Further, 10 and 15 nm-thick AZO overlayers on rippled-Si, show blue shift in the excitonic peak which is attributed to quantum confinement effect and spatial arrangement of AZO grains driven by the morphology of the underlying rippled-Si templates. The observed trend of shift in the position of the free excitonic peak matches well with the theoretical calculations by taking into account the quantum confinement effect. It is also concluded that due to the polar nature of AZO, the absorbed species like H<sub>2</sub>O

and OH on the surface of the AZO samples suppress the free excitonic emission with increasing film thickness.

## **6.2 Growth of AZO on nanofaceted Si**

### **6.2.1 Tunable antireflection from conformal Al-doped ZnO films on nanofaceted Si templates**

#### **6.2.1.1 Introduction**

Aluminium-doped ZnO – a transparent conducting oxide (TCO) is becoming increasingly popular, not only for the study of optical properties but as a window layer and top electrode, for next generation highly efficient silicon-based heterojunction solar cells[41-44]. An essential criterion to enhance the efficiency of silicon-based solar cells is to reduce the front surface reflection. However, commercial silicon wafers show surface reflection more than 30% [45]. Such a high level of reflection can be minimized by growing a suitable antireflection (AR) coating, preferably in the form of a TCO. On the basis of thin film interference property, these dielectric coatings reduce the intensity of the reflected wave. However, this approach needs a large number of layers to achieve well-defined AR properties. In addition, coating materials with good AR properties and low absorption in the ultraviolet (UV) range is rare in the literature. An alternative to the lone usage of dielectric coating is therefore, required that can overcome some of these difficulties.

An optimal antireflective surface should contain subwavelength features where the index matching at the substrate interface leads to improved AR performance. For instance, by using a surface texture on TCO (e.g. AZO) [46] and/or Si substrate[47] one can govern the light propagation and in turn the AR property due to the formation of graded refractive index [48,49]. In particular, for solar cell applications, a patterned AZO film on a flat silicon substrate shows a significant decrease in average reflectance up to 5% [50] whereas a thick AZO layer on silicon nanopillars is found to give an overall reflectance of ~10% [47]. In the latter case, a

higher photocurrent density was achieved ( $5.5 \text{ mA cm}^{-2}$ ) as compared to AZO deposited on planar silicon ( $1.1 \text{ mA cm}^{-2}$ ). It is, therefore, exigent to have more control on pattern formation and optimization of AZO thickness to achieve improved AR performance.

Majority of the patterning processes are based on conventional lithographic techniques [51]. As a result, these are time consuming and involve multiple processing steps. On the other hand, low energy ion-beam sputtering has shown its potential as a single step and fast processing route to produce large area (size tunable), self-organized nanoscale patterned surfaces [22]—compatible to the present semiconductor industry and thus, may be considered to be challenging to develop AR surfaces for photovoltaics.

In our study, we show the efficacy of one step ion-beam fabricated nanofaceted silicon templates [52] for growth of conformal AZO overlayer and correlate its thickness-dependent (in the range of 30-90 nm) AR property. We show that growth of an optimum AZO overlayer thickness can help achieving maximum reduction in surface reflectance. As a possible application of such heterostructures in photovoltaics, photoresponsivity of AZO deposited on pristine and faceted Si has also been investigated. The results show that by using nanofaceted silicon templates it is possible to enhance the fill factor ( $FF$ ) of the device by a factor of 2.5.

### **6.2.1.2 Experimental**

The substrates used in the experiments were cut into small pieces (area:  $1 \times 1 \text{ cm}^2$ ) from a  $p$ -Si(100) wafer. An ultrahigh vacuum (UHV)-compatible experimental chamber [Prevac, Poland] was used which is equipped with a 5-axes sample manipulator and an electron cyclotron resonance (ECR)-based broad beam, filamentless ion source [GEN-II, Tectra GmbH, Germany]. Silicon pieces were fixed on a sample holder where a sacrificial silicon wafer ensured a low impurity environment. The beam diameter and the fixed ion-flux were measured to be 3 cm and  $1.3 \times 10^{14} \text{ ions cm}^{-2} \text{ s}^{-1}$ , respectively. Corresponding to this flux of 500 eV  $\text{Ar}^+$

ions, the rise in sample temperature is expected to be nominal from room temperature (RT). Experiments were carried out at an ion incidence angle of  $72.5^\circ$  (with respect to the surface normal) and for an optimized fluence of  $3 \times 10^{18}$  ions  $\text{cm}^{-2}$  to fabricate nanofaceted silicon templates. The substrates were immediately transferred to the sputtering chamber (base pressure  $3 \times 10^{-7}$  mbar) for growth of AZO overlayers. A commercial (purity 99.99%) target [Testbourne, UK] composed of  $\text{ZnO}:\text{Al}_2\text{O}_3$  (2 wt.%) was used for deposition of AZO films at RT and at an optimized angle of  $50^\circ$ . During film growth, the argon gas flow rate was maintained at 30 sccm resulting in the working pressure of  $5 \times 10^{-3}$  mbar. The distance from the sample to the target was 10 cm and the pulsed dc power was maintained at 100 W. Figure 6.8 shows a schematic representation of the process flow towards the synthesis of nanofaceted silicon and the growth of AZO overlayer on the same thicknesses (in the range of 30-90 nm) were measured by using a surface profilometer [Ambios, XP-200, USA].

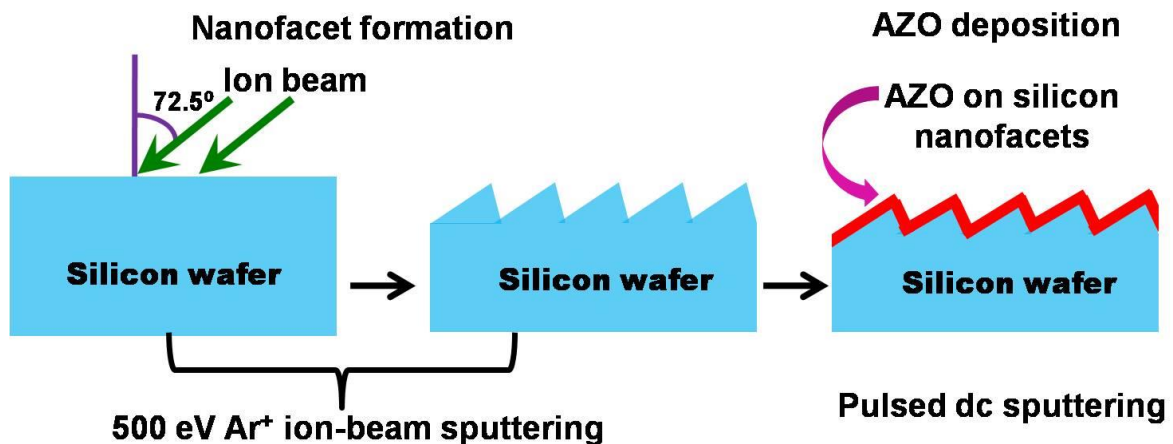


Figure 6.8: Flow chart for ion-beam fabrication of nanofaceted Si followed by conformal growth of AZO films on the same.

Field emission scanning electron microscopy (SEM) [Carl-Zeiss, Germany] was employed to study the sample microstructures and to ensure the uniformity of the structures. Sample morphologies were studied by using an atomic force microscope (AFM) [Asylum Research, MFP3D, USA] in the tapping mode. AFM images were analysed by using WSxM and

Gwyddion softwares [27,28]. Crystallinity and phase identification of the films were investigated by x-ray diffraction (XRD) [Bruker, D8-Discover, Germany] whereas the optical reflectance measurements were carried out by using a UV-Vis-NIR spectrophotometer [Shimadzu, 3101PC, Japan] in the wavelength range of 300-800 nm with unpolarized light. A specular geometry was used for these measurements where the incident light fell on the target at an angle of  $45^{\circ}$  with respect to the surface normal. Photoresponsivity studies were performed out using a spectral response system [Sciencetech, Canada] under air mass 0 and 1 sun illumination conditions in the spectral range of 300-800 nm. The incident light power was measured with a calibrated silicon photodiode at wavelengths below 1100 nm and the spectra were normalized to the power. In the reflectance measurement, we recorded the data corresponding to specular reflectance values only. It may be mentioned that all the reflectance spectra shown in the present thesis do not contain any contribution from diffuse reflectance.

### 6.2.1.3 Results and discussion

Figure 6.9(a) shows the SEM image of a typical ion-beam fabricated silicon template under consideration, manifesting distinct faceted morphology with striations on its walls. Corresponding AFM image, shown in Fig. 6.9(b), indicates that the Si facets are oriented in the direction of incident ion-beam. Analysis of this image provides rms roughness value of 52.5 nm whereas the average silicon facet height turns out to be  $\sim 180$  nm. Two-dimensional (2D) fast Fourier transform (FFT) image, obtained by using Gwyddion software, is depicted in the inset of Fig. 6.9(b) where a clear anisotropy in the surface morphology is visible along the direction perpendicular to the ion-beam projection onto the surface. One-dimensional (1D) power spectral density as well as autocorrelation function (not shown here), along both  $x$ - and  $y$ -directions, do not reveal any periodicity in case of Si nanofacets. This corroborates well with the absence of any distinct spots symmetrically spaced about the central spot seen in the FFT image. Figures 6.9(c) and (d) depict the morphologies of nanofaceted Si templates after

deposition of AZO overlayers having nominal thicknesses of 30 and 75 nm, respectively. Both these

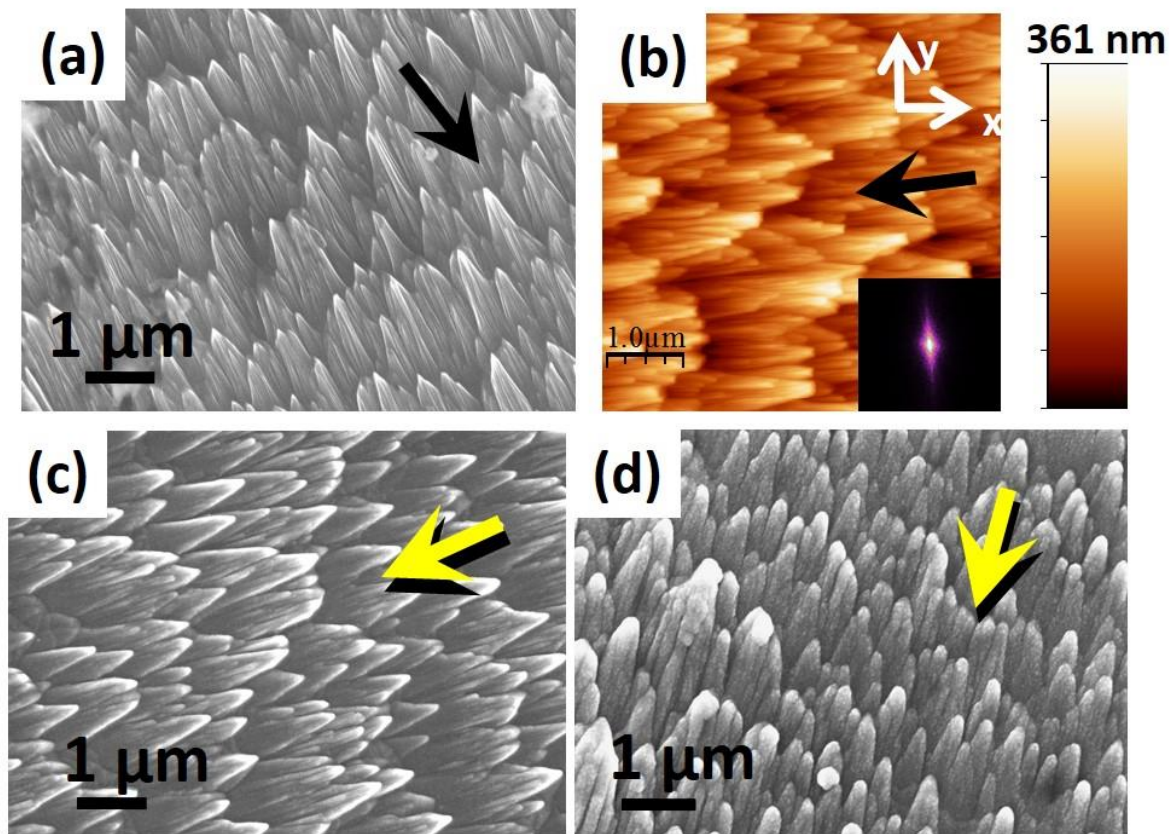


Figure 6.9: Plan-view SEM images: (a) Faceted-Si nanostructures, (b) AFM topographic image where inset shows the 2D FFT, (c) and (d) after growing AZO films on nanofaceted Si having thicknesses of 30 and 75 nm, respectively. The black arrows indicate the direction of ion-beam bombardment whereas the yellow arrows represent the direction of AZO flux during sputter deposition.

images clearly manifest the conformal growth of AZO on Si facets albeit, with increasing AZO thickness, sharpness of the facets reduces and they gradually transform from conical shapes into rod-like structures. Figure 6.9(d) documents the existence of nanoscale grains on the conformally grown AZO facets.

The elemental composition of these samples was studied by energy dispersive x-ray spectrometry (EDS) analysis which does not reveal the presence of any metallic impurity in these facets. A representative EDS spectrum corresponding to the 60 nm-thick AZO film on

nanofaceted-Si is depicted in Fig. 6.10(a). Thickness dependent EDS study demonstrates that concentration of Zn increases with increasing film thickness, while that of silicon decreases rapidly [Fig. 6.10(b)].

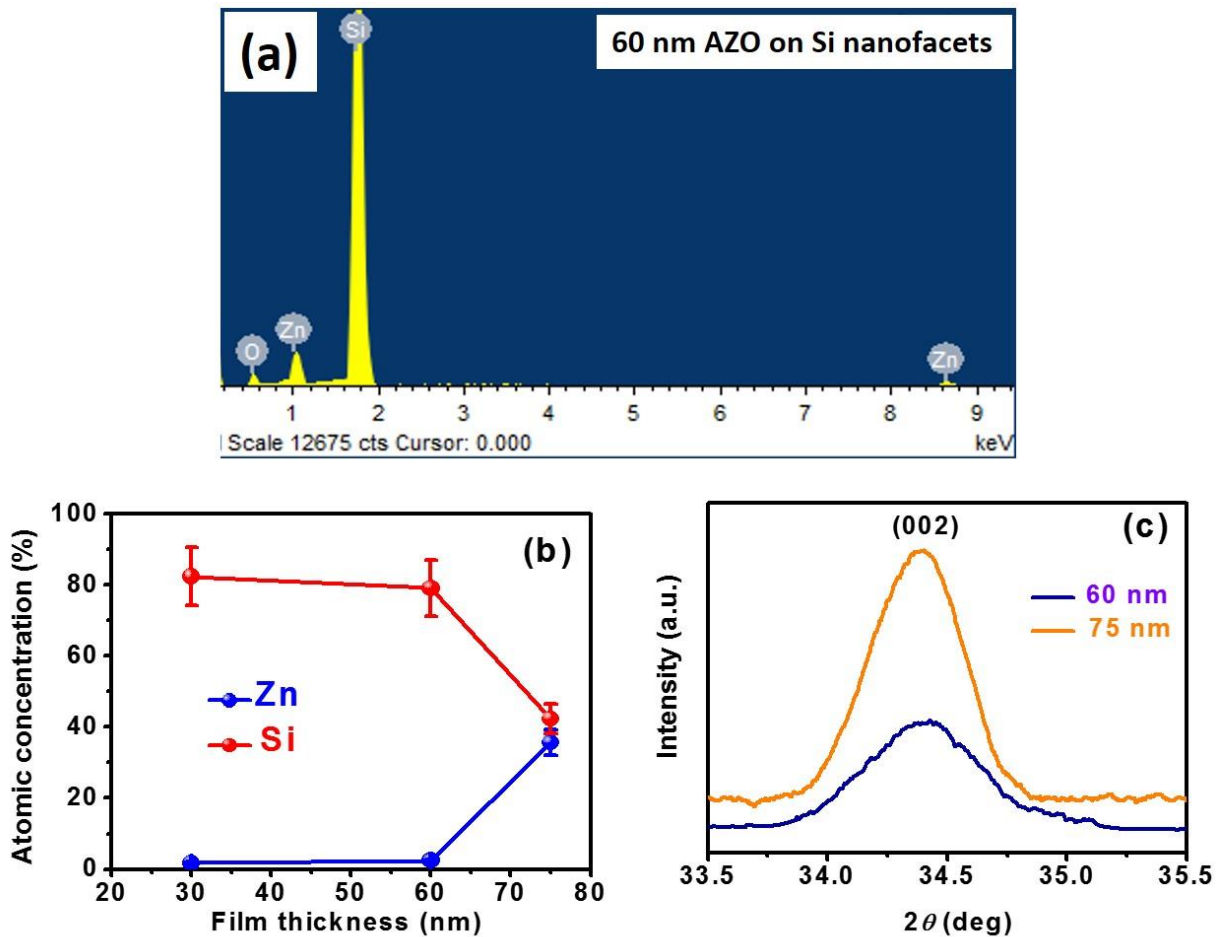


Figure 6.10: (a) Representative EDS spectrum of 60 nm thick AZO overlayer grown on Si nanofacets, showing the presence of Si, Zn, and O; (b) plot of atomic concentration versus AZO overlayer thickness obtained from EDS analyses. The solid lines are guide to the eyes; (c) X-ray diffractograms of AZO films grown on nanofaceted silicon. The signal corresponding to the 30 nm thick AZO overlayer is not strong and therefore, the corresponding diffractogram is not shown here.

Subsequent elemental mapping exhibits Zn-rich apex of the conformally grown AZO faceted structures. Morphological evolution for AZO overlayer more than 75 nm thick is not presented here since the reflectance minimum goes beyond the spectral range (will be discussed later). Crystalline nature of the AZO overlayers was revealed from XRD studies [Figure 6.10(c)]; where the appearance of only one peak, in addition to the substrate silicon signal (not shown),

can be attributed to the oriented nature of grains. This peak, at all thicknesses, matches well with the (002) reflection of the hexagonal wurzite phase of AZO indicating a preferential growth along the *c*-axis [53]. The average grain size determined from Scherrer's formula is seen to grow bigger with increasing AZO thickness [54]. This corroborates well with the grain size analysis performed on the basis of the SEM studies.

The key result is the change in surface reflectance with increasing AZO thickness on nanofaceted Si templates (Fig.6.11). In particular, it presents the reflectance data of pristine and faceted silicon along with those obtained from AZO films of varying thicknesses [Fig. 6.11(a)]. Due to the faceted structures, the calculated average residual reflectance [55], over the spectral range of 300-800 nm, reduces by 58.5% (compared to that of pristine Si). It is evident from Fig. 6.11(a) that upon coating the Si template (nanofaceted Si substrate) by a 30 nm thick AZO film, it exhibits a low average residual reflectance of 6.4% whereas conformally grown 60 nm thick AZO film leads to a further reduction down to 3.1%. However, an increased film thickness of 75 nm causes a nominal increase in the average residual reflectance up to 3.8% which increases further for thicknesses higher than this. A careful observation of the reflectance spectra reveals that the local reflectance minimum of each spectrum (corresponding to different AZO film thickness) gets red shifted [Fig. 6.11(b)]. For instance, 30 nm thick AZO film shows reflectance below 1% for a spectral range of 385-445 nm with a local minimum of ~0.5% at 415 nm. Likewise, for the 60 nm thick overlayer, this range shifts to 530-655 nm and the minimum reflectance is found to be ~0.3% at 585 nm. Further increase in AZO layer thickness (75 nm) leads to the minimum reflectance of ~0.5% at 745 nm. Such shifts in the local minima were previously reported by Boden *et al.* [56] for an antireflective Si surface. Thus, one can infer that tunable AR property of conformally grown AZO films on nanofaceted Si templates can be achieved by varying the thickness and there exists a critical thickness (60

nm in the present case) which exhibits the best AR performance over the given spectral range (300 to 800 nm).

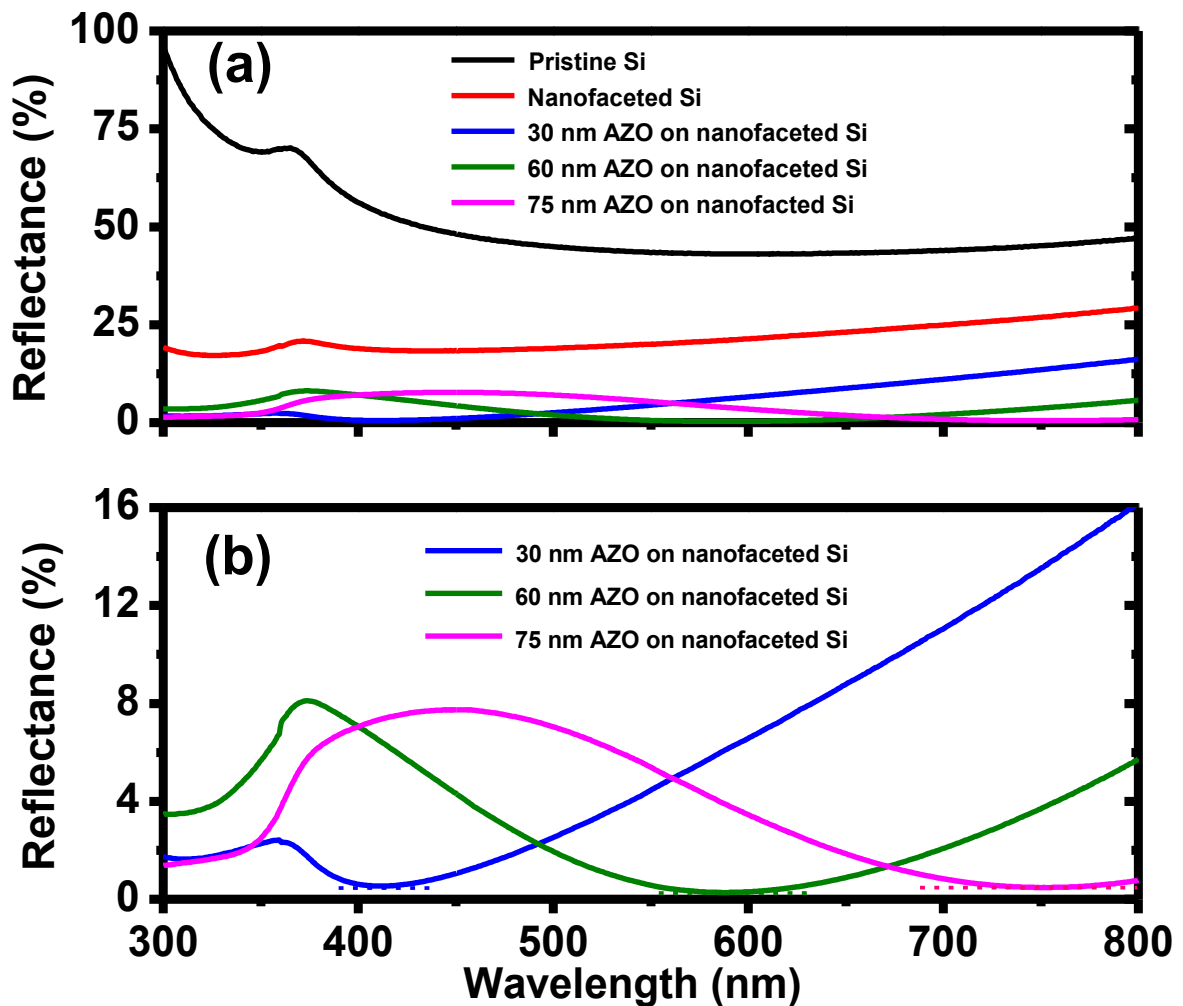


Figure 6.11: (a) Reflectance spectra corresponding to pristine-Si, nanofaceted-Si, and AZO overlayers grown on faceted Si having thicknesses of 30 nm, 60 nm, and 75 nm. (b) Reflectance spectra obtained from 30, 60, and 75 nm thick AZO films deposited on faceted Si where the dashed line corresponds to the domain of reflectance minima for different AZO layer thickness (all the reflectance spectra shown here do not contain any contribution from diffuse reflectance).

It may be mentioned that effect of the experimental geometry was tested by subsequent measurement of the surface reflectance after giving a perpendicular rotation to the samples. However, no difference in the reflectance values (within the experimental error) was observed in both cases. To understand this behaviour we calculated the average aspect ratio of the faceted structures (i.e. height : lateral dimension) along  $x$ - and  $y$ -directions which turned out to be 0.25

and 0.24, respectively. It is well-known that reflectance depends on the aspect ratio of the surface features [57].

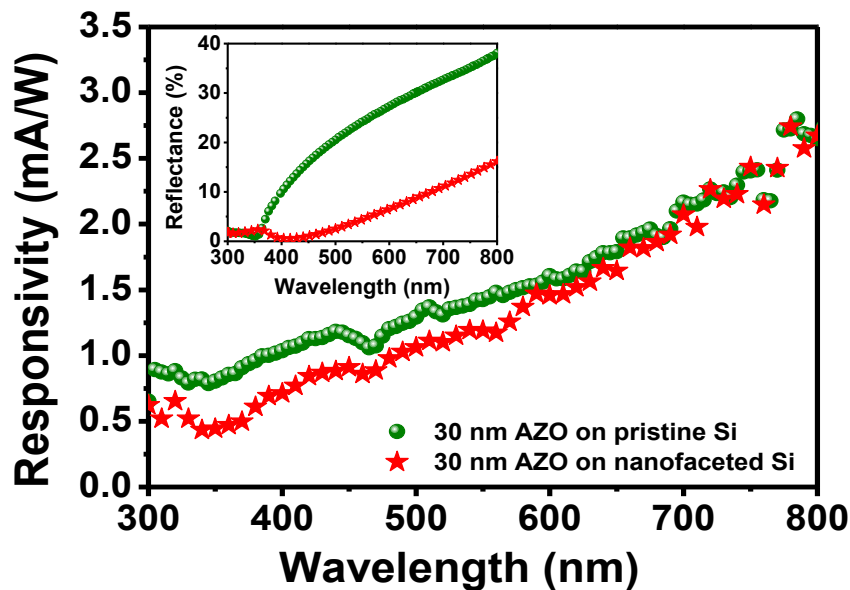


Figure 6.12: Photoresponsivity spectra of 30 nm thick AZO overlayer grown on planar and nanofaceted Si in the spectral range of 300-800 nm. The inset shows the optical reflectance spectra for these two samples mentioned above.

Thus, the observed absence of change in surface reflectance, due to different directions of incident light, can be attributed to the comparable aspect ratio of the faceted structures along  $x$ - and  $y$ -directions.

Figure 6.12 shows RT photoresponsivity of two sets of samples, viz. 30 nm AZO deposited on pristine and faceted silicon. It is observed that the photoresponsivity reduces in case of the latter one in the projected wavelength range. Different parameters such as short circuit current densities ( $J_{SC}$ ), open-circuit voltages ( $V_{OC}$ ), and  $FF$  for the above samples are summarized in Table 6.3 under air mass zero and 1 sun illumination condition for other AZO thicknesses as well. The  $FF$  is defined as  $FF = (V_M J_M) / (V_{OC} J_{SC})$  where  $V_M J_M$  is the maximum power density.

From Table 6.3, one can see that the  $FF$  increases by a factor of two in case of AZO overlayer grown on faceted silicon as compared to the one on pristine silicon, whereas  $V_{OC}$  is found to be

half the value obtained from the latter one. In addition,  $J_{SC}$  becomes one order of magnitude higher in case of AZO-coated faceted silicon and the same trend is followed for higher AZO thicknesses. From Table 6.3, it is observed that the  $FF$  reaches maximum at 60 nm AZO on faceted silicon (0.361) as compared to others. This improvement in  $FF$  can be attributed to the effective light trapping in the visible region in case of conformally grown AZO films on nanofaceted silicon template [58].

**Table 6.3**

Sample	$J_{sc}$ (mA/cm <sup>2</sup> )	$V_{oc}$ (V)	$FF$
30 nm AZO on Pristine-Si*	$1.24 \times 10^{-3}$	0.133	0.142
30 nm AZO on Nanofaceted-Si	$3.0 \times 10^{-2}$	0.075	0.279
60 nm AZO-on nanofaceted-Si	$5.35 \times 10^{-2}$	0.087	0.361
75 nm AZO on nanofaceted-Si	$37.57 \times 10^{-2}$	0.055	0.252

\* Higher AZO thicknesses (beyond 30 nm) deposited on planar silicon substrate did not show any significant photoresponsivity.

This would ensure the usage of more photo generated power leading to an increase in the cell efficiency. Such enhancement in light trapping is found to be directly associated with the enhanced AR property of the same film (inset of Figure 6.12). However, the reduced  $V_{oc}$  can be attributed to the existence of defect centres in the native oxide at the AZO/Si interface and ion-beam produced traps on silicon facets. It may be mentioned that AZO/Si heterostructures, in general, yield low  $FF$  values and can be improved by using nanofaceted silicon substrates [59]. Thus, our experimental results suggest that besides tunable AR property (Fig. 6.11),  $FF$  can also be improved by adjusting the AZO overlayer thickness.

Compared to the inverted pyramid approach [60,61], which yields the reflectance values between 3 to 5% for an optimized AR coating thickness between 400 to 1000 nm, our results

show a better (by a factor of 10) performance with a smaller (30 to 75 nm) AZO film thickness. Among the available techniques reported in the literature, our novel approach of fabricating faceted nanostructures is simple and can be seamlessly integrated with the modern thin film solar cell technology for better photon harvesting with the help of proper understanding of AR property of AZO films. For a flat surface having an AR overlayer, using Fresnel's reflection formula, we measured the reflectance at different wavelengths. It is observed that with varying film thickness the position of the reflection minima shifts, while a change in the refractive index modifies the amount of surface reflectance [62]. Although similar trends are quite evident, the experimentally observed average surface reflectance turns out to be much lower over the spectral range under consideration.

In order to explain these results, let us first try to understand the role of the Si template which is practically an ensemble of ion-beam fabricated self-organized conical nanofacets at the top of the Si substrate. It is known that a grating on any surface can be used to achieve arbitrary refractive index if the geometry of the grating structures can be tuned. For instance, if we consider a binary grating, its effective refractive index,  $n_{\text{eff}}$ , can be expressed as  $n_{\text{eff}} = (n_1 - 1)DC + 1$ , where  $n_1$  is the refractive index of the grating and  $DC$  is the duty cycle and is defined as the ratio of the grating line width to the grating period [63]. If the surrounding medium is taken as air and the grating is of the same material as the substrate, the optimized duty cycle (to meet the AR criterion) can be expressed as  $DC = \frac{\sqrt{n_2} - 1}{n_2 - 1}$  where  $n_2$  is the refractive index of the substrate [63]. Such binary gratings are expected to exhibit the AR property over a very narrow spectral range. This range can be broadened by continuous tuning of the refractive index ( $n_{\text{eff}}$ ) between the two surrounding media. This would essentially mean a continuous change in  $DC$  along the depth (from the apex towards the base of the facets) of the grating lines, which is possible to be achieved by having tapered/conical gratings. When the grating and the substrate materials are the same, the matching of refractive index at the substrate interfaces can

exhibit highly improved AR property [64]. This explains the enhanced AR performance observed here for the faceted Si surface formed on the Si substrate. Following the same argument, further improved AR performance is expected due to the conformal growth of an AZO overlayer on nanofaceted Si template. Indeed, the experimental findings confirm the same where increasing AZO thickness leads to a systematic red shift in the reflection minima. However, such small variations in the thickness may not be sufficient to cause any significant difference in depth dependent change of the effective refractive index for the AZO coated faceted Si template which corroborates well with the experimentally measured reflectance minima values.

#### **6.2.1.4 Conclusions**

In conclusion, we show that conformally grown AZO films on ion-beam fabricated self-organized nanofaceted Si templates can work in tandem to yield improved AR performance. It is observed that tunable AR property can be achieved by varying the thickness of AZO overlayer and there exists a critical thickness (60 nm in the present case) which exhibits the best AR performance over the given spectral range (300 to 800 nm). Reduction in surface reflectance for Si templates can be understood in light of gradient refractive index effect arising from a continuous change in the effective refractive index along the depth (from the apex towards the base of the facets) and refractive index matching at the substrate interface because of self-organized nanofaceted Si structures. Following the same argument, further enhancement in the AR performance is observed due to conformal growth of AZO overlayers on Si templates. This is accompanied by a thickness-dependent systematic red shift in the reflection minima. The fabricated AZO/Si heterostructures, both on planar and faceted silicon, show significant photoresponsivity where thickness-dependent fill factor increases by a factor up to three owing to improved light absorption in the latter case. This study indicates that

conformally grown AZO overlayer on nanofaceted silicon may be a promising candidate as AR coatings by optimizing the process parameters.

## **6.2.2 Thickness-controlled photoresponsivity of ZnO:Al/Si heterostructures : Role of junction barrier height**

### **6.2.2.1 Introduction**

Metal-oxide-semiconductors (MOS) have attracted much attention in optoelectronic applications due to their unique optical and electrical properties [65]. For instance, ZnO is considered to be a promising material for light-emitting diodes, laser diodes, photodetectors, and solar cells [65]. Due to several issues like deep acceptor levels and low dopant solubility, reproducible fabrication of *p*-type ZnO for *p-n* homojunctions is difficult and thus, it gives rise to the need for ZnO/Si heterojunctions. It may be noticed that the conductivity of *n*-type ZnO can be enhanced up to three to four orders of magnitude after doping with Group-III elements (especially Al) [43]. In fact, due to a mismatch in the work functions of Si (~4.2 eV) and AZO (~4.8 eV), a potential barrier is formed where the barrier height depends not only on the work functions but also on AZO thickness [66,53]. Although *I-V* characteristics of AZO/Si heterojunctions are well-studied [66,53], effect of AZO thickness on the potential barrier at AZO/nanostructured-Si interface and in turn change in photoresponsivity is yet to be studied in a systematic manner. Since AZO films deposited on Si nanostructured surfaces show promising optical properties [47], it will be important to grow AZO overlayers on textured Si surface and study their optoelectronic properties.

Ion-beam induced self-organization process is a fast and cost-effective way to synthesize various nanopatterns over a large area in a single step [52]. In the present study, we have used ion-beam fabricated nanofaceted-Si as the template for growing AZO films of various

thicknesses (in the range of 30-75 nm). AZO/nanofaceted-Si heterojunction properties were investigated by employing current–voltage ( $I$ - $V$ ) and capacitance–voltage ( $C$ - $V$ ) measurements whereas the photoresponsivity of  $n$ -AZO/ $p$ -faceted-Si heterostructures were studied as a function of AZO overlayer thickness. In fact, as a novelty, we show AZO thickness-dependent tunable photoresponsivity of AZO/nanofaceted-Si heterojunctions and correlated this behaviour with decrease in corresponding junction barrier heights.

### 6.2.2.2 Experimental

In the present study, we used 500 eV Ar-ions to fall on  $p$ -Si surface at an oblique incidence of  $72.5^\circ$ , resulting in nanoscale facet formation of nanofaceted arrays at the surface [52]. A commercial target composed of ZnO:Al<sub>2</sub>O<sub>3</sub> (2 wt.%) was used for pulsed dc magnetron sputter deposition of AZO films on nanofaceted-Si at room temperature with argon gas flow rate of 30 sccm (working pressure of  $5 \times 10^{-3}$  mbar). The distance from the sample to the target was 10 cm, and the power was maintained at 100 W. Three different film thicknesses (in the range of 30 to 75 nm) were simultaneously deposited on nanofaceted as well as pristine Si substrates [53]. Field emission gun scanning electron microscopy (FEGSEM) [Carl Zeiss, Germany] and atomic force microscopy (AFM) [Asylum Research, USA] were employed to study the respective sample microstructure and surface morphology. For each sample, several AFM images were collected from various places (including the edges and the central part of the films), confirming the homogeneity of our films. AFM images were analyzed by using Gwyddion software [28]. Photoresponsivity studies were carried out by using a spectral response system [Sciencetech, Canada] under air mass 0 and 1 sun illumination conditions in the spectral range of 300 to 800 nm. Silver paste (~2 mm in diameter) was used to make electrical contacts on the top of AZO films and the back side of the Si substrates. Formation of Ag/AZO/nanofaceted-Si/Ag heterostructure diodes was verified by taking  $I$ - $V$  characteristics using a source meter [Keithley 2410]. In addition, the junction barrier height was investigated

by performing capacitance-voltage ( $C$ - $V$ ) measurements using a precision LCR meter [HP 4284A].

### 6.2.2.3 Results and discussion

Figures 6.13(a) and (b) show AFM images corresponding to nanofaceted Si substrate and 75 nm AZO film grown on the same. It is observed that with increasing film thickness, the sharp Si nanofacets transform into a bit rounded ones. However, no significant change in the root mean square (rms) surface roughness is observed with increasing film thickness (Table 6.4).

**Table 6.4** List of parameters calculated from AFM,  $I$ - $V$ , and  $C$ - $V$  measurements

Sample	AFM	I-V			C-V
AZO on faceted Si*	Roughness (nm)	Turn-on potential (V)	Series resistance (k $\Omega$ )	Ideality factor ( $\eta$ )	Barrier height (eV)
30 nm	49.53	2.01	48.8	2.3	0.90
60 nm	52.48	1.42	10.4	2.8	0.72
75 nm	51.7	0.93	1.1	3.48	0.41

\*Nanofaceted Si has rms roughness of 52.21 nm

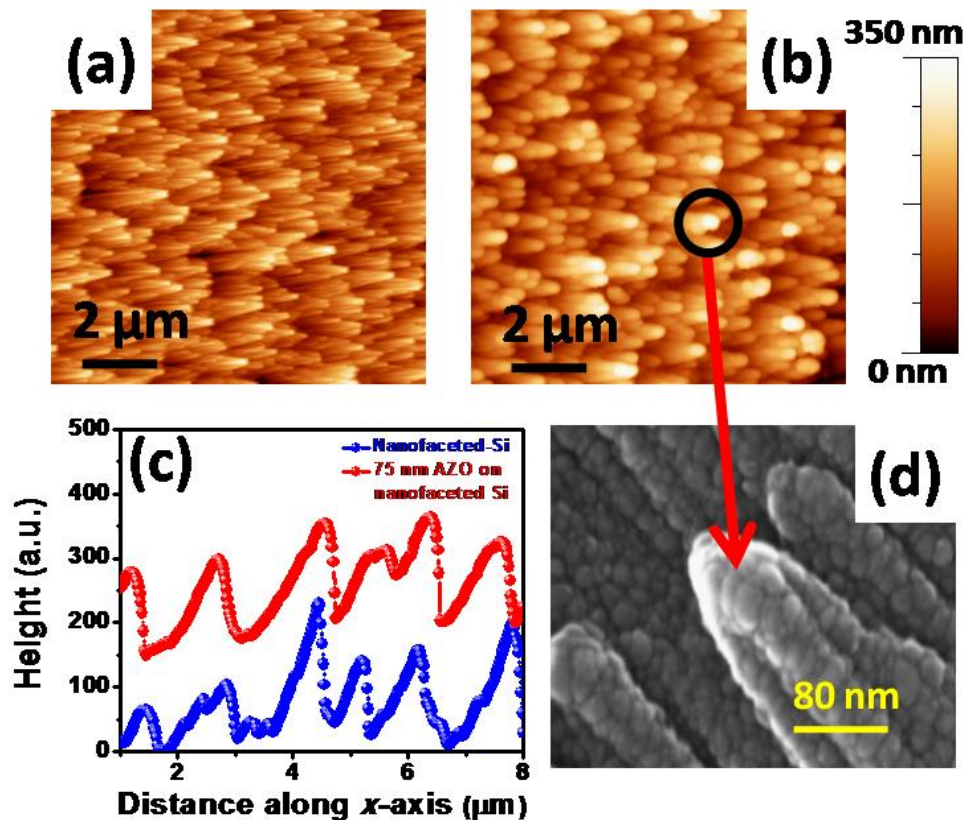


Figure 6.13: AFM images corresponding to (a) nanofaceted-Si template and (b) 75 nm AZO grown on nanofaceted-Si. Line profiles drawn on (a) and (b) are shown in (c) and (d) shows a high-resolution SEM image of (b).

Line profiles drawn on Figs. 6.13(a) and (b) confirm the conformal growth of AZO films [Fig 6.13(c)]. In addition, a high-resolution plan-view SEM image, corresponding to Fig. 6.13(b), is also shown in Fig. 6.12(d) where a magnified portion of the facet-apex ensures the conformity and the closely packed granular nature of the AZO film (with average grain size ~25 nm).

Prior to the electrical characterization of AZO/nanofaceted-Si heterojunction, the Ohmic nature of the silver contact with AZO was confirmed from the linear  $I$ - $V$  characteristics [53]. However,  $I$ - $V$  characteristics of all the Ag/AZO/nanofaceted-Si/Ag heterojunction diodes show a rectifying property [Fig. 6.14(a)] where schematic view of such a diode is depicted in the inset. It is seen that with increasing AZO thickness, the turn-on potential decreases systematically from 2.02 to 0.93 V. The diode ideality factor ( $\eta$ ) and its series resistance ( $R_s$ ) were calculated and listed in Table 6.4 where one sees a clear increase in  $\eta$  with increasing AZO overlayer thickness, indicating a degradation of diode characteristics. Due to a large lattice mismatch between the AZO layer and Si(100) substrate, dislocations appearing at the AZO/Si interface can lead to an increase in  $\eta$ . Since the AZO/Si interface plays an important role in carrier injection, we believe that AZO thickness-dependent increase in  $\eta$  is most likely associated with the minority carrier injection and recombination [53]. This is consistent with the increase in reverse saturation current ( $I_0$ ) with increasing AZO film thickness which in turn takes part in suppressing the turn-on potential by decreasing the barrier height at the AZO/Si interface.

The barrier height,  $\phi_B$ , at a temperature  $T$  can be determined from  $I_0 = A^* S T^2 \exp(-\phi_B/k_B T)$ , where  $S$  is the surface area of the diode,  $k_B$  is Boltzmann constant, and  $A^*$  is Richardson constant [53]. Since the presence of a thin native  $\text{SiO}_x$  at the interface of AZO/nanofaceted-Si heterojunction cannot be avoided, the calculated  $\phi_B$  may be incorrect. Thus, in order to determine the actual  $\phi_B$ ,  $C$ - $V$  measurements, at a frequency of 1 MHz, by sweeping 6 to -6 V

were carried out. Figure 6.14(b) shows the  $1/C^2$ - $V$  plot where the extrapolated straight line intercept of  $1/C^2$  on the  $V$ -axis turns out to be the measure of  $\phi_B$ . The calculated values of  $\phi_B$  corresponding to different AZO overlayer thicknesses are listed in Table 6.4 where an increasing barrier height results due to a decrease in the film thickness. Thus, the reduction in the turn-on potential as a function of AZO thickness (mentioned above) in case of AZO/Si heterojunction diodes can be attributed to the reduced barrier height. It is noticed that a similar behavior, viz. reduction in the turn-on potential was reported for AZO films deposited on pristine Si substrate as well [53]. However, the turn-on potential obtained in the present case is reduced by a factor of 1.5 in comparison to the same thickness of AZO films deposited on pristine Si substrate which may be attributed due to interface effect arising from different morphologies of the substrates.

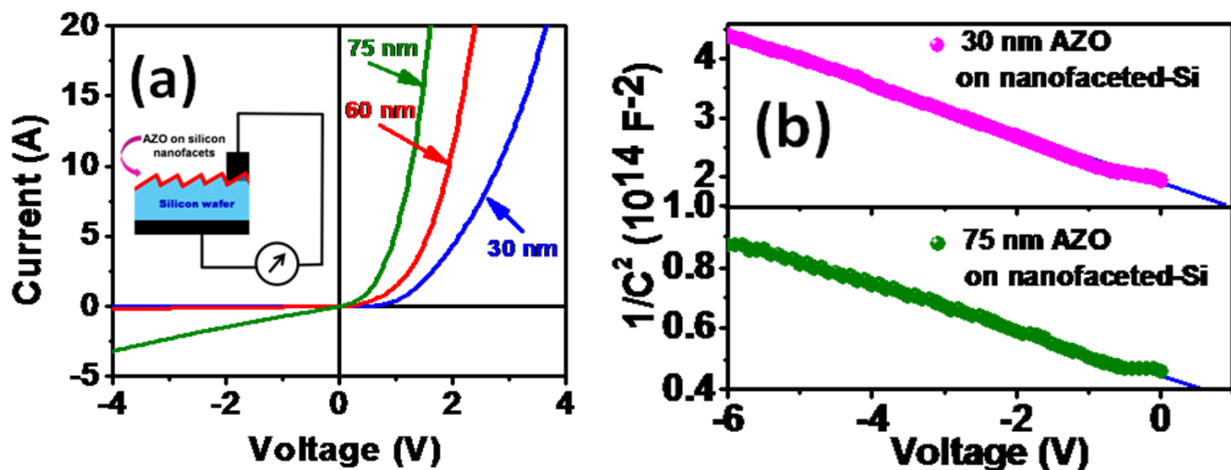


Figure 6.14: (a) Thickness-dependent nonlinear  $I$ - $V$  characteristics where the inset shows a schematic view of an AZO/Si heterojunction diode. (b)  $1/C^2$ - $V$  characteristics for different AZO film thicknesses.

In order to understand the role of the barrier height, in particular for optoelectronics applications, we measured the photoresponsivity at different wavelength ranges. It is known that AZO/Si heterostructure devices, in general, yield low photoresponsivity. Figure 6.15

shows the photoresponsivity spectra under a forward bias of 0.5 V corresponding to different AZO overlayer thicknesses where an increment in the photoresponsivity with AZO thickness is observed. As a matter of fact, the energy band-diagram of AZO/Si heterojunction, under forward bias, shows a valence band offset of 2.55 eV which is greater than the conduction band offset of 0.4 eV [66]. Since the transmittance of AZO on a glass substrate was measured to be ~80% in the visible range, visible light gets absorbed in the underlying *p*-Si substrate (decorated by nanofaceted arrays on its surface) after transmitting through the AZO overlayer and generates electron-hole pairs inside Si. The electric field drives the photo-generated holes towards *n*-AZO but they face the potential barrier across the interface of the heterojunction. It is evident from the inset of Fig. 6.15 that the barrier height decreases with increasing AZO overlayer thickness, and hence, the photo-generated holes can overcome the interface barrier more easily at a higher AZO thickness (e.g. 75 nm) in comparison to the lower one (30 nm).

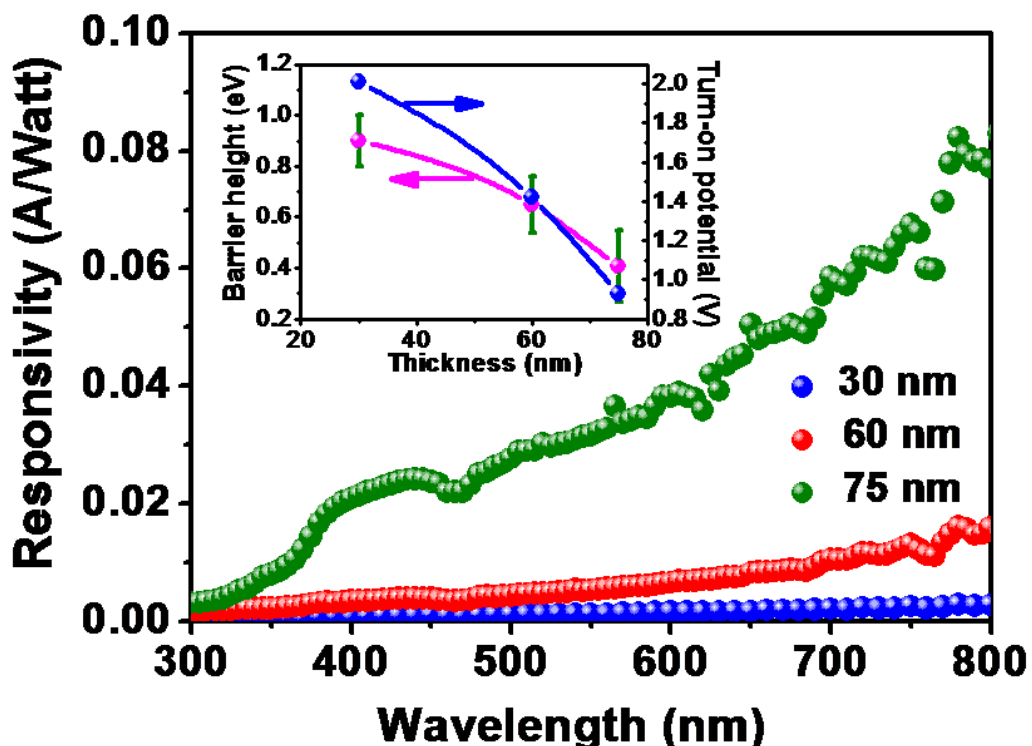


Figure 6.15: Thickness-dependent photoresponsivity spectra in the wavelength range of 300-800 nm. The inset shows variation in the barrier height and turn-on potential as a function of AZO thickness.

The easy conduction of photo-generated carriers leads to the overall enhancement in the photoresponsivity as a function of AZO overlayer thickness.

#### 6.2.2.4 Conclusions

In summary, we fabricated AZO/Si heterojunction diodes where ion-beam sputtered nanofaceted *p*-Si templates were used for conformal growth of *n*-AZO overlayers by pulsed dc magnetron sputtering. *I-V* characteristics and photoresponsivity were studied as a function of film thickness. It is observed that with increasing AZO thickness, turn-on potential of the present *n*-AZO/*p*-Si diodes decreases (by a factor of ~2) whereas photoresponsivity enhances significantly (up to a factor of ~5). The observed thickness-dependent photoresponsivity is attributed to the decrease in AZO/nanofaceted-Si junction barrier height. The results are quite promising for the fabrication of AZO-based advanced optoelectronics devices.

## Bibliography

1. A. B. Djurišić, A. M. C. Ng, X. Y. Chen, *Prog. Quant. Electron.* 34 (2010) 191.
2. Z. L. Wang, *Appl. Phys. A* 88 (2007) 7.
3. D. S. Ginley, H. Hosono, D. C. Paine, *Handbook of Transparent Conductors* (Springer, New York, 2010).
4. A. Sandhu, *Nat. Photonics* 1 (2007) 38.
5. A. Tsukazaki *et al.*, *Nat. Mater.* 4 (2005) 42.
6. B. Monemar, *Phys. Rev. B* 10 (1974) 676.
7. S. W. Koch, M. Kira, G. Khitrova, H. M. Gibbs, *Nat. Mater.* 5 (2006) 523.
8. Z-M Liao *et al.*, *Sci. Rep.* 2 (2012) 452.
9. K. Johnston, M. O. Henry, D. McCabe, E. McGlynn, M. Dietrich, E. Alves, M. Xia, *Phys. Rev. B* 73 (2006) 165.
10. G. D. Scholes, G. Rumbles, *Nat. Mater.* 5 (2006) 683.

11. M. A. Zimmler, T. Voss, C. Ronning, F. Capasso, *Appl. Phys. Lett.* 94 (2009) 241120.
12. Y. S. Choi, J. W. Kang, D. K. Hwang, S. J. Park, *IEEE Trans. Electron. Dev.* 57 (2010) 26.
13. R. D. Schaller, V. M. Agranovich, V. I. Klimov, *Nat. Phys.* 1(2005) 189.
14. V. I. Klimov, A. A. Mikhailovsky, S. Xu, A. Malko, J. A. Hollingsworth, C. A. Leatherdale, H.-J. Eisler, M. G. Bawendi, *Science* 290 (2000) 314.
15. T. D. Krauss, *Nature* 447 (2007) 385.
16. H. Zhao, W. Xiong, M. Z. Zhu, *Int. J. Mod. Phys. B* 21 (2007) 5237.
17. H. M. Cheng, K. F. Lin, H. C. Hsu, W. F. Hsieh, *Appl. Phys. Lett.* 88 (2006) 261909.
18. L. Dallali, S. Jaziri, J. El Haskouri, P. Amorós, *Superlattice. Microst.* 46 (2009) 907.
19. J. C. Nie, J. Y. Yang, Y. Piao, H. Li, Y. Sun, Q. M. Xue, C. M. Xiong, R. F. Dou, Q. Y. Tu, *Appl. Phys. Lett.* 93 (2008) 173104.
20. T. W. H. Oates, *Appl. Surf. Sci.* 258 (2012) 9278.
21. C. Martella, D. Chiappe, P. D. Veneri, L. V. Mercaldo, I. Usatii, and F. B. de Mongeot, *Nanotechnol.* 24 (2013) 225201.
22. T. Som and D. Kanjilal, *Nanofabrication by Ion-Beam Sputtering: Fundamentals and Applications* (Pan Stanford, Singapore. 2012)
23. M. Ranjan, S. Facsko, T. Dekorsy, C. Trappe, and H. Kurz, *Microelectron. Eng.* 53 (2000) 245.
24. T. Basu, M. Kumar, P. K. Sahoo, A. Kanjilal, and T. Som, *Nanoscale Res. Lett.* 9 (2014) 192.
25. T. Basu, J. R. Mohanty, T. Som, *Appl. Surf. Sci.* 258 (2012) 9944.
26. M. Kumar, A. Kanjilal, T. Som, *AIP Adv.* 3 (2013) 092126.
27. [www.nanotec.es/products/wsxm/](http://www.nanotec.es/products/wsxm/)
28. <http://gwyddion.net/>

29. L. Xu, B. Wei, W. Liu, H. Zhang, C. Su, J. Che, *Nanoscale Res. Lett.* 8 (2013) 536;  
JCPDS Card No. 36-1451.
30. M. N. Islam, T. B. Ghosh, K. L. Chopra, H. N. Acharya, *Thin Solid Films* 280 (1996) 20.
31. H. B. Fan, S. Y. Yang, P. F. Zhang, H. Y. Wei, X. L. Liu, C. M. Jiao, Q. S. Zhu, Y. H. Chen, Z. G. Wang, *Chin. Phys. Lett.* 24 (2007) 2108.
32. T. P. Rao, M. C. S. Kumar, A. Safarulla, V. Ganesan, S. R. Barman, C. Sanjeeviraja, *Physica B* 405 (2010) 2226.
33. A. Uedono, T. Koida, A. Tsukazaki, M. Kawasaki, Z. Q. Chen, S.F. Chichibu, H. Koinuma, *J. Appl. Phys.* 93 (2003) 2481.
34. A. G. Holmes-Siedle, *Nature* 250 (1974) 689.
35. A. B. Djurišić, Y. H. Leung, K. H. Tam, Y. F. Hsu, L. Ding, W. K. Ge, Y. C. Zhong, K. S. Wong, W. K. Chan, H. L. Tam, K. W. Cheah, W. M. Kwok, D. L. Phillips, *Nanotechnol.* 18 (2007) 095702.
36. Y. Wang, Q. Y. Xu, X. L. Du, Z. X. Mei, Z. Q. Zeng, Q. K. Xue, Z. Zhang, *Phys. Lett. A* 320 (2004) 322.
37. M. W. Allen, D. Y. Zemlyanov, G. I. N. Waterhouse, J. B. Metson, T. D. Veal, C. F. McConville, S. M. Durbin, *Appl. Phys. Lett.* 98 (2011) 101906.
38. H. S. Taylor, *Nature* 128 (1931) 636.
39. H. Zhou *et al.*, *Physica Status Solidi B* 229 (2002) 825.
40. Geoffrey K. H. Pang, K. Z. Baba-Kishi, A. Patel, *Ultramicroscopy* 81 (2000) 35.
41. K. Schulze, B. Maennig, K. Leo, Y. Tomita, C. May, J. Hüpkes, E. Brier, E. Reinold, P. Bäuerle, *Appl. Phys. Lett.* 91(2007) 073521.
42. G. B. Murdoch, S. Hinds, E. H. Sargent, S. W. Tsang, L. Mordoukhovski, Z. H. Lu, *App. Phys. Lett.* 94 (2009) 213301.

43. J. G. Lu, Z. Z. Ye, Y. J. Zeng, L. P. Zhu, L. Wang, J. Yuan, B. H. Zhao, Q. L. Liang, J. Appl. Phys. 100 (2006) 073714.
44. O. Lupan, S. Shishiyanu, V. Ursaki, H. Khallaf, L. Chow, T. Shishiyanu, V. Sontea, E. Monaco, S. Railean, Sol. Energy Mat. Sol. C. 93 (2009) 1417.
45. S. Strehlke, S. Bastide, C. Levy-Clément, Sol. Energy Mat. Sol. C 58 (1999) 399.
46. J. W. Leem, Y. M. Song, Y. T. Lee, J. S. Yu, Appl. Phys. B 99 (2010) 695.
47. S-W Jee, S-J Park, J. Kim, Y. C. Park, J-H Choi, J-H Jeong, J-H Lee, Appl. Phys. Lett. 99 (2011) 053118.
48. E. B. Grann, M. G. Moharam, and D. A. Pommet, J. Opt. Soc. Am. A 12 (1995) 333.
49. J-Q Xi, M. F. Schubert, J. K. Kim, E. F. Schubert, M. Chen, S-Y Lin, W. Liu, and J. A. Smart, Nat. Photonics 1 (2007) 176.
50. J. W. Leem, D. H. Joo, and J. S. Yu, Sol. Energy Mat. Sol. C. 95 (2011) 2221.
51. L. Sainiemi, V. Jokinen, A. Shah, M. Shpak, S. Aura, P. Suvanto, and S. Franssila, Adv. Mat. 23 (2011) 122.
52. T. Basu, D. P. Datta, and T. Som, Nanoscale Res. Lett. 8 (2013) 289.
53. M. Kumar, A. Kanjilal, and T. Som, AIP Adv. 3 (2013) 092126.
54. M. I. Mendelson, J. Am. Ceram. Soc. 52 (1969) 443.
55. A. V. Tikhonravov, M. K. Trubetskov, T. V. Amotchkina, and J. A. Dobrowolski, Appl. Opt. 47 (2008) C124.
56. S. A. Boden, D. M. Bagnall, Appl. Phys. Lett. 93 (2008) 133108.
57. P. Yi-Hao, F-S Meng, C-J Lin, H-C Kuo, S-H Hsu, Chang Yia-Chung, and G-R Lin, Nanotechnol. 20 (2009) 035303.
58. X. Yu, X. Yu, J. Zhang, Z. Hu, G. Zhao, Y. Zhao, Sol. Energy Mat. Sol. C. 121 (2014) 28.

59. L. Shen, Z. Q. Ma, C. Shen, F. Li, B. He, F. Xu, *Superlattice Microstruct.* 48 (2010) 426.
60. J. Y. Lee and S. W. Glunz, *Sol. Energy Mat. Sol. C.* 90 (2006) 82.
61. J. Zhao, A. Wang, P. P. Altermatt, S. R. Wenham, and M. A. Green, *Sol. Sol. Energy Mat. Sol. C.* 41 (1996) 87.
62. <http://pveducation.org/pvcdrom/design/anti-reflection-coatings>
63. B. Päiväranta, P. K. Sahoo, E. Tocce, V. Auzelyte, Y. Ekinici, H. H. Solak, C-C Liu, K. O. Stuen, P. F. Nealey, C. David, *ACS Nano* 5 (2011) 1860.
64. Y. Ono, Y. Kimura, Y. Ohta, and N. Nishida, *Appl. Opt.* 26 (1987) 1142.
65. K. Ellmer, A. Klein and B. Rech, *Transparent Conductive Zinc Oxides: Basics and Applications in Thin Film Sol. C.* (Springer, Berlin, 2007).
66. M. Dutta and D. Basak, *Appl. Phys. Lett.* 92 (2008) 212112.

---

# CHAPTER 7

---

## 7. Summary and future scope

In summary, we have carried out extensive experimental investigations on the evolution of self-organized nanoscale patterns (mostly ripples and facets) on silicon surface during low energy ion irradiation. Besides understanding the underlying mechanisms giving rise to such nanopatterns, work was also carried out to realize the potential applications of nano-facets in the form of anti-reflecting surfaces and field emitters. Further, in order to make use of the anisotropic morphology of the patterned surfaces to tune optical, electrical, and photovoltaic properties of functional thin film(s), we have performed some case studies through conformal growth of Al-doped ZnO (AZO) thin films on rippled- and nanofaceted-Si.

In this thesis, in the introduction, we have outlined the ion-induced nanopatterning and the scope of the process in synthesis and modification of materials, with a special emphasis on different shortcomings in the existing theoretical models and experimentation. The experimental techniques used to perform the studies presented in this thesis were described in the next chapter. Subsequently, the statistical methods of characterization of surfaces were briefly introduced and the existing theoretical models of ion-induced surface evolution were outlined.

Our in-depth study reveals hitherto unobserved aspects of low energy ion-beam induced pattern evolution. In particular, we have experimentally shown the validity of the solid flow model (over a large angular window – wherever parallel-mode ripples exist) in predicting the intrinsic timescale without involving into the complicated calculation of stress gradient term. Extensive experimentations were carried out to identify the critical angle for ripple formation along with

linear and nonlinear regimes of ripple evolution. In the linear regime, roughness grows exponentially and ripple wavelengths remain constant, whereas in the nonlinear regime, in general, ripple coarsening is observed. In the nonlinear regime, our angle-dependent study reveals ripple rotation through a series of intermediate pattern formation. These include a very special case of ripple to facet transition over a narrow angular window of  $\theta=70^\circ$  to  $72.5^\circ$ . This particular observation pattern formation has been attributed to the shadowing of incident ions by the surface features. We have also shown a coarsening of facets which is explained by taking into account non-local phenomenon like reflection of primary ions from to its neighbouring facets. We have also checked the role of concurrent substrate rotation during ion irradiation. In this process, we have shown that the flat surface remains flat whereas ripples and facets gets transformed into mounds. In the linear regime, under substrate rotation, a reduction in the rms roughness is observed compared to the static case which can be explained by a linear partial differential equation proposed for rotating substrates. For the first time, we have observed “interrupted coarsening” behaviour of mounds under concurrent substrate rotation. Based on our experimental results, we have created a parametric phase diagram (energy,  $E$ , versus angle of incidence,  $\theta$ , plot) which summarizes an overview of pattern formation on silicon surface under low energy ion irradiation for static and rotating substrate conditions.

From the microstructural analysis of nanostructured-Si surfaces, we have confirmed the amorphization of the top layer in case of ripples, whereas in case of facets, valleys remained crystalline with the presence of an ultra-thin native oxide layer on top of the facet apexes. Compositional analysis revealed no metallic impurity in the near-surface region. We have demonstrated that the observed facets shows anti-reflection and room temperature photoluminescence properties. The antireflection property is explained in the light of the graded refractive index effect, while the photoluminescence is attributed to various defect-related luminescence centres present at the  $\text{SiO}_x/\text{Si}$  interface. Fluence-dependent optical studies

reveal that the antireflective Si nanofacets actually help in enhancing the photoluminescence by orders of magnitude. In addition, as a case study, we have also demonstrated that the nanofacets are capable of giving rise to field emission property at room temperature. In the process of understanding the origin of field emission from nanofacets, by using AFM-based dual pass tunnelling current microscopy (DPTCM), we have discovered that the apexes of the Si nanofacets do not contribute to the field emission since they are covered by ultra-thin layer of native oxide.

From the application point of view, we have also used rippled- and nanofaceted-Si templates for conformal growth of AZO overlayers. AZO overlayers, grown on rippled-Si demonstrate thickness-dependent blue shift of the free excitonic peak in photoluminescence spectra. The observed blue shift is attributed to the quantum confinement effect, resulting from the AZO grain size and their spatial arrangement on rippled-Si surface. On the other hand, AZO films grown on faceted-Si shows a tunable antireflection property as a function of thickness. An optimized thickness of 60 nm shows the maximum reduction in the surface reflectance. At the same time, photoresponsivity studies reveal an enhancement in the fill factor by a factor of 2.5 (compared to same thickness of AZO grown on pristine-Si surface) in case of 60 nm AZO deposited on nanofaceted-Si. It has been pointed out that improved anti-reflection property drives AZO/nanofaceted-Si heterojunction towards a higher fill factor. In addition, the role of junction barrier height towards thickness-dependent enhancement in the photoresponsivity has also been presented.

Thus, a comprehensive study of low energy ion-induced ripple pattern evolution on silicon surface and their prospective applications are presented in this thesis. The physical processes leading to ripple formation have also been pointed out. Based on our results, further experimental investigations can be taken up which will lead to a much deeper understanding of this self-organized patterning process, needed for optimization of features for particular

applications. For instance, the pattern formation at higher oblique angle of incidence ( $\theta > 67^\circ$ ) needs to be checked by using other ion species (like Kr and Xe) which will help to understand the contribution of sputtering in ripple formation in greater detail. It is also imperative to carry out low energy ion irradiation of Silicon by using other projectiles like Kr, Xe and O to have a better understanding of facet formation at higher incidence angles. From the structural point of view, by varying the incidence ion energy and tuning the thickness of the amorphous layer on top of the ripples offers a possibility of decorating it with metal particles having unique electronic, optoelectronic, or magnetic properties. Statistical analysis of ripples and facets should be important for understanding the scaling behaviour which may help to develop patterned surfaces for particular applications by varying the fluence and angle of incidence. Similarly, there is a room to study the morphological parameters at higher fluences and subsequently tune the wettability of patterned surfaces. It may be mentioned that, our studies on the variation of rotational speed during irradiation could not be extended for larger rotational speed due to instrumental limit. However, it remains as a future scope to check the effect of rotational speed variation over a wider range.

From the application perspective, low temperature photoluminescence measurement can be carried out to understand the role of defects accurately. In addition, a fluence-dependent field emission measurement may lead to a tunability of the field emission property which would be exigent for device fabrication. It would be also exciting to use nanofaceted-Si substrates to grow other materials (other than AZO) towards enhancing the solar cell efficiency.

# **Ion-beam induced nanostructuring of silicon and its applications**

**Name:** Tanmoy Basu

**Institute Name:** Institute of Physics, Bhubaneswar

## **Abstract**

Low energy ion-beam induced self-organized nanostructure formation at surfaces has attracted interest due to its potential application as templates for deposition of functional thin films. From the material point of view, silicon is one of the most studied materials for its obvious importance in industrial applications. However, a systematic study of low energy ion induced pattern evolution in silicon, with particular attention to the features formed at higher oblique incidence angles of the ion-beam remains unexplored till date. For example, ripple evolution with a proper prediction of the time scale for demarcation of linear and nonlinear regime needs attention. In addition, the effect of shadowing at higher oblique incidences has not been touched upon till date. Therefore, addressing these issues are essential for applying those patterns towards nanofunctionalization.

In this thesis, formation of self-organized surface patterns and its understanding have been revisited in case of silicon. In brief, morphological evolution on silicon surface by varying ion-energy, -incidence angle, -fluence, and -flux has been studied. Singly charged low energy argon ions (250-1750 eV) are used for the present work. The surface morphological evolution on Si surface was evaluated primarily by atomic force microscopy (AFM) which is duly complemented by scanning electron microscopy (SEM) and transmission electron microscopy (TEM). Rigorous experimentation was carried out to show that starting from normally incident ions to obliquely incident ions up to  $50^\circ$  and beyond  $80^\circ$  silicon surface remains stable (i.e. no pattern formation takes place), while patterns evolve in the angular window of  $51^\circ$  to  $77.5^\circ$ . The observed patterns (in the form of parallel-mode ripples) in the above angular window has been modelled using a linear continuum theory-based *solid flow model*. With the help of this model, the linear and nonlinear regimes of pattern formation are identified. In fact, detail study reveals that in the linear regime, ripple wavelength remains constant with time (ion fluence), while in the nonlinear regime, ripple coarsening takes place with increasing ion fluence. On the other hand, in the angular range of  $70^\circ$  to  $72.5^\circ$ , due to ion-beam shadowing effect, ripples undergo a transition to faceted structures in the nonlinear regime. Further, morphological evolution (over the entire angular window of  $0^\circ$  to  $85^\circ$ ) under concurrent substrate rotation shows that a stable surface remains stable, while ripples undergo a transition to mound structures. This was modelled to address the underlying mechanisms behind these observations.

We have further measured different physical properties of faceted structures, viz. anti-reflection, photoluminescence, and field emission. With the help of dual pass tunnelling current microscopy (DPTCM) and scanning Kelvin probe force microscopy (SKPM), we have identified that field emission takes place primarily from the sidewalls and valleys of the facets, which is explained on the basis of the presence of a native oxide layer at the apexes of the facets (duly confirmed from TEM studies). In context of utilizing the patterned substrates as templates, the efficacy of ripple-patterned and faceted silicon were used for conformal growth of aluminium-doped zinc oxide (AZO) thin films. AZO thin films grown on rippled-Si substrates show blue shift up to a critical thickness of AZO overlayer (in contrast to similar thicknesses grown on flat-Si substrates), which is attributed to the morphological anisotropy-driven quantum confinement effect. On the other hand, films grown on faceted-Si substrates exhibit an enhanced anti-reflection property (compared to the bare faceted-Si substrates), followed by a thickness-dependent red shift in the reflection minima. Thickness-dependent tunable anti-reflection property is understood in light of depth-dependent refractive index. Further, enhancements in fill factor and photoresponsivity from such heterostructures (*n*-AZO/faceted *p*-Si) are demonstrated which corroborate well with the critical thickness that shows maximum anti-reflection property. The present thesis thus, shows the importance of using patterned-Si substrates to bring around change in various functional properties materials.

### List of Publications on which the thesis is based

1. Tailoring room temperature photoluminescence of antireflective silicon nanofacets by **T. Basu**, M. Kumar, A. Kanjilal, J. Ghatak, P.K. Sahoo, and T. Som: *Journal of Applied Physics* 114 (2014) 114309.
2. Thickness-controlled photoresponsivity of ZnO:Al/Si heterostructures: Role of junction barrier height by **T. Basu**, M. Kumar, and T. Som: *Materials Letters* 135 (2014) 188
3. Tunable antireflection from conformal Al-doped ZnO films on nanofaceted Si templates by **T. Basu**, M. Kumar, P.K. Sahoo, A. Kanjilal, and T. Som: *Nanoscale Research Letters* 9 (2014) 192.
4. Temporal evolution of ripple pattern on silicon surface: An ion induced solid flow approach by **T. Basu**, and T. Som: *Applied Surface Science* 310 (2014) 142.
5. Transition from ripples to faceted structures under low-energy argon ion bombardment of silicon: Understanding the role of shadowing and sputtering by **T. Basu**, D.P. Datta, and T. Som: *Nanoscale Research Letters* 8 (2013) 289.
6. Unusual pattern formation on Si(100) due to low energy ion bombardment by **T. Basu**, J.R. Mohanty, and T. Som: *Applied Surface Science* 258 (2012) 9944.

### To be communicated

1. Roughness engineering using continuous substrate rotation during sputtering of silicon, **T. Basu**, M. Kumar, R.M. Bradley, and T. Som.
2. Field emission from Si nanofacets: Role of native oxide layer, **T. Basu**, M. Kumar, and T. Som.
3. Substrate morphology-driven shift in excitonic peak of Al-doped ZnO nanobeads on rippled silicon surface, **T. Basu**, M. Kumar, S. Nandy, B. Satpati, and T. Som.